



UNIVERSIDADE D
COIMBRA

Rafael Tiago Pereira Martins Aroso

**COMPUTATIONAL DESIGN AND SYNTHESIS
OF MOLECULES FOR APPLICATION IN
ANTIMICROBIAL THERAPIES**

**Tese no âmbito do doutoramento em Química, ramo de Química
Médica orientada pela Professora Doutora Maria Miguéns
Pereira, co-orientada pelo Professor Doutor Mário José Ferreira
Calvete e apresentada ao Departamento de Química da Faculdade
de Ciências e Tecnologia da Universidade de Coimbra**

Abril de 2022

Universidade de Coimbra
Departamento de Química - Faculdade de Ciências e Tecnologia

COMPUTATIONAL DESIGN AND SYNTHESIS OF MOLECULES FOR APPLICATION IN ANTIMICROBIAL THERAPIES

Rafael Tiago Pereira Martins Aroso

Tese no âmbito do doutoramento em Química, ramo de Química Médica orientada pela Professora Doutora Maria Miguéns Pereira, co-orientada pelo Professor Doutor Mário José Ferreira Calvete e apresentada ao Departamento de Química da Faculdade de Ciências e Tecnologia da Universidade de Coimbra

Abril de 2022

Agradecimentos

A conclusão desta etapa da minha formação académica só foi possível devido a um vasto conjunto de pessoas com quem contactei e que me enriqueceram pessoalmente e profissionalmente. A todos aqueles que contribuíram de forma direta ou indireta para o meu sucesso científico, gostaria de expressar os meus mais sinceros agradecimentos.

Em primeiro lugar, gostaria de agradecer à professora Mariette Pereira pela sua orientação ao longo destes anos. Muito obrigado por todos os conhecimentos que me transmitiu, pela incessante ajuda e disponibilidade, que tiveram um papel fundamental para o sucesso do meu percurso académico e, em particular, desta etapa.

Ao professor Mário Calvete pela co-orientação deste trabalho, por estar sempre disponível para me ajudar, e pela boa disposição. Muito obrigado por todo o apoio dado durante o meu doutoramento e, em particular, na escrita desta dissertação.

Aos professores Luís Arnaut e Rui Moreira pela criação do programa doutoral MedChemTrain, do qual orgulhosamente fiz parte. Agradeço o apoio financeiro à Fundação para a Ciência e Tecnologia (FCT) pela bolsa concedida com a referência PD/BD/143123/2019.

À professora Gabriela Jorge da Silva por me ter aberto as portas do seu laboratório de microbiologia, pela simpatia e conhecimentos que me transmitiu. Um agradecimento aos seus alunos pelo apoio que me deram e, em particular, ao Tiago pelas imensas repicagens de bactérias e enorme espírito de entreajuda. À Sandra pelo importantíssimo apoio ao meu trabalho de microbiologia e por todas as conversas aluadas e divertidas.

Gostaria também de agradecer à professora Rita Guedes pela colaboração e apoio na área de química computacional durante a minha estadia na Faculdade de Farmácia da Universidade de Lisboa. À professora Ana Paula Leandro e Catarina Madeira por terem efetuado os ensaios bioquímicos de inibição da *E. coli* DNA girase.

Ao professor Vanderlei Bagnato do Centro de Pesquisa em Óptica e Fotónica (CEPOF) e seus colaboradores Kate Blanco, Fernanda Alves e Jennifer Soares pelas contribuições efetuadas no âmbito dos estudos da fototerapia dual e, em particular, pela condução dos estudos em animais.

Ao Fábio Schaberle pelo apoio prestado nos estudos de fotofísica e fotoquímica e pelo auxílio na aquisição, manutenção e medição das fontes de luz, essenciais para os meus ensaios biológicos.

Ao professor Rui Brito e ao Pedro Cruz do serviço de Ressonância Magnética Nuclear (RMN) agradeço toda a sua disponibilidade na obtenção dos espectros de RMN.

A todos os funcionários do Departamento de Química e em especial à D. Lurdes, D. Fátima, ao Sr. Jorge, Sr. António Manuel e à D. Maria João, pela simpatia e apoio importante à minha investigação. Um agradecimento à Doutora Sílvia Gramacho pelas análises de GC-MS e pela constante boa disposição.

A todos os antigos membros do grupo de Catálise e Química Fina que acompanharam o meu percurso, contribuíram para o sucesso da minha formação e me enriqueceram cientificamente: Carlos Monteiro, César Henriques, Lucas Dias, Nídia Maldonado-Carmona, Vanessa Tomé, Carolina Vinagreiro e Liliana Damas. Gostaria de agradecer em especial ao Carlos, o meu primeiro orientador científico, por me ter ajudado a dar os primeiros passos no mundo da investigação. À Carolina pela “amizade” de outrora...

Aos atuais membros do grupo de Catálise e Química Fina pelo espírito de entreajuda e companheirismo: Rui Carrilho, Sara Pinto, Inês Fonseca, Alexandre Felgueiras, Vitaliy Masliy, Zoé Arnaut, Iúri Tavares, Diana Marques, Madalena Silva, Carolina Domingos, Daniela Teixeira, Giusi Piccirillo, Andreia Gonzalez e Fábio Rodrigues. Agradeço à Sara pelo espírito de entreajuda essencial para ultrapassar os “tormentos” que sofremos com as porfirinas e suas formas reduzidas. Ao Rui por me ter integrado sempre nos seus trabalhos e pela excelente colaboração que se estabeleceu entre nós. À Diana Marques por ser a nossa “fada do laboratório”, pela sua boa disposição e empenho. Embora não pertencente ao grupo de Catálise, gostaria de agradecer ao Jaime pela ajuda, convivência e sempre divertidas conversas de corredor.

E porque a ensinar também se aprende imenso, queria deixar um agradecimento especial às meninas cujo trabalho pude acompanhar mais de perto: Carolina Domingos, Daniela Teixeira, Madalena Silva e Anita Amorim. À Carolina, a minha primeira tutoranda, pela tua incomparável “meme-quality” boa disposição e excelente capacidade de aprendizagem que tornou o meu trabalho muito mais fácil. À Daniela, a minha tutoranda adotada, pela sintonia que se estabeleceu entre nós, excelente espírito

de dedicação e por teres aprendido tão exemplarmente todos os meus procedimentos experimentais “express maravilha”. Tenho um enorme orgulho em todas vós!

Durante este meu percurso, regozijo-me pelo o facto de ter feito três grandes amigos, aos quais tenho de agradecer um por um.

Ao meu *bro* Fábio, pela tua generosidade e altruísmo, tanto a nível profissional como pessoal. Obrigado pela tua boa energia sempre presente em todas as atividades em conjunto que realizámos, pelos nossos momentos divertidos a jogar jogos de tabuleiro e pelas nossas inúmeras conversas filosóficas de almoço altamente estimulantes.

À Andreia por teres conseguido tão exemplarmente aturar o meu “mau feitio intermitente” (palavras tuas) e por alinhares nas nossas épicas picardias que destroem por completo a monotonia do quotidiano. Acima de tudo, obrigado pela tua grande amizade e viva o Francisco Miguel!

Giusi, dizer que estás presente todos os dias não é exagero nenhum, é uma realidade incontestável. Obrigado por todas as conversas profundas, pelo apoio a qualquer dia e a qualquer hora, pelas brincadeiras que dão um brilho especial aos meus dias e por tantas outras coisas que não caberiam numa só página de agradecimentos. A tua amizade é única e inigualável!

Aos respetivos cônjuges Pedro, Patrícia e, em especial, ao Marcos pelos inúmeros convívios juntos e por serem sempre ótimas companhias.

À Diana Gomes ou Lady Di, como eu gosto de te chamar, pela amizade que se tem fortalecido ao longo do tempo, apesar da maior distância física que atualmente existe entre nós. Obrigado pela tua alegria contagiante e por estares sempre presente!

Aos meus colegas do MedChemTrain e, em particular, ao André Luz pela convivência e pelos bons tempos passados em Lisboa durante o primeiro ano de doutoramento.

A todos os meus amigos e em especial ao João, pelas nossas “bilharadas” de fim de semana. Aos meus colegas e amigos da secção de bilhar da Académica de Coimbra e do Clube de Bilhar de Coimbra que acrescentam a este meu hobby muita diversão, convivência e me ajudam a desanuviar do stress do dia-a-dia. Gostaria de agradecer em especial ao Kiko e ao Edgar pelo seu enorme espírito de camaradagem, pelos treinos em conjunto e ensinamentos que me foram transmitindo e também pelas inúmeras boleias.

Por último, mas não menos importante, à minha família que sem a qual certamente que nunca conseguiria desenvolver este trabalho. Um agradecimento especial aos meus pais e ao meu irmão por todo o apoio e por me aturarem!

Table of Contents

Abstract	i
Resumo	v
Abbreviations and symbols	ix
Nomenclature	xv
Chapter 1 - Introduction	1
1.1 – Overview of drug-resistant infectious diseases	1
1.2 – Computer-aided drug design for development of new antibiotics	6
1.2.1 – <i>E. coli</i> DNA gyrase B as a potential bacterial target	9
1.2.2 – <i>E. coli</i> DNA gyrase inhibitors – state of the art	12
1.3 – Photodynamic inactivation (PDI) of bacteria	19
1.3.1 – <i>In vivo</i> and clinical studies using PDI	22
1.3.2 – PDI combined with antibiotics (dual phototherapy)	27
1.4 – Work proposal	29
1.5 – References	31
Chapter 2 – Photoinactivation of <i>E. coli</i> by dual phototherapy	45
2.1 – Synthesis and characterization of photosensitizers	45
2.2 – Photodynamic inactivation of <i>E. coli</i> in combination with ciprofloxacin	54
2.3 – Photodynamic inactivation of multi-drug resistant <i>E. coli</i> combined with ciprofloxacin	65
2.4 – <i>In vivo</i> studies	72
2.5 – Conclusion	79

2.6 – References	81
Chapter 3 - Computer-aided drug design of new <i>E. coli</i> gyrase B inhibitors	85
3.1 – Computational studies	85
3.1.1 - Construction of pharmacophore model	86
3.1.2 – Docking studies: selection of best scoring function for gyrB	98
3.1.3 – Screening of the NCI database	101
3.1.4 – <i>De novo</i> design and screening of a virtual library	103
3.2 – Synthesis and modulation of 2,5(6)-substituted benzimidazole derivatives	105
3.3 – Biological studies	130
3.4 – Conclusion	138
3.5 – References	140
Chapter 4 - Experimental	145
4.1 – General information	145
4.2 – Experimental of Chapter 2	148
4.2.1 – Synthesis of photosensitizers	148
4.2.2 – EcoScale calculations	153
4.2.3 – <i>In vitro</i> biological studies	157
4.2.4 – <i>In vivo</i> dual phototherapy	160
4.3 – Experimental of Chapter 3	163
4.3.1 – Computer-aided drug design methods	163
4.3.2 – Synthesis of benzimidazole compound family	165
4.4 – References	179

Abstract

The work presented in this PhD thesis is focused on the development of alternative antimicrobial therapies and new molecules for the inactivation of *Escherichia coli*, whose infections by multi-drug resistant (MDR) strains are a major concern for healthcare systems. These studies include potentiation of ciprofloxacin's antibacterial activity through the use of photodynamic inactivation (PDI) and the synthesis of potential *E. coli* DNA gyrase B inhibitors, guided by computer-aided drug design (CADD) tools.

In Chapter 1, a summary of the scientific challenges associated with infections by MDR microorganisms is given, with particular focus on *E. coli*, together with a brief overview on the prospects of CADD for the development of new antimicrobials. Then, a critical analysis of the state of the art on the biological role of the bacterial DNA gyrase and enzyme inhibitors is presented. Finally, a brief outline of PDI and its combination with antibiotics for the management of topical infections is presented.

The first part of Chapter 2 describes the optimization of synthetic methods, using sustainable alternative reaction activation technologies (microwave and ultrasound irradiation) for preparation of cationic photosensitizers (PS). Under the newly developed conditions, cationic imidazolyl phthalocyanines (**IPc-Zn-Et⁴⁺**, **IPc-In-Et⁴⁺**) and porphyrins (**IP-H-Me²⁺**, **IP-H-Me⁴⁺**, **IP-Zn-Me⁴⁺**) were obtained with yields up to 59%, 63%, 95%, 92% and 90%, respectively.

In the second part of Chapter 2, structure-activity studies using these cationic photosensitizers in the photoinactivation of *E. coli* through PDI and its combination with ciprofloxacin (dual phototherapy) were performed. The effects of the cationic macrocycle structure (*i.e.* porphyrin or phthalocyanine-based), number of positive charges, coordinating central metal and amphiphilicity were evaluated. Overall, in PDI monotherapy all photosensitizers were active against *E. coli* in the nM concentration range even using very low light doses (1.8 J/cm²). The best outcome was obtained with the tetra-cationic porphyrin family (**IP-H-Me⁴⁺** and **IP-Zn-Me⁴⁺**) where 5 log CFU *E. coli* reduction was achieved, at 32 nM PS concentration and 1.8 J/cm² light dose. Then, aiming to achieve a synergistic effect between the combination of PDI with ciprofloxacin

(CIP) an optimization of dual phototherapy protocol was carried out. The best result of this therapy for *E. coli* inhibition was achieved when PDI using **IP-H-Me⁴⁺** as photosensitizer at 16 nM concentration and 5.4 J/cm² light dose was followed by CIP administration (0.004 mg/L). This is a remarkable result that potentiated CIP antimicrobial activity, requiring 64-fold less CIP concentration (reduction from 0.25 mg/L – monotherapy to 0.004 mg/L – dual phototherapy) to achieve full *E. coli* inhibition. The dual phototherapy studies proceeded with the transposition to *in vivo* studies, for the treatment of mice wounds infected with *E. coli*. The animal studies revealed that the combination therapy (PDI + CIP) was more efficient than each individual monotherapy (PDI or CIP) both in the inactivation of bacteria and improvement of wound healing.

Chapter 3 describes the use of CADD tools (*i.e.* pharmacophore modeling and molecular docking) for the discovery of potential new inhibitors of the *E. coli*'s DNA gyrase B subunit. Firstly, optimized pharmacophore models were constructed based on the structural and biological data of known inhibitors reported in literature. Their performance in discriminating between active and inactive compounds was assessed, revealing a > 90% true active hit rate and a < 10% false positive rate. The pharmacophore models were combined with molecular docking (ChemScore function from GOLD software) to screen the National Cancer Institute (NCI) database and the most six promising structures were selected for biological evaluation. In parallel, both CADD tools were used to screen a virtually designed set of new derivatives of 2-(2-aminophenyl)-5(6)-substituted-1*H*-benzimidazoles, which led to the selection of three promising molecules to pursue their chemical synthesis: 2-(2-aminophenyl)-5(6)-(3,4,5-trimethoxyphenyl)-1*H*-benzimidazole (**3.14**), 2-(2-aminophenyl)-5(6)-(3-fluoro-4-(methoxycarbonyl)phenyl)-1*H*-benzimidazole (**3.15**), 2-(2-aminophenyl)-N-(3-(methylsulfonyl)phenyl)-1*H*-benzimidazol-5(6)-amine (**3.16**). The preparation of such compounds encompassed condensation of 4-bromo-1,2-diaminobenzene with 2-nitrobenzaldehyde to give the base scaffold 5(6)-bromo-2-(2-nitrophenyl)-1*H*-benzimidazole **3.1** with 62% yield in multi-gram scale. After benzimidazole NH protection, the 5(6) position was modulated through Pd-catalyzed coupling reactions, namely Suzuki-Miyaura (yields up to 72%) and Buchwald-Hartwig (yield up to 81%). Finally, Pd-catalyzed hydrogenation allowed to obtain the desired compounds **3.14** -

3.16 in yields up to 91%. Methylation of **3.11** in DMF gave the cationic 1,3-dimethyl-5(6)-(3,4,5-trimethoxyphenyl)-2-(2-nitrophenyl)-1*H*-benzimidazol-3-ium iodide (**3.17**) in 96% yield. Both the synthesized molecules and the ones supplied by NCI were evaluated in DNA gyrase and *E. coli* inhibition, but no activity was detected with concentrations lower than 100 μ M and 250 mg/L, respectively. Nevertheless, some compounds acquired from NCI (number 647083, **NCI-4**) and from the newly synthesized benzimidazole family (**3.17**) displayed appreciable *Staphylococcus aureus* antimicrobial activity, with minimum inhibitory concentration (MIC) values of 42 and 125 mg/L, respectively.

In Chapter 4, the experimental procedures and full compound characterization are presented.

Keywords: DNA gyrase, Benzimidazole, Photosensitizer, Photodynamic inactivation (PDI), Dual phototherapy.

Resumo

O trabalho apresentado nesta tese de doutoramento é centrado no desenvolvimento de terapias antimicrobianas alternativas e novas moléculas para a inativação de *Escherichia coli*, cujas infeções por estirpes multirresistentes (MDR) são uma grande preocupação para os sistemas de saúde. Os estudos efetuados incluem a potenciação da atividade antibacteriana da ciprofloxacina através do uso da inativação fotodinâmica (PDI) e a síntese de potenciais inibidores da *E. coli* DNA girase, guiada por ferramentas de *design* de fármacos assistida por computador (CADD).

No Capítulo 1 encontra-se um resumo dos desafios científicos associados a infeções por microrganismos do tipo MDR, com um foco particular na *E. coli*, juntamente com uma visão geral sobre as perspetivas do CADD para o desenvolvimento de novos antibacterianos. De seguida, é apresentada uma análise crítica do estado da arte sobre o papel biológico da DNA girase bacteriana e seus inibidores. Finalmente, é apresentado um breve sumário da PDI e da sua combinação com antibióticos para aplicação no tratamento de infeções tópicas.

A primeira parte do Capítulo 2 descreve a otimização de métodos sintéticos através de tecnologias sustentáveis para a ativação de reações (irradiação de micro-ondas e ultrassons) para a preparação de fotossensibilizadores (PS) catiónicos. Sob as condições desenvolvidas, ftalocianinas (**IPc-Zn-Et⁴⁺**, **IPc-In-Et⁴⁺**) e porfirinas (**IP-H-Me²⁺**, **IP-H-Me⁴⁺**, **IP-Zn-Me⁴⁺**) do tipo imidazolil catiónicas foram obtidas com rendimentos até 59%, 63%, 95%, 92% e 90%, respetivamente.

Na segunda parte do Capítulo 2 são apresentados estudos de estrutura-atividade utilizando estes fotossensibilizadores catiónicos na fotoinativação da *E. coli*, utilizando PDI e a sua combinação com ciprofloxacina (fototerapia dual). Foi avaliado o efeito da estrutura do macrociclo (porfirina ou ftalocianina), número de cargas positivas, metal central e anfifilicidade. De um modo geral, todos fotossensibilizadores foram ativos na fotoinativação de *E. coli* em concentrações na ordem dos nM e usando doses de luz muito baixas (1.8 J/cm²). O melhor resultado foi obtido com a família de porfirinas tetra-catiónicas (**IP-H-Me⁴⁺** e **IP-Zn-Me⁴⁺**), com a quais foi obtida uma redução em 5 log de unidades formadoras de colónias (UFC) de *E. coli*, utilizando 32 nM de PS e uma dose de luz de 1.8 J/cm². Posteriormente, foi efetuada uma otimização do protocolo de

fototerapia dual, tendo em vista alcançar um efeito sinérgico entre a combinação de PDI com ciprofloxacina (CIP). O melhor resultado em fototerapia dual para a inativação de *E. coli* foi alcançado usando **IP-H-Me⁴⁺** como PS, numa concentração de 16 nM e dose de luz de 5.4 J/cm², seguido da administração de CIP (0.004 mg/L). Este é um resultado notável, conduzindo à potenciação da atividade da CIP, sendo necessária uma concentração de CIP 64 vezes inferior (redução de 0.25 mg/L – monoterapia para 0.004 mg/L – fototerapia dual) para a inibição total de *E. coli*. Os estudos de fototerapia dual prosseguiram com a transposição para estudos *in vivo*, no tratamento de feridas de murganho infetadas com *E. coli*. Os estudos em animais evidenciaram a eficiência da fototerapia dual (PDI + CIP) quando comparado com as monoterapias individuais (PDI ou CIP), tanto na inativação de bactérias, como na melhoria da cicatrização das feridas.

O Capítulo 3 descreve o uso de ferramentas CADD (*i.e.* modelos de farmacóforo e *docking* molecular) para a descoberta de novos potenciais inibidores da subunidade B da *E. coli* DNA gyrase. Em primeiro, foram construídos modelos de farmacóforo otimizados, baseados em informações estruturais e biológicas de inibidores reportados na literatura. O seu desempenho em distinguir entre moléculas ativas e inativas foi avaliado, revelando uma taxa > 90% na identificação de ativos e < 10% de falsos positivos. Os modelos de farmacóforo foram combinados com *docking* (função de ChemScore do *software* GOLD) para filtrar a base de dados do National Cancer Institute (NCI) e as seis moléculas mais promissoras foram selecionadas para avaliação biológica. Em paralelo, as ferramentas de CADD foram utilizadas para filtrar uma base de dados de novos derivados de 2-(2-aminofenil)-5(6)-substituídos-1*H*-benzimidazoles desenhados virtualmente, levando assim à seleção de três moléculas promissoras para prosseguir com a sua síntese química: 2-(2-aminofenil)-5(6)-(3,4,5-trimetoxifenil)-1*H*-benzimidazole (**3.14**), 2-(2-aminofenil)-5(6)-(3-fluoro-4-(metoxicarbonil)fenil)-1*H*-benzimidazole (**3.15**), 2-(2-aminofenil)-N-(3-(metilsulfonil)fenil)-1*H*-benzimidazol-5(6)-amina (**3.16**). A preparação destes compostos envolveu a condensação do 4-bromo-1,2-diaminobenzeno com 2-nitrobenzaldeído, obtendo-se a molécula base 5(6)-bromo-2-(2-nitrofenil)-1*H*-benzimidazole **3.1** na escala de multi-grama, com 62% de rendimento. Após proteção do grupo NH do benzimidazole, a posição 5(6) foi modulada através de reações de acoplamento catalisadas por Pd, nomeadamente do tipo Suzuki-Miyaura

(rendimentos até 72%) e Buchwald-Hartwig (rendimentos até 81%). Finalmente, os compostos idealizados **3.14** - **3.16** foram obtidos com rendimentos até 91%, mediante hidrogenação com Pd. A metilação de **3.11** em DMF permitiu obter o composto catiónico iodeto de 1,3-dimetil-5(6)-(3,4,5-trimetoxifenil)-2-(2-nitrofenil)-1*H*-benzimidazol-3-íon (**3.17**) com 96% de rendimento. Tanto as moléculas sintetizadas como as fornecidas pelo NCI foram avaliadas na inibição da DNA girase e de *E. coli*, no entanto não foi observada atividade em concentrações abaixo de 100 µM e 250 mg/L, respetivamente. No entanto, alguns compostos do NCI (número 647083, **NCI-4**) e da nova família de benzimidazóis recém-sintetizados (**3.17**) demonstraram uma atividade antimicrobiana significativa contra *Staphylococcus aureus*, com valores de concentração mínima inibitória (CMI) de 42 e 125 mg/L, respetivamente.

No Capítulo 4, são apresentados os procedimentos experimentais e a caracterização completa dos compostos sintetizados.

Palavras-chave: DNA girase, Benzimidazole, Fotossensibilizador, Inativação fotodinâmica (PDI), Fototerapia dual.

Abbreviations and Symbols

$[M]^+$	Molecular ion
$[M+H]^+$	Protonated molecular ion
δ	Chemical shift
ϵ_{\max}	Maximum molar absorption coefficient
η	Yield
λ	Wavelength
Φ_{Δ}	Singlet oxygen quantum yield
1D	One-dimensional
3D	Tridimensional
$^1\text{H-NMR}$	Proton nuclear magnetic resonance
$^{13}\text{C-NMR}$	Carbon 13 nuclear magnetic resonance
$^1\text{H-}^1\text{H NMR}$	Proton-proton coupling bidimensional nuclear magnetic resonance
$^1\text{H-}^{13}\text{C NMR}$	Proton-carbon coupling bidimensional nuclear magnetic resonance
J	Coupling constant
3J	Three-bond coupling constant
4J	Four-bond coupling constant
Ac	Acetyl
Ani	Anionic group
Aro	Aromatic group
ATCC	American Type Culture Collection
BINAP	2,2'-bis(diphenylphosphino)-1,1'-binaphthyl
Boc	<i>Tert</i> -butyloxycarbonyl group
Boc ₂ O	Di- <i>tert</i> -butyl dicarbonate
<i>br</i>	Broad signal
CADD	Computer-aided drug design
CFU	Colony forming units

CH	Conventional heating
CIP	Ciprofloxacin
COSY	Correlated spectroscopy
COVID-19	Coronavirus disease 2019
Da	Dalton
DCM	Dichloromethane
<i>d</i>	Doublet
<i>dd</i>	Doublet of doublets
<i>ddd</i>	Doublet of doublet of doublets
ddH ₂ O	Double distilled water
DMAE	Dimethylaminoethanol
DMAP	4-Dimethylaminopyridine
DME	Dimethoxyethane
DMF	Dimethyl formamide
DMSO	Dimethyl sulfoxide
DNA	Deoxyribonucleic acid
DPEphos	Bis[(2-diphenylphosphino)phenyl] ether
EHT	Extended Hückel theory
EI	Electron impact
EMA	European Medicines Agency
ESI	Electrospray ionization
EtOH	Ethanol
FIC	Fractional inhibitory concentration
GOLD	Genetic optimisation for ligand <i>d</i> ocking
<i>gyr</i>	DNA gyrase
<i>gyrA</i>	Subunit A of DNA gyrase
<i>gyrB</i>	Subunit B of DNA gyrase
h	Hours
H-Ac	Hydrogen bond acceptor
H-Ac2	Projected partner for hydrogen bond acceptor
H-bond	Hydrogen bond

H-Don	Hydrogen bond donor
H-Don2	Projected partner for hydrogen bond donor
HMBC	Heteronuclear multiple bond correlation
HSQC	Heteronuclear single quantum correlation
MS	Mass spectrometry
HTS	High throughput screening
Hyd	Hydrophobic group
IC	Internal conversion
IC ₅₀	Half maximal inhibitory concentration
ICH	International Council for Harmonization
IR	Infra-red
ISC	Intersystem crossing
IUPAC	International Union of Pure and Applied Chemistry
LD	Light dose
LDC	Light dose correction factor
LED	Light-emitting diode
logP	Partition coefficient
m/z	Mass-to-charge ratio
MB	Methylene blue
MDR	Multi-drug resistant
Me	Methyl
MeOH	Methanol
MH	Mueller-Hinton
MIC	Minimum inhibitory concentration
MIC _{CIP}	Ciprofloxacin minimum inhibitory concentration
MOE	Molecular Operating Environment
MRSA	Methicillin-resistant <i>Staphylococcus aureus</i>
MW	Microwave/Molecular weight
NCI	National Cancer Institute
NMR	Nuclear magnetic resonance
NOESY	Nuclear overhauser effect spectroscopy

OAc	Acetate
OD	Optical density
P	Potency
PAINS	Pan-assay interference compounds
PDB	Protein Data Bank
PDI	Photodynamic inactivation
pH	Potential of hydrogen
Ph	Phenyl
PhNO ₂	Nitrobenzene
P _{max}	Maximum potency
ppm	Parts per million
PS	Photosensitizer
<i>q</i>	Quartet
R&D	Research and development
RNA	Ribonucleic acid
ROS	Reactive oxygen species
rpm	Rotations per minute
RS	Reduced susceptibility
rt	Room temperature
<i>s</i>	Singlet
S ₀	Ground singlet state
S ₁	First order excited singlet state
S ₂	Second order excited singlet state
SARS-CoV-2	Severe acute respiratory syndrome coronavirus 2
S _n	n order excited singlet state
t	Time
T ₁	First order excited triplet state
TBAI	Tetrabutylammonium iodide
<i>td</i>	Triplet of doublets
TFA	Trifluoroacetic acid
THF	Tetrahydrofuran

TLC	Thin-layer chromatography
TMS	Tetramethylsilane
TOF	Time of flight
TPSA	Topological polar surface area
US	Ultrasound
UTI	Urinary tract infection
UV	Ultraviolet
VES	Volume exclusion spheres
VR	Vibrational relaxation
WHO	World Health Organization
XPhos	Dicyclohexyl[2',4',6'-tris(propan-2-yl)[1,1'-biphenyl]-2-yl]phosphane

Nomenclature

In this thesis, the IUPAC guidelines were routinely followed for compound naming and numbering, with some exceptions that will be detailed below.

Phthalocyanines

Regarding the phthalocyanine precursors, the designation of “phthalonitrile” will be employed instead of the IUPAC name “1,2-dicyanobenzene”.¹ The phthalonitrile numbering system is in accordance with IUPAC nomenclature (Figure I).

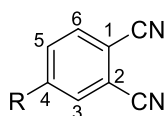


Figure I: Numbering system of phthalonitriles.

For the numbering of phthalocyanines, the IUPAC rules were used (Figure II).² The numbering starts in a carbon of the benzenic ring that is vicinal to a fusion carbon between the pyrrolic ring and the benzenic ring. Then, consecutive numbers are given to all atoms that make up the exterior of the macrocycle followed by the numbering of the interior pyrrolic nitrogens. Since the phthalocyanines synthesized in this thesis have mono-substituted phthalonitrile as precursors, four positional isomers will be formed, and thus the alternative positions that substituents occupy in each isomer are indicated in parenthesis.

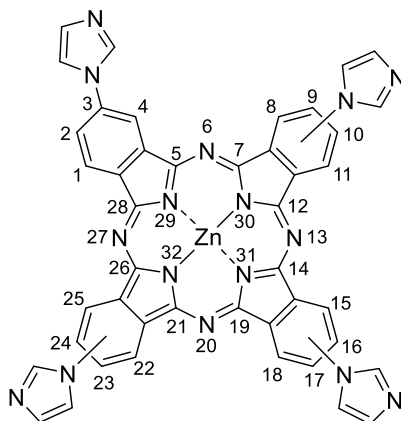


Figure II: IUPAC numbering system for the phthalocyanine macrocycle.

For the phthalocyanine presented in Figure II, the systematic name will be given as 2(3),9(10),16(17),23(24)-tetrakis(1*H*-imidazol-1-yl)phthalocyaninato zinc (II).

Porphyrins

For the systematic naming of porphyrins, the IUPAC numbering system was used,³ which consists in the numbering of all macrocycle carbon atoms from 1 to 20 and the internal nitrogens from 21 to 24 (Figure III). The positions 5, 10, 15 and 20 will be designated as *meso* and positions 2,3,7,8,12,13,17 and 18 as β -pyrrolic.

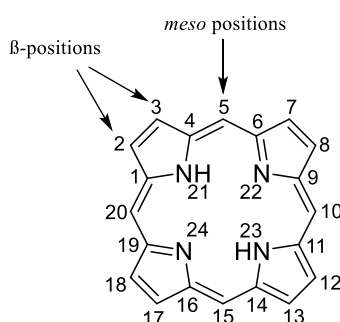


Figure III: IUPAC numbering system and terminology used for porphyrins positions.

In the case of non-symmetric porphyrins with two different substituents in the *meso* positions (A_2B_2 type), a *trans* designation will be employed when employed when group A is in positions 5 and 15 and group B in positions 10 and 20 (Figure IV).

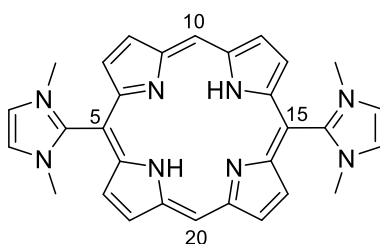


Figure IV: Example of a *trans*- A_2B_2 type porphyrin: 5,15-bis(1-methylimidazol-2-yl)porphyrin

Benzimidazoles

For the numbering of benzimidazoles, the IUPAC rules were used (Figure V).⁴ The numbering priority is given to the sp^3 nitrogen, which is assigned with the number 1. Then, the carbon in the imidazole ring is numbered as 2 and the sp^2 nitrogen as 3. Finally,

the benzenic portion is numbered 4 to 7, with fused carbons numbered 3a and 7a. Due to the presence of tautomerism, substituents in the benzenic ring will have two possible numberings, depending on which nitrogen has sp^3 hybridization. Thus, for the example presented in Figure V, the alternative position of the substituent is given in parenthesis: 5(6)-bromo-1*H*-benzimidazole.

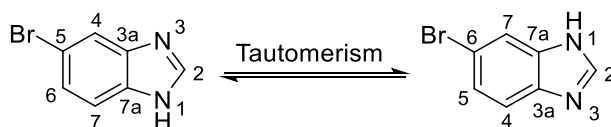


Figure V: Tautomeric equilibrium of benzimidazoles and their IUPAC numbering system.
Example for: 5(6)-bromo-1*H*-benzimidazole.

- [1] Sharman, W. M.; Lier, J. E. V., 97 - *Synthesis of Phthalocyanine Precursors*, in The Porphyrin Handbook, Volume 15: Phthalocyanines: Synthesis. Eds Academic Press: Amsterdam, **2003**.
- [2] Merritt, J. E.; Loening, K. L., Nomenclature of tetrapyrroles. *Pure & Applied Chemistry*, **1979**, *51*, 2251-2304.
- [3] Moss, G. P., Nomenclature of tetrapyrroles (Recommendations 1986). In *Pure & Applied Chemistry*, **1987**, *59*, 779-832.
- [4] McNaught, A. D.; Wilkinson, A., *IUPAC Compendium of Chemical Terminology – Gold Book*. Blackwell Scientific Publications: Oxford, **2014**.

CHAPTER 1

Introduction

1.1 – Overview of drug-resistant infectious diseases

The management of infectious diseases is one of the cornerstones of modern healthcare, on which the worldwide economic and social well-being is heavily dependent.¹⁻³ Indeed, the uncontrolled spread of microorganisms can quickly result in millions of deaths, disruption of healthcare systems, country shutdowns and incalculable financial losses. This is perfectly exemplified by the 1918 Spanish flu pandemic and, more recently, by the COVID-19 pandemic.⁴ Infections can be caused by different types of microorganisms, such as bacteria, viruses, fungi or parasites, or by misfolded proteins called prions. Microorganisms are surprisingly resilient, undoubtedly due to their high reproduction rate and genetic plasticity, which allows a quick adaptation to unfavorable conditions.⁵ Current approaches to curb infections rely on vaccines as a preventative measure and antimicrobials (antibiotics, antivirals, antifungals and antiparasitics) as therapeutic options.⁶ While antimicrobials were considered highly effective at the time of their discovery, their widespread overuse along several decades has triggered the development of multiple resistance mechanisms. This is aggravated by our increasingly interconnected world, where the spread of multi-drug resistant (MDR) microorganisms and their genes is strongly facilitated.⁷ Despite the most recent pandemics being of viral origin, the yet-undeclared “pandemic” of MDR bacteria should be a major cause of concern to governments and healthcare systems in the near future. This discreet ever-growing pandemic has a long-term potential to become the source of some of the deadliest diseases of the modern

world.⁸⁻⁹ Recent studies estimate a total of 1.27 million deaths in 2019 caused directly by bacterial MDR infections.¹⁰ This number is projected to reach 10 million annual deaths in 2050, if no active measures are taken by science to answer the unmet needs of MDR infections management.¹¹ To induce perception, this number surpasses the annual death toll of cancer, diabetes and cholera combined and is double the official reported deaths by COVID-19 in its first two years.¹²

The fight against bacteria can be traced back to ancient Nubia, where it is believed that a tetracycline-rich diet helped to prevent bacterial infections.¹³ Humanity had yet to wait two millennia before the first microscopic observations of fungi and bacteria, by Robert Hooke and Antoni van Leeuwenhoek, in the 1665-83 period.¹⁴ Two centuries later, in 1867, Joseph Lister took a significant step in the promotion of widespread implementation of antiseptics in surgery, with consequent decrease of post operatory infections.¹⁵ A few decades later, in 1928, the groundbreaking serendipitous discovery of penicillin by Alexander Fleming marked the beginning of the “golden antibiotic era”.¹³ Since then, dozens of new antibiotic classes were discovered, from natural, semi-synthetic or synthetic sources.¹⁶⁻¹⁷ However, resistance mechanisms to each antibiotic were observed just a few years after, or even before their market introduction and widespread clinical use.¹⁸ These mechanisms include i) reduction of antibiotic accessibility to the target; ii) target modification through genetic mutations; iii) target protection using other biomolecules; iv) modifications of antibiotics by antibiotic-degrading enzymes.¹⁹ It is worth noting that the benign bacteria that colonize the human gut can become resistant through exposure to antibiotics and then transfer those resistance genes to pathogenic bacteria, often encountered in hospital environment, in a process called horizontal gene transfer.²⁰

From a biological perspective, bacteria can be divided in two groups, gram-positive and gram-negative, depending on their membrane capability to retain the crystal violet stain, in a process developed by Hans Christian Gram, in 1844.²¹ This empiric grouping methodology is the reflection of the significant morphological and physiological differences between the cell walls of gram-positive and gram-negative bacteria. The understanding of bacteria’s biological barriers is essential in the development of new antibiotics and thus, in Figure 1.1, a schematic representation of the cell wall of gram-positive and gram-negative bacteria is presented.²² The cytoplasm

of gram-positive bacteria is surrounded by a single lipid bilayer, composed mainly by phosphatidylglycerol ($\approx 70-80\%$) and cardiolipin ($\approx 20\%$),²³ in which some proteins are embedded. Facing the outer leaflet are multiple strands of peptidoglycan stacked one upon another and cross-linked for additional strength. Inside the peptidoglycan layer there are copolymers of glycerol phosphate or ribitol phosphate and carbohydrates, linked via phosphodiester bonds, called teichoic acids and lipoteichoic acids (Figure 1.1, Gram-positive). These layers have a high degree of porosity that allow even large macromolecules to diffuse readily through the cytoplasmic membrane.²⁴ Some clinically relevant MDR gram-positive bacteria include *Staphylococcus aureus*, *Streptococcus pneumoniae* and *Enterococcus faecalis*.

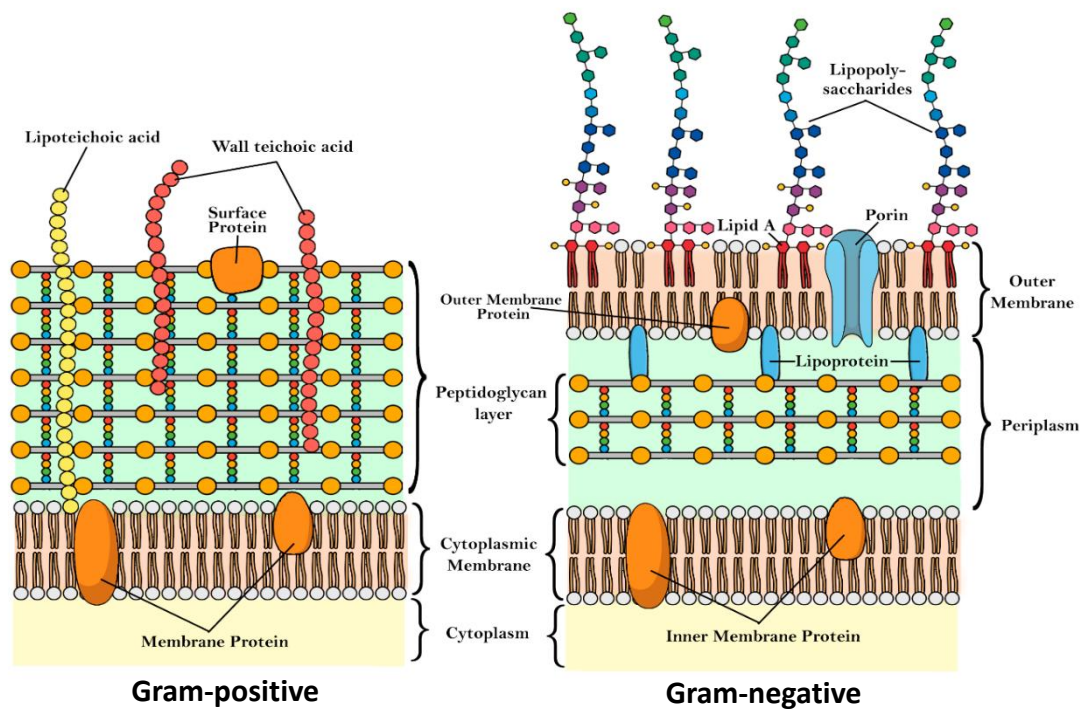
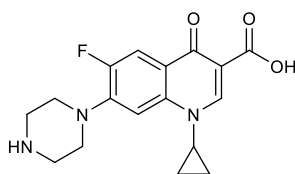


Figure 1.1: Schematic representation of the biological membranes in gram-positive and gram-negative bacteria. Copyright 2021 SpringerNature.²⁵

The cytoplasm of gram-negative bacteria is surrounded by an inner phospholipid bilayer containing embedded membrane proteins. This membrane is followed by a small peptidoglycan layer, which anchors the outer membrane bilayer through lipoproteins. This outer membrane contains lipopolysaccharides, rich in negatively charged phosphate groups, composed by a lipid portion (lipid A, Figure 1.1, Gram-negative)

linked to polysaccharides.²⁶⁻²⁷ The porin channels embedded in the outer membrane allow the uptake of polar molecules such as water and nutrients. Overall, this outer membrane, exclusive to gram-negative bacteria, can be regarded as a tightly packed negatively charged barrier, capable of limiting uptake by passive diffusion of hydrophilic molecules and also the ones with molecular weight (MW) higher than 600 Da.^{24,28} Nevertheless, cationic antibiotics can efficiently target gram-negative bacteria membranes through favorable electrostatic interactions with the anionic lipopolysaccharides. This is the case of the polycationic antibiotic colistin (MW = 1 155 Da), whose mechanism relies on binding to gram-negative bacteria membranes and promoting a disruption of the membrane integrity, ultimately leading to bacterial death.²⁹

The eradication of gram-negative bacteria is without a doubt one of the greatest challenges for Medicinal Chemistry given the intrinsic resistance mechanisms imposed by their biological barriers.³⁰⁻³¹ A 2017 report by the World Health Organization (WHO) highlighted three types of gram-negative bacteria (*Acinetobacter baumannii*, *Pseudomonas aeruginosa* and *Enterobacteriales*) for which development of new antimicrobial molecules and therapies is of critical priority.³² Among the family of *Enterobacteriales*, *Escherichia coli* is a colonizer of the normal gut microbiota,³³ but pathogenic strains can cause urinary tract infections (UTI), chronic wounds, diarrhea, among other diseases.³⁴⁻³⁵ For the treatment of these types of infections, fluoroquinolones, in particular ciprofloxacin (CIP), have been widely used, in topical or systemic administrations.³⁶⁻³⁷



Ciprofloxacin (CIP)

One of the major drawbacks of ciprofloxacin treatments is the high potential for bacterial resistance development, of which many different mechanisms are known.³⁸⁻³⁹ Undoubtedly, this poses severe challenges, not just in the management of *E. coli* bacterial infections in the present, but especially at medium/long term, as resistance to

fluoroquinolones has been continuously increasing over the last few years.⁴⁰ The 2021 Global Antimicrobial Resistance WHO report indicates that 43% of UTIs caused by *E. coli* are currently resistant to CIP. Moreover, these clinically isolated *E. coli* strains also demonstrate resistance to other relevant antibiotics such as cephalosporins (40-50% of all isolates), trimethoprim/sulfamethoxazole (55%) and ampicillin (78%).⁴¹ Regarding infected wounds, a 2017-2019 study found that *E. coli* was present in 12% of cases, being the second most common gram-negative bacteria reported. It was found that 76% of *E. coli* isolates showed resistance to at least one antibiotic, with 30% being MDR strains.⁴² Furthermore, this high resistance prevalence is supported by other recent studies.⁴³⁻⁴⁴

Regrettably, the numerous warnings and projections by the WHO^{32,45-46} and other scientific literature¹⁰⁻¹¹ have yet to produce a significant effect on the pharmaceutical companies' drug pipeline. Indeed, during the 21st century, the introduction in clinic of new, truly innovative antibiotics has been scarce. In particular, the discovery of new antibiotic classes effective against gram-negative bacteria is non-existent.³⁰ Thus, the new antibiotics that have been marketed during the last few decades are merely combinations or next-generation derivatives from previous antibiotic classes, for which resistance is already widespread.⁴⁷⁻⁴⁸ Indeed, the development of new antibiotics suffers from major setbacks, which are not always present in drugs for other therapeutic areas. From a research and development point of view, it is difficult to design drugs that can both effectively interact with a specific biological target in bacteria and concomitantly avoid their morphologic and physiologic intrinsic resistance mechanisms. In addition, the discovery of new antibiotics is not financially attractive to pharmaceutical companies, since antibiotics are administered during short periods of time, as opposed to medications for chronic illnesses. Moreover, the quick development of resistant bacteria to new antibiotics severely limits their lifetime, which contributes to the low investment of pharmaceutical industry in antibiotic R&D. In sum, the high development costs and low revenue prospects hinder the chances of truly innovative antibiotics to reach the market, despite their undeniable social benefit.⁴⁹

In order to circumvent the currently established resistance mechanisms, the information presented so far clearly highlight the need to develop new antibacterial drugs or therapies that ideally target underexplored bacterial macromolecules. The

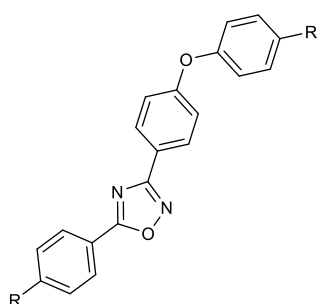
main goal of the studies presented in this thesis is entirely in line with this scientific challenge, aiming to computer design/synthesize new antimicrobial molecules (DNA gyrase inhibitors) and implementing alternative dual phototherapies.

The next subsection will feature an overview of the state of the art on the use of computer-aided drug design (CADD) as a potential tool for the discovery of new antibiotics, in particular for DNA gyrase. This will be followed by a subsection detailing the use of photodynamic inactivation (PDI) as a potential complementary therapy to antibiotics.

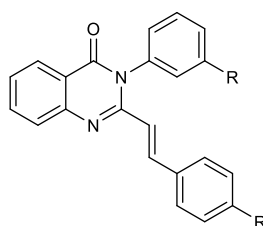
1.2 – Computer-aided drug design for development of new antibiotics

Most antibiotics in clinical use were discovered from natural sources, in particular from soil bacteria and fungi. This strategy of drug discovery, despite giving access to vast libraries of complex compounds with relevant biological actions, has some disadvantages. Firstly, the natural organisms that produce antibacterial molecules already possess genes that confer them intrinsic resistance, which can be transmitted when in contact with pathogenic bacterial strains through horizontal gene transfer.⁵⁰ Thus, there is a significant interest in developing new purely synthetic antibiotic classes, for which there are no established resistance genes in nature. Besides that, the screening of just natural compounds excludes potential antibiotic families with chemical scaffolds that can only be obtained through chemical synthesis. The transposition from natural-based antibiotic molecules (*e.g.* β -lactams)⁵¹⁻⁵³ to the fully synthetic ones (*e.g.* fluoroquinolones)⁵⁴⁻⁵⁵ required the synthesis of large molecular libraries to find lead compounds. However, an alternative for guiding the research and development process of new synthetic antibiotics appeared in the last few decades, consisting in the use of computer-aided drug design (CADD) tools.⁵⁶ CADD has proven to be an alternative to traditional high-throughput screenings (HTS), which use automated processes to screen chemical libraries of thousands of compounds and often give a very low hit rate.⁵⁷ Because CADD tries to assess therapeutic activity at a molecular level, it can lead to more targeted screenings, which can filter large digital compound libraries into a smaller set of compounds that can then be synthesized and tested. Indeed, CADD is a powerful tool not only for lead discovery but also for its rational optimization in order to increase its

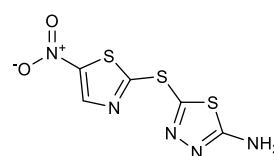
affinity and selectivity for the intended target.⁵⁸ Over the years, CADD has contributed to the discovery of important drugs currently in clinical use like captopril (hypertension; approved in 1981), saquinavir, ritonavir and indinavir (treatment of HIV; approved in 1995-1996).⁵⁹ So far, CADD has not shared the same success in the discovery of new clinically approved antibiotic classes.⁶⁰⁻⁶² However, some efforts carried out in the past decade have yielded promising molecules with antimicrobial activity that may open the way for an eventual transposition to clinical use. Of particular relevance is the discovery of quinazolinone and oxadiazole scaffolds that can target the penicillin-binding proteins of methicillin-resistant *S. aureus* (MRSA), which may constitute an alternative to β -lactam antibiotics.⁶³⁻⁶⁴ In addition, CADD has also contributed to the discovery of new druggable bacterial targets such as the heme oxygenase⁶⁵ and to the research and structural optimization of antimicrobial peptides.⁶⁶ A recent study using neural networks discovered halicin, a molecule previously developed for diabetes but abandoned due to the lack of efficacy, as a potential new antibiotic that sequesters iron inside bacteria and leads to dysfunctions in their pH homeostasis. *In vivo* murine model studies confirmed its *in vitro* efficacy and broad spectrum activity against infections with gram-positive or gram-negative bacteria.⁶⁷ With the continued investment in artificial intelligence and high processing supercomputers, CADD may yet play a decisive role in the management of MDR infections, being this also one of specific goals of this work.⁶⁸



Oxadiazoles⁶³



Quinazolinones⁶⁴



Halicin⁶⁷

In CADD, studies can be carried out using structure or ligand-bases approaches, or a mixture of both. Ligand-based methods are usually employed when there is no information on the structure of the target and therefore take advantage of physicochemical and biological properties of actives and inactives, in order to predict the activity of new molecules.⁶⁹ Pharmacophore modeling is a prime example of a

ligand-based approach.⁷⁰ Pharmacophores are tridimensional schematic representations of the most important structural features that allow molecular recognition by a particular target.⁷¹ A pharmacophore model is composed by features, which can be based on topology, function (*i.e.* aromatic ring, hydrogen bond acceptor/donor, acidic, basic or hydrophobic groups) or in a specific atom. After appropriate validation, these models can be used as queries to screen chemical libraries. For each molecule, a set of low-energy conformations is generated and each is fitted to the pharmacophore query by aligning the molecules with the established pharmacophore features. If a molecule can fit the query features, it is considered a hit.⁷⁰⁻⁷¹ On the other hand, structure-based CADD makes use of 3D structures of biological molecules, usually determined by X-ray crystallography, NMR or, more recently, cryo-electron microscopy. Typical structure-based approaches include molecular docking, which can be used in combination with molecular dynamics to predict target flexibility.⁵⁷⁻⁵⁸

The first step towards the implementation of these CADD techniques in the pursuit of new antibiotics is the selection of an adequate bacterial target. There are many possible bacterial targets, being the traditional ones the cell wall (lipids or embedded proteins), ribosomes, proteins involved in the transcription and replication of genetic information, among other proteins with enzymatic functions.⁷² Other non-traditional targets include signaling proteins and host-pathogen interaction mediators.⁷³⁻⁷⁴ The B subunit of DNA gyrase has recently gathered some attention due to its well-conserved structure and pivotal role in bacterial DNA replication/transcription. To date, a sufficiently safe and effective antibiotic for widespread clinical use that targets DNA gyrase B does not exist, and thus, this protein retains a relatively underexplored potential for the R&D of new antibiotics.⁷⁵ For this reason, DNA gyrase B was selected by us as the target for the design of new inhibitors using CADD approaches. Thus, in the next subchapter, a detailed information on the morphology and function of DNA gyrase will be given, combined with an overview of the efforts conducted so far for the inhibition of *E. coli's* DNA gyrase.

1.2.1 – *E. coli* DNA gyrase B as a potential bacterial target

DNA gyrase is a type II topoisomerase that has a pivotal role in DNA replication and transcription processes, due to its ability to induce negative supercoiling in the DNA double-strands through hydrolysis of ATP.⁷⁵ This biological role makes DNA gyrase an essential enzyme for bacteria, but is absent in humans, which makes it an attractive target for a selective destruction of bacteria. This enzyme is a heterotetramer, composed by two A subunits and two B subunits, which associate to form an A₂B₂ complex in the active enzyme (Figure 1.2).⁷⁶

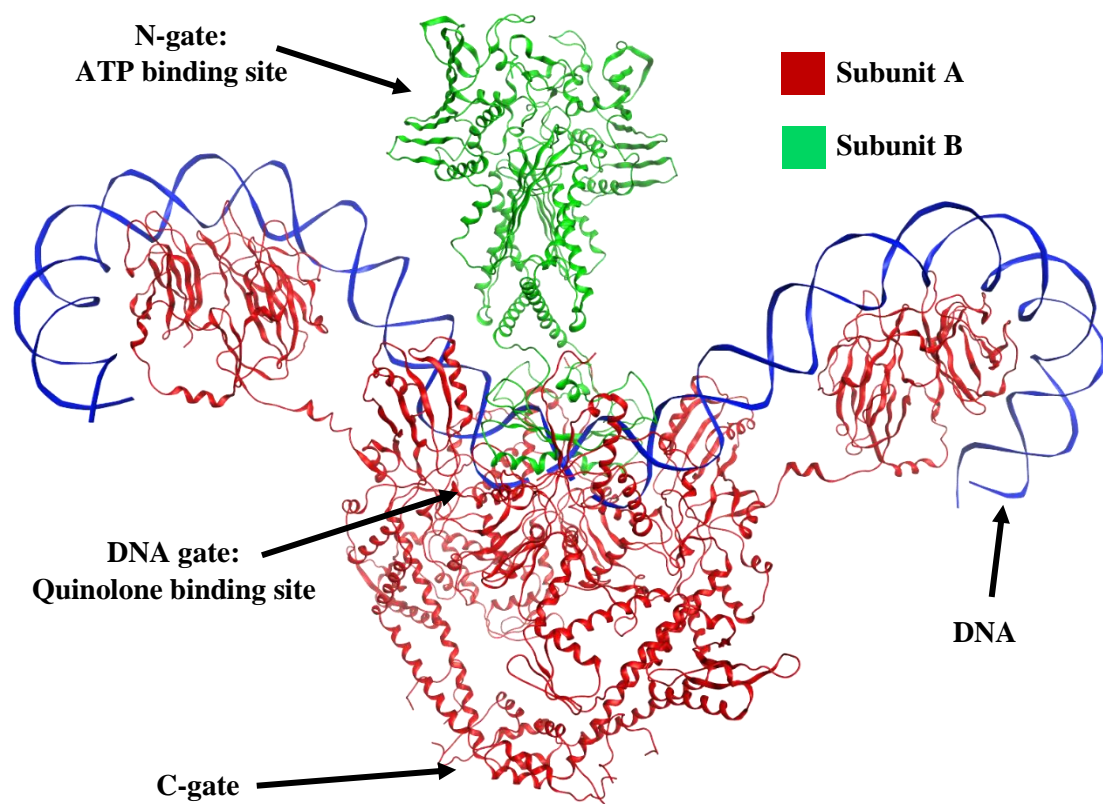


Figure 1.2: *E. coli* DNA gyrase complexed with DNA (PDB entry 6RKW).⁷⁶ The crystallographic structure was visualized in MOE software⁷⁷ and color-coded: i) blue – DNA molecule; ii) red – subunit A; iii) green – subunit B.

Broadly speaking, subunit A (gyrA; Figure 1.2 – red) is involved with interactions with DNA (Figure 1.2 – blue) and the subunit B (gyrB; Figure 1.2 – green) contains the ATP binding site (located in the N-gate).⁷⁸ When DNA gyrase is not connected with DNA, this heterotetramer is stabilized by two protein-protein interactions: i) the C-gate which connects the two A subunits and ii) the DNA gate which connects subunits A with

subunits B. When bound to DNA and catalytically active (*i.e.* when ATP enters its binding site in subunit B), an additional protein-protein interaction occurs, the N-gate, which stabilizes the interaction between both B-subunits.⁷⁹

Quinolones and fluoroquinolones bind preferentially to the DNA gate, located in the subunit A. Mutations in the genes that encode *gyrA* (common) or *gyrB* (rare) affect the affinity of fluoroquinolones to their binding site, being this the most prevalent resistance mechanism. This rise of antimicrobial resistance to fluoroquinolones has led to the study of *gyrB* as a potential target, in particular the ATP binding site. Although the class of aminocoumarins (novobiocin and clorobiocin) display inhibition of GyrB, their use has not implied significant clinical success, due to poor efficiency and toxicity,⁵⁵ thus enabling the development of drugs that can provide a better risk/benefit relation.

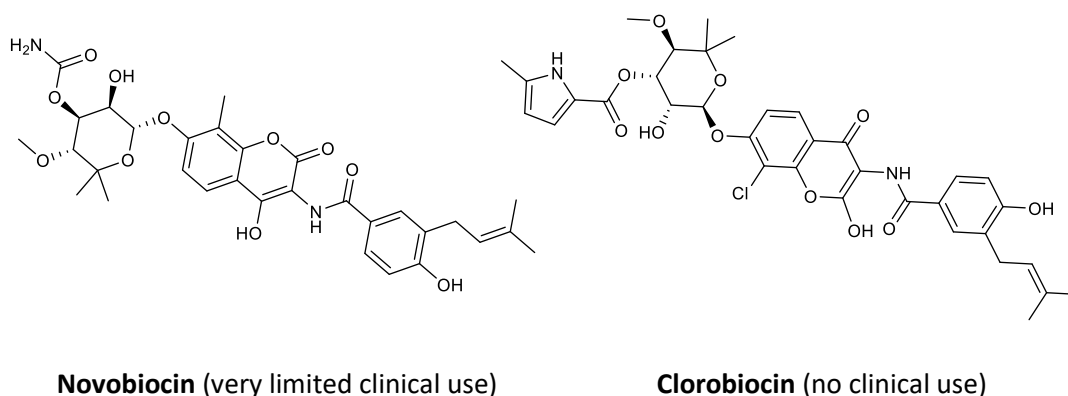


Figure 1.3 presents a simplified biological mechanism of DNA gyrase, encompassing all the main steps that involve the transformation of a positive supercoil into a negative supercoil. Positive supercoils are formed during DNA replication or transcription, as a consequence of the increase in DNA tensile strain,⁸⁰ and therefore need to be removed before these processes can continue.⁸¹ In Figure 1.3, a positive supercoil of circular DNA (common in bacteria) is depicted as the substrate of DNA gyrase (*gyr*). After DNA binding to *gyr* (**A**), two ATP molecules enter their binding sites, located one in each *gyrB* unit, leading to the cleavage of the double-stranded DNA (**B**). The aminocoumarin antibiotics can enter the ATP binding site and act as competitive inhibitors, which will prevent further DNA replication and transcription.⁸² After DNA cleavage (**B**), the other side of the circular DNA strand is passed through the cleaved DNA strand (**C**). Then, hydrolysis of both ATP molecules allows the reconnection of the

DNA strand (**D**). Antibiotics of the quinolone and fluoroquinolone class act through inhibition of this DNA reconnection step. Thus, there is an accumulation of cleaved DNA strands in bacteria, which will ultimately compromise the integrity of bacteria's genetic material and lead to their death.³⁷ When DNA reconnection is successful (*i.e.* in the absence of antibiotics), *gyr* releases the circular DNA strand, but this time with a negative supercoil. This process can be repeated several times, in order to introduce more negative supercoils.⁷⁸

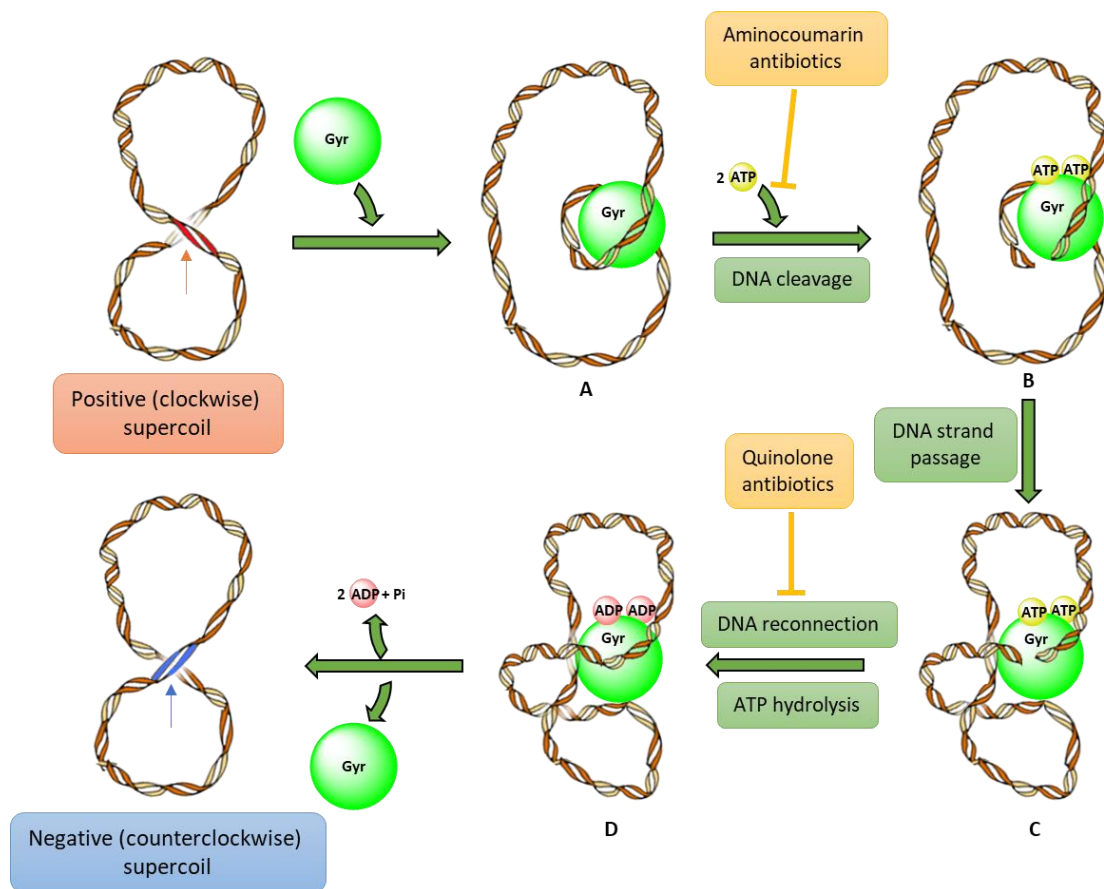


Figure 1.3: Simplified mechanism of DNA gyrase for the introduction of negative supercoils in DNA, and relieving the DNA tensional stress induced by positive supercoils.^{79,83}

It is worth noting that, eventually, these negative supercoils will be reconverted into positive supercoils when DNA tension increases (*i.e.* when more replications/transcriptions are required), and thus the catalytic action of DNA gyrase is continuously needed, which explains its vital role in maintaining bacteria's normal function and homeostasis.⁷⁹

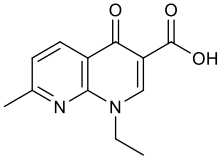
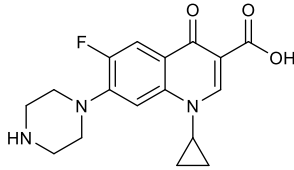
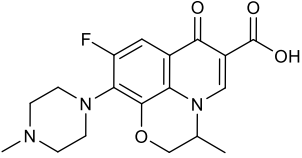
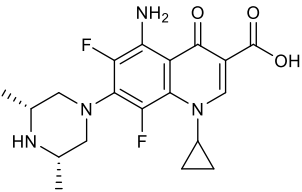
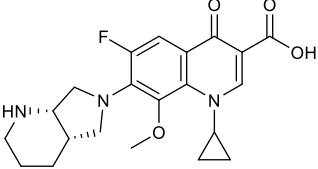
Since our study is focused on the design and development of new *E. coli* DNA gyrase inhibitors, a critical analysis of the literature is presented in the next section.

1.2.2 – *E. coli* DNA gyrase inhibitors – state of the art

In this subsection, a brief summary on the most relevant *E. coli* DNA gyrase inhibitors is given, with focus on the inhibitors of *gyrA* (quinolones and fluoroquinolones) and *gyrB* (aminocoumarins and recently discovered scaffolds).

Quinolones and fluoroquinolones comprise an antibiotic class discovered in the 1960s, when a by-product of chloroquine manufacture displayed modest antibacterial activity, leading to the development of nalidixic acid, the first antibiotic of the quinolone class (Table 1.1, entry 1).⁸⁴ This first generation molecule was approved in 1967 for treatment of UTIs and was moderately effective against most gram-negative bacteria, including *E. coli*, with a minimum inhibitory concentration (MIC) of 8 mg/L. However, its safety concerns and high resistance development have led researchers to optimize quinolones activity and toxicity. It was soon found that the addition of a fluorine atom to the aromatic ring improved their spectrum of activity and the introduction of a piperazine in the same ring improved its potency against gram-negative bacteria.⁸⁵ The second-generation fluoroquinolones, introduced in the 1980s, contain both of these modifications, being ciprofloxacin (Table 1.1, entry 2) and ofloxacin (Table 1.1, entry 3) some of the landmark molecules. In particular, ciprofloxacin displays an impressive activity against *E. coli*, with a MIC of 0.03 mg/L. Further modifications in the piperazine ring and aromatic ring led to the discovery of the third and fourth generation fluoroquinolones, of which sparfloxacin and moxifloxacin are examples, respectively (Table 1.1, entries 4 and 5). These antibiotics possess a broader spectrum of activity and are more effective against gram-positive bacteria.⁵⁴⁻⁵⁵ For these more recent fluoroquinolone generations, it is worth mentioning that, although DNA gyrase is the primary target, the closely related topoisomerase IV can also be inhibited, but such mechanism will not be detailed in this thesis. Regrettably, the market introduction of new fluoroquinolone generations has stalled in the 21st century so far.⁸⁵

Table 1.1: Landmark molecules from each of the four generations (Gen) of quinolone/fluoroquinolone-type antibiotics.

#	Name/structure	Gen	Year of approval	Activity spectrum	MIC <i>E. coli</i> (mg/L)
1	 Nalidixic acid	1st	1967	All gram-negative bacteria except <i>Pseudomonas</i> species	8
2	 Ciprofloxacin	2nd	1987	All gram-negative bacteria	0.03
3	 Ofloxacin	2nd	1985	All gram-negative bacteria, some gram-positive bacteria such as <i>S. aureus</i> and some atypical bacteria	0.12
4	 Sparfloxacin	3rd	1993	All gram-negative bacteria, expanded gram-positive and atypical bacteria coverage	0.06
5	 Moxifloxacin	4th	1999	Similar to 3rd Gen, but better activity against anaerobic bacteria	0.06

Nonetheless, interest in fluoroquinolones did not fade and there are a lot of recently published derivatives that aim to increase their potency, pharmacokinetic properties, activity spectrum or to circumvent existing resistance mechanisms.⁸⁶ Interestingly, since the discovery of ciprofloxacin, no noteworthy improvement on the activity of fluoroquinolones against *E. coli* was observed. Indeed, the *E. coli* MIC is in general slightly higher in fluoroquinolones of third and fourth generation.⁸⁵ The unmatched activity of ciprofloxacin against *E. coli* has made it one of the medicines of choice for treatment of infections caused by this pathogen, as was highlighted in the introductory subsection of this thesis.

Now that the molecular mechanisms involved in DNA gyrase and fluoroquinolone activity have been detailed, it is easy to understand the resistance mechanisms of *E. coli* against ciprofloxacin (Figure 1.4):⁸⁷⁻⁸⁸

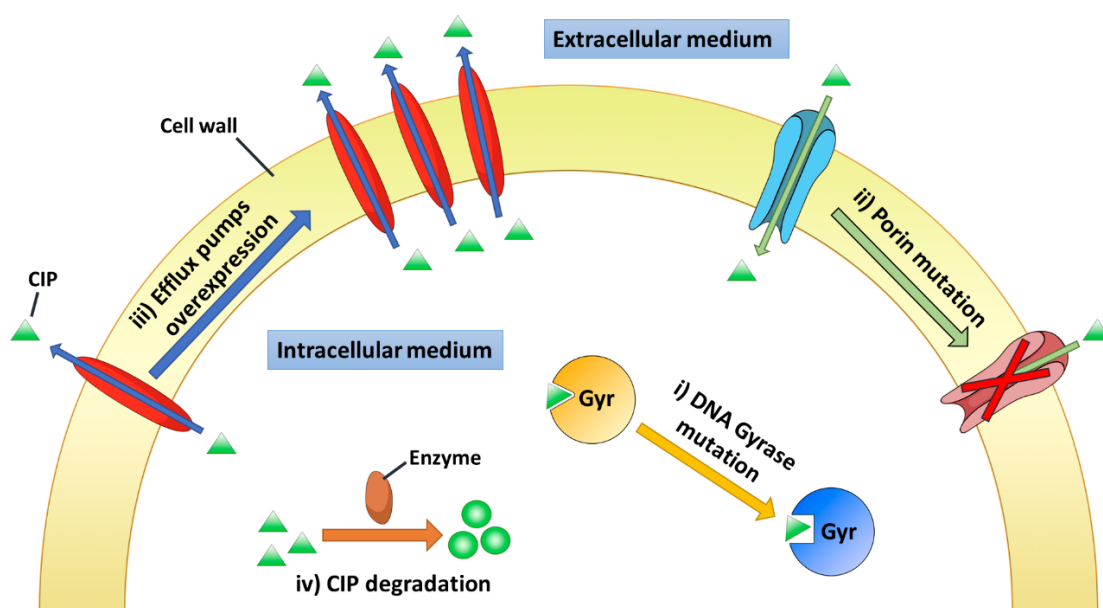


Figure 1.4: Main resistance mechanisms of *E. coli* against ciprofloxacin.

- i) Mutations in the genes that encode DNA gyrase and that affect the affinity of the antibiotic to its binding site;
- ii) Decrease in membrane permeability. Given that DNA gyrase is an intracellular target, alteration of the porin transporters present in the outer membrane can impact the uptake of these modestly hydrophilic molecules.

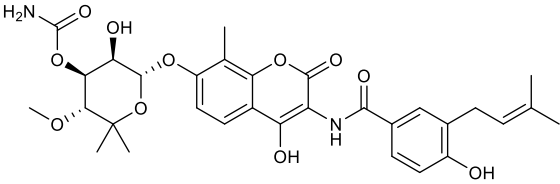
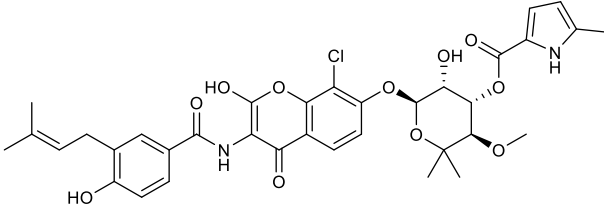
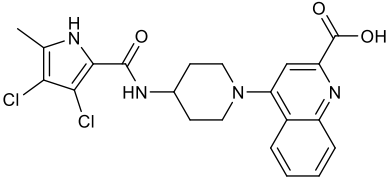
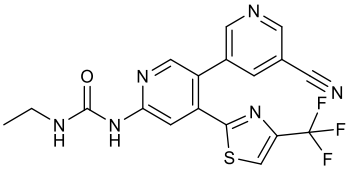
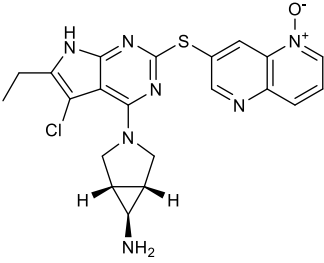
- iii) Overexpression of efflux pumps, which decreases intracellular drug concentration. This mechanism is often associated with high-level fluoroquinolone resistance.
- iv) Production of enzymes that acetylates ciprofloxacin, reducing its affinity for DNA gyrase.⁸⁹

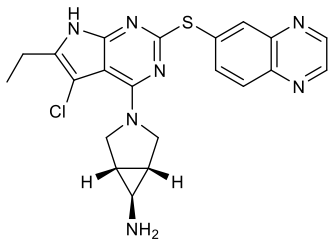
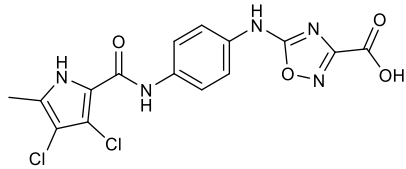
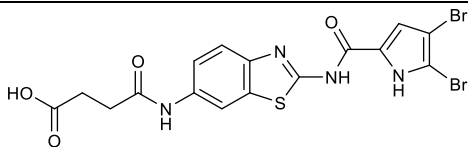
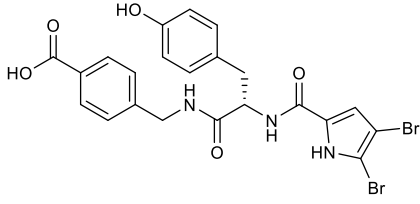
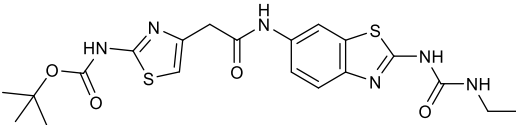
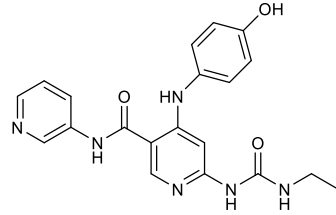
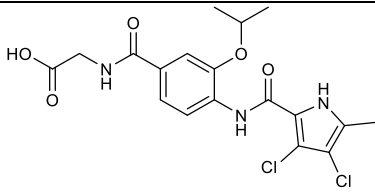
These resistance mechanisms can be present either separately or in a combination, often acting synergically and rendering ciprofloxacin completely ineffective. It is clear that new therapeutic approaches are needed, to both circumvent existing ciprofloxacin resistance mechanisms and prevent the development of additional resistance. The search for such alternative therapies sets the stage for the work developed in Chapter 2 of this thesis, where ciprofloxacin will be combined with photodynamic inactivation (PDI).

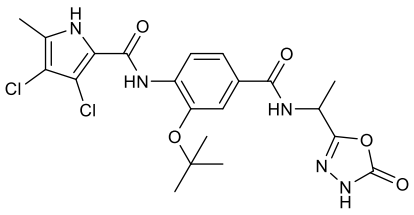
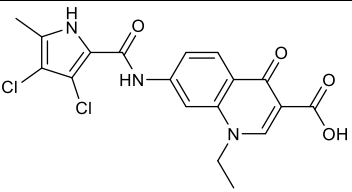
On the subject of *gyrB* inhibitors that interact with the ATP binding site, there has recently been an active search for new chemical families. These include compounds with promising activity against *E. coli*'s *gyrB*.⁹⁰⁻⁹¹ In Table 1.2 the structures and biological activity of representative molecules published so far for this specific target are depicted. The members of the already mentioned class of aminocoumarins, novobiocin and clorobiocin (entries 1-2) display good *E. coli* gyrase inhibition (IC_{50} of 30 - 80 nM), however their MIC values in *E. coli* are considerably high (250 and 16 mg/L respectively), when compared to those presented in Table 1.1 for fluoroquinolones. As previously mentioned in the analysis of Figure 1.1, the outer membrane of gram-negative bacteria is tightly packed and therefore it's not surprising that these molecules (MW > 600 Da) are so inefficient when tested against *E. coli* bacteria instead of a biochemical assay, where only the protein is present.⁹² A good bacterial uptake is essential when dealing with intracellular targets, and here lies one of the key motives for the clinical failure of this antibiotic class.

Through NMR screening, Eakin *et al* discovered a set of low molecular weight pyrrole-based fragments that were later used to synthesize a library of derivatives. Of these pyrrolamide molecules, compound **1.1** showed the best biological activity, with 0.9 nM IC_{50} and an *E. coli* MIC of 8 mg/L (Table 1.2, entry 3).⁹³

Table 1.2: Selected representative molecules from the various GyrB inhibitor families described so far in the literature, and corresponding biological data.

#	Compound/structure	<i>E. coli</i> gyr IC ₅₀ (nM)	MIC <i>E. coli</i> (mg/L)	Ref
1	 <p style="text-align: center;">Novobiocin</p>	80	250	92
2	 <p style="text-align: center;">Clorobiocin</p>	30	16	92
3	 <p style="text-align: center;">1.1</p>	0.9	8	93
4	 <p style="text-align: center;">1.2</p>	<10	>64	94
5	 <p style="text-align: center;">1.3</p>	<0.5	2	95

6	 <p style="text-align: center;">1.4</p>	<0.5	>64	95
7	 <p style="text-align: center;">1.5</p>	1200	No activity	96
8	 <p style="text-align: center;">1.6</p>	33	No activity	97
9	 <p style="text-align: center;">1.7</p>	619	>256	98
10	 <p style="text-align: center;">1.8</p>	3900	No activity	99
11	 <p style="text-align: center;">1.9</p>	28	>64	100
12	 <p style="text-align: center;">1.10</p>	47	No activity	101

13	 <p style="text-align: center;">1.11</p>	85	>250	102
14	 <p style="text-align: center;">1.12</p>	1000 ± 200	>32	103

In a fragment-to-lead CADD approach, Basarab discovered a set of pyridylureas such as **1.2**, which exhibited gyr inhibition in the low nM range. However, this set of compounds was surprisingly inefficient in *E. coli* growth inhibition (MIC > 64 mg/L), which was attributed to low intracellular concentrations, caused by *E. coli*'s efflux pumps (Table 1.2, entry 4).⁹⁴ Trzoss *et al* reported a set of structure-activity relationship studies, highlighting the potential of pyrrolopyrimidine inhibitors, of which **1.3** and **1.4** are examples (Table 1.2, entries 5-6). Remarkably, although both possess very good gyr inhibition (< 0.5 nM), only **1.3** possessed good activity against *E. coli* (MIC = 2 mg/L).⁹⁵ In another study, pyrrolamide derivatives containing oxadiazole motifs, such as **1.5**, were also efficient gyr inhibitors, with a 1.2 μM IC₅₀, however the compounds displayed no antibacterial activity when tested against *E. coli* (Table 1.2, entry 7).⁹⁶ This tendency of low *E. coli* activity is also present in works describing derivatives of pyrrole-2-carboxamido moieties (Table 1.2, entry 8),⁹⁷ pyrrolamines (entry 9),⁹⁸ 1-ethyl-3-(thiazol-2-yl)urea (entry 10),⁹⁹ pyridine-3-carboxamide-6-yl-ureas (entry 11)¹⁰⁰ and N-phenylpyrrolamides (entries 12-14).¹⁰¹⁻¹⁰³ However, when some of these compounds were tested against efflux pump-deficient *E. coli* mutants, their activity improved considerably, which suggests that these scaffolds are being recognized by bacteria's intrinsic defenses, such as efflux pumps, which reduces their intracellular concentration.¹⁰¹

Clearly, the examples presented in Table 1.2 demonstrate that the ideal *E. coli* gyrB inhibitor is yet to be discovered, since, in most cases, their biochemical gyr inhibition does not translate to a significant *E. coli* antibacterial activity. Compounds **1.1** and **1.3** are relevant exceptions, however the observed *E. coli* MICs of 2-8 mg/L are still too high when compared with ciprofloxacin's (0.03 mg/L, Table 1.1, entry 2). Overall, there is a need to continue pursuing the discovery of new molecules and to perform further structural optimizations before any gyrB inhibitor can be regarded as a viable alternative to ciprofloxacin in the treatment of *E. coli* infections. Indeed, new scaffolds are required that can maintain the already excellent *in vitro* gyr inhibitory activity and concomitantly avoid recognition by *E. coli*'s efflux pumps, which consistently seem to hinder their antibacterial activity. This will be the basis of Chapter 3, which will describe the attempts at the discovery of new molecules with gyrB inhibitory activity.

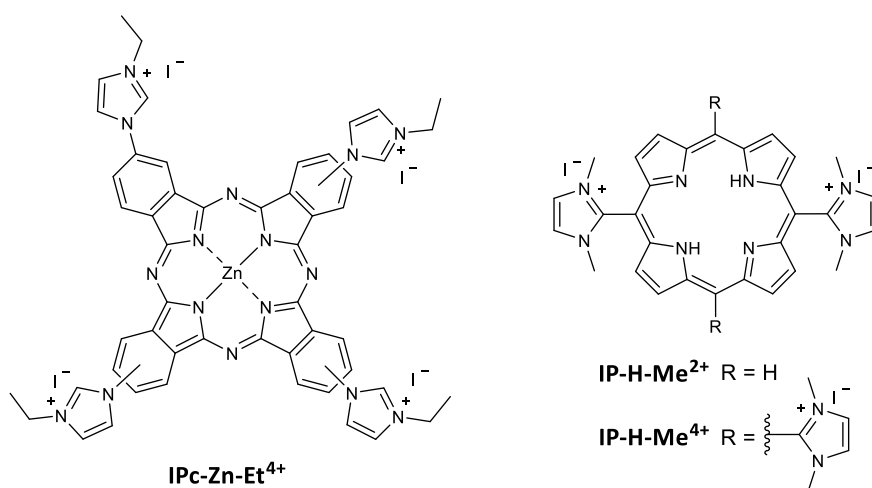
Besides the discovery of new gyrase inhibitors, this thesis will also focus on the optimization of alternative therapies such as photodynamic inactivation (PDI) and explore its possible synergic combination with ciprofloxacin. The principles of PDI and its state of the art will be presented in the following subsection.

1.3 – Photodynamic inactivation (PDI) of bacteria

The photodynamic inactivation of microorganisms dates back to the beginning of the 20th century, when Oscar Rabb discovered that paramecia incubated with acridine orange could be killed after exposure to sunlight.¹⁰⁴ However, PDI remained largely unexplored during most of the 20th century, due to the great investment on antibiotics discovery and production that started with the large-scale use of penicillin in World War II. Instead, studies on the photodynamic effect were directed to oncology, where it met considerable success, with various clinically approved molecules.¹⁰⁵⁻¹⁰⁹ However, the onset of bacterial resistance has fueled the interest in PDI as an alternative therapy for the treatment of localized infections by both antibiotic-susceptible or MDR bacteria.¹¹⁰ A simplified mechanism of PDI is presented in Figure 1.5.^{108,111}

their high reactivity towards different biomolecules ensures that PDI is a multi-target approach to control infectious diseases, which reduces the efficacy of drug resistance mechanisms.¹¹⁶⁻¹¹⁸ For the management of localized infections¹¹⁹ the photosensitizer can be applied locally and, after a proper drug-to-light interval, the infected area is irradiated. Examples of localized infections include periodontal diseases, burn infections, surgical wound infections and infected wounds originated by venous, pressure or diabetic ulcers.¹²⁰⁻¹²² In addition, PDI shows great promise in the management of viral infections by influenza¹²³ or SARS-CoV-2,¹²⁴ through nasal decontamination.

Over the years, several excellent reviews on PDI have been published,^{24,114,125-135} also with a focus on the treatment of multi-resistant bacteria in planktonic suspensions or in biofilms,¹¹⁰ as well as fungi¹³⁶ and viruses.^{115,137-139} Many efforts have been dedicated to the synthesis of new photosensitizers and to improved strategies for PDI,^{110,126-127,140-142} including the combination with antimicrobials.¹⁴³⁻¹⁴⁵ Furthermore, reports on *in vitro* PDI studies have also been extensively reviewed in recent years.^{132,146-161} Among all PS tested in inactivation of bacteria, we highlight the cationic imidazolyl phthalocyanines (**IPc-Zn-Et⁴⁺**) and porphyrins (**IP-H-Me⁴⁺** and **IP-H-Me²⁺**) as some of the best PS reported so far for *in vitro* *E. coli* inactivation, with bactericide activity at low concentrations (nM range) and light doses (< 10 J/cm²).¹⁴⁰⁻¹⁴¹



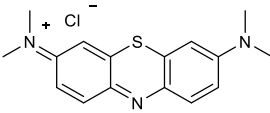
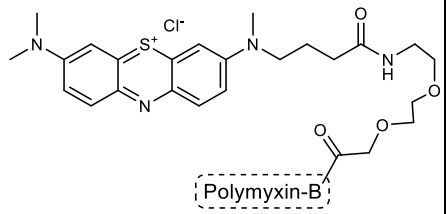
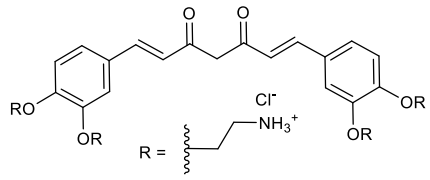
Since our goal is to study the combination of PDI with ciprofloxacin (dual phototherapy, Chapter 2) and its transposition to *in vivo* studies, the next pages will

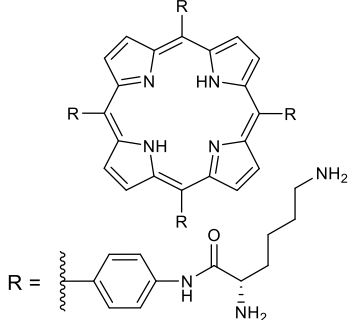
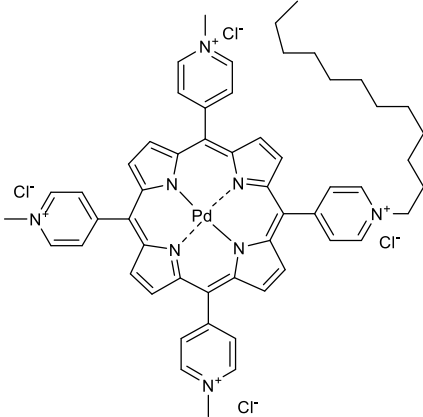
discuss the literature revision regarding the use of photosensitizers for photoinactivation of *E. coli* infections in animal models and clinic.

1.3.1 – *In vivo* and clinical studies using PDI

Some relevant *in vivo/ex vivo* pre-clinical studies on *E. coli* inactivation and the corresponding photosensitizers' structural properties are presented in Table 1.3.

Table 1.3: Chemical properties and biological activity of photosensitizers used in *in vivo/ex vivo* pre-clinical studies for treatment of infections by *E. coli*.

#	Photosensitizer / Structure	Model	PDI studies
1	 <p>Methylene Blue (1.13)¹⁶²</p> <p>Charge: +1</p> <p>MW = 284 Da</p>	<i>In vivo</i> : Female BALB/c mice infected with cecal slurry (<i>E. coli</i> , <i>E. faecalis</i> , among others)	Outcome: Improved wound healing [PS]: 100 μM Light dose: 24 J/cm ² (LED λ=632 nm)
2	 <p>MB-PMX (1.14)¹⁶³</p> <p>Charge: +1</p> <p>MW = 1723 Da</p>	<i>Ex vivo</i> : Porcine skin infected with <i>E. coli</i> ATCC 25922	Outcome: 7 log ₁₀ CFU reduction [PS]: 50 μM Light dose: 288 J/cm ² (LED λ=625 nm)
3	 <p>SACUR-3 (1.15)¹⁶⁴</p> <p>Charge: 0 to +4</p> <p>MW = 517 Da</p>	<i>Ex vivo</i> : Porcine skin infected with <i>E. coli</i> ATCC 25922	Outcome: 3 log ₁₀ CFU reduction [PS]: 50 μM Light dose: 34 J/cm ² (LED λ=435±10 nm)

4	 <p>Tetra-lysine porphyrin (1.16)¹⁶⁵ Charge: 0 to +8 (pH dependent) MW = 1188 Da</p>	<i>In vivo:</i> Sprague– Dawley rats with wound infected by mixed bacteria (<i>E. coli</i> , <i>S.</i> <i>aureus</i> , <i>P.</i> <i>aeruginosa</i>)	Outcome: 5 log ₁₀ CFU reduction, 7 days after treatment [PS]: 40 μM Light dose: 50-100 J/cm ² (Laser λ=650nm)
5	 <p>FS111-Pd (1.17)¹⁴² Charge: +4 MW = 938 Da</p>	<i>In vivo:</i> Adult female BALB/c mice with wound infection by <i>E.</i> <i>coli</i>	Outcome: 4 log ₁₀ CFU reduction initially. Complete inactivation 4 days after treatment [PS]: 50 μM (50+20+20 μL) Light dose: 80 J/cm ² (Light λ=415nm)

The use of cationic phenothiazinium dyes such as methylene blue (**1.13**) in PDI has been widespread, surely due to its previously approved clinical use for cancer photodynamic therapy.²⁵ For instance, in one *in vivo* experiment, mice wounds were infected with cecal slurry, which contained *E. coli*, among others. Using 100 μM PS concentration and a 24 J/cm² light dose, improvement in wound healing was observed, when compared with the control experiments (Table 1.3, entry 1).¹⁶²

Additionally, a methylene blue-polymyxin B conjugate (**1.14**) was reported.¹⁶³ Polymyxin B is a potent antibiotic, selective for the inactivation of gram-negative bacteria, which acts through disruption of bacterial membranes by interaction with the anionic LPS layer. This PS-antibiotic conjugate reduced 7 log₁₀ colony-forming units (CFU)

of an *E. coli* *ex vivo* infection, using 100 μM conjugate, but with quite high light doses (288 J/cm^2 ; Table 1.3, entry 2).¹⁶³

Another example relied on the use of SACUR-3 (**1.15**), a cationic derivative of the natural PS curcumin, whose protocol employed 50 μM PS concentration and 34 J/cm^2 . This PDI system showed quite modest antibacterial activity (only 3 \log_{10} CFU reduction), when compared with **1.14**, for the same infection model (Table 1.3, entry 3).¹⁶⁴

In the field of tetrapyrrolic macrocycles, a porphyrin-lysine conjugate with four units (**1.16**) reduced by $\approx 5 \log_{10}$ CFU the bacteria in wounds infected by multiple strains (*E. coli*, *S. aureus* and *P. aeruginosa*), measured 7 days after treatment. This study compared the effects of different light doses (12.5, 25, 50 and 100 J/cm^2) on PDI. It was found that 100 J/cm^2 was the best light dose for killing bacteria *in vivo*, but this dose worsened wound healing considerably when compared to lower light doses (Table 1.3, entry 4).¹⁶⁵ This demonstrates the need to promote a fine-tuning of PDI protocols to achieve a good compromise between bacterial inactivation and host damage.

One of the most successful cases of reducing *E. coli* bacterial infections on mice models is based on the use of Pd(II) tetra-cationic pyridyl-based porphyrin (FS111-Pd, **1.17**; Table 1.3, entry 5).¹⁴² PDI with FS111-Pd was more effective (complete inactivation 4 days after treatment with 50 μM photosensitizer concentration and 80 J/cm^2) than with the corresponding free base macrocycle. The amphiphilicity of the compound was ensured with three methylpyridinium groups and one pyridinium group linked to a C12 alkyl chain, and Pd (II) promoted intersystem crossing to the triplet state, increasing its quantum yield and, consequently, the ROS formation.

Overall, there are relatively few cases of topical PDI *in vivo* where the reduction in CFU achieves an acceptable bactericidal level and is sustained for several days.²⁵ For the inactivation of gram-negative bacteria such as *E. coli*, the presence of cationic groups is a key aspect to ensure good photoinactivation results. These positively charged groups can either be intrinsic (*i.e.* methylene blue **1.13** or the alkylpyridinium groups of **1.17**) or can be basic alkylamines, which are partially protonated at physiological pH values (*i.e.* **1.15** and **1.16**). Mechanistic studies highlight that the success of cationic PS results from the efficient interactions between positively charged photosensitizers with the negatively-charged LPS that are present in the outer membrane layer of gram-negative bacteria (see Figure 1.1). Another interesting conclusion is that the tetrapyrrolic

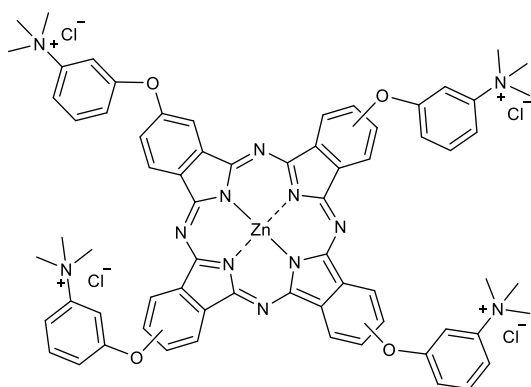
macrocycles usually offer a better antimicrobial efficiency with less harsh PDI protocols, with lower PS concentrations and light doses, which can help wound healing. The success of tetrapyrrolic macrocycles may be partially attributed to their good photophysical, photochemical properties, such as high absorption coefficient, different type of ROS generation and photostability, which are key features for the success of PDI.^{25,166}

To date, the most widespread application of PDI in clinical practice has been for the management of oral infections in dentistry.¹⁶⁷⁻¹⁷² Besides this clinical application, PDI has been studied in the treatment of lower limb infections, often associated with diabetes.¹⁷³ A more comprehensive overview of PDI in clinical practice was given in a published review, ahead to the writing of this thesis.²⁵ Therefore, herein we discuss only selected clinical studies results using PDI for treatment of lower limb wounds, where *E. coli* may be present, among other bacteria.⁴²

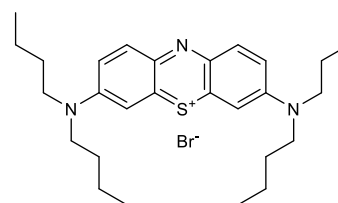
One of the most promising PS studied so far is the near-IR absorbing tetra-cationic phthalocyanine **RLP068**, for which many clinical studies have already been reported.¹⁷⁴⁻¹⁷⁸ When this PS was tested in a single-dose PDI clinical trial, a reduction of bacterial load was observed after treatment ($-3.00 \pm 1.82 \log_{10}$ CFU/mL for 3.5 mM PS concentration and 60 J/cm² light dose vs $-1.00 \pm 1.02 \log_{10}$ CFU/mL with placebo). However, bacterial regrowth occurred in the PDI-treated groups, being the CFU/mL values similar to the placebo group, 3 days after treatment.¹⁷⁴ Further clinical studies comprising sequential treatments over several weeks led to better clinical outcomes, with significant ulcer reduction in 66% of patients.¹⁷⁷

The phenothiazinium dye **PPA-904** was also investigated in PDI of infected diabetic ulcers for photoinactivation of several types of microorganisms. Similar to **RLP068**, a single PDI treatment showed a reduction in bacterial load immediately post-treatment but no difference between treatment and placebo groups was observed 24 h after the treatment.

A successful example of clinical PDI is based on the use of methylene blue and toluidine blue (36 mM PS concentrations and 6-30 J/cm² light dose) in treating diabetic patients with osteomyelitis. After several treatments, foot amputation was prevented in 17 of 18 patients versus 0 of 16 in the control group.¹⁷⁹⁻¹⁸¹



RLP068



PPA-904

Topical application of 5-ALA or MAL (precursors of protoporphyrin IX), also showed clinically significant bacterial load reductions, requiring in general 4-8 treatment sessions.¹⁸²⁻¹⁸³

Overall, the transposition from *in vitro* to *in vivo* studies is challenging, since there are multiple factors that need to be accounted. These include the heterogeneity of tissues, light dispersion/penetration, diffusion of the photosensitizer into the wound, the lowered amount of oxygen in poorly irrigated tissues and the competitive reactions of ROS with endogenous biomolecules present in the wound.²⁵ This means that complete bacterial inactivation after a single PDI treatment is not a realistic clinical outcome and, invariably, the surviving fraction can regrow and recurrence of infection is observed. The only way, yet known, to address this issue is to perform multiple PDI treatments, spread over weeks or even months. To enhance PDI efficiency, there are several examples in recent literature that describe the association of PDI with antibiotics as a promising alternative, herein referenced as dual phototherapy. The next subsection will present a critical analysis of the state of the art regarding combination of PDI with antibiotics, since this is one of the goals of this work, whose results are presented in Chapter 2.

1.3.2 – PDI combined with antibiotics (dual phototherapy)

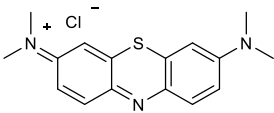
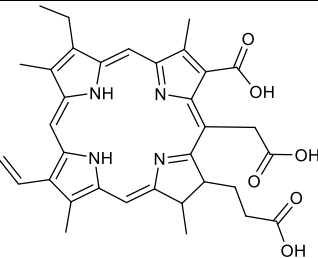
Since PDI-induced oxidative damage only occurs during light irradiation, the combination with molecules (antibiotics) that can inhibit bacterial regrowth in the dark may improve PDI clinical outcomes. So far, dozens of different PDI + antibiotic

combinations were reported, which were recently compiled in a review by Hasan *et al.*¹⁴⁵ The PS used for this type of dual phototherapy include compounds from the tetrapyrrole (porphyrins and chlorins) and phenothiazinium (methylene blue, toluidine blue) classes, among others. Additionally, a great diversity of antibiotics has been reported in these dual phototherapy studies, ranging from membrane synthesis inhibitors (extracellular targets) to protein and DNA synthesis inhibitors (intracellular targets). Regarding *E. coli* inactivation, successful *in vitro* protocols have been devised, using chlorophyllin, cationic and anionic synthetic porphyrins, chlorin-e6, methylene blue, protoporphyrin IX, eosin Y, rose bengal as photosensitizers, in combination with the following antibiotics: polymyxins,^{163,184-185} cationic peptides,¹⁸⁶⁻¹⁸⁸ glycopeptides,¹⁸⁹ β -lactams,¹⁹⁰⁻¹⁹¹ chloramphenicol,¹⁹² aminoglycoside¹⁹¹⁻¹⁹³ and fluoroquinolones.¹⁹⁴⁻¹⁹⁶ Since the objective of this work is to find new therapies to treat *E. coli* through potentiation of DNA gyrase inhibitors (*i.e.* ciprofloxacin, CIP), Table 1.4 presents the single three examples that report PDI + CIP combinations.

PDI with methylene blue (20 μ M; 2.8 J/cm²) was combined with CIP (0.002 μ g/mL) to treat wild-type *E. coli* (ATCC 25922). Two treatment modalities were investigated: CIP treatment followed by PDI, or PDI treatment followed by CIP addition. The best results were obtained by adding CIP after PDI treatment, where an improved antibacterial activity (up to 4 log₁₀ CFU reduction) was achieved when compared with PDI monotherapy. Despite the claims by the authors, it is not possible to conclude that the observed effect is indeed due to a synergic interaction due to the lack of controls with CIP monotherapy (Table 1.4, entry 1).¹⁹⁴

Another example described the combination of a mixture of essential oils extracted from the leaves of *Eugenia jambolana* with CIP in a simultaneous PDI + CIP treatment, using blue (470 nm) or red (625 nm) light irradiation. However, no statistically significant effect was observed in the PDI + CIP therapy, when compared with CIP monotherapy (Table 1.4, entry 2).¹⁹⁵

Table 1.4: Photosensitizers, protocols and outcomes of PDI + CIP dual phototherapy for the inactivation of *E. coli* bacteria *in vitro*.

#	Photosensitizer / Structure	PDI+CIP conditions	Outcome
1	 <p>Methylene blue (1.13)¹⁹⁴</p>	<p>Strain = <i>E. coli</i> ATCC 25922</p> <p>Modality = PDI before CIP</p> <p>[PS] = 20 μM</p> <p>[CIP] = 0.002 μg/mL</p> <p>Light = 2.8 J/cm²</p>	<p>Improved antibacterial activity (up to 4 log₁₀ CFU reduction) when compared with PDI monotherapy. Insufficient evidence to access synergism.</p>
2	<p>Essential oils from <i>Eugenia jambolana</i>¹⁹⁵</p>	<p>Strain = <i>E. coli</i> ATCC 9027</p> <p>Modality = Simultaneous</p> <p>[PS] = 10 μL of extract</p> <p>[CIP] = 5 μg disc</p> <p>Light = 470 nm or 625 nm LED; 10 min irradiation</p>	<p>No statistical difference between CIP monotherapy and dual therapy</p>
3	 <p>Chlorin-e6 (1.18)¹⁹⁶</p>	<p>Strain = <i>E. coli</i> UPEC060</p> <p>Modality = CIP before PDI</p> <p>[PS] = 168 μM</p> <p>[CIP] = 0.002 μg/mL</p> <p>Light = 120 J/cm²</p>	<p>3 h after treatment: ≈0.5 log₁₀ CFU reduction compared with CIP monotherapy</p>

A more recent study used Chlorin-e6 as PS and evaluated the effect of *E. coli* pre-incubation with CIP (0.002 μg/mL), followed by PDI treatment (≈16 h later, 84-168 μM PS concentration, 70-120 J/cm²). Three hours after PDI treatment, there was a statistically significant effect of the combination therapy when compared with CIP monotherapy (≈0.5 log CFU difference), but only using the highest PS concentration and light dose. However, in all study groups including the PDI + CIP group, bacterial regrowth was observed (Table 1.4, entry 3).¹⁹⁶

Overall, the studies published so far on PDI + CIP combinations suffer from a number of issues that must be addressed before translation to *in vivo* studies. First, a judicious selection of the most appropriate PS structure needs to be carried out, in order to require less harsh PDI protocols (PS concentration and light doses). The photosensitizers tested so far are not among the best reported in literature for the inactivation of *E. coli*.²⁵ As mentioned in the analysis of Table 1.3, multi-cationic photosensitizers of the tetrapyrrole family seem to yield the best results, particularly in the inactivation of gram-negative bacteria. This is corroborated by the poor results described for chlorin-e6, an anionic photosensitizer at physiological pH, that required quite high light doses and PS concentrations. This poses a problem for *in vivo* applications, since they usually require much higher PDI doses than *in vitro* studies, which raises concerns of toxicity towards the host.¹⁶⁵ In addition, there is a need to study the effect of the variables associated with the PDI + CIP combination itself, namely the order in which the treatments are performed, *i.e.*, whether they will give a better outcome when used simultaneously or sequentially. All these *in vitro* optimizations are crucial to ensure a successful transposition to *in vivo* studies and fully take advantage of the synergism between both therapies.¹⁹⁷⁻²⁰² However, so far to the best of our knowledge, there are no *in vivo* assays reported in the literature using PDI + CIP combinations.

The work described in Chapter 2 of this thesis takes a step forward to increase the synergism between PDI + CIP combinations, being able to develop efficient protocols for transposition of dual phototherapy to *in vivo* models.

1.4 – Work proposal

The main goal of this thesis is the development of dual phototherapy as an alternative therapy (Chapter 2) and synthesize computationally designed new antimicrobial molecules (Chapter 3) for the inactivation of *E. coli* (Figure 1.6).

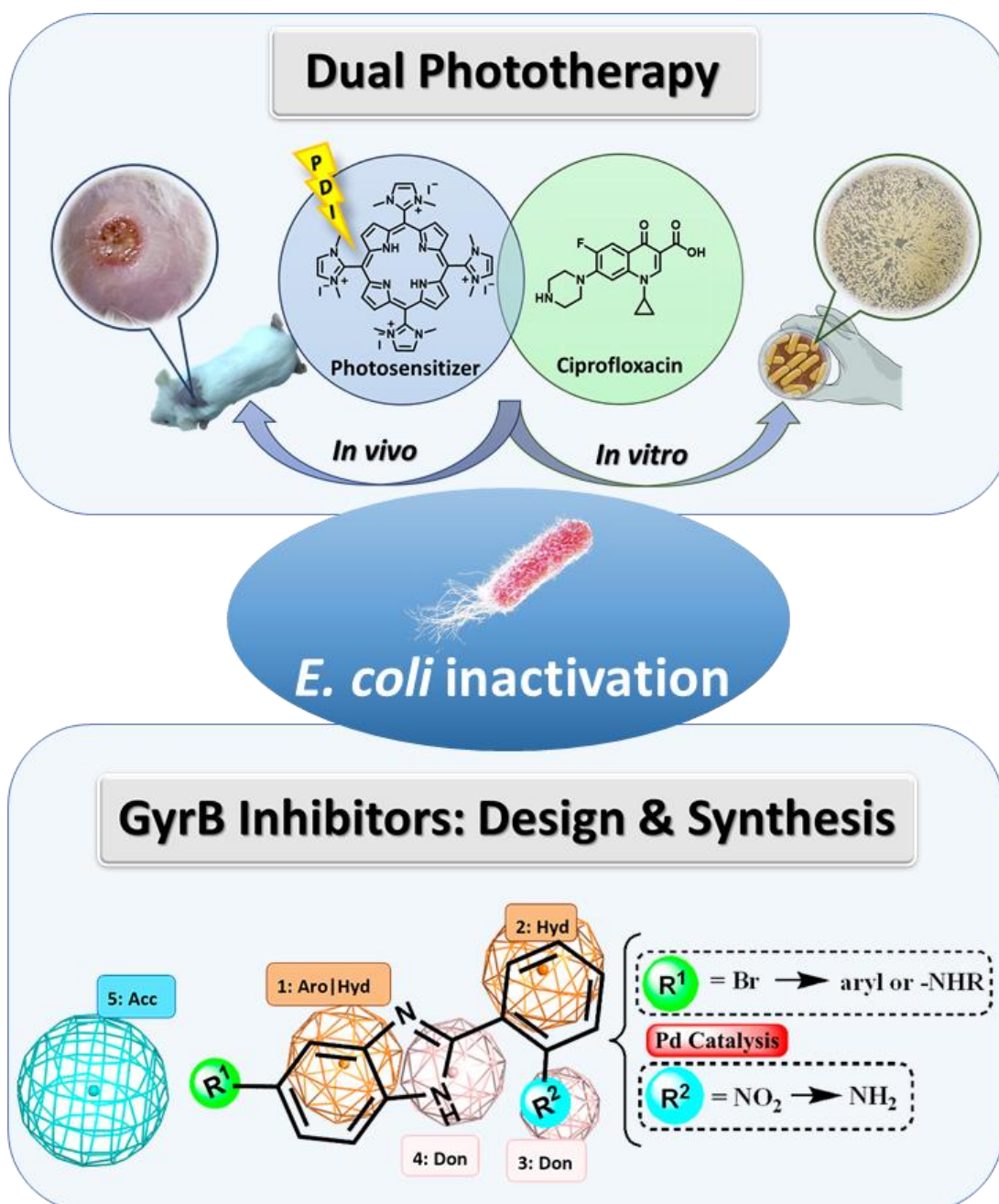


Figure 1.6: Thesis graphical abstract.

The work presented in Chapter 2 intends to explore the combination of PDI with ciprofloxacin (dual phototherapy) for *in vitro* and *in vivo* microbicide activity against *E. coli*. The specific objectives consist in performing structure-activity studies in order to choose the best *in vitro* protocol to promote an efficient translation to *in vivo* studies (PS structure, light dose, CIP concentration, order of treatments, among others). Thus, the final goal of this chapter is to implement a synergic dual phototherapy protocol for an efficient treatment of mice wounds infected with *E. coli*.

The work presented in Chapter 3 aims the design/discovery of new potential *E. coli* GyrB inhibitors, through the use of CADD tools such as pharmacophore modelling and molecular docking. Then, based on these outputs, we aim to develop new synthetic methodologies to obtain promising molecules with potential *E. coli* antibacterial activity through DNA gyrase inhibition.

1.5 – References

- [1] Cloeckeaert, A.; Kuchler, K., Grand Challenges in Infectious Diseases: Are We Prepared for Worst-Case Scenarios?, *Frontiers in Microbiology*, **2020**, *11*, 613383.
- [2] Fauci, A. S.; Morens, D. M., The Perpetual Challenge of Infectious Diseases, *The New England Journal of Medicine*, **2012**, *366*, 454-461.
- [3] Van Der Meer, J., The infectious disease challenges of our time, *Frontiers in Public Health*, **2013**, *1*, 7.
- [4] Piret, J.; Boivin, G., Pandemics Throughout History, *Frontiers in Microbiology*, **2021**, *11*, 631736.
- [5] Davies, J.; Davies, D., Origins and evolution of antibiotic resistance, *Microbiology and Molecular Biology Reviews*, **2010**, *74*, 417-433.
- [6] Micoli, F.; Bagnoli, F.; Rappuoli, R.; Serruto, D., The role of vaccines in combatting antimicrobial resistance, *Nature Reviews Microbiology*, **2021**, *19*, 287-302.
- [7] Ventola, C. L., The antibiotic resistance crisis: part 1: causes and threats. *Pharmacy and Therapeutics* Apr, 2015, pp 277-283.
- [8] van Duin, D.; Paterson, D. L., Multidrug-Resistant Bacteria in the Community: Trends and Lessons Learned, *Infectious Disease Clinics of North America*, **2016**, *30*, 377-390.
- [9] Medina, E.; Pieper, D. H., Tackling Threats and Future Problems of Multidrug-Resistant Bacteria. In *How to Overcome the Antibiotic Crisis : Facts, Challenges, Technologies and Future Perspectives*, Stadler, M.; Dersch, P., Eds. Springer International Publishing: Cham, **2016**; pp 3-33.
- [10] Murray, C. J. L.; Ikuta, K. S.; Sharara, F.; Swetschinski, L.; Robles Aguilar, G.; Gray, A.; Han, C.; Bisignano, C.; Rao, P.; Wool, E.; Johnson, S. C.; Browne, A. J.; Chipeta, M. G.; Fell, F., *et al.*, Global burden of bacterial antimicrobial resistance in 2019: a systematic analysis, *The Lancet*, **2022**, *399*, 629-655.
- [11] O'Neill, J., *Antimicrobial Resistance: Tackling a crisis for the health and wealth of nations. The Review on Antimicrobial Resistance*; 2014; pp 1-18.
- [12] Adam, D., The pandemic's true death toll: millions more than official counts, *Nature*, **2022**, *601*, 312-315.
- [13] Aminov, R. I., A brief history of the antibiotic era: lessons learned and challenges for the future, *Frontiers in Microbiology*, **2010**, *1*, 134-134.
- [14] Gest, H., The discovery of microorganisms by Robert Hooke and Antoni van Leeuwenhoek, Fellows of The Royal Society, *The Royal Society Journal of the History of Science*, **2004**, *58*, 187-201.

- [15] Worboys, M., Joseph Lister and the performance of antiseptic surgery, *Notes and records of the Royal Society of London*, **2013**, *67*, 199-209.
- [16] Hutchings, M. I.; Truman, A. W.; Wilkinson, B., Antibiotics: past, present and future, *Current Opinion in Microbiology*, **2019**, *51*, 72-80.
- [17] Ribeiro da Cunha, B.; Fonseca, L. P.; Calado, C. R. C., Antibiotic Discovery: Where Have We Come from, Where Do We Go?, *Antibiotics*, **2019**, *8*, 45.
- [18] Lewis, K., Platforms for antibiotic discovery, *Nature Reviews Drug Discovery*, **2013**, *12*, 371-387.
- [19] Blair, J. M.; Webber, M. A.; Baylay, A. J.; Ogbolu, D. O.; Piddock, L. J., Molecular mechanisms of antibiotic resistance, *Nature Reviews Microbiology*, **2015**, *13*, 42-51.
- [20] Munita, J. M.; Arias, C. A., Mechanisms of Antibiotic Resistance, *Microbiology Spectrum*, **2016**, *4*, 2.
- [21] Coico, R., Gram Staining, *Current Protocols in Microbiology*, **2006**, A.3C.1-A.3C.2.
- [22] Silhavy, T. J.; Kahne, D.; Walker, S., The bacterial cell envelope, *Cold Spring Harbor Perspectives in Biology*, **2010**, *2*, a000414.
- [23] Hayami, M.; Okabe, A.; Kariyama, R.; Abe, M.; Kanemasa, Y., Lipid Composition of Staphylococcus aureus and Its Derived L-forms, *Microbiology and Immunology*, **1979**, *23*, 435-442.
- [24] Jori, G.; Fabris, C.; Soncin, M.; Ferro, S.; Coppellotti, O.; Dei, D.; Fantetti, L.; Chiti, G.; Roncucci, G., Photodynamic therapy in the treatment of microbial infections: Basic principles and perspective applications, *Lasers in Surgery and Medicine*, **2006**, *38*, 468-481.
- [25] Aroso, R. T.; Schaberle, F. A.; Arnaut, L. G.; Pereira, M. M., Photodynamic disinfection and its role in controlling infectious diseases, *Photochemical & Photobiological Sciences*, **2021**, *20*, 1497-1545.
- [26] Madigan, M. T.; Bender, K. S.; Buckley, D. H.; Sattley, W. M.; Stahl, D. A., *Brock Biology of Microorganisms*. 15th ed.; Pearson: Upper Saddle River, NJ, **2017**.
- [27] Hancock, R. E. W., Alterations in outer membrane permeability, *Annual Review of Microbiology*, **1984**, *38*, 237-264.
- [28] Delcour, A. H., Outer membrane permeability and antibiotic resistance, *Biochimica et Biophysica Acta (BBA) - Proteins and Proteomics*, **2009**, *1794*, 808-816.
- [29] Andrade, F. F.; Silva, D.; Rodrigues, A.; Pina-Vaz, C., Colistin Update on Its Mechanism of Action and Resistance, Present and Future Challenges, *Microorganisms*, **2020**, *8*, 1716.
- [30] Lewis, K., The Science of Antibiotic Discovery, *Cell*, **2020**, *181*, 29-45.
- [31] Breijyeh, Z.; Jubeh, B.; Karaman, R., Resistance of Gram-Negative Bacteria to Current Antibacterial Agents and Approaches to Resolve It, *Molecules*, **2020**, *25*, 1340.
- [32] World Health Organization - Global Priority List of Antibiotic Resistant Bacteria to Guide Research, Discovery, and Development of New Antibiotics, *World Health Organization, Geneva*, **2017**, 1-7.
- [33] Vila, J.; Saez-Lopez, E.; Johnson, J. R.; Romling, U.; Dobrindt, U.; Canton, R.; Giske, C. G.; Naas, T.; Carattoli, A.; Martinez-Medina, M.; Bosch, J.; Retamar, P.; Rodriguez-Bano, J.; Baquero, F., *et al.*, Escherichia coli: an old friend with new tidings, *FEMS Microbiology Reviews*, **2016**, *40*, 437-463.

- [34] Negut, I.; Grumezescu, V.; Grumezescu, A. M., Treatment Strategies for Infected Wounds, *Molecules*, **2018**, *23*, 2392.
- [35] Kaper, J. B.; Nataro, J. P.; Mobley, H. L., Pathogenic Escherichia coli, *Nature Reviews Microbiology*, **2004**, *2*, 123-140.
- [36] Jackson, M. A.; Schutze, G. E., The Use of Systemic and Topical Fluoroquinolones, *Pediatrics*, **2016**, *138*, e20162706.
- [37] Davis, R.; Markham, A.; Balfour, J. A., Ciprofloxacin, *Drugs*, **1996**, *51*, 1019-1074.
- [38] Tchesnokova, V.; Radey, M.; Chattopadhyay, S.; Larson, L.; Weaver, J. L.; Kisiela, D.; Sokurenko, E. V., Pandemic fluoroquinolone resistant Escherichia coli clone ST1193 emerged via simultaneous homologous recombinations in 11 gene loci, *Proceedings of the National Academy of Sciences of the United States of America*, **2019**, *116*, 14740-14748.
- [39] Zhu, D. M.; Li, Q. H.; Shen, Y.; Zhang, Q., Risk factors for quinolone-resistant Escherichia coli infection: a systematic review and meta-analysis, *Antimicrobial Resistance and Infection Control*, **2020**, *9*, 11.
- [40] Zhang, D.; Cui, Y.; Zhang, X., Estimating Factors Related to Fluoroquinolone Resistance Based on One Health Perspective: Static and Dynamic Panel Data Analyses From Europe, *Frontiers in Pharmacology*, **2019**, *10*, 1145.
- [41] World Health Organization, Global Antimicrobial Resistance and Use Surveillance System (GLASS) Report, **2021**. World Health Organization, Genève. <https://www.who.int/publications/i/item/9789240027336> (accessed on 28/02/2022).
- [42] Puca, V.; Marulli, R. Z.; Grande, R.; Vitale, I.; Niro, A.; Molinaro, G.; Prezioso, S.; Muraro, R.; Di Giovanni, P., Microbial Species Isolated from Infected Wounds and Antimicrobial Resistance Analysis: Data Emerging from a Three-Years Retrospective Study, *Antibiotics*, **2021**, *10*, 1162.
- [43] Alharbi, N. S.; Khaled, J. M.; Kadaikunnan, S.; Alobaidi, A. S.; Sharafaddin, A. H.; Alyahya, S. A.; Almana, T. N.; Alsughayier, M. A.; Shehu, M. R., Prevalence of Escherichia coli strains resistance to antibiotics in wound infections and raw milk, *Saudi Journal of Biological Sciences*, **2019**, *26*, 1557-1562.
- [44] Bessa, L. J.; Fazii, P.; Di Giulio, M.; Cellini, L., Bacterial isolates from infected wounds and their antibiotic susceptibility pattern: some remarks about wound infection, *International Wound Journal*, **2015**, *12*, 47-52.
- [45] WHO report on surveillance of antibiotic consumption, **2019**, World Health Organization, Genève. <https://www.who.int/publications/i/item/who-report-on-surveillance-of-antibiotic-consumption> (accessed on 28/02/2022).
- [46] WHO Regional Office for Europe/European Centre for Disease Prevention and Control, Antimicrobial resistance surveillance in Europe: 2020 data, **2022**, Copenhagen: WHO Regional Office for Europe.
- [47] Yusuf, E.; Bax, H. I.; Verkaik, N. J.; van Westreenen, M., An Update on Eight “New” Antibiotics against Multidrug-Resistant Gram-Negative Bacteria, *Journal of Clinical Medicine*, **2021**, *10*, 1068.
- [48] Karaiskos, I.; Lagou, S.; Pontikis, K.; Rapti, V.; Poulakou, G., The “Old” and the “New” Antibiotics for MDR Gram-Negative Pathogens: For Whom, When, and How, *Frontiers in Public Health*, **2019**, *7*, 151.
- [49] Ventola, C. L., The Antibiotic Resistance Crisis: Part 1: Causes and Threats, *Pharmacy and Therapeutics*, **2015**, *40*, 277-283.

- [50] Nesme, J.; Simonet, P., The soil resistome: a critical review on antibiotic resistance origins, ecology and dissemination potential in telluric bacteria, *Environmental Microbiology*, **2015**, *17*, 913-930.
- [51] Elander, R. P., Industrial production of β -lactam antibiotics, *Applied Microbiology and Biotechnology*, **2003**, *61*, 385-392.
- [52] Demain, A. L.; Elander, R. P., The β -lactam antibiotics: past, present, and future, *Antonie Van Leeuwenhoek*, **1999**, *75*, 5-19.
- [53] Bush, K.; Bradford, P. A., β -Lactams and β -Lactamase Inhibitors: An Overview, *Cold Spring Harbor Perspectives in Medicine*, **2016**, *6*, a025247.
- [54] Andersson, M. I.; MacGowan, A. P., Development of the quinolones, *Journal of Antimicrobial Chemotherapy*, **2003**, *51*, 1-11.
- [55] Collin, F.; Karkare, S.; Maxwell, A., Exploiting bacterial DNA gyrase as a drug target: current state and perspectives, *Applied Microbiology and Biotechnology*, **2011**, *92*, 479-497.
- [56] Sabe, V. T.; Ntombela, T.; Jhamba, L. A.; Maguire, G. E. M.; Govender, T.; Naicker, T.; Kruger, H. G., Current trends in computer aided drug design and a highlight of drugs discovered via computational techniques: A review, *European Journal of Medicinal Chemistry*, **2021**, *224*, 113705.
- [57] Sliwoski, G.; Kothiwale, S.; Meiler, J.; Lowe, E. W., Computational Methods in Drug Discovery, *Pharmacological Reviews*, **2014**, *66*, 334-395.
- [58] Leelananda, S. P.; Lindert, S., Computational methods in drug discovery, *Beilstein Journal of Organic Chemistry*, **2016**, *12*, 2694-2718.
- [59] Dar, K. B.; Bhat, A. H.; Amin, S.; Hamid, R.; Anees, S.; Anjum, S.; Reshi, B. A.; Zargar, M. A.; Masood, A.; Ganie, S. A., Modern Computational Strategies for Designing Drugs to Curb Human Diseases: A Prospect, *Current Topics in Medicinal Chemistry*, **2018**, *18*, 2702-2719.
- [60] Bruch, E. M.; Petrella, S.; Bellinzoni, M., Structure-Based Drug Design for Tuberculosis: Challenges Still Ahead, *Applied Sciences*, **2020**, *10*, 4248.
- [61] Torres, M. D. T.; de la Fuente-Nunez, C., Toward computer-made artificial antibiotics, *Current Opinion in Microbiology*, **2019**, *51*, 30-38.
- [62] Murphy, K. E.; Sloan, G. F.; Lawhern, G. V.; Volk, G. E.; Shumate, J. T.; Wolfe, A. L., Advances in antibiotic drug discovery: reducing the barriers for antibiotic development, *Future Medicinal Chemistry*, **2020**, *12*, 2067-2087.
- [63] O'Daniel, P. I.; Peng, Z.; Pi, H.; Testero, S. A.; Ding, D.; Spink, E.; Leemans, E.; Boudreau, M. A.; Yamaguchi, T.; Schroeder, V. A.; Wolter, W. R.; Llarrull, L. I.; Song, W.; Lastochkin, E., *et al.*, Discovery of a new class of non- β -lactam inhibitors of penicillin-binding proteins with Gram-positive antibacterial activity, *Journal of the American Chemical Society*, **2014**, *136*, 3664-3672.
- [64] Bouley, R.; Kumarasiri, M.; Peng, Z.; Otero, L. H.; Song, W.; Suckow, M. A.; Schroeder, V. A.; Wolter, W. R.; Lastochkin, E.; Antunes, N. T.; Pi, H.; Vakulenko, S.; Hermoso, J. A.; Chang, M., *et al.*, Discovery of antibiotic (E)-3-(3-carboxyphenyl)-2-(4-cyanostyryl)quinazolin-4(3H)-one, *Journal of the American Chemical Society*, **2015**, *137*, 1738-1741.
- [65] Furci, L. M.; Lopes, P.; Eakanunkul, S.; Zhong, S.; MacKerell, A. D.; Wilks, A., Inhibition of the Bacterial Heme Oxygenases from *Pseudomonas aeruginosa* and *Neisseria meningitidis*: Novel Antimicrobial Targets, *Journal of Medicinal Chemistry*, **2007**, *50*, 3804-3813.

- [66] Aronica, P. G. A.; Reid, L. M.; Desai, N.; Li, J.; Fox, S. J.; Yadahalli, S.; Essex, J. W.; Verma, C. S., Computational Methods and Tools in Antimicrobial Peptide Research, *Journal of Chemical Information and Modeling*, **2021**, *61*, 3172-3196.
- [67] Stokes, J. M.; Yang, K.; Swanson, K.; Jin, W.; Cubillos-Ruiz, A.; Donghia, N. M.; MacNair, C. R.; French, S.; Carfrae, L. A.; Bloom-Ackermann, Z.; Tran, V. M.; Chiappino-Pepe, A.; Badran, A. H.; Andrews, I. W., *et al.*, A Deep Learning Approach to Antibiotic Discovery, *Cell*, **2020**, *180*, 688-702.e613.
- [68] Melo, M. C. R.; Maasch, J. R. M. A.; de la Fuente-Nunez, C., Accelerating antibiotic discovery through artificial intelligence, *Communications Biology*, **2021**, *4*, 1050.
- [69] Macalino, S. J. Y.; Gosu, V.; Hong, S.; Choi, S., Role of computer-aided drug design in modern drug discovery, *Archives of Pharmacal Research*, **2015**, *38*, 1686-1701.
- [70] Santosh, A. K.; Alpeshkumar, K. M.; Evans, C. C.; Sudha, S., Pharmacophore Modeling in Drug Discovery and Development: An Overview, *Medicinal Chemistry*, **2007**, *3*, 187-197.
- [71] Kim, K.-H.; Kim, N. D.; Seong, B.-L., Pharmacophore-based virtual screening: a review of recent applications, *Expert Opinion on Drug Discovery*, **2010**, *5*, 205-222.
- [72] Gualerzi, C.; Brandi, L.; Fabbretti, A.; Pon, C., *Antibiotics: Targets, Mechanisms and Resistance*. 1st Edition ed.; Wiley-VCH: Weinheim, Germany, **2014**.
- [73] Monserrat-Martinez, A.; Gambin, Y.; Sierrecki, E., Thinking Outside the Bug: Molecular Targets and Strategies to Overcome Antibiotic Resistance, *International Journal of Molecular Sciences*, **2019**, *20*, 1255.
- [74] Belete, T. M., Novel targets to develop new antibacterial agents and novel alternatives to antibacterial agents, *Human Microbiome Journal*, **2019**, *11*, 100052.
- [75] Khan, T.; Sankhe, K.; Suvarna, V.; Sherje, A.; Patel, K.; Dravyakar, B., DNA gyrase inhibitors: Progress and synthesis of potent compounds as antibacterial agents, *Biomedicine and Pharmacotherapy*, **2018**, *103*, 923-938.
- [76] Vanden Broeck, A.; Lotz, C.; Ortiz, J.; Lamour, V., Cryo-EM structure of the complete E. coli DNA gyrase nucleoprotein complex, *Nature Communications*, **2019**, *10*, 4935.
- [77] Chemical Computing Group ULC. Molecular Operating Environment (MOE). <https://www.chemcomp.com/Products.htm> (accessed on 07/01/2021).
- [78] Reece, R. J.; Maxwell, A., DNA Gyrase: Structure and Function, *Critical Reviews in Biochemistry and Molecular Biology*, **1991**, *26*, 335-375.
- [79] Klostermeier, D., Towards Conformation-Sensitive Inhibition of Gyrase: Implications of Mechanistic Insight for the Identification and Improvement of Inhibitors, *Molecules*, **2021**, *26*, 1234.
- [80] Basu, A.; Parente, A. C.; Bryant, Z., Structural Dynamics and Mechanochemical Coupling in DNA Gyrase, *Journal of Molecular Biology*, **2016**, *428*, 1833-1845.
- [81] Wang, J. C., Cellular roles of DNA topoisomerases: a molecular perspective, *Nature Reviews Molecular Cell Biology*, **2002**, *3*, 430-440.
- [82] Flatman, R. H.; Eustaquio, A.; Li, S.-M.; Heide, L.; Maxwell, A., Structure-activity relationships of aminocoumarin-type gyrase and topoisomerase IV inhibitors obtained by combinatorial biosynthesis, *Antimicrobial Agents and Chemotherapy*, **2006**, *50*, 1136-1142.

- [83] Vologodskii, A., Computational Analysis of DNA Gyrase Action, *Biophysical Journal*, **2004**, *87*, 3066-3073.
- [84] Bisacchi, G. S., Origins of the Quinolone Class of Antibacterials: An Expanded "Discovery Story", *Journal of Medicinal Chemistry*, **2015**, *58*, 4874-4882.
- [85] Pham, T. D. M.; Ziora, Z. M.; Blaskovich, M. A. T., Quinolone antibiotics, *MedChemComm*, **2019**, *10*, 1719-1739.
- [86] Ezelarab, H. A. A.; Abbas, S. H.; Hassan, H. A.; Abu-Rahma, G. E.-D. A., Recent updates of fluoroquinolones as antibacterial agents, *Archiv der Pharmazie*, **2018**, *351*, 1800141.
- [87] Redgrave, L. S.; Sutton, S. B.; Webber, M. A.; Piddock, L. J. V., Fluoroquinolone resistance: mechanisms, impact on bacteria, and role in evolutionary success, *Trends in Microbiology*, **2014**, *22*, 438-445.
- [88] Hooper, D. C.; Jacoby, G. A., Mechanisms of drug resistance: quinolone resistance, *Annals of the New York Academy of Sciences*, **2015**, *1354*, 12-31.
- [89] Conley, Z. C.; Bodine, T. J.; Chou, A.; Zechiedrich, L., Wicked: The untold story of ciprofloxacin, *PLoS Pathogens*, **2018**, *14*, e1006805.
- [90] Gurram, S. R.; Azam, M. A., GyrB inhibitors as potential antibacterial agents: a review, *Monatshefte für Chemie - Chemical Monthly*, **2021**, *152*, 725-744.
- [91] Barančoková, M.; Kikelj, D.; Ilaš, J., Recent progress in the discovery and development of DNA gyrase B inhibitors, *Future Medicinal Chemistry*, **2018**, *10*, 1207-1227.
- [92] Alt, S.; Mitchenall, L. A.; Maxwell, A.; Heide, L., Inhibition of DNA gyrase and DNA topoisomerase IV of *Staphylococcus aureus* and *Escherichia coli* by aminocoumarin antibiotics, *Journal of Antimicrobial Chemotherapy*, **2011**, *66*, 2061-2069.
- [93] Eakin, A. E.; Green, O.; Hales, N.; Walkup, G. K.; Bist, S.; Singh, A.; Mullen, G.; Bryant, J.; Embrey, K.; Gao, N.; Breeze, A.; Timms, D.; Andrews, B.; Uria-Nickelsen, M., *et al.*, Pyrrolamide DNA Gyrase Inhibitors: Fragment-Based Nuclear Magnetic Resonance Screening To Identify Antibacterial Agents, *Antimicrobial Agents and Chemotherapy*, **2012**, *56*, 1240-1246.
- [94] Basarab, G. S.; Manchester, J. I.; Bist, S.; Boriack-Sjodin, P. A.; Dangel, B.; Illingworth, R.; Sherer, B. A.; Sriram, S.; Uria-Nickelsen, M.; Eakin, A. E., Fragment-to-Hit-to-Lead Discovery of a Novel Pyridylurea Scaffold of ATP Competitive Dual Targeting Type II Topoisomerase Inhibiting Antibacterial Agents, *Journal of Medicinal Chemistry*, **2013**, *56*, 8712-8735.
- [95] Trzoss, M.; Bensen, D. C.; Li, X.; Chen, Z.; Lam, T.; Zhang, J.; Creighton, C. J.; Cunningham, M. L.; Kwan, B.; Stidham, M.; Nelson, K.; Brown-Driver, V.; Castellano, A.; Shaw, K. J., *et al.*, Pyrrolopyrimidine inhibitors of DNA gyrase B (GyrB) and topoisomerase IV (ParE), Part II: development of inhibitors with broad spectrum, Gram-negative antibacterial activity, *Bioorganic & Medicinal Chemistry Letters*, **2013**, *23*, 1537-1543.
- [96] Jakopin, Z.; Ilas, J.; Barancokova, M.; Brvar, M.; Tammela, P.; Sollner Dolenc, M.; Tomasic, T.; Kikelj, D., Discovery of substituted oxadiazoles as a novel scaffold for DNA gyrase inhibitors, *European Journal of Medicinal Chemistry*, **2017**, *130*, 171-184.

- [97] Gjorgjieva, M.; Tomasic, T.; Barancokova, M.; Katsamakas, S.; Ilas, J.; Tammela, P.; Peterlin Masic, L.; Kikelj, D., Discovery of Benzothiazole Scaffold-Based DNA Gyrase B Inhibitors, *Journal of Medicinal Chemistry*, **2016**, *59*, 8941-8954.
- [98] Cotman, A. E.; Trampuž, M.; Brvar, M.; Kikelj, D.; Ilaš, J.; Peterlin-Mašič, L.; Montalvão, S.; Tammela, P.; Frlan, R., Design, Synthesis, and Evaluation of Novel Tyrosine-Based DNA Gyrase B Inhibitors, *Archiv der Pharmazie*, **2017**, *350*, 1700087.
- [99] Tomašič, T.; Barančoková, M.; Zidar, N.; Ilaš, J.; Tammela, P.; Kikelj, D., Design, synthesis, and biological evaluation of 1-ethyl-3-(thiazol-2-yl)urea derivatives as Escherichia coli DNA gyrase inhibitors, *Archiv der Pharmazie*, **2018**, *351*, 1700333.
- [100] Yule, I. A.; Czaplewski, L. G.; Pommier, S.; Davies, D. T.; Narramore, S. K.; Fishwick, C. W. G., Pyridine-3-carboxamide-6-yl-ureas as novel inhibitors of bacterial DNA gyrase: Structure based design, synthesis, SAR and antimicrobial activity, *European Journal of Medicinal Chemistry*, **2014**, *86*, 31-38.
- [101] Durcik, M.; Tammela, P.; Barancokova, M.; Tomasic, T.; Ilas, J.; Kikelj, D.; Zidar, N., Synthesis and Evaluation of N-Phenylpyrrolamides as DNA Gyrase B Inhibitors, *ChemMedChem*, **2018**, *13*, 186-198.
- [102] Durcik, M.; Lovison, D.; Skok, Ž.; Durante Cruz, C.; Tammela, P.; Tomašič, T.; Benedetto Tiz, D.; Draskovits, G.; Nyerges, Á.; Pál, C.; Ilaš, J.; Peterlin Mašič, L.; Kikelj, D.; Zidar, N., New N-phenylpyrrolamide DNA gyrase B inhibitors: Optimization of efficacy and antibacterial activity, *European Journal of Medicinal Chemistry*, **2018**, *154*, 117-132.
- [103] Tiz, D. B.; Skok, Ž.; Durcik, M.; Tomašič, T.; Mašič, L. P.; Ilaš, J.; Zega, A.; Draskovits, G.; Révész, T.; Nyerges, Á.; Pál, C.; Cruz, C. D.; Tammela, P.; Žigon, D., *et al.*, An optimised series of substituted N-phenylpyrrolamides as DNA gyrase B inhibitors, *European Journal of Medicinal Chemistry*, **2019**, *167*, 269-290.
- [104] Sharma, S. K.; Mroz, P.; Dai, T.; Huang, Y.-Y.; St Denis, T. G.; Hamblin, M. R., Photodynamic Therapy for Cancer and for Infections: What Is the Difference?, *Israel Journal of Chemistry*, **2012**, *52*, 691-705.
- [105] Macdonald, I. J.; Dougherty, T. J., Basic principles of photodynamic therapy, *Journal of Porphyrins and Phthalocyanines*, **2001**, *5*, 105-129.
- [106] Agostinis, P.; Berg, K.; Cengel, K. A.; Foster, T. H.; Girotti, A. W.; Gollnick, S. O.; Hahn, S. M.; Hamblin, M. R.; Juzeniene, A.; Kessel, D.; Korbelik, M.; Moan, J.; Mroz, P.; Nowis, D., *et al.*, Photodynamic therapy of cancer: An update, *CA: A Cancer Journal for Clinicians*, **2011**, *61*, 250-281.
- [107] Allison, R. R.; Downie, G. H.; Cuenca, R.; Hu, X.-H.; Childs, C. J. H.; Sibata, C. H., Photosensitizers in clinical PDT, *Photodiagnosis and Photodynamic Therapy*, **2004**, *1*, 27-42.
- [108] Dąbrowski, J. M.; Arnaut, L. G., Photodynamic therapy (PDT) of cancer: from local to systemic treatment, *Photochemical & Photobiological Sciences*, **2015**, *14*, 1765-1780.
- [109] Frochot, C.; Mordon, S.; Donohoe, C.; Senge, M. O.; Arnaut, L. G. L. G.; Gomes-da-Silva, L. C.; Yan, W.; Gu, L.; Ren, W.; Ma, X.; Qin, M.; Lyu, M.; Wang, S.; Wilkinson, F., *et al.*, Update of the situation of clinical photodynamic therapy in Europe in the 2003–2018 period, *Journal of Porphyrins and Phthalocyanines*, **2019**, *23*, 347-357.

- [110] Hu, X.; Huang, Y. Y.; Wang, Y.; Wang, X.; Hamblin, M. R., Antimicrobial Photodynamic Therapy to Control Clinically Relevant Biofilm Infections, *Frontiers in Microbiology*, **2018**, *9*, 1299.
- [111] Hamblin, M. R., Antimicrobial photodynamic inactivation: a bright new technique to kill resistant microbes, *Current Opinion in Microbiology*, **2016**, *33*, 67-73.
- [112] Silva, E. F. F.; Serpa, C.; Dąbrowski, J. M.; Monteiro, C. J. P.; Formosinho, S. J.; Stochel, G.; Urbanska, K.; Simões, S.; Pereira, M. M.; Arnaut, L. G., Mechanisms of Singlet-Oxygen and Superoxide-Ion Generation by Porphyrins and Bacteriochlorins and their Implications in Photodynamic Therapy, *Chemistry – A European Journal*, **2010**, *16*, 9273-9286.
- [113] Wainwright, M., The emerging chemistry of blood product disinfection, *Chemical Society Reviews*, **2002**, *31*, 128-136.
- [114] Hamblin, M. R.; Hasan, T., Photodynamic therapy: a new antimicrobial approach to infectious disease?, *Photochemical & Photobiological Sciences*, **2004**, *3*, 436-450.
- [115] Wiehe, A.; O'Brien, J. M.; Senge, M. O., Trends and targets in antiviral phototherapy, *Photochemical & Photobiological Sciences*, **2019**, *18*, 2565-2612.
- [116] Maisch, T., Resistance in antimicrobial photodynamic inactivation of bacteria, *Photochemical & Photobiological Sciences*, **2015**, *14*, 1518-1526.
- [117] Casas, A.; Venosa, G. D.; Hasan, T.; Al, B., Mechanisms of Resistance to Photodynamic Therapy, *Current Medicinal Chemistry*, **2011**, *18*, 2486-2515.
- [118] Soares, J. M.; Inada, N. M.; Bagnato, V. S.; Blanco, K. C., Evolution of surviving *Streptococcus pyogenes* from pharyngotonsillitis patients submit to multiple cycles of antimicrobial photodynamic therapy, *Journal of Photochemistry and Photobiology B: Biology*, **2020**, *210*, 111985.
- [119] Dai, T.; Huang, Y.-Y.; Hamblin, M. R., Photodynamic therapy for localized infections—State of the art, *Photodiagnosis and Photodynamic Therapy*, **2009**, *6*, 170-188.
- [120] Rowan, M. P.; Cancio, L. C.; Elster, E. A.; Burmeister, D. M.; Rose, L. F.; Natesan, S.; Chan, R. K.; Christy, R. J.; Chung, K. K., Burn wound healing and treatment: review and advancements, *Critical Care*, **2015**, *19*, 243.
- [121] Ramirez-Acuña, J. M.; Cardenas-Cadena, S. A.; Marquez-Salas, P. A.; Garza-Veloz, I.; Perez-Favila, A.; Cid-Baez, M. A.; Flores-Morales, V.; Martinez-Fierro, M. L., Diabetic Foot Ulcers: Current Advances in Antimicrobial Therapies and Emerging Treatments, *Antibiotics*, **2019**, *8*, 193.
- [122] Kinane, D. F.; Stathopoulou, P. G.; Papapanou, P. N., Periodontal diseases, *Nature Reviews Disease Primers*, **2017**, *3*, 17038.
- [123] Aroso, R. T.; Piccirillo, G.; Arnaut, Z. A.; Gonzalez, A. C. S.; Rodrigues, F. M. S.; Pereira, M. M., Photodynamic inactivation of influenza virus as a potential alternative for the control of respiratory tract infections, *Journal of Photochemistry and Photobiology*, **2021**, *7*, 100043.
- [124] Duguay, B. A.; Herod, A.; Pringle, E. S.; Monro, S. M. A.; Hetu, M.; Cameron, C. G.; McFarland, S. A.; McCormick, C., Photodynamic Inactivation of Human Coronaviruses, *Viruses*, **2022**, *14*, 110.
- [125] Maisch, T., Strategies to optimize photosensitizers for photodynamic inactivation of bacteria, *Journal of Photochemistry and Photobiology B: Biology*, **2015**, *150*, 2-10.

- [126] Sobotta, L.; Skupin-Mrugalska, P.; Piskorz, J.; Mielcarek, J., Porphyrinoid photosensitizers mediated photodynamic inactivation against bacteria, *European Journal of Medicinal Chemistry*, **2019**, *175*, 72-106.
- [127] Pucelik, B.; Paczyński, R.; Dubin, G.; Pereira, M. M.; Arnaut, L. G.; Dąbrowski, J. M., Properties of halogenated and sulfonated porphyrins relevant for the selection of photosensitizers in anticancer and antimicrobial therapies, *PloS One*, **2017**, *12*, 1-22.
- [128] Mesquita, M. Q.; Dias, C. J.; Neves, M. G. P. M. S.; Almeida, A.; Faustino, M. A. F., Revisiting current photoactive materials for antimicrobial photodynamic therapy, *Molecules*, **2018**, *23*, 2424.
- [129] Abrahamse, H.; Hamblin, M. R., New photosensitizers for photodynamic therapy, *Biochemical Journal*, **2016**, *473*, 347-364.
- [130] Cieplik, F.; Deng, D.; Crielaard, W.; Buchalla, W.; Hellwig, E.; Al-Ahmad, A.; Maisch, T., Antimicrobial photodynamic therapy - what we know and what we don't, *Critical Reviews in Microbiology*, **2018**, *44*, 571-589.
- [131] Galstyan, A., Turning Photons into Drugs: Phthalocyanine-Based Photosensitizers as Efficient Photoantimicrobials, *Chemistry – A European Journal*, **2021**, *27*, 1903-1920.
- [132] Ribeiro, C. P. S.; Lourenço, L. M. O., Overview of cationic phthalocyanines for effective photoinactivation of pathogenic microorganisms, *Journal of Photochemistry and Photobiology C: Photochemistry Reviews*, **2021**, *48*, 100422.
- [133] Klausen, M.; Ucuncu, M.; Bradley, M., Design of Photosensitizing Agents for Targeted Antimicrobial Photodynamic Therapy, *Molecules*, **2020**, *25*, 5239.
- [134] Wainwright, M.; Maisch, T.; Nonell, S.; Plaetzer, K.; Almeida, A.; Tegos, G. P.; Hamblin, M. R., Photoantimicrobials - are we afraid of the light?, *The Lancet Infectious Diseases*, **2017**, *17*, e49-e55.
- [135] Oyama, J.; Fernandes Herculano Ramos-Milaré, Á. C.; Lopes Lera-Nonose, D. S. S.; Nesi-Reis, V.; Galhardo Demarchi, I.; Alessi Aristides, S. M.; Juarez Vieira Teixeira, J.; Gomes Verzignassi Silveira, T.; Campana Lonardoní, M. V., Photodynamic therapy in wound healing in vivo: a systematic review, *Photodiagnosis and Photodynamic Therapy*, **2020**, *30*, 101682.
- [136] Calzavara-Pinton, P.; Rossi, M. T.; Sala, R.; Venturini, M., Photodynamic antifungal chemotherapy, *Photochemistry and Photobiology*, **2012**, *88*, 512-522.
- [137] Lebedeva, N. S.; Gubarev, Y. A.; Koifman, M. O.; Koifman, O. I., The Application of Porphyrins and Their Analogues for Inactivation of Viruses, *Molecules*, **2020**, *25*, 4368.
- [138] Mariewskaya, K. A.; Tyurin, A. P.; Chistov, A. A.; Korshun, V. A.; Alferova, V. A.; Ustinov, A. V., Photosensitizing Antivirals, *Molecules*, **2021**, *26*, 3971.
- [139] Willis, J. A.; Cheburkanov, V.; Kassab, G.; Soares, J. M.; Blanco, K. C.; Bagnato, V. S.; Yakovlev, V. V., Photodynamic viral inactivation: Recent advances and potential applications, *Applied Physics Reviews*, **2021**, *8*, 021315.
- [140] Vinagreiro, C. S.; Zangirolami, A.; Schaberle, F. A.; Nunes, S. C. C.; Blanco, K. C.; Inada, N. M.; Da Silva, G. J.; Pais, A. A. C. C.; Bagnato, V. S.; Arnaut, L. G.; Pereira, M. M., Antibacterial Photodynamic Inactivation of Antibiotic-Resistant Bacteria and Biofilms with Nanomolar Photosensitizer Concentrations, *ACS Infectious Diseases*, **2020**, *6*, 1517-1526.

- [141] Aroso, R. T.; Calvete, M. J. F.; Pucelik, B.; Dubin, G.; Arnaut, L. G.; Pereira, M. M.; Dąbrowski, J. M., Photoinactivation of microorganisms with sub-micromolar concentrations of imidazolium metallophthalocyanine salts, *European Journal of Medicinal Chemistry*, **2019**, *184*, 111740.
- [142] Xuan, W.; Huang, L.; Wang, Y.; Hu, X.; Szewczyk, G.; Huang, Y. Y.; El-Hussein, A.; Bommer, J. C.; Nelson, M. L.; Sarna, T.; Hamblin, M. R., Amphiphilic tetracationic porphyrins are exceptionally active antimicrobial photosensitizers: In vitro and in vivo studies with the free-base and Pd-chelate, *J Biophotonics*, **2019**, *12*, 1-13.
- [143] Wozniak, A.; Grinholc, M., Combined Antimicrobial Activity of Photodynamic Inactivation and Antimicrobials-State of the Art, *Frontiers in Microbiology*, **2018**, *9*, 930.
- [144] Pérez-Laguna, V.; Gilaberte, Y.; Millán-Lou, M. I.; Agut, M.; Nonell, S.; Rezusta, A.; Hamblin, M. R., A combination of photodynamic therapy and antimicrobial compounds to treat skin and mucosal infections: A systematic review, *Photochemical & Photobiological Sciences*, **2019**, *18*, 1020-1029.
- [145] Feng, Y.; Coradi Tonon, C.; Ashraf, S.; Hasan, T., Photodynamic and antibiotic therapy in combination against bacterial infections: efficacy, determinants, mechanisms, and future perspectives, *Advanced Drug Delivery Reviews*, **2021**, *177*, 113941.
- [146] Polat, E.; Kang, K., Natural Photosensitizers in Antimicrobial Photodynamic Therapy, *Biomedicines*, **2021**, *9*, 584.
- [147] Suvorov, N.; Pogorilyy, V.; Diachkova, E.; Vasil'ev, Y.; Mironov, A.; Grin, M., Derivatives of Natural Chlorophylls as Agents for Antimicrobial Photodynamic Therapy, *International Journal of Molecular Sciences*, **2021**, *22*, 6392.
- [148] Habermeyer, B.; Chilingaryan, T.; Guilard, R., Bactericidal efficiency of porphyrin systems, *Journal of Porphyrins and Phthalocyanines*, **2021**, *25*, 359-381.
- [149] Pérez, C.; Zúñiga, T.; Palavecino, C. E., Photodynamic therapy for treatment of Staphylococcus aureus infections, *Photodiagnosis and Photodynamic Therapy*, **2021**, *34*, 102285.
- [150] Oyim, J.; Omolo, C. A.; Amuhaya, E. K., Photodynamic Antimicrobial Chemotherapy: Advancements in Porphyrin-Based Photosensitizer Development, *Frontiers in Chemistry*, **2021**, *9*, 635344.
- [151] Vallejo, M. C. S.; Moura, N. M. M.; Gomes, A. T. P. C.; Joaquineto, A. S. M.; Faustino, M. A. F.; Almeida, A.; Gonçalves, I.; Serra, V. V.; Neves, M. G. P. M. S., The Role of Porphyrinoid Photosensitizers for Skin Wound Healing, *International Journal of Molecular Sciences*, **2021**, *22*, 4121.
- [152] Niculescu, A.-G.; Grumezescu, A. M., Photodynamic Therapy—An Up-to-Date Review, *Applied Sciences*, **2021**, *11*, 3626.
- [153] Correia, J. H.; Rodrigues, J. A.; Pimenta, S.; Dong, T.; Yang, Z., Photodynamic Therapy Review: Principles, Photosensitizers, Applications, and Future Directions, *Pharmaceutics*, **2021**, *13*, 1332.
- [154] Maldonado-Carmona, N.; Ouk, T.-S.; Leroy-Lhez, S., Latest trends on photodynamic disinfection of Gram-negative bacteria: photosensitizer's structure and delivery systems, *Photochemical & Photobiological Sciences*, **2022**, *21*, 113-145.
- [155] Souza, T. H. S.; Sarmiento-Neto, J. F.; Souza, S. O.; Raposo, B. L.; Silva, B. P.; Borges, C. P. F.; Santos, B. S.; Cabral Filho, P. E.; Rebouças, J. S.; Fontes, A.,

- Advances on antimicrobial photodynamic inactivation mediated by Zn(II) porphyrins, *Journal of Photochemistry and Photobiology C: Photochemistry Reviews*, **2021**, *49*, 100454.
- [156] Spesia, M. B.; Durantini, E. N., Evolution of Phthalocyanine Structures as Photodynamic Agents for Bacteria Inactivation, *The Chemical Record*, **2022**, e202100292.
- [157] Dharmaratne, P.; Sapugahawatte, D. N.; Wang, B.; Chan, C. L.; Lau, K.-M.; Lau, C. B. S.; Fung, K. P.; Ng, D. K. P.; Ip, M., Contemporary approaches and future perspectives of antibacterial photodynamic therapy (aPDT) against methicillin-resistant *Staphylococcus aureus* (MRSA): A systematic review, *European Journal of Medicinal Chemistry*, **2020**, *200*, 112341.
- [158] Sobotta, L.; Skupin-Mrugalska, P.; Piskorz, J.; Mielcarek, J., Non-porphyrinoid photosensitizers mediated photodynamic inactivation against bacteria, *Dyes and Pigments*, **2019**, *163*, 337-355.
- [159] Verónica Almeida-Marrero, J. A. G.-D., Tomás Torres, Emerging Perspectives on Applications of Porphyrinoids for Photodynamic Therapy and Photoinactivation of Microorganisms, *Macroheterocycles*, **2019**, *12*, 8-16.
- [160] Amos-Tautua, B. M.; Songca, S. P.; Oluwafemi, O. S., Application of Porphyrins in Antibacterial Photodynamic Therapy, *Molecules*, **2019**, *24*, 2456.
- [161] Jia, Q.; Song, Q.; Li, P.; Huang, W., Rejuvenated Photodynamic Therapy for Bacterial Infections, *Advanced Healthcare Materials*, **2019**, *8*, 1900608.
- [162] Karner, L.; Drechsler, S.; Metzger, M.; Hacobian, A.; Schädli, B.; Slezak, P.; Grillari, J.; Dungal, P., Antimicrobial photodynamic therapy fighting polymicrobial infections – a journey from in vitro to in vivo, *Photochemical & Photobiological Sciences*, **2020**, *19*, 1332-1343.
- [163] Ucuncu, M.; Mills, B.; Duncan, S.; Staderini, M.; Dhaliwal, K.; Bradley, M., Polymyxin-based photosensitizer for the potent and selective killing of Gram-negative bacteria, *Chemical Communications*, **2020**, *56*, 3757-3760.
- [164] Tortik, N.; Steinbacher, P.; Maisch, T.; Spaeth, A.; Plaetzer, K., A comparative study on the antibacterial photodynamic efficiency of a curcumin derivative and a formulation on a porcine skin model, *Photochemical & Photobiological Sciences*, **2016**, *15*, 187-195.
- [165] Xu, Z.; Gao, Y.; Meng, S.; Yang, B.; Pang, L.; Wang, C.; Liu, T., Mechanism and In Vivo Evaluation: Photodynamic Antibacterial Chemotherapy of Lysine-Porphyrin Conjugate, *Frontiers in Microbiology*, **2016**, *7*, 242.
- [166] Hamblin, M. R.; Jori, G., *Photodynamic Inactivation of Microbial Pathogens*. The Royal Society of Chemistry: Cambridge, **2011**.
- [167] Azaripour, A.; Dittrich, S.; Van Noorden, C. J. F.; Willershausen, B., Efficacy of photodynamic therapy as adjunct treatment of chronic periodontitis: a systematic review and meta-analysis, *Lasers in Medical Science*, **2018**, *33*, 407-423.
- [168] Plotino, G.; Grande, N. M.; Mercade, M., Photodynamic therapy in endodontics, *International Endodontic Journal*, **2019**, *52*, 760-774.
- [169] Carrera, E. T.; Dias, H. B.; Corbi, S. C. T.; Marcantonio, R. A. C.; Bernardi, A. C. A.; Bagnato, V. S.; Hamblin, M. R.; Rastelli, A. N. S., The application of antimicrobial photodynamic therapy (aPDT) in dentistry: a critical review, *Laser Physics*, **2016**, *26*, 123001.

- [170] Bordea, I. R.; Hanna, R.; Chiniforush, N.; Gradinaru, E.; Campian, R. S.; Sirbu, A.; Amaroli, A.; Benedicenti, S., Evaluation of the outcome of various laser therapy applications in root canal disinfection: A systematic review, *Photodiagnosis and Photodynamic Therapy*, **2020**, *29*, 101611.
- [171] Diogo, P.; MA, F. F.; MG, P. M. S. N.; Palma, P. J.; I, P. B.; Goncalves, T.; Santos, J. M., An Insight into Advanced Approaches for Photosensitizer Optimization in Endodontics-A Critical Review, *Journal of Functional Biomaterials*, **2019**, *10*, 44.
- [172] Tişler, C.-E.; Badea, M.-E.; Buduru, S.; Kui, A.; Floria, M.; Popescu, Ş.; Mitariu, M.; Negucioiu, M.; Dogaru, G., Biofilm Inactivation using Photodynamic Therapy in Dentistry: a review of literature, *Balneo Research Journal*, **2020**, *11*, 279-287.
- [173] Kawczyk-Krupka, A.; Pucelik, B.; Międzybrodzka, A.; Sieroń, A. R.; Dąbrowski, J. M., Photodynamic therapy as an alternative to antibiotic therapy for the treatment of infected leg ulcers, *Photodiagnosis and Photodynamic Therapy*, **2018**, *23*, 132-143.
- [174] Mannucci, E.; Genovese, S.; Monami, M.; Navalesi, G.; Dotta, F.; Anichini, R.; Romagnoli, F.; Gensini, G., Photodynamic topical antimicrobial therapy for infected foot ulcers in patients with diabetes: A randomized, double-blind, placebo-controlled study - The D.A.N.T.E (Diabetic ulcer Antimicrobial New Topical treatment Evaluation) study, *Acta Diabetologica*, **2014**, *51*, 435-440.
- [175] Mosti, G.; Picerni, P.; Licau, M.; Mattaliano, V., Photodynamic therapy in infected venous and mixed leg ulcers: a pilot experience, *Journal of Wound Care*, **2018**, *27*, 816-821.
- [176] Martinelli, N.; Curci, V.; Quarantiello, A.; Saldalamacchia, G., The benefits of antimicrobial photodynamic therapy with RLP068 in the management of diabetic foot ulcers, *Drugs in context*, **2019**, *8*, 212610.
- [177] Brocco, E.; Curci, V.; Da Ros, R.; Miranda, C.; Boschetti, G.; Barone, S.; Tedeschi, A.; Salutini, E.; Anichini, R., Photodynamic Topical Antimicrobial Therapy for Infected Diabetic Foot Ulcers in Patients With Diabetes: A Case Series, *The International Journal of Lower Extremity Wounds*, **2020**, 1-4.
- [178] Pantò, F.; Adamo, L.; Giordano, C.; Licciardello, C., Efficacy and safety of photodynamic therapy with RLP068 for diabetic foot ulcers: a review of the literature and clinical experience, *Drugs in context*, **2020**, *9*, 2019-2010-2013.
- [179] Tardivo, J. P.; Adami, F.; Correa, J. A.; Pinhal, M. A.; Baptista, M. S., A clinical trial testing the efficacy of PDT in preventing amputation in diabetic patients, *Photodiagnosis and Photodynamic Therapy*, **2014**, *11*, 342-350.
- [180] Carrinho, P. M.; Andreani, D. I. K.; Morete, V. A.; Iseri, S.; Navarro, R. S.; Villaverde, A. B., A Study on the Macroscopic Morphometry of the Lesion Area on Diabetic Ulcers in Humans Treated with Photodynamic Therapy Using Two Methods of Measurement, *Photomedicine and Laser Surgery*, **2018**, *36*, 44-50.
- [181] Shen, X.; Dong, L.; He, X.; Zhao, C.; Zhang, W.; Li, X.; Lu, Y., Treatment of infected wounds with methylene blue photodynamic therapy: An effective and safe treatment method, *Photodiagnosis and Photodynamic Therapy*, **2020**, *32*, 102051.
- [182] Devirgiliis, V.; Panasiti, V.; Fioriti, D.; Anzivino, E.; Bellizzi, A.; Cimillo, M.; Curzio, M.; Melis, L.; Roberti, V.; Gobbi, S.; Lieto, P.; Richetta, A. G.; Calvieri, S.; Chiarini, F., *et al.*, Antibacterial Activity of Methyl Aminolevulinate Photodynamic Therapy

- in the Treatment of a Cutaneous Ulcer, *International Journal of Immunopathology and Pharmacology*, **2011**, *24*, 793-795.
- [183] Mavilia, L.; Cantarella, C.; Cicero, F.; Mercuri, S. R., Effective use of photodynamic therapy on the treatment of chronic leg ulcers: a pilot study, *Dermatologic Therapy*, **2015**, *28*, 276-278.
- [184] Richter, P.; Krüger, M.; Prasad, B.; Gastiger, S.; Bodenschatz, M.; Wieder, F.; Burkovski, A.; Geißdörfer, W.; Lebert, M.; Strauch, S. M., Using Colistin as a Trojan Horse: Inactivation of Gram-Negative Bacteria with Chlorophyllin, *Antibiotics*, **2019**, *8*, 158.
- [185] Le Guern, F.; Ouk, T.-S.; Grenier, K.; Joly, N.; Lequart, V.; Sol, V., Enhancement of photobactericidal activity of chlorin-e6-cellulose nanocrystals by covalent attachment of polymyxin B, *Journal of Materials Chemistry B*, **2017**, *5*, 6953-6962.
- [186] Johnson, G. A.; Muthukrishnan, N.; Pellois, J.-P., Photoinactivation of Gram Positive and Gram Negative Bacteria with the Antimicrobial Peptide (KLAKLAK)₂ Conjugated to the Hydrophilic Photosensitizer Eosin Y, *Bioconjugate Chemistry*, **2013**, *24*, 114-123.
- [187] Dosselli, R.; Gobbo, M.; Bolognini, E.; Campestrini, S.; Reddi, E., Porphyrin–Apidaecin Conjugate as a New Broad Spectrum Antibacterial Agent, *ACS Medicinal Chemistry Letters*, **2010**, *1*, 35-38.
- [188] Liu, F.; Soh Yan Ni, A.; Lim, Y.; Mohanram, H.; Bhattacharjya, S.; Xing, B., Lipopolysaccharide Neutralizing Peptide–Porphyrin Conjugates for Effective Photoinactivation and Intracellular Imaging of Gram-Negative Bacteria Strains, *Bioconjugate Chemistry*, **2012**, *23*, 1639-1647.
- [189] Huang, L.; Wang, M.; Huang, Y.-Y.; El-Hussein, A.; Wolf, L. M.; Chiang, L. Y.; Hamblin, M. R., Progressive cationic functionalization of chlorin derivatives for antimicrobial photodynamic inactivation and related vancomycin conjugates, *Photochemical & Photobiological Sciences*, **2018**, *17*, 638-651.
- [190] Almeida, J.; Tomé, J. P. C.; Neves, M. G. P. M. S.; Tomé, A. C.; Cavaleiro, J. A. S.; Cunha, Â.; Costa, L.; Faustino, M. A. F.; Almeida, A., Photodynamic inactivation of multidrug-resistant bacteria in hospital wastewaters: influence of residual antibiotics, *Photochemical & Photobiological Sciences*, **2014**, *13*, 626-633.
- [191] Cahan, R.; Swissa, N.; Gellerman, G.; Nitzan, Y., Photosensitizer–Antibiotic Conjugates: A Novel Class of Antibacterial Molecules, **2010**, *86*, 418-425.
- [192] Dastgheyb, S. S.; Eckmann, D. M.; Composto, R. J.; Hickok, N. J., Photo-activated porphyrin in combination with antibiotics: Therapies against Staphylococci, *Journal of Photochemistry and Photobiology B: Biology*, **2013**, *129*, 27-35.
- [193] Nieves, I.; Hally, C.; Viappiani, C.; Agut, M.; Nonell, S., A porphycene-gentamicin conjugate for enhanced photodynamic inactivation of bacteria, *Bioorganic Chemistry*, **2020**, *97*, 103661.
- [194] Ronqui, M. R.; de Aguiar Coletti, T. M.; de Freitas, L. M.; Miranda, E. T.; Fontana, C. R., Synergistic antimicrobial effect of photodynamic therapy and ciprofloxacin, *Journal of Photochemistry and Photobiology B: Biology*, **2016**, *158*, 122-129.
- [195] Pereira, N. L. F.; Aquino, P. E. A.; Junior, J.; Cristo, J. S.; Vieira Filho, M. A.; Moura, F. F.; Ferreira, N. M. N.; Silva, M. K. N.; Nascimento, E. M.; Correia, F. M. A.; Cunha, F. A. B.; Boligon, A. A.; Coutinho, H. D. M.; Ribeiro-Filho, J., *et al.*, Antibacterial activity and antibiotic modulating potential of the essential oil

- obtained from *Eugenia jambolana* in association with led lights, *Journal of Photochemistry and Photobiology B: Biology*, **2017**, *174*, 144-149.
- [196] Tichaczek-Goska, D.; Wojnicz, D.; Symonowicz, K.; Ziółkowski, P.; Hendrich, A. B., Photodynamic enhancement of the activity of antibiotics used in urinary tract infections, *Lasers in Medical Science*, **2019**, *34*, 1547-1553.
- [197] Lu, Z.; Dai, T.; Huang, L.; Kurup, D. B.; Tegos, G. P.; Jahnke, A.; Wharton, T.; Hamblin, M. R., Photodynamic therapy with a cationic functionalized fullerene rescues mice from fatal wound infections, *Nanomedicine: Nanotechnology, Biology, and Medicine*, **2010**, *5*, 1525-1533.
- [198] Shih, M.-H.; Huang, F.-C., Effects of Photodynamic Therapy on Rapidly Growing Nontuberculous Mycobacteria Keratitis, *Investigative Ophthalmology and Visual Science*, **2011**, *52*, 223-229.
- [199] Zhao, Z.; Ma, J.; Wang, Y.; Xu, Z.; Zhao, L.; Zhao, J.; Hong, G.; Liu, T., Antimicrobial Photodynamic Therapy Combined With Antibiotic in the Treatment of Rats With Third-Degree Burns, *Frontiers in Microbiology*, **2021**, *12*, 622410.
- [200] Tanaka, M.; Mroz, P.; Dai, T.; Huang, L.; Morimoto, Y.; Kinoshita, M.; Yoshihara, Y.; Shinomiya, N.; Seki, S.; Nemoto, K.; Hamblin, M. R., Linezolid and vancomycin decrease the therapeutic effect of methylene blue-photodynamic therapy in a mouse model of MRSA bacterial arthritis, *Photochemistry and Photobiology*, **2013**, *89*, 679-682.
- [201] Sun, K.; Yang, H.; Huang, X.; Gong, N.; Qin, Q.; Lu, W.; Lei, X., ALA-PDT combined with antibiotics for the treatment of atypical mycobacterial skin infections: Outcomes and safety, *Photodiagnosis and Photodynamic Therapy*, **2017**, *19*, 274-277.
- [202] Gong, N.; Tan, Y.; Li, M.; Lu, W.; Lei, X., ALA-PDT combined with antibiotics for the treatment of multiple skin abscesses caused by *Mycobacterium fortuitum*, *Photodiagnosis and Photodynamic Therapy*, **2016**, *15*, 70-72.

CHAPTER 2

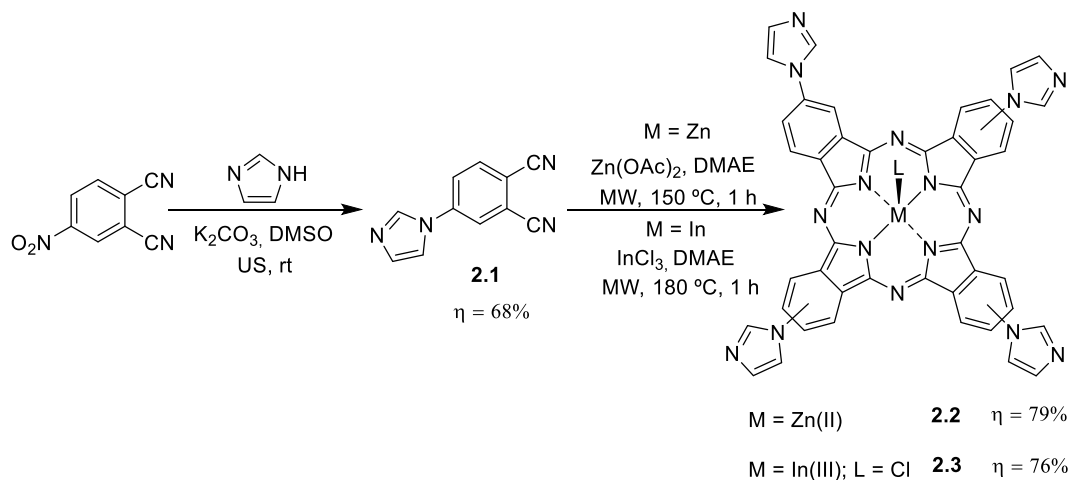
Photoinactivation of *E. coli* by dual phototherapy

2.1 – Synthesis and characterization of photosensitizers

For the studies concerning photodynamic inactivation of *E. coli*, in a monotherapy approach or in combination with ciprofloxacin (dual phototherapy), a set of cationic imidazolyl-substituted tetrapyrrolic macrocycle PS were synthesized. The selection of PS structures was driven by the need to evaluate the influence of the macrocycle base structure (phthalocyanine or porphyrin), absorption (blue or near-IR light), number of positive charges, amphiphilicity, and central coordinating metal.

First, we studied an alternative synthesis of β -tetra-imidazolyl substituted Zn(II) and In(III)Cl phthalocyanine metal complexes, which was previously reported under conventional heating methodologies.¹⁻² This strategy encompasses a two-step approach that starts with the structural modulation of the phthalonitrile precursor, followed by its cyclotetramerization with the appropriate metal salt. For this work, the phthalonitrile modulation with the imidazole group and the synthesis of the metallophthalocyanines were optimized under more sustainable reaction conditions, including ultrasound and microwave irradiation. (Scheme 2.1). Starting with the synthesis of 4-imidazolyl phthalonitrile **2.1**, several optimization parameters were studied and the results are presented in Table 2.1. The previously described conditions (conventional synthesis) used DMF as solvent and K_2CO_3 as base, requiring 48 h of stirring, at room temperature, to achieve complete substrate conversion. After reaction completion, the work-up procedure involved filtration of the base, addition of water to induce product

precipitation, followed by washing with hot methanol. The intended product **2.1** was obtained with 56% yield (Table 2.1, entry 1).



Scheme 2.1: Phthalonitrile and imidazolyl-substituted metallophthalocyanines synthesis, under ultrasound and microwave irradiation, respectively.

Aiming the increase of the sustainability of the process, the reaction was then carried out under ultrasound (US) irradiation, also at room temperature, resulting in a time reduction from 48 h to just 9 h and a slight yield increase to 62% (Table 2.1, entry 2). The beneficial effects of ultrasound irradiation on S_N reactions, namely in aromatic nucleophilic substitution have been previously described.³⁻⁵ Sonochemistry acts through the formation and subsequent collapse of microbubbles, in a process called acoustic cavitation. This results in the formation of hot-spots in the reaction medium, with high local temperature and pressure, which facilitates crossing of the activation energy barrier required for these S_N reactions.⁶

Table 2.1: Synthesis optimization of **2.1** under sustainable conditions.^(a)

#	Heating methodology	Solvent	Reaction time (h) ^(b)	Isolated yield (%)	EcoScale
1	Conventional	DMF	48	56	39
2	Ultrasound	DMF	9	62	41
3	Ultrasound	Acetone	24	Trace	-
4	Ultrasound	DMSO	8	68	60

^(a) Standard reaction conditions: 4-nitroththalonitrile (10 mmol), imidazole (12 mmol), K_2CO_3 (15 mmol) dissolved in designated solvent; stirring at room temperature during designated time; ^(b) Time required for complete conversion of the starting reagent.

From a sustainability standpoint, the most concerning issue in this reaction is related to the use of DMF as solvent. It is widely known that DMF is associated with reproductive toxicity and thus belongs to the list of “substances of very high concern for authorization”, according to the European Chemicals Agency.⁷ Indeed, according to the International Council for Harmonization (ICH) of Technical Requirements for Registration of Pharmaceuticals for Human Use of the European Medicines Agency (EMA), DMF is classified as a class 2 solvent, which limits its use in pharmaceuticals manufacture, being 880 ppm the maximum allowed residual concentration in drug substances.⁸ On the other hand, other polar aprotic solvents such as acetone and DMSO are considered class 3 solvents, for which there are less strict limitations on residual quantities. In Table 2.2 the conclusions of studies conducted by three pharmaceutical industries (Pfizer, GSK and Sanofi) concerning environmental, health and safety issues of selected commonly used polar aprotic solvents, are presented.⁹ While DMF is unanimously considered a bad solvent choice, DMSO and acetone are more favorably regarded.

Table 2.2: Color-coded solvent selection guide according to Pfizer, GSK and Sanofi for selected polar aprotic solvents.⁹

Solvent	Conclusion (Pfizer)	Conclusion (GSK)	Conclusion (Sanofi)
DMF	Undesirable	Major issues	Substitution requested
Acetone	Preferred	Some issues	Recommended
DMSO	Usable	Some issues	Substitution advisable

Taking into account the solvent preferences by pharmaceutical companies, acetone was first selected for the substitution of DMF for the synthesis of **2.1** (Table 2.1, entry 3). However, after 24 h reaction time, the solution had acquired an intense dark brown color and no product formation was observed. The fact that acetone can undergo enolization and act as a nucleophile may explain the failure of this reaction attempt. The second solvent choice for the substitution of DMF was DMSO (Table 2.1, entry 4). When compared with DMF, under ultrasound irradiation, a similar reaction time was observed

(9 h in DMF, 8 h in DMSO). Nonetheless, the reaction conducted in DMSO gave no appreciable water-insoluble side products, unlike the reaction conducted in DMF. Thus, the product could be precipitated from the reaction crude by addition of water, which also dissolved all reaction impurities. This resulted in a simpler workup procedure, as it was not required to wash the precipitated product with hot methanol. Under these conditions, the **2.1** was isolated in 68% yield, which is a slight increase relatively to the previous reaction attempts, but a great step regarding the sustainability of the process. Indeed, these optimized conditions led to a calculated EcoScale¹⁰ value of 60 (details in Chapter 4 - Experimental), which is considerably higher than the value calculated for the conventional heating methodology using DMF (EcoScale of 39, entry 1).

The synthetic route proceeded with the synthesis of metallophthalocyanines through phthalonitrile cyclotetramerization. The synthesis of both Zn(II) and In(III) complexes under conventional heating methodologies have been previously reported² and, again, reaction optimizations were carried out (Table 2.3).

Table 2.3: Reaction conditions for the optimization of phthalocyanine synthesis under sustainable conditions.^(a)

#	Metal	Heating methodology	T (°C)	Solvent	Reaction time (h) ^(b)	Isolated Yield (%)	EcoScale
1	Zn(II) 2.2	CH	140	DMAE	24	71	57
2	Zn(II) 2.2	MW	140	DMAE	1	69	55
3	In(III) 2.3	CH	180	Quinoline	8	67	55
4	In(III) 2.3	MW	180	Quinoline	1	66	53
5	In(III) 2.3	MW	180	DMAE	1	76	63

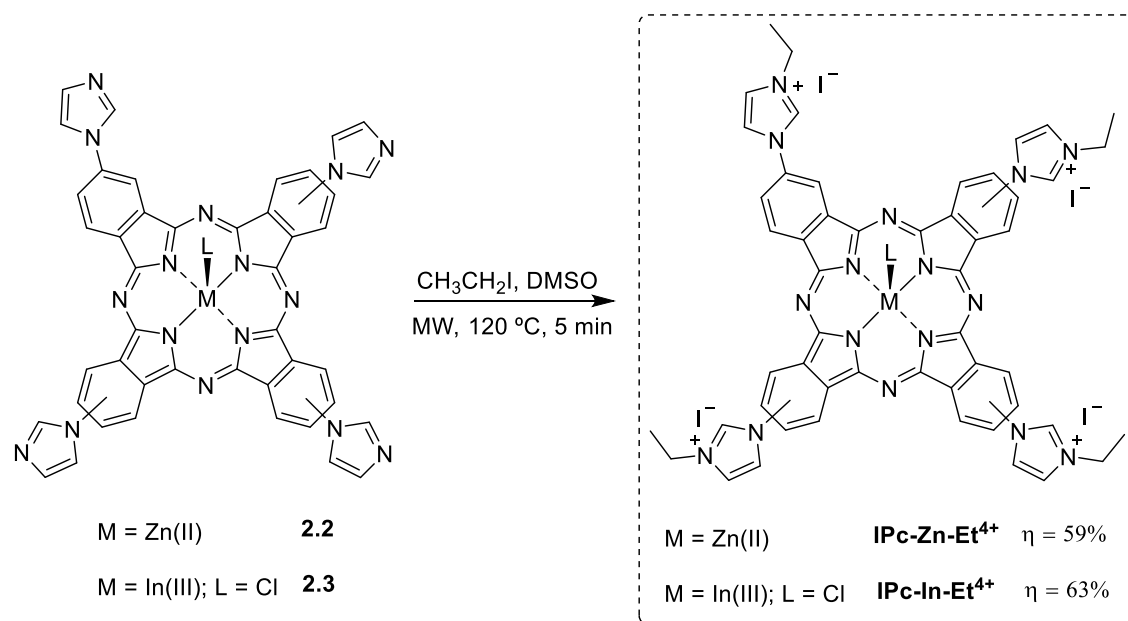
^(a) Standard reaction conditions: phthalonitrile **2.1** (1.5 mmol), Zn(OAc)₂·2H₂O or InCl₃ (0.5 mmol) dissolved in designated solvent; stirring at 140 or 180 °C during designated time; ^(b) Time required for complete conversion of the starting reagent.

Starting with the Zn(II) complex, the conventional synthesis was carried out at 140 °C during 24 h, using DMAE as solvent (Table 2.3, entry 1). The work-up procedure involved product precipitation from the crude mixture by addition of methanol, followed by washing with water and acetone. When attempting the reaction under microwave

irradiation ($P_{\max} = 150 \text{ W}$), at the same temperature, the reaction time was reduced to just 1 h, while keeping similar yield (69%) (Table 2.3, entry 2). The synthesis of the In(III) complex, under conventional heating, was carried out at 180 °C for 8 h, in quinoline as solvent (Table 2.3, entry 3). Due to the increased ionic size of In^{3+} , when compared to Zn^{2+} , the metal template effect on the phthalocyanine formation is less efficient due to a poorer coordination with the nitrogen atoms on the interior cavity. Thus, higher reaction temperatures are required, requiring the substitution of DMAE by a higher boiling point solvent such as quinoline. When this reaction was conducted under microwave irradiation, again a significant reduction in reaction time was observed, to just 1 h, with no discernible difference in reaction yield (Table 2.3, entry 4). However, the use of quinoline as solvent presented two major issues: i) the reaction crude contained a brown-colored impurity which required washing with a copious volume of organic solvents; ii) it is a likely human carcinogen. These shortcomings were addressed by using DMAE as reaction solvent (Table 2.3, entry 5). DMAE is well-tolerated by humans, being used in cosmetics,¹¹ and thus is the ideal solvent for the synthesis of phthalocyanines, due to the formation of residues with low toxicity. While this solvent's boiling point at ambient pressure is 133 °C, it can be overheated in a closed vessel under microwave irradiation and reach the required 180 °C for the reaction to occur. This significantly improved the purification procedures, as fewer side products were obtained, resulting in a higher isolated yield (76%) and EcoScale value (63).

Microwave assisted chemistry is regarded as a greener alternative to conventional synthesis, due to its higher energy efficiency.¹² One of the most relevant advantages of MW irradiation over conventional heating can be explained by thermal effects. On the one hand, conventional heating is through convection, which means that the heating occurs from the periphery to the center. This means that the reaction flask is heated first and then transfers its energy to the solvent. On the other hand, in microwave irradiation, there is an inverse heat transfer, which means that the reaction is heated from the center to the periphery. The polar reaction components will interact with the microwave irradiation and heat the reaction mixture first. Overall, this promotes a faster and more energy efficient heating mechanism and, as a consequence, this may result in chemical reactions with lower reaction times, more reproducibility and higher product yields.¹³

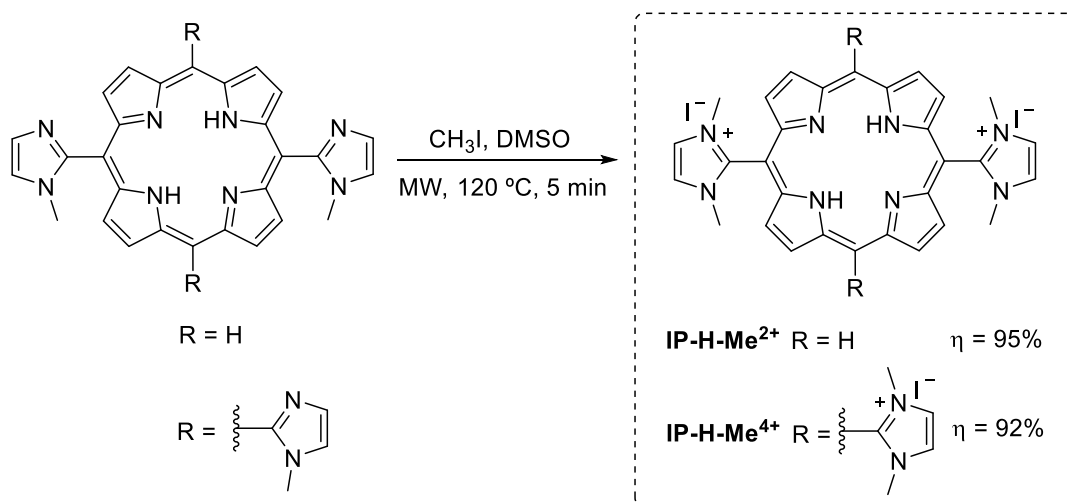
The modulation of the metallophthalocyanines intended for bacterial inactivation proceeded with the cationization of the imidazole groups with iodoethane, in order to obtain the corresponding tetra-cationic Zn(II) and In(III) metallophthalocyanines (Scheme 2.2). As mentioned in the introductory chapter, the use of cationic photosensitizers is crucial for promoting efficient interactions with the negatively charged residues in *E. coli*'s cell wall. The target cationic compounds were selected based on structure-activity studies previously conducted in the work leading up to the MSc thesis.² Indeed, it was found that phthalocyanines bearing four positive charges and cationized with a small alkyl chain (ethyl) were more effective in *E. coli* inactivation. Thus, we optimized, under more sustainable conditions, the previously reported cationization procedure carried out under conventional heating, at 70 °C, over 48 h, and using DMF as solvent.¹ The alternative approach (Scheme 2.2) used microwave irradiation as heating source and, at 120 °C ($P_{\max} = 150$ W), the cationization reactions of both Zn(II) and In(III) metallophthalocyanine were complete after just 5 minutes. The work-up procedure consisted in a simple precipitation from the reaction crude using acetone, followed by filtration.



Scheme 2.2: Synthesis of cationic metallophthalocyanines under microwave irradiation.

The desired products **IPc-Zn-Et⁴⁺** and **IPc-In-Et⁴⁺** were obtained in 59% and 63% yields, respectively, which represents a 7-10% yield improvement over the conventional synthetic method.¹

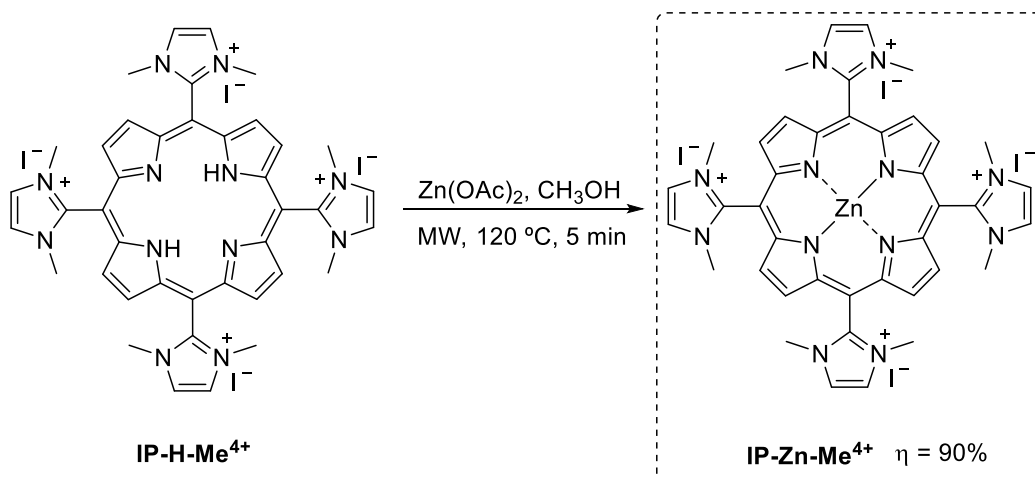
To study the influence of the macrocycle core structure on dual phototherapy, we then proceeded with the synthesis of cationic imidazolyl-based porphyrins (Scheme 2.3). Two base structures were used: a *trans*-di-substituted imidazolyl porphyrin and a tetra-substituted imidazolyl porphyrin, both commercially acquired. Again, previously described cationization procedures utilized DMF as solvent and conventional heating methodologies, taking up to 24 h for reaction completion.¹⁴ Thus, similarly to the previously mentioned procedure, the cationization reaction was carried out in MW, by adding iodomethane, in DMSO at 120 °C, during 5 min. In both cases, the reaction products were precipitated from the crude by the addition of a mixture of acetone and pentane, and then filtered off. The di-cationic **IP-H-Me²⁺** was obtained in 95% yield and the tetra-cationic **IP-H-Me⁴⁺** in 92% yield, which are comparable to the reported values for the conventional synthesis.¹⁴



Scheme 2.3: Synthesis of cationic imidazolyl-based porphyrins under microwave irradiation.

Finally, to evaluate the effect of Zn(II) in the porphyrin's central cavity, the corresponding Zn(II) complex of the tetra-cationic porphyrin **IP-H-Me⁴⁺** was synthesized (Scheme 2.4). The previously reported method, under conventional heating, employed DMF as solvent, at 100 °C during 4 h. Under the newly developed method herein described, microwave irradiation ($P_{\text{max}} = 150 \text{ W}$) was used and DMF was exchanged for methanol. Under a closed vessel, methanol could be overheated beyond its boiling

point, up to 120 °C, where the reaction only required 5 min to achieve full porphyrin metalation, as determined by UV-Vis spectroscopy. The desired product **IP-Zn-Me⁴⁺** was isolated in 90% yield after purification by size-exclusion chromatography (Sephadex G-10) in order to remove the excess Zn(OAc)₂ used.



Scheme 2.4: Synthesis of the tetra-imidazolyl porphyrins Zn(II) complex under microwave irradiation

In sum, we have been able to obtain significant improvements on the synthesis of quite relevant cationic imidazolyl-based photosensitizers, enabling their transposition to a larger scale, under more sustainable conditions. In the next sections, the evaluation of the photosensitizers' structural effect on the development of an optimized dual phototherapy protocol for the inactivation of *E. coli* is described.

Photophysical properties

In order to guarantee a uniformity of the light dose delivered to each cationic PS, we first carried out studies on the overlap of each PS absorption spectrum with the corresponding LED light source emission (Figure 2.1). A red LED (659 nm) was selected for the phthalocyanines (Figure 2.1a), while a blue LED (415 nm) was chosen for the porphyrins (Figure 2.2b). The graphs showed different levels of overlap with the light source, especially among the porphyrin family. Indeed, the di-cationic **IP-H-Me²⁺**, owing to its maximum absorption peak at 395 nm, has a lower overlap with the 415 nm LED than the tetra-cationic **IP-H-Me⁴⁺** and **IP-Zn-Me⁴⁺**. So, if all porphyrins were subjected to the same irradiation time, the photoinactivation potential of **IP-H-Me²⁺**

would be underestimated since a lower number of photons would be truly absorbed by this PS.

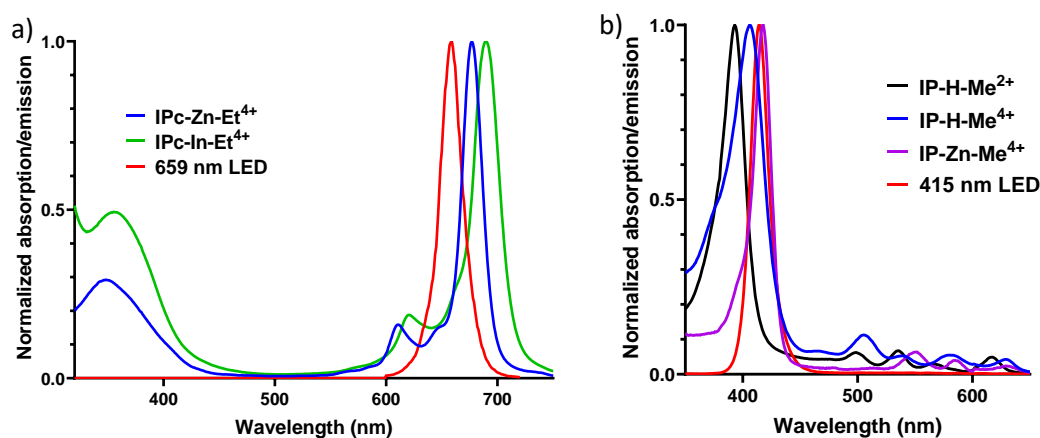


Figure 2.1: Overlap of photosensitizer absorption spectra with light source emission: a) **IPc-Zn-Et⁴⁺** and **IPc-In-Et⁴⁺** with red LED (659 nm, 4.0 mW/cm²); b) Porphyrins **IP-H-Me²⁺**, **IP-H-Me⁴⁺** and **IP-Zn-Me⁴⁺** with blue LED (415 nm, 3.0 mW/cm²).

This has led us to calculate correction factors¹⁵ that were applied to adjust the irradiation times in order to obtain the same light dose absorbed by each compound, and thus allowing a more trustworthy comparison between all PS. This is showed in equation (i), where the actual light dose absorbed (LD) is obtained by multiplication of the light source potency (P) with time (t) and the light dose correction factor (LDC), which can vary between 0 and 1.

$$LD = P \times t \times LDC \quad (i)$$

The LDC for each PS, along with previously described relevant photophysical and photochemical properties and photoinactivation studies on *E. coli* are presented in Table 2.4.^{1,14} Overall, all PS have high molar absorption coefficients, typically in the 10⁵ M⁻¹cm⁻¹ range, with the exception of **IP-H-Me²⁺**, where a value of 5.4 x 10⁴ M⁻¹cm⁻¹ is observed. This seems to be compensated by its higher (0.69) singlet oxygen production quantum yield (Φ_{Δ}), when compared with the tetra-cationic porphyrins ($\Phi_{\Delta} = 0.14$ and 0.44). It should be noted that the reported biological data are merely indicative and should not be used for direct comparisons, as there are many different variables that can influence the outcome, namely the type of *E. coli* strain used, light doses and LED emission/PS absorption overlap.

Table 2.4: Summary of relevant photophysical, photochemical properties and previous biological studies on *E. coli* for each cationic photosensitizer.

PS	ϵ_{\max} , M ⁻¹ cm ⁻¹ (λ , nm)	Φ_{Δ}	LDC	Previous PDI studies on <i>E. coli</i>
IPc-Zn-Et⁴⁺ 1	2.8x10 ⁵ (677) ^(a)	0.66 ^(a)	0.34 ^(d)	Outcome: 7 log CFU reduction [PS]: 100 nM Light dose: 10 J/cm ² (white light)
IPc-In-Et⁴⁺ 1	1.9x10 ⁵ (690) ^(a)	0.52 ^(a)	0.28 ^(d)	-
IP-H-Me²⁺	5.4x10 ⁴ (395) ^(b)	0.69 ^(b)	0.25 ^(e)	-
IP-H-Me⁴⁺ 14	1.7x10 ⁵ (407) ^(c)	0.14 ^(c)	0.69 ^(e)	Outcome: 7 log CFU reduction [PS]: 1 μ M Light dose: 2 J/cm ² (LED 415 nm)
IP-Zn-Me⁴⁺ 14	2.7x10 ⁵ (417) ^(c)	0.44 ^(c)	0.63 ^(e)	Outcome: 7 log CFU reduction [PS]: 100 nM Light dose: 2 J/cm ² (LED 415 nm)

^(a) in DMSO; ^(b) in ethanol; ^(c) in PBS; ^(d) relative to 659 nm LED light source; ^(e) relative to 415 nm LED light source

2.2 – Photodynamic inactivation of *E. coli* in combination with ciprofloxacin

In this subchapter, we present the biological studies conducted on the effect of PDI using the above synthesized cationic photosensitizers, in the presence or absence of ciprofloxacin (CIP). The studies encompassed *in vitro* optimizations of the dual phototherapy protocol, regarding the two possible combination modalities: i) simultaneous PDI and antibiotic CIP therapy or ii) PDI therapy before administration of the antibiotic CIP. Additionally, we studied the influence of the PS structure and concentration, light dose and matrix where PDI is performed (*i.e.* distilled H₂O or culture medium) on the inactivation of *E. coli* in combination with CIP. Then, our findings were translated into a burn wound mice model infected with *E. coli*, using the best PS + CIP combination determined.

The *in vitro* minimum inhibitory concentration (MIC) studies started with an *E. coli* strain isolated in the laboratory, with a lower susceptibility to ciprofloxacin (CIP), when compared with the wild-type non-resistant American Type Culture Collection (ATCC) strain. This strain will be designated *E. coli* RS. The MIC is one of the most relevant parameters in microbiology for the assessment of the antimicrobial activity of compounds and represents the minimum compound concentration required to inhibit visible bacterial growth, after 20-24 h incubation at 37 °C.¹⁶ In Table 2.5 the MIC values measured in the dark for CIP and all the cationic PS, against this *E. coli* strain are depicted.

Table 2.5: Minimum inhibitory concentration (MIC) values in the dark determined for the antibiotic ciprofloxacin and cationic photosensitizers against *E. coli* RS.

Compound	MIC (dark)
Ciprofloxacin	0.25 mg/L; 754 nM
IPc-Zn-Et⁴⁺	250 mg/L; 170 μM
IPc-In-Et⁴⁺	250 mg/L; 161 μM
IP-H-Me²⁺	250 mg/L; 330 μM
IP-H-Me⁴⁺	125 mg/L; 109 μM
IP-Zn-Me⁴⁺	125 mg/L; 102 μM

Regarding the minimum inhibitory concentration of CIP (MIC_{CIP}), the value of 0.25 mg/L is considerably higher than the literature value for the wild-type ATCC strain (0.004 mg/L).¹⁷ Moreover, this value is just below the clinical breakpoint defined for resistance to ciprofloxacin (> 0.5 mg/L),¹⁸ making this an intermediate strain regarding resistance to CIP. This means that the MIC is too high for this strain to be considered as “susceptible” to CIP, but also too low for being considered as “resistant” to CIP.

All the cationic PS were toxic in the dark at concentrations above 100 μM. This dark toxicity is in the same range (10-200 μM) of the values reported for other photosensitizers in literature, containing cationic pyridyl, aminophenyl or alkyl amine groups.¹⁹⁻²¹ It is worth reminding that *E. coli* possesses Mg²⁺ and Ca²⁺ ions in their bacterial wall, which act as counter ions to the negatively charged groups present in the lipopolysaccharides. The cationic groups in PS can displace these divalent counter ions

and promote a destabilization of *E. coli*'s cell wall, consequently leading to their inactivation in the dark when using high cationic PS concentrations (> 100 μM).²² It is worth noting that bacterial growth inhibition, represented by the MIC, does not necessarily mean the death of bacteria, *i.e.* bacteria can regrow if the antibiotic agent is removed from the medium. However, for CIP and these cationic PS, they possess a bactericide action, which means that the dose required for complete bacterial killing is very close to the MIC. This was corroborated by experimental observation, where no viable bacteria were present after 24 h incubation with these cationic PS at their respective MIC concentrations or with CIP at 2 x MIC (0.5 mg/L).

While it is known that CIP's inhibitory activity is independent of light, the main action mechanism of cationic PS is through light-dependent ROS formation. Therefore, before starting the dual phototherapy studies, we proceeded with the assessment of the photoinactivation efficiency of each PS, in a monotherapy approach, using a 1.8 J/cm^2 light dose (Figure 2.2). This will allow the determination of sub-bactericidal PDI doses. For all of these studies, the standard initial inoculum of 5×10^5 CFU/mL was used, in accordance to ISO-20776-1 guidelines.²³

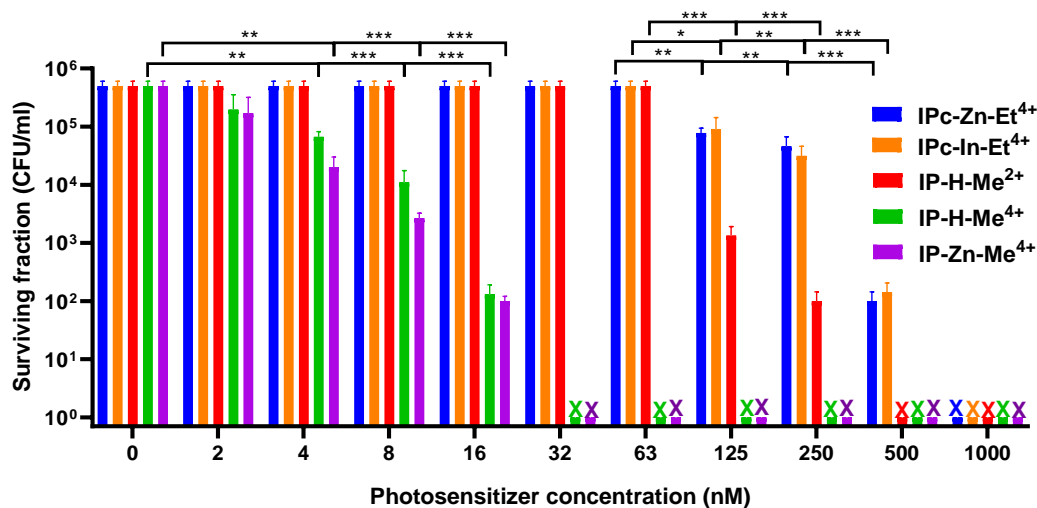
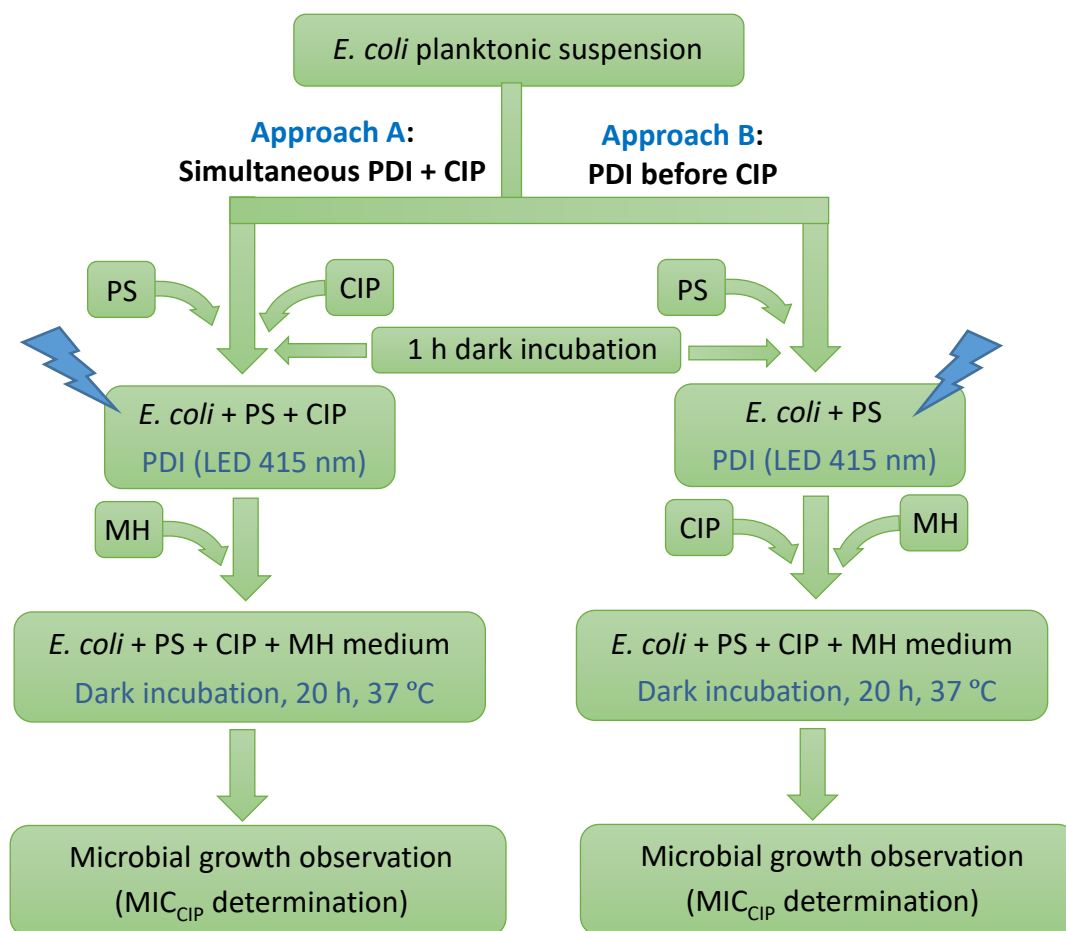


Figure 2.2: PDI in planktonic cultures of *E. coli* RS in double distilled water ddH₂O, using various photosensitizers concentrations (2-1000 nM) after 1 h dark incubation and irradiation with an adjusted light dose of 1.8 J/cm^2 . "X" denotes complete inactivation of the inoculum. The labels * ($p < 0.05$), ** ($p < 0.01$) and *** ($p < 0.001$) represent statistical difference.

Under an adjusted light dose of 1.8 J/cm², all compounds were bactericidal at concentrations >1000 nM, with a complete (5.5 log CFU) reduction of the initial inoculum. By lowering the concentration to 500 nM, both imidazolyl porphyrins have shown bactericidal activity, while the tetra-cationic phthalocyanines **IPc-Zn-Et⁴⁺** and **IPc-Zn-Et⁴⁺** induced only a sub-bactericidal effect (3.5 log CFU reduction). Finally, in the concentration range of 32-250 nM, the tetra-cationic porphyrins **IP-H-Me⁴⁺** and **IP-Zn-Me⁴⁺** induced total inactivation, while **IPc-Zn-Et⁴⁺**, **IPc-In-Et⁴⁺** and **IP-H-Me²⁺** showed a lower bactericidal effect (Figure 2.2). Clearly, in this case, the metals present in the porphyrin macrocycle cavity were not the driving force for the photoinactivation of *E. coli*. Regarding the metallophthalocyanines, despite the Zn(II) PS having higher singlet oxygen generation than the In(III) PS (Table 2.4), no significant difference in *E. coli* photoinactivation was observed. However, the nature of the macrocycle (*i.e.* phthalocyanine or porphyrin) and the number of positive charges seem to play a great role. The low efficacy of phthalocyanines may be attributed to their higher aggregation in water than porphyrins, which results in the presence of dimeric species that rapidly decay to the ground state through internal conversion and do not generate ROS. This led us to choose the porphyrin family for further studies using dual phototherapy. Among the porphyrin family, the results correlate well with the general knowledge that very hydrophilic molecules with a high number of positively charged groups are more effective in the inactivation of gram-negative bacteria in planktonic cultures.²⁴ Since ROS have a very short lifetime, they can only travel a few nanometers before being deactivated. The higher number of positive charges promotes more favorable interactions with the anionic bacterial lipopolysaccharide and thus increases proximity between the PS and the bacterial cell wall components (*i.e.* lipids and proteins), which are one of the most important targets in PDI.

The obtained PDI results prompted us to select the appropriate sub-bactericidal concentration of each cationic porphyrin to pursue the dual phototherapy studies. Since our goal was to evaluate the possible synergic combination between PDI and CIP, we selected these sub-bactericidal concentrations of photosensitizers (2-16 nM for **IP-H-Me⁴⁺** and **IP-Zn-Me⁴⁺**, and 63-250 nM for **IP-H-Me²⁺**) for combination with previously determined sub-inhibitory concentrations of CIP (< 0.25 mg/L), using the same 1.8 J/cm² light dose.

For the dual phototherapy studies, two possible combination modalities of PDI with CIP were investigated (Scheme 2.5).



Scheme 2.5: Methodology used for the combination of PDI with CIP, highlighting the two possible approaches: simultaneous PDI and CIP (approach **A**), and PDI before CIP (approach **B**).

In approach **A** (simultaneous PDI and CIP application), the selected PS and CIP were added to the *E. coli* bacterial suspension in ddH₂O and after 1 h incubation, PDI (1.8 J/cm² light dose) was performed. On the other hand, in approach **B** (CIP administration after PDI), the PS was added to the bacterial inoculum in ddH₂O (1 h dark incubation) followed by PDI, performed under the same light conditions, and then CIP was added to the previously PDI-treated inoculum. In both experiments, Mueller-Hinton (MH) culture medium was added after PDI and bacterial growth was analyzed, after 20 h incubation, at 37 °C. For each PDI concentration used, a gradient of different concentrations of CIP was tested, in order to determine the MIC_{CIP}. Thus, this protocol allowed us to evaluate the efficacy of PDI in reducing the amount of antibiotic required

to inhibit bacterial growth, represented here by the MIC_{CIP}. The dual phototherapy results obtained for all porphyrin photosensitizers are depicted in Figure 2.3a-c. For comparison purposes, we present in Figure 2.3d the results using methylene blue, a PS previously used in dual phototherapy studies with CIP for *E. coli* inactivation.²⁵

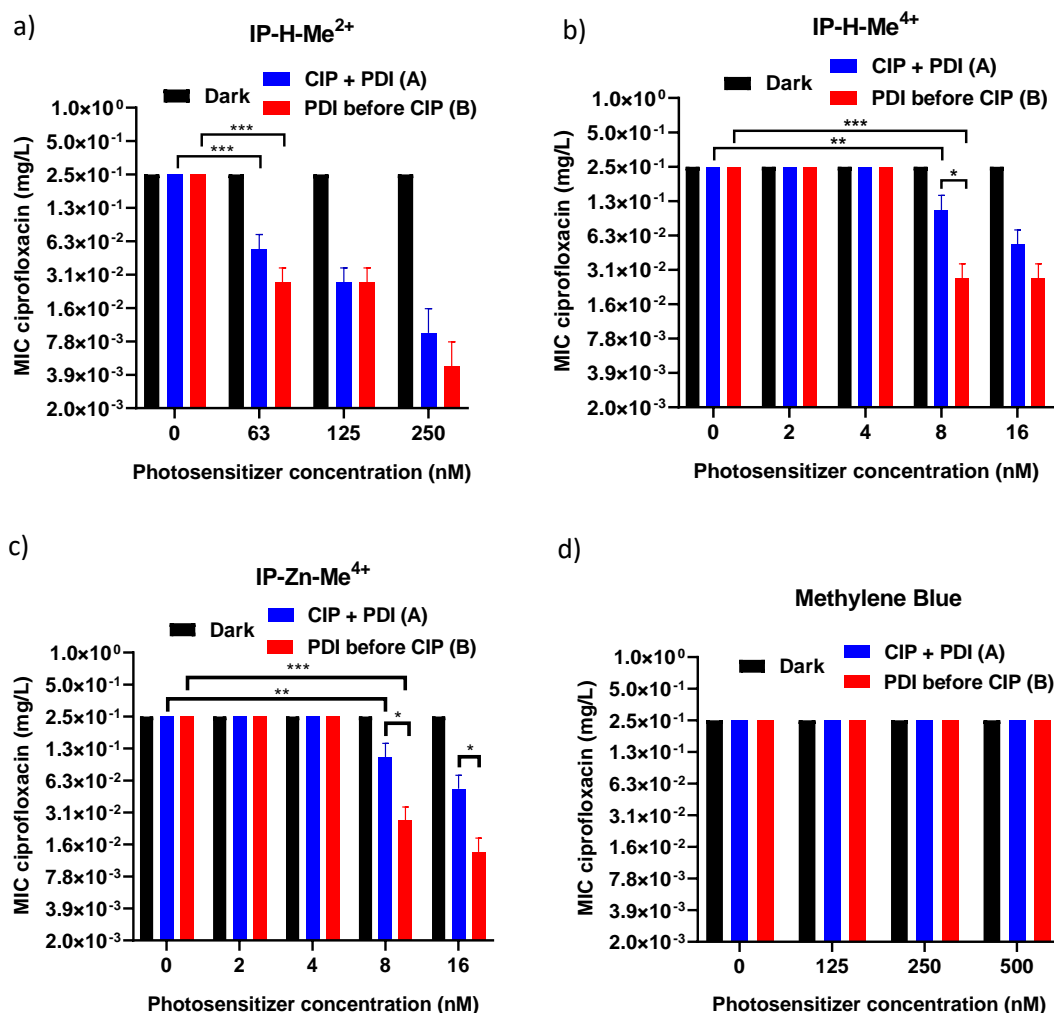


Figure 2.3: Dual phototherapy studies using sub-bactericidal PDI treatments with each photosensitizer in ddH₂O, in combination with CIP (combination approaches **A** and **B**), using an adjusted light dose of 1.8 J/cm² for a) IP-H-Me²⁺; b) IP-H-Me⁴⁺; c) IP-Zn-Me⁴⁺; d) Methylene blue. Results are presented as the MIC of CIP for *E. coli* RS in function of PS concentration used in the photoinactivation. The labels * (p < 0.05), ** (p < 0.01) and *** (p < 0.001) represent statistical difference.

Independently of the PS used, no changes to the MIC_{CIP} were observed in the dark. This correlates well with the results presented in Table 2.5, which show that these PS only possess antimicrobial activity in the dark for concentrations > 100 μM. However, upon light irradiation (1.8 J/cm²), the values of MIC_{CIP} showed a great dependence on

the experimental protocol approach (**A** or **B**), porphyrin structure and concentration range.

Regarding the protocol, we found that, for both tetra-cationic porphyrins **IP-H-Me⁴⁺** and **IP-Zn-Me⁴⁺**, approach **B** (CIP administration after PDI; Figure 2.3 – red) was more efficient than approach **A** (CIP + PDI simultaneously; Figure 2.3 - blue). It should be mentioned that, in the case of **IP-H-Me²⁺**, the difference between both approaches was not statistically significant, while with **IP-H-Me⁴⁺** and **IP-Zn-Me⁴⁺** a significant difference between both approaches was observed, being protocol **B** selected to pursue the studies.

Regarding the influence of the PS structure, we observed that, under protocol **B**, the number of charges is a key issue, since the sub-bactericidal concentrations of the tetra-cationic porphyrins **IP-H-Me⁴⁺** and **IP-Zn-Me⁴⁺** when compared with **IP-H-Me²⁺**, in combination with the same CIP concentration (0.031 mg/L), are approximately 8-fold lower (8 and 63 nM, respectively; Figure 2.3).

Additionally, it should be stated that the combination of PDI with CIP, independently of the cationic porphyrin used, was more efficient in the inactivation of *E. coli* than methylene blue (no activity was observed for the concentration range of 125-500 nM). This is a remarkable result when compared with the literature, where the combination of CIP with methylene blue (**MB⁺**) for inactivation of *E. coli* required significantly drastic PDI conditions (20 μ M and 2.8 J/cm²).²⁵ This strengthens the relevance of the photosensitizers' structure, particularly the number of positive charges since the final output of *E. coli* PDI dual photoinactivation follows the order **IP-H-Me⁴⁺** / **IP-Zn-Me⁴⁺** > **IP-H-Me²⁺** > **MB⁺**.

Overall, there was a negligible difference in dual phototherapy between both tetra-cationic porphyrins **IP-H-Me⁴⁺** and **IP-Zn-Me⁴⁺**. The synthetic procedure and subsequent work-up of **IP-Zn-Me⁴⁺**, as described in the previous subchapter, makes it less suitable for scale-up envisioning *in vivo* studies, since it requires purification through size exclusion chromatography. In addition, it is well established that Zn(II) metalloporphyrins are labile, and demetallation may occur *in vivo*, since skin is acidic in nature (average pH = 4.7).²⁶ Thus, only the free-base porphyrin **IP-H-Me⁴⁺** was selected to proceed with the studies.

Another relevant issue for obtaining a good output of dual phototherapy is the optimization of the light dose. The critical analysis of the literature shows that the light doses required for photodynamic inactivation of *E. coli* used in culture medium²⁷ or *in vivo*²⁸ are generally superior to the herein described. Thus, to appraise the sub-bactericidal PDI doses, before starting the combination of PDI with CIP, we evaluated the effect of increasing the light dose from 1.8 to 5.4 J/cm² for PS concentration between 32-500 nM for **IP-H-Me²⁺** and 2-32 nM for **IP-H-Me⁴⁺**. The results are presented in Figure 2.4.

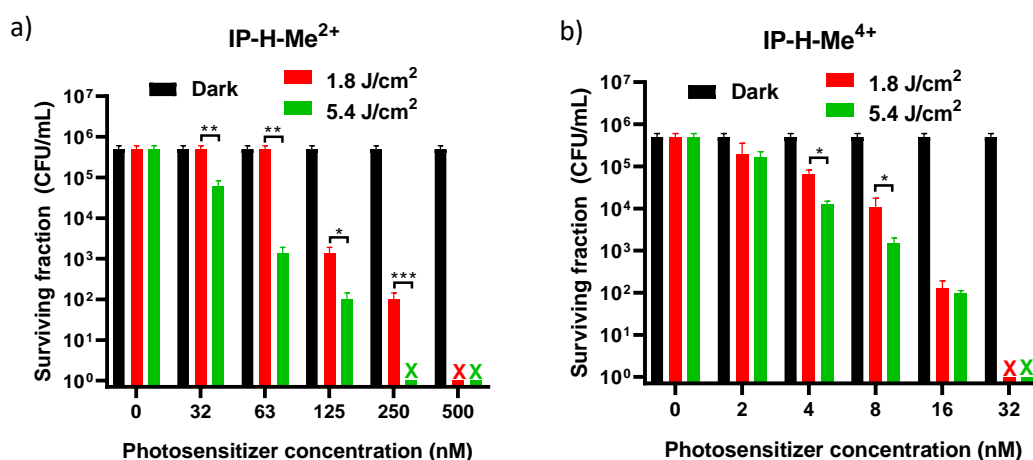


Figure 2.4: PDI in planktonic cultures of *E. coli* RS in ddH₂O, using various photosensitizers concentrations of a) **IP-H-Me²⁺** (32-500 nM) and b) **IP-H-Me⁴⁺** (2-32 nM). Adjusted light dose of 1.8 J/cm² (red) or 5.4 J/cm² (green). "X" denotes complete inactivation of the inoculum (bactericidal dose). The labels * (p < 0.05), ** (p < 0.01) and *** (p < 0.001) represent statistical difference.

From the analysis of Figure 2.4, we observe that for both photosensitizers the PDI efficiency increases with the enhancement of light dose from 1.8 J/cm² to 5.4 J/cm², being this effect more pronounced when **IP-H-Me²⁺** is used. For this PS, the minimum concentration required for a full inoculum inactivation changed from 500 nM to 250 nM, when the light dose was increased from 1.8 J/cm² to 5.4 J/cm². In the case of **IP-H-Me⁴⁺**, there was only a statistically significant light dose effect at 4 and 8 nM PS concentrations.

Then, we pursued with the evaluation of the light dose effect (1.8 J/cm² and 5.4 J/cm²) on the dual phototherapy studies, still using both photosensitizers, under the sub-bactericidal PS concentrations observed above (Figure 2.4; 32-250 nM for **IP-H-Me²⁺**

and 4-16 nM for **IP-H-Me⁴⁺**), and the sub-MIC_{CIP} concentrations (< 0.25 mg/L, Table 2.5). Protocol **B** was selected for these studies. The results are presented in Figure 2.5.

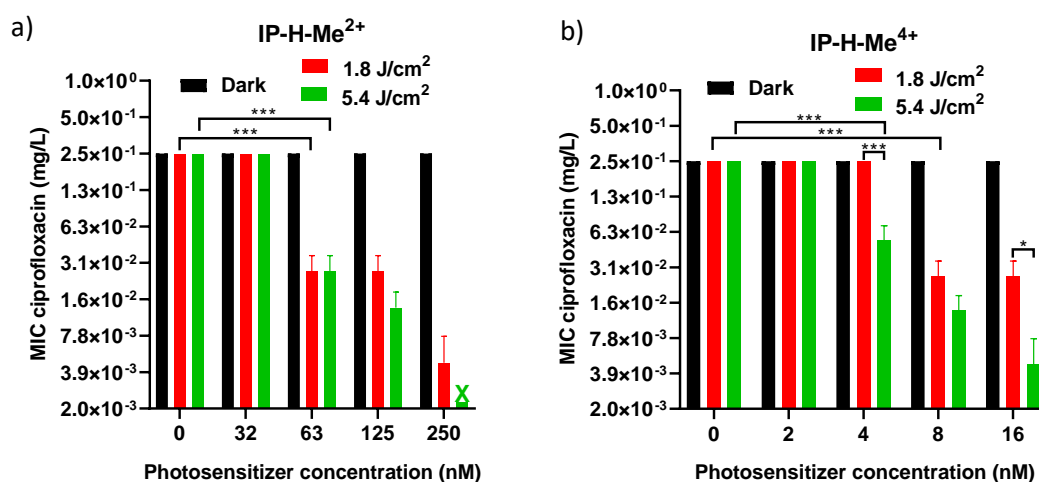


Figure 2.5: Dual phototherapy studies (PDI before CIP, modality **B**) with sub-bactericidal PDI treatments with a) **IP-H-Me²⁺** b) **IP-H-Me⁴⁺** in ddH₂O, in combination with CIP, using 1.8 and 5.4 J/cm² light doses. Results are presented as the MIC of CIP for *E. coli* RS in function of PS concentration used in the photoinactivation. “X” denotes complete inactivation of the inoculum using PDI alone (bactericidal dose). The labels * (p < 0.05) and *** (p < 0.001) represent statistical difference.

The results show that, when using **IP-H-Me²⁺**, no statistical difference on MIC_{CIP} was observed between 1.8 and 5.4 J/cm² light doses. On the other hand, a MIC_{CIP} dependence on the light dose used was observed for some concentrations of **IP-H-Me⁴⁺**. For instance, at 4 nM, no effect was observed using a 1.8 J/cm² light dose, however a decrease in MIC_{CIP} to 0.063 mg/L was obtained using 5.4 J/cm². The best result obtained so far (64-fold MIC_{CIP} reduction; MIC_{CIP} = 0.004 mg/L) was achieved for the combination of **IP-H-Me⁴⁺** (16 nM) and 5.4 J/cm² light dose. Remarkably, this MIC_{CIP} value corresponds to the wild-type *E. coli* reported in the literature.¹⁷ For these reasons, we selected **IP-H-Me⁴⁺** for further studies, including an *in vivo* dual phototherapy assay.

For **IP-H-Me⁴⁺**, it is interesting to note that there is a greater light dose effect on *E. coli* inactivation when dual phototherapy was implemented (using protocol **B**; Figure 2.5b), than when PDI monotherapy was carried out (Figure 2.4b). For example, no significant difference in viable bacteria is obtained at 16 nM from increasing the light dose from 1.8 to 5.4 J/cm² in PDI monotherapy (Figure 2.4b), but in dual phototherapy (Figure 2.5b), an 8-fold difference in MIC_{CIP} is observed. This suggests that the longer

exposure to ROS, triggered by increasing the light dose, may cause bacterial damage that does not necessarily decrease the number of bacteria (*i.e.* non-bactericidal), but may change the susceptibility of bacteria to antibiotics. Indeed, the combination of PDI with CIP may reduce the amount of antibiotic required (MIC_{CIP}) due to an additive or synergistic effect. An additive effect results from the trivial diminution of viable bacteria after PDI, which leads to a lower inoculum and consequently, to a lower MIC_{CIP} . Synergism may occur if PDI with **IP-H-Me**⁴⁺ causes bacterial damage by a mechanism that increases their susceptibility to antibiotic treatment. In order to investigate which type of combination effect best explains our results, first we studied the effect of the inoculum size on the MIC_{CIP} , in non-PDI treated *E. coli* RS (Figure 2.6).

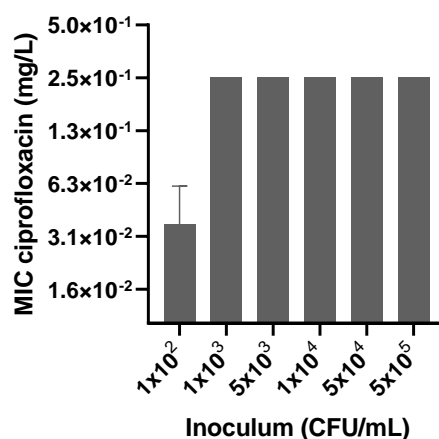


Figure 2.6: Variation of the MIC_{CIP} value in function of the inoculum size, in non-PDI treated *E. coli* RS.

Figure 2.6 shows that the MIC_{CIP} of 0.25 mg/L is constant in the range of 1×10^3 to 5×10^5 CFU/mL (standard inoculum size used in our experiments) and only at 1×10^2 CFU/mL a significant MIC_{CIP} decrease is observed. In conclusion, the MIC_{CIP} does not show a strong dependence on the number of viable bacteria, which is consistent with other reports, where lower inoculum sizes relatively to the standard also had a small influence in changing antimicrobials' MIC.²⁹⁻³⁰ Comparing the results shown in Figure 2.6 (effect of the inoculum size on MIC_{CIP}) with the surviving fractions (CFU/mL) obtained after PDI alone, presented in Figure 2.4, it can be concluded that sub-bactericidal doses of **IP-H-Me**⁴⁺ (4-8 nM concentrations and 5.4 J/cm² light dose) do not change *E. coli*'s susceptibility to CIP, merely by lowering the amount of CFU/mL present after PDI treatment (1×10^3 – 1×10^4 CFU/mL). Indeed, the results from Figure 2.5 show that, in

these conditions, the MIC_{CIP} is strongly affected after PDI, which suggests that between 4-8 nM concentrations a synergistic PDI + ciprofloxacin effect is observed (Figure 2.7 – green). On the contrary, when a PDI experiment was carried out using 16 nM PS, only 1x10² CFU/mL remained and, followed by CIP administration, may show an additive (CIP = 0.125 – 0.031 mg/L) or synergic effect (0.016 – 0.004 mg/L) (Figure 2.7 – yellow and green, respectively).

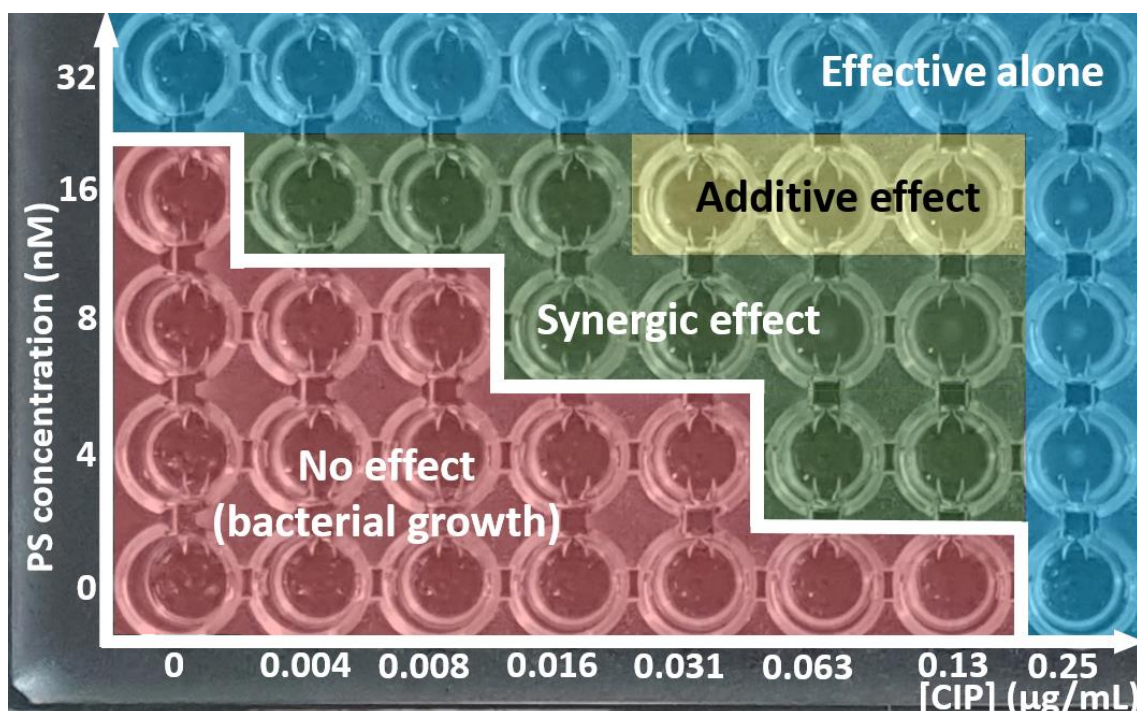


Figure 2.7: Schematic representation of dual phototherapy results under the best optimized protocol obtained for inactivation of *E. coli* RS, using IP-H-Me⁴⁺ as photosensitizer and a 5.4 J/cm² light dose (415 nm LED).

Figure 2.7 summarizes the overall results and clearly demonstrates that, for PS concentrations at or above 32 nM, total *E. coli* RS inactivation is observed independently of the CIP dose (Figure 2.7 – blue). Additionally, for PS concentrations below 16 nM, the bacterial inactivation is strongly dependent on the CIP dose: at 8 nM of PS and CIP doses below 0.016 mg/L, there is bacterial growth (Figure 2.7 – red), while for 4 nM of PS, at least 0.063 mg/L of CIP is required to inhibit bacterial growth through a synergic interaction (Figure 2.7 – green).

The assessment that this PS + CIP combination possessed a synergic effect was further confirmed by means of a checkerboard analysis, which is a standardized test

recommended by a recent review on the combination of PDI with antibiotics.³¹ This compares the individual activity of two antimicrobial agents with the activity of their combination through a Fractional Inhibitory Concentration (FIC) index value, which is a theoretical value calculated using the following equation:³²

$$\text{FIC index} = \frac{A}{\text{MIC}_A} + \frac{B}{\text{MIC}_B} \quad (\text{ii})$$

where A and B are the concentrations of the two antimicrobials when in combination and MIC_A and MIC_B are the MIC of each molecule individually. If the FIC index is < 0.5, then the combination displays synergism. For a FIC index > 0.5, the combination is predicted to be additive. The results obtained for each PS + CIP combination used in this work are presented on Table 2.6.

Table 2.6: Synergism evaluation using the checkerboard analysis for dual therapy inactivation of *E. coli* RS, using **IP-H-Me**⁴⁺ and a 5.4 J/cm² light dose, where the FIC index is presented in brackets and “A” (yellow) denotes additive effect, “S” (green) denotes synergist effect and “-” (red) denotes no effect.

[CIP] mg/L \ [PS] nM	0.125	0.063	0.031	0.016	0.008
16	A (1.0)	A (0.75)	A (0.63)	A (0.56)	A (0.53)
8	A (0.75)	A (0.50)	S (0.38)	S (0.31)	-
4	A (0.63)	S (0.38)	-	-	-

The calculated concentrations for giving a synergic PDI/CIP combination (green highlighted; Table 2.6) are in good agreement with the experimental observations depicted in Figure 2.7.

2.3 – Photodynamic inactivation of multi-drug resistant *E. coli* combined with ciprofloxacin

Treatment of infections caused by MDR bacteria is clearly the most urgent clinical application for PDI. Thus, preliminary *in vitro* studies were carried out to access the efficacy of PDI in combination with CIP in the treatment of MDR *E. coli*. This strain (*E. coli* 243) was specifically selected for its high resistance to CIP (MIC = 32 mg/L), which is

well beyond the defined limit for a strain to be considered as resistant to CIP (MIC > 0.5 mg/L).¹⁸ In addition, this strain is also resistant to tetracyclines and amoxicillin. Following our previous results, we set out to determine if the optimized dual phototherapy protocol could be successfully applied to this bacterial strain, for which more extensive resistance mechanisms are expected.

First, studies on the photodynamic inactivation of MDR *E. coli* using **IP-H-Me⁴⁺** were carried out, in order to determine the bactericidal and sub-bactericidal PS concentration/light dose conditions (Figure 2.8).

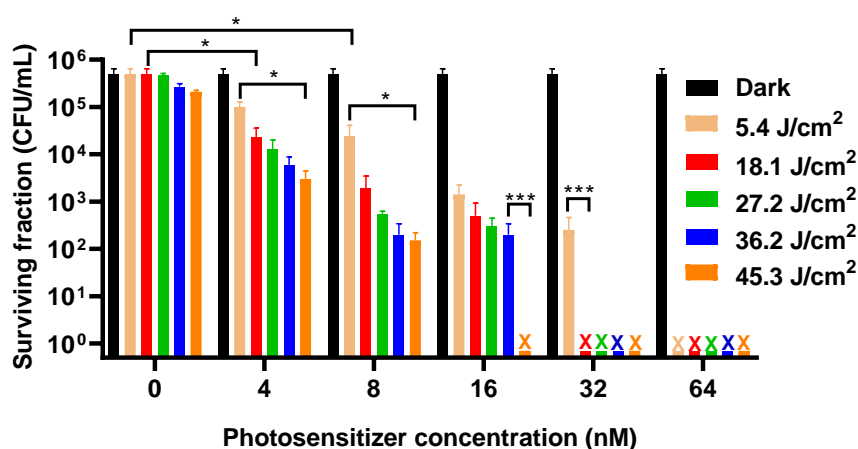


Figure 2.8: Surviving colonies after PDI in planktonic cultures of MDR *E. coli* in ddH₂O, using various **IP-H-Me⁴⁺** concentrations, and irradiation using different light doses (415 nm LED). “X” denotes complete inactivation of the inoculum. The labels * (p < 0.05) and *** (p < 0.001) represent statistical difference.

This photosensitizer exerted a statistically significant photodynamic inactivation effect at concentrations equal or above 4 nM, using 18.1-45.3 J/cm² light doses. The CFU/ml reduction increased with PS concentration and also with light dose used. The total inactivation of the inoculum was observed at 32 nM PS concentration, under light doses of 18.1 - 45.3 J/cm², or at 64 nM under a 5.4 J/cm² light dose.

When comparing the effect of PDI monotherapy (5.4 J/cm² light dose) on inactivation of MDR *E. coli* (Figure 2.8) and with the non-resistant *E. coli* RS (Figure 2.4), only very slight differences were observed regarding the bactericidal PS concentration (64 and 32 nM, respectively). These results highlight the potential of PDI using these highly active imidazolyl PS for the treatment of MDR bacteria since, fortunately, there is no correlation between resistance to antibiotics and susceptibility to PDI.³³ Indeed, the

molecular mechanisms that confer resistance to antibiotics (e.g. target modification, upregulation of efflux pumps, increased membrane impermeability or production of inactivating enzymes)³⁴ are distinct from those affecting PS uptake and ROS-mediated oxidative stress.

The sub-bactericidal concentrations of **IP-H-Me⁴⁺** (4-32 nM), together with the appropriate light dose (5.4 - 45.3 J/cm²) were selected for combination with CIP, in order to determine if they could reduce the MIC_{CIP} and thus regain *E. coli*'s susceptibility to CIP. The protocol used for the dual phototherapy is the same as Scheme 2.4 (PDI before CIP, modality **B**). The results are presented in Figure 2.9.

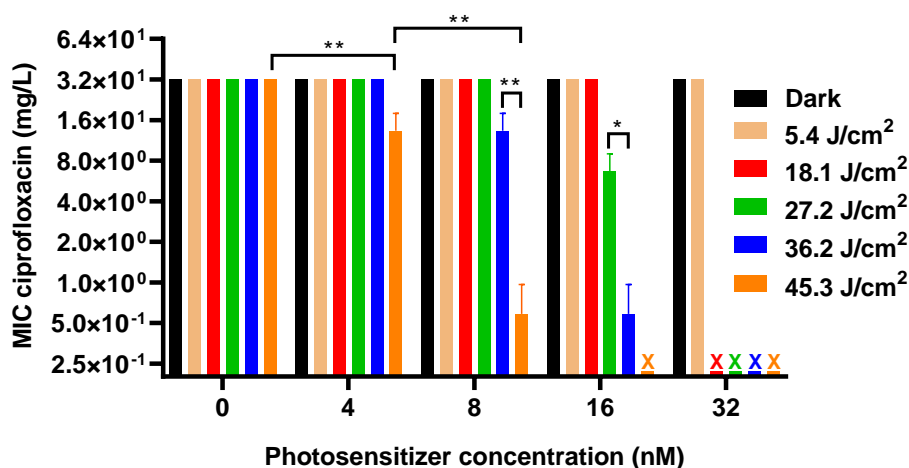


Figure 2.9: Dual phototherapy studies using sub-bactericidal PDI treatments with **IP-H-Me⁴⁺** in ddH₂O, in combination with CIP (PDI before CIP, modality **B**), using different light doses for MDR *E. coli*. Results are presented as the MIC of CIP for MDR *E. coli* in function of PS concentration used in the photoinactivation. “X” denotes complete inactivation of the inoculum using PDI alone. The labels * (p < 0.05) and ** (p < 0.01) represent statistical difference.

Surprisingly, while a 5.4 J/cm² light dose and 8 - 32 nM PS concentrations resulted in an appreciable decrease in viable CFU/mL (Figure 2.8) no alteration of the MIC_{CIP} was observed under these conditions (Figure 2.9). A minimum of 27.2 J/cm² was required for a significant change in susceptibility to CIP, with a 4-fold decrease of MIC_{CIP} from 32 mg/L to 8 mg/L, when using PS at 16 nM. Overall, the observed MIC_{CIP} was heavily dependent on the light dose used, besides the photosensitizer concentration. Under the highest light dose tested (45.3 J/cm²), only 8 nM of photosensitizer was sufficient for a 64-fold decrease of the MIC_{CIP} to 0.5 mg/L. It is worth reminding that this value is the limit that

defines an *E. coli* strain as clinically resistant to CIP. So far to the best of our knowledge, this is the first example of the application of dual phototherapy for inactivation of MDR *E. coli*, using CIP as antibiotic.

Again, to investigate the existence of a synergic effect, the variation of the MIC_{CIP} value in function of the inoculum size was determined in non-PDI treated MDR *E. coli* (Figure 2.10).

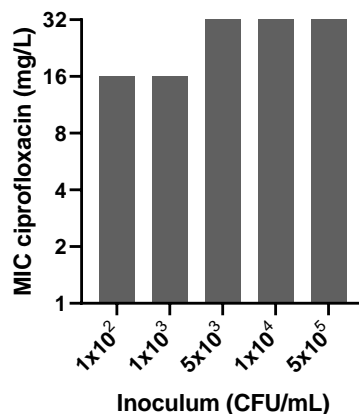


Figure 2.10: Variation of the MIC_{CIP} value in function of the inoculum size, in non-PDI treated MDR *E. coli*.

It was found that, for inoculum sizes below 5×10^3 CFU/mL, the MIC_{CIP} decreased from 32 to 16 mg/L. In order to evaluate which PS and antibiotic CIP combinations produce a synergic (green) or additive (yellow) effect in the inactivation of MDR *E. coli*, the information depicted in Figures 2.8, 2.9 and 2.10 is graphically presented in Figure 2.11. For instance, when using 8 nM of **IP-H-Me⁴⁺** and 45.3 J/cm^2 , the surviving bacteria after PDI are approximately 1×10^2 CFU/mL. According to Figure 2.10, this inoculum size only reduces MIC_{CIP} from 32 to 16 mg/L in non-PDI treated bacteria. In this case, there is an additive effect when using CIP at 16 mg/L (Figure 2.11 – yellow) and a synergic effect, with 0.5 – 8 mg/L CIP concentrations (Figure 2.11 – green). The studies on MDR *E. coli* were further complemented by analyzing its growth over time when subjected to dual phototherapy and each monotherapy (PDI or CIP). In the first (control) experiment, we studied the effect of just light irradiation (without PS or CIP) on bacterial growth when compared with a dark control (Figure 2.12).

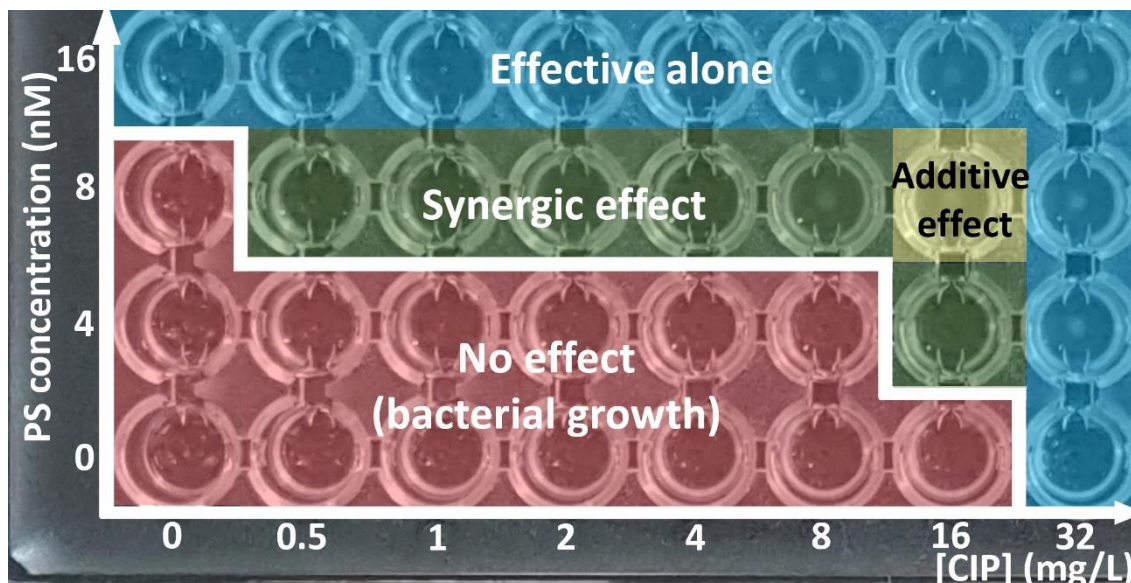


Figure 2.11: Schematic representation of dual therapy results under the best optimized protocol obtained for inactivation of MDR *E. coli*, using IP-H-Me⁴⁺ as photosensitizer and a 45.3 J/cm² light dose (415 nm LED).

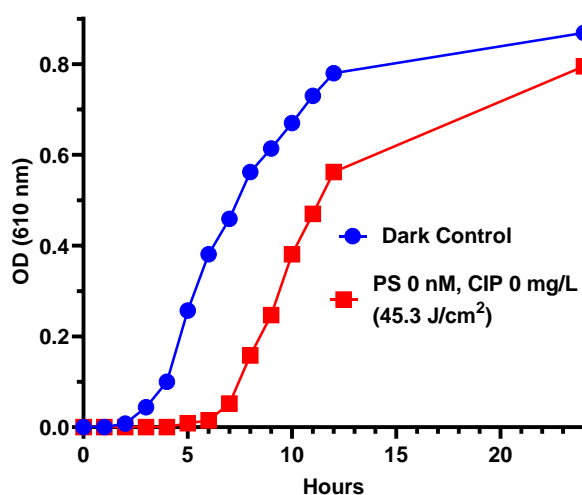


Figure 2.12: Comparison of growth of MDR *E. coli* (without PS or CIP) after exposure to 45.3 J/cm², in ddH₂O with its corresponding dark control. After light treatment (or dark incubation) samples were left under MH culture medium at 4 °C for 16 h. Then, at t = 0, samples were incubated in the dark at 37 °C and 300 rpm.

In one group, bacteria in ddH₂O were treated with the highest light dose used on the dual phototherapy studies (45.3 J/cm²), while in another group bacteria were kept in the dark during the irradiation period. Then, MH medium was added to both groups and the samples were left refrigerated at 4 °C overnight (16 h). In the next day, the samples from both groups were incubated at 37 °C and 300 rpm, corresponding to t = 0

in Figure 2.12, and the optical density (OD) was measured over 12 h at 610 nm. Microbial growth gradually increases the turbidity of the planktonic suspension, which can be quantitatively measured through the light scattering at 610 nm. The dark control showed a typical bacterial growth curve, starting 2 h after incubation at 37 °C, which indicates that the osmotic stress caused by having bacteria in distilled water during the irradiation time does not result in a significant change in microbial growth. On the other hand, light irradiation alone seems to delay microbial growth by approximately 3 h, when compared to the dark control. This can be explained by the antimicrobial properties of blue light, which promotes ROS formation through excitation of bacteria's endogenous chromophores.³⁵ However, this only seems to increase the lag phase (period before exponential growth) since the light dose used does not significantly change the number of viable bacteria, as was determined in the light control of PDI studies previously presented in Figure 2.8. Indeed, reports from literature with antimicrobial blue light have highlighted that it has, at most, a bacteriostatic effect on *E. coli*, under these light doses.³⁶ A bactericidal effect is only observed at incredibly high (> 1 800 J/cm²) light doses.³⁷

In another set of experiments, we analyzed the bacterial growth by OD at 610 nm, along 12 h, of light-treated MDR *E. coli*, in the presence or absence of photosensitizer (4 nM). In both cases, the PDI-treated bacteria were incubated with different quantities of CIP (0, 4, 8 or 16 mg/L, Figure 2.13), in accordance with protocol **B**. In all experiments, after CIP addition, MH medium was added and each bacterial sample was left at room temperature (20 °C) overnight (16 h). In the next day, the samples were incubated at 37 °C and 300 rpm in the dark (t = 0), and the values of OD 610 nm are presented in Figure 2.13. The dark control (Figure 2.13 - blue) had already reached the stationary growth phase at t = 0, because growth already occurred overnight at 20 °C and the increase of temperature to 37 °C did not change OD over 12 h. When the experiment was performed without the presence of PS or CIP (light control; Figure 2.13 - red), the exponential growth phase was initiated after 1 h and reached a plateau (0.7 OD) at the end of the 12 h period. In the samples where either PS or CIP were added, after PDI, a delay in bacterial growth was observed when compared with the light control. Bacteria treated with PDI monotherapy (PS 4 nM, CIP 0 mg/L, orange), suffered the least significant delay (approximately 5 h). This is a consequence of the

reduction of the number of viable bacterial cells in the sample, possibly combined with damage of macromolecules involved in the mechanisms of bacterial replication.

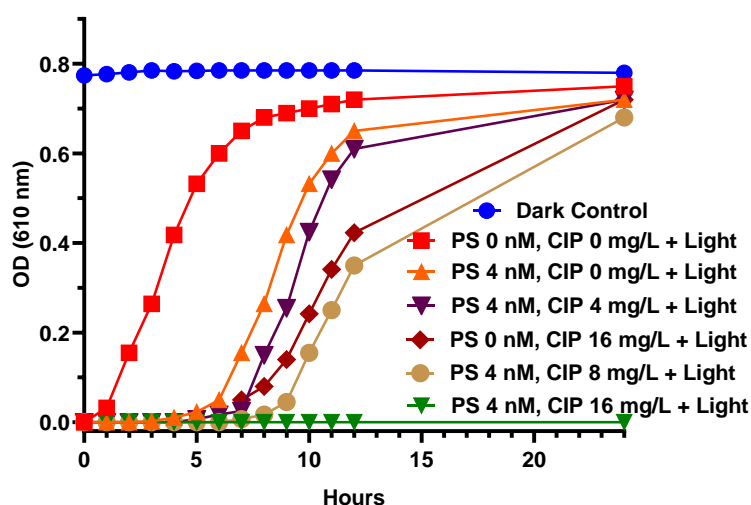


Figure 2.13: Comparison of growth of MDR *E. coli* after exposure to 45.3 J/cm² with or without 4 nM PS concentration, followed by addition of CIP, giving 0 - 16 mg/L final concentrations. After CIP addition, samples were left under MH culture medium at 20 °C for 16 h. Then, at t = 0, samples were incubated in the dark at 37 °C and 300 rpm.

Since the photosensitizer only promotes ROS-induced oxidative stress during light irradiation, it does not show a significant inhibitory effect along the 12 h incubation at 37 °C, as previously demonstrated in Table 2.5 (MIC values of photosensitizers in the dark). This clearly exemplifies one of the main drawbacks of using PDI treatments without an adjuvant therapy, because sub-bactericidal doses lead only to the partial inactivation of the inoculum. Then, the remaining live bacterial can thrive in the dark and reach a similar value of OD as non-PDI treated bacteria (Figure 2.13 – orange and red, respectively), with only a delay of a few hours. When PDI-treated bacteria are incubated in the presence of sub-inhibitory concentrations of CIP, namely 4 (purple) or 8 nM (light brown) a gradual dose-dependent delay in growth was observed. However, after 24 h, the OD values are similar for all experiments. These results point out that when using 4 nM PS the bacterial growth was progressively delayed with the increase of CIP (4 - 8 mg/L), but this combination did not avoid growth during 12 - 24 h. On the other hand, when PDI (4 nM PS) was combined with CIP at 16 mg/L (green), no growth occurred over 24 h, which is consistent with the results previously depicted in Figure 2.9.

This undoubtedly demonstrates the advantage of dual phototherapy as opposed to these two monotherapies administered separately. Indeed, one of the main causes of bacterial resistance to antibiotics is their exposure to sub-bactericidal/sub-inhibitory concentrations, which leads to a selective pressure for the proliferation of bacteria with genes that confer them a higher chance of survival and growth. Overall, the combination of CIP with PDI may have concomitant effects regarding both the treatment and prevention of MDR bacteria development, as it has the potential to i) reduce bacterial exposure to antibiotics, by requiring lower doses to induce an inhibitory effect; ii) inactivate or weaken a small number of drug resistant bacteria that can be present in an otherwise antibiotic-susceptible inoculum, and thus avoid that these bacteria persist after antibiotic treatment and generate drug resistant colonies; iii) increase MDR bacteria susceptibility to clinically used antibiotics, which may decrease the number of potential fatal infections. Certainly, the purpose of dual phototherapy on MDR bacteria is to take advantage of an alternative therapy for which bacteria are highly susceptible, such as PDI, in order to damage them and allow a higher antibiotic effectiveness. Recent mechanistic studies by Garcez *et al.*³⁸ demonstrated that ROS-promoted peroxidation of membrane lipids may contribute to membrane damage and consequently open the way for long-life active antibiotics against *E. coli*.

2.4 – *In vivo* studies

Dual phototherapy in Mueller-Hinton culture medium for *in vivo* transposition

One of the major issues in the transposition of *in vitro* studies to *in vivo* models is the emergence of other non-bacterial biomolecules, typically from the host, that act as ROS quenchers.³⁹ Some of these molecules (*e.g.* hemoglobin and melanin) possess absorption in the blue-violet region, which reduces light penetration, and consequently the amount of light that reaches the photosensitizer when irradiation is carried out in the Soret band.²⁸ In the case of porphyrins, the Soret band has a considerably higher molar absorption coefficient than the red-shifted Q bands, so irradiation is usually carried out at the Soret band, despite the low penetration of blue light.³³ Thus, in order to mimic more closely these conditions, we repeated the dual phototherapy

experiments on *E. coli* RS, but using Mueller-Hinton medium during PDI treatment, instead of distilled water. This culture medium possesses some absorption (Figure 2.14) that overlaps with **IP-H-Me⁴⁺** Soret band (absorption maximum at 407 nm) which is why many studies with porphyrins are carried out in sterile water or saline.^{27,40} In addition, the proteins present in the medium may also act as quenchers of singlet oxygen.⁴¹

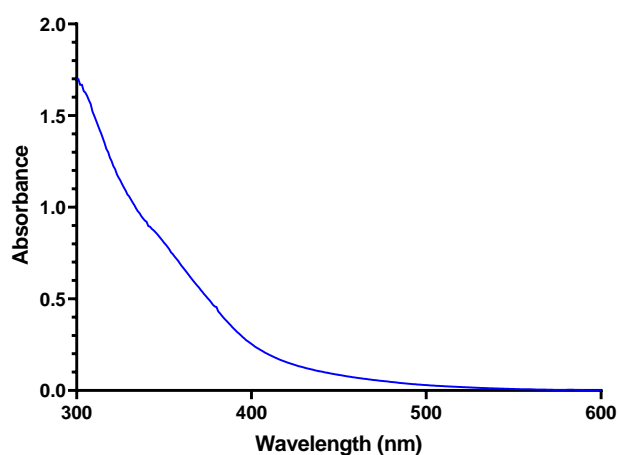


Figure 2.14: UV-Vis spectrum of Mueller-Hinton (MH) broth.

The PDI results of *E. coli* RS in MH medium using **IP-H-Me⁴⁺** monotherapy and 5.4 J/cm² light dose are presented in Figure 2.15a. It is possible to observe that the PS concentrations required for a significant reduction of the bacterial inoculum increased significantly, when compared with the experiment performed using distilled water (Figure 2.4). For instance, a minimum of 4 μM of **IP-H-Me⁴⁺** was needed for a complete inactivation of the initial inoculum, which is a value 125-fold higher than the concentration needed to achieve the same inactivation under ddH₂O (32 nM). The lower efficiency of PDI carried out under culture medium has been previously reported when performed in monotherapy²⁷ and in the combination with antibiotics.⁴⁰ The sub-bactericidal doses of 0.125 - 2 μM were selected to evaluate the dual phototherapy efficiency in MH medium (Figure 2.15b). In the dual phototherapy studies, there was a photosensitizer dose-dependent effect, where a 2 μM concentration showed the highest effect on MIC_{CIP} reduction (32-fold decrease from 0.25 to 0.008 mg/L). Despite requiring higher PS concentrations, the effects of sub-bactericidal photosensitizer doses on MIC_{CIP} reduction are quite similar to those obtained in ddH₂O (Figure 2.5). Indeed, this shows the robustness of our dual phototherapy protocol (**IP-H-Me⁴⁺** - PDI + CIP) for

inactivation of *E. coli*, when compared with some of the previously reported dual phototherapy protocols that failed when performed in culture medium instead of ddH₂O, as described in a recent comprehensive review.⁴⁰

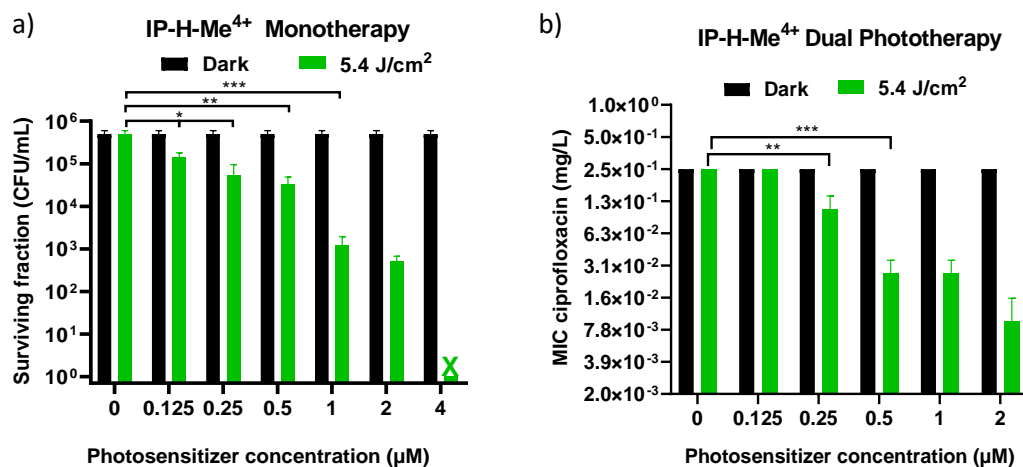


Figure 2.15: a) PDI in planktonic cultures of *E. coli* RS in MH medium, using different **IP-H-Me⁴⁺** PS concentrations, after 1 h dark incubation followed by irradiation with an adjusted light dose of 5.4 J/cm². b) Dual phototherapy using sub-bactericidal doses of **IP-H-Me⁴⁺**, against *E. coli* RS, performed under MH medium. Results are presented as the MIC of CIP for *E. coli* RS in function of PS concentration used in the photoinactivation. The labels * ($p < 0.05$), ** ($p < 0.01$) and *** ($p < 0.001$) represent statistical difference.

Optimized protocol transposition to the treatment of infected mice wounds

As explained in Chapter 1, while *E. coli* is more associated with urinary infections, it is also one of the most common gram-negative bacteria present in wounds.⁴² Thus, for *in vivo* studies, the animal model chosen consisted of immunocompromised mice with an induced wound infection with *E. coli*. The experiments were conducted by Fernanda Alves and Kate C. Blanco of the Biophotonics Lab of São Carlos Physics Institute of the University of São Paulo, headed by Vanderlei S. Bagnato.

The *in vitro* studies described above were the starting point for transposition to *in vivo* studies, namely: i) selection of **IP-H-Me⁴⁺** as the best PS; ii) selection of the best dual phototherapy protocol (CIP administration after PDI, protocol **B**); iii) selection of PDI doses (the experiments conducted in MH medium clearly showed the need for higher PDI doses, since light absorption/scattering and ROS quenching are present). In addition to these issues, the heterogeneity of animal tissues may lead to a lower

diffusion and consequently reduce bacterial uptake of both the PS and CIP, when compared with *in vitro* studies, where all components are present in a homogeneous solution. Taking all these factors into account, the *in vivo* experiments were conducted using both the optimized protocol for MH medium (low dose protocol - 2 μM PS, 5.4 J/cm^2 and 0.125 mg/L CIP; Table 2.7 “PDI LD + CIP”) and another protocol where all variables were increased by a factor of 10 (high dose protocol - 20 μM PS, 50 J/cm^2 and 1.25 mg/L CIP; Table 2.7 “PDI HD + CIP”). All the animal groups used for this experiment are summarized in Table 2.7.

Table 2.7: Study groups for the *in vivo* dual phototherapy treatment of mice wounds infected with *E. coli*.

#	Study group	Experimental conditions
1	Control	No addition of PS or CIP. Wound kept in the dark.
2	Light	No addition of PS or CIP. Wound irradiation with 50 J/cm^2 .
3	PS (Dark)	Topical application of PS (20 μM) only. Wound kept in the dark.
4	CIP	Topical application of CIP (1.25 mg/mL) only. Wound kept in the dark.
5	PS + CIP (Dark)	Topical application of PS (20 μM) and CIP (1.25 mg/mL). Wound kept in the dark.
6	PDI LD (Low Dose)	Topical application of PS (2 μM) only, followed by 1 h dark incubation and then irradiation with 5.4 J/cm^2 .
7	PDI LD + CIP	Topical application of PS (2 μM), followed by 1 h dark incubation and then irradiation with 5.4 J/cm^2 . Then, CIP (0.125 mg/mL) is added.
8	PDI HD (High Dose)	Topical application of PS (20 μM) only, followed by 1 h dark incubation and then irradiation with 50 J/cm^2 .
9	PDI HD + CIP	Topical application of PS (20 μM), followed by 1 h dark incubation and then irradiation with 50 J/cm^2 . Then, CIP (1.25 mg/mL) is added.

We considered two control groups (dark and light), where neither PS nor CIP are added (entries 1-2), besides groups where PS, CIP and PS + CIP therapies were performed without light irradiation (entries 3-5). As mentioned above, for the treatment groups, two PDI doses were used: a low dose (LD) and a high dose (HD). For each dose, PDI was carried out in monotherapy (entries 6 and 8) or in combination with CIP (entries 7 and 9).

In this study, 40 animals were immunosuppressed in the first day of the experiment and, in the following day, under anesthesia, 3 mm wounds were inflicted and infected with an *E. coli* suspension. The infection was allowed to grow for 6 days and then the animals were divided in several treatment groups according to Table 2.7. One hour after each treatment (controls, PDI monotherapy, CIP monotherapy or PDI + CIP), the wounds were swabbed and the number of viable bacteria present (CFU/mL) was determined (Figure 2.16, "After 1 h", blue columns).

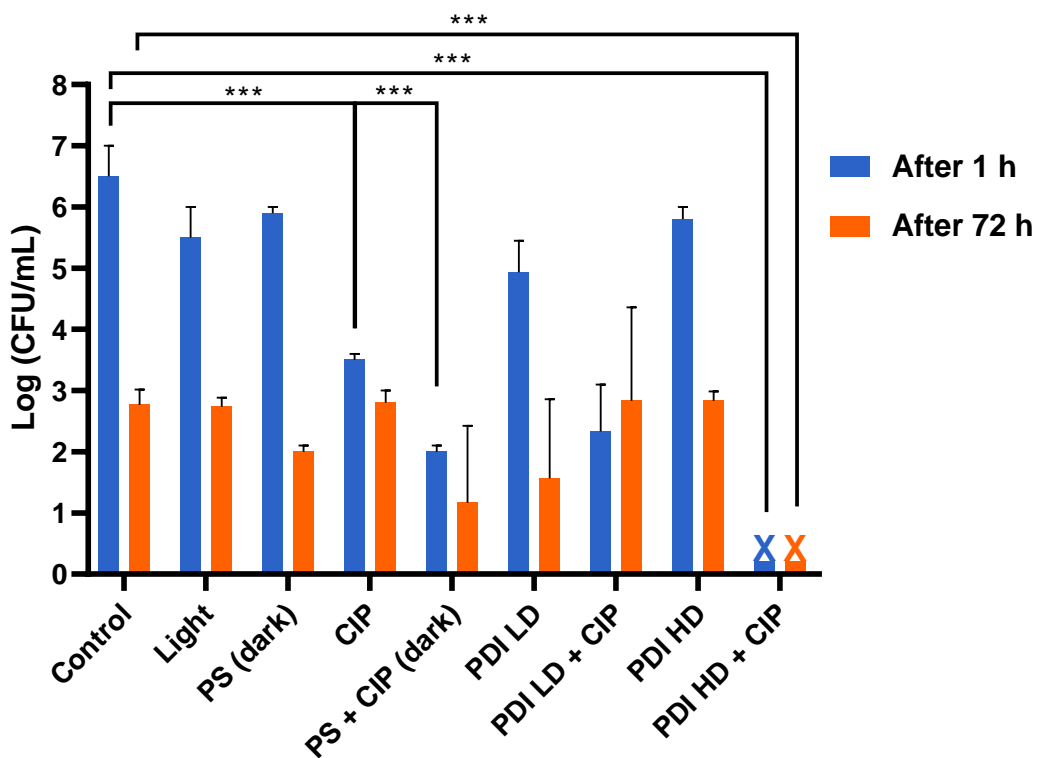


Figure 2.16: *In vivo* evaluation of PDI in combination with CIP for treatment of mice wounds infected with *E. coli* bacteria, using IP-H-Me⁴⁺ as PS. The results are presented in log (CFU/mL) of *E. coli* bacteria extracted from mice wounds: 1 h (blue blocks) and 72 h (orange blocks) after the selected treatment. The label *** ($p < 0.001$) represents statistical difference.

Then, 72h after treatment, the number of viable bacteria was again determined (Figure 2.16, "After 72 h", orange columns). After this period, the animals were euthanized according the protocol approved by the Ethic Committee on Animal Use of the Physics Institute of Sao Carlos - Sao Paulo University (CEUA/IFSC).

The microbiological data presented in Figure 2.16 show that wound treatment with light alone or upon topical application of the PS in the dark did not result in a statistical difference in viable bacteria, when compared with the control group, both after 1 h and 72 h. In the group where only CIP was administered, a significant decrease in viable bacteria was observed after 1 h. However, this value stabilizes over time and, after 72 h, the number of viable bacteria is similar to the control group. The same occurs with the PS + CIP (dark) control group, where the number of viable bacteria after 72 h is also not statistically different relatively to the control group. The results in these last two groups (CIP and PS + CIP (dark)) illustrate a common clinical scenario, where the antibiotic doses used in the treatment of an infection are insufficient for a complete inactivation of all bacteria. In this case, there is a risk that the remaining bacteria, after CIP treatment, can develop resistance to this antibiotic and thus contribute to the proliferation of MDR strains. In the PDI LD and PDI HD groups, the sub-inhibitory doses used (2 μM PS and 5.4 J/cm^2 or 20 μM PS and 50 J/cm^2 , respectively) did not result in any difference, relatively to the control group, either after 1 h or 72 h. Furthermore, when combining the lower PDI dose with CIP (PDI LD + CIP), the log CFU/ml reduction after 1 h was similar to the CIP and PS + CIP (dark) groups and, after 72 h, there was no difference relatively to the control group. In other words, PDI using the exact same dose (PS concentration and light dose) as in the *in vitro* assays, was not effective in potentiating the antimicrobial effect of CIP. This result was expected due to the complexity of tissues in *in vivo* experiments, as was explained above, which justifies the need for an increase of PDI doses. The combination of PDI HD + CIP successfully addressed this issue and allowed a complete inactivation of bacteria in the wounds (below the limit of detection) of all mice, both 1 h and 72 h after treatment. This dual phototherapy protocol shows a remarkable synergic effect between PDI and CIP, already demonstrated *in vitro*, since the combined therapy was significantly more active than either monotherapy (PDI or CIP). The quick burst of oxidative damage to bacteria caused seems to improve CIP efficiency *in vivo*. By eliminating all viable bacteria in wounds

almost immediately (1 h) after treatment, PDI + CIP therapy prevents bacterial regrowth in the following days, as illustrated by the 72 h column. Indeed, this can substantially reduce the probability of resistance development to CIP, which was one of the main goals of this work.

Photos of wounds in the initial stages (before treatments) and 72 h after treatment for each type of treatment were taken to illustrate the effect of each therapy in wound healing (Figure 2.17).

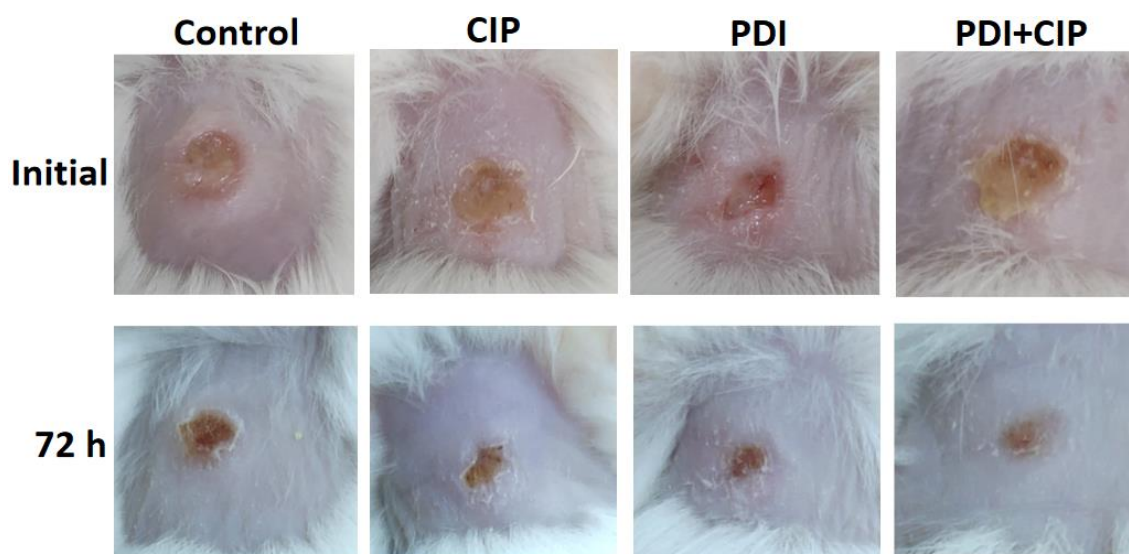


Figure 2.17: Evolution of wound healing in control and treatment groups (CIP, PDI, PDI + CIP), both in the initial stage and 72 h after treatment.

Wound healing depends not only in the reduction of bacteria in wounds, but also on the low toxicity of the therapy towards the host's cells. Indeed, previous reports showed that very high PDI doses can have a significant effect on the reduction of viable bacteria but also cause damage to tissues, with consequent disruption of wound healing.⁴³ In this regard, we can observe a considerable decrease in wound area in all treatment groups (CIP, PDI and PDI + CIP) at 72 h, when compared with the initial stages and control group. Additionally, wound healing in the PDI + CIP group after 72 h was superior to the other groups treated with monotherapies (PDI or CIP), which points out that the dual phototherapy was the best approach both in bacterial inactivation and improvement of wound healing.

2.5 – Conclusion

To ensure the successful introduction of PDI as a widespread alternative treatment to localized infections, there are a number of topics that need to be addressed in the pre-clinical stages. These include i) development of sustainable synthetic methods for photosensitizers, easily transposable into a larger scale; ii) photosensitizers *in vitro* screening and selection of the lead molecules, based on their photophysical/photochemical properties and antimicrobial activity; iii) optimization of photoinactivation protocols and possible combination therapies that can boost PDI and improve its activity spectrum. The work detailed in this chapter sought to address these three issues.

First, cationic phthalocyanines (**IPc-Zn-Et⁴⁺**, **IPc-In-Et⁴⁺**) and their corresponding phthalonitrile precursors were prepared under more sustainable reaction conditions. This entailed the use of alternative reaction heating methodologies, namely ultrasound and microwave irradiation, which resulted in a significant reduction of reaction times and improvements in product yields up to 12%, when comparing with classical conditions. Ultrasound irradiation proved to be more efficient for phthalonitrile modulation, which involves S_NAr reactions, and microwave irradiation was more suited for metallophthalocyanine synthesis and corresponding cationization. Additionally, toxic solvents such as DMF and quinoline were replaced by safer alternative (DMSO and DMAE, respectively), in accordance with guidelines from the pharmaceutical industry. In some cases, all these optimizations facilitated product purification and ensured an easier scale-up. The di- (**IP-H-Me²⁺**) and tetra-cationic porphyrins (**IP-H-Me⁴⁺**), were obtained by cationization of the corresponding precursor porphyrins under microwave irradiation, with reaction times of just 5 min. Moreover, **IP-Zn-Me⁴⁺** was obtained in the same reaction time, through complexation of **IP-H-Me⁴⁺** with Zn(OAc)₂. Regarding the porphyrin modulation, DMF was substituted by DMSO for the cationization and by methanol for the Zn(II) metalation, resulting in similar yields to those reported in the literature. The set of synthesized cationic photosensitizers allowed to understand the influence of structural features such as i) tetrapyrrolic macrocycle family (porphyrin or phthalocyanine); ii) the coordinating metal; iii) number of positive charges and iv)

amphiphilicity, for the photoinactivation of *E. coli*, in monotherapy and in combination with CIP.

Regarding the tetrapyrrolic macrocycle family, *in vitro* studies have showed that cationic imidazolyl-substituted porphyrins (**IP-H-Me²⁺**, **IP-H-Me⁴⁺** and **IP-H-Me⁴⁺**) were better suited than cationic phthalocyanines (**IPc-Zn-Et⁴⁺**, **IPc-In-Et⁴⁺**) to pursue an efficient dual phototherapy protocol for *E. coli* inactivation in combination with CIP. The order on which each therapy (PDI and CIP) is performed influences the outcome of the therapy, and “PDI treatment before CIP administration” (approach **B**) was found to be the best combination modality. In addition, while all porphyrins used were highly active in the nM range, the structure-activity relationship studies performed have highlighted the tetra-cationic *meso*-imidazolyl porphyrins **IP-H-Me⁴⁺** and **IP-Zn-Me⁴⁺** as the most promising PS. Since there was no significant difference between free base and Zn(II) porphyrins, concerns regarding the Zn(II) complex stability and synthesis transposition to larger scale have led us to select **IP-H-Me⁴⁺** as the lead photosensitizer. The best results for **IP-H-Me⁴⁺** were obtained with 16 nM of this PS and 5.4 J/cm², where a synergic 64-fold reduction of MIC_{CIP} (from 0.25 to 0.004 mg/L) was observed. Dual phototherapy was also efficient in boosting CIP activity on a MDR *E. coli* strain (MIC_{CIP} reduced from 32 to 0.5 mg/L), with similar PS concentrations, but higher light doses (45.3 J/cm²). Complementary studies have demonstrated that **IP-H-Me⁴⁺** - PDI + CIP combination is synergic and also efficient when performed in more complex matrixes such as MH culture medium. Considering the challenges arising from the transition from planktonic *in vitro* studies to *in vivo* studies, this dual phototherapy protocol was further optimized for the treatment of mice wounds infected with *E. coli*. The animal studies revealed that the combination therapy (PDI + CIP) was more efficient than each monotherapy (PDI or CIP) both in the inactivation of bacteria and improvement of wound healing.

Overall, the results from the *in vitro* and animal studies illustrates the potential of combining PDI with antibiotics in clinical settings. In particular, the synergistic combination with CIP can be effective in the treatment of bacteria with reduced susceptibility to antibiotics and also reduce the probability of resistance development. This may play a vital role in the quest for treatments for widespread use that offer a long-lasting efficacy, capable of serving multiple generations.

2.6 – References

- [1] Aroso, R. T.; Calvete, M. J. F.; Pucelik, B.; Dubin, G.; Arnaut, L. G.; Pereira, M. M.; Dąbrowski, J. M., Photoinactivation of microorganisms with sub-micromolar concentrations of imidazolium metallophthalocyanine salts, *European Journal of Medicinal Chemistry*, **2019**, *184*, 111740.
- [2] Aroso, R. T. *Síntese e estudo de novos fotossensibilizadores com potencial para terapia antimicrobiana*. MSc Thesis, Chemistry Department, Universidade de Coimbra, **2017**.
- [3] Gonzalez, A. C. S.; Felgueiras, A. P.; Aroso, R. T.; Carrilho, R. M. B.; Pereira, M. M., Al(III) phthalocyanine catalysts for CO₂ addition to epoxides: Fine-tunable selectivity for cyclic carbonates versus polycarbonates, *Journal of Organometallic Chemistry*, **2021**, *950*, 121979.
- [4] Gonzalez, A. C. S.; Aroso, R. T.; Carrilho, R. M. B.; Claver, C.; Masdeu-Bultó, A. M.; Pereira, M. M., Sustainable Synthesis of Polymeric Materials versus Fine Chemicals via CO₂ Addition to Epoxides, *Chemistry Proceedings*, **2021**, *3*, 17.
- [5] Mečiarová, M.; Toma, Š.; Magdolen, P., Ultrasound effect on the aromatic nucleophilic substitution reactions on some haloarenes, *Ultrasonics Sonochemistry*, **2003**, *10*, 265-270.
- [6] Mason, T. J.; Peters, D., *Practical Sonochemistry: Power Ultrasound Uses and Applications*. 2nd Edition ed.; Woodhead Publishing: Cambridge, **2002**.
- [7] European Chemicals Agency (ECHA) Candidate list of substances of very high concern for authorisation, **2015**, <http://echa.europa.eu/candidatelist-table> (accessed in 08/10/2021).
- [8] ICH guideline Q3C (R8) on impurities: guideline for residual solvents. <https://www.ema.europa.eu/en/ich-q3c-r6-residual-solvents> (accessed in 08/10/2021).
- [9] Byrne, F. P.; Jin, S.; Paggiola, G.; Petchey, T. H. M.; Clark, J. H.; Farmer, T. J.; Hunt, A. J.; Robert McElroy, C.; Sherwood, J., Tools and techniques for solvent selection: green solvent selection guides, *Sustainable Chemical Processes*, **2016**, *4*, 7.
- [10] Van Aken, K.; Streckowski, L.; Patiny, L., EcoScale, a semi-quantitative tool to select an organic preparation based on economical and ecological parameters, *Beilstein Journal of Organic Chemistry*, **2006**, *2*, 3.
- [11] Grossman, R., The Role of Dimethylaminoethanol in Cosmetic Dermatology, *American Journal of Clinical Dermatology*, **2005**, *6*, 39-47.
- [12] Kappe, C. O., Controlled Microwave Heating in Modern Organic Synthesis, *Angewandte Chemie International Edition*, **2004**, *43*, 6250-6284.
- [13] Kumar, A.; Kuang, Y.; Liang, Z.; Sun, X., Microwave chemistry, recent advancements, and eco-friendly microwave-assisted synthesis of nanoarchitectures and their applications: a review, *Materials Today Nano*, **2020**, *11*, 100076.
- [14] Vinagreiro, C. S.; Zangirolami, A.; Schaberle, F. A.; Nunes, S. C. C.; Blanco, K. C.; Inada, N. M.; da Silva, G. J.; Pais, A.; Bagnato, V. S.; Arnaut, L. G.; Pereira, M. M., Antibacterial Photodynamic Inactivation of Antibiotic-Resistant Bacteria and Biofilms with Nanomolar Photosensitizer Concentrations, *ACS Infectious Diseases*, **2020**, *6*, 1517-1526.

- [15] Schaberle, F. A., Assessment of the actual light dose in photodynamic therapy, *Photodiagnosis and Photodynamic Therapy*, **2018**, *23*, 75-77.
- [16] Kowalska-Krochmal, B.; Dudek-Wicher, R., The Minimum Inhibitory Concentration of Antibiotics: Methods, Interpretation, Clinical Relevance, *Pathogens (Basel, Switzerland)*, **2021**, *10*, 165.
- [17] Machuca, J.; Recacha, E.; Briales, A.; Díaz-de-Alba, P.; Blazquez, J.; Pascual, Á.; Rodríguez-Martínez, J.-M., Cellular Response to Ciprofloxacin in Low-Level Quinolone-Resistant *Escherichia coli*, *Frontiers in Microbiology*, **2017**, *8*, 1370.
- [18] Dellgren, L.; Claesson, C.; Högdahl, M.; Forsberg, J.; Hanberger, H.; Nilsson, L. E.; Hällgren, A., Phenotypic screening for quinolone resistance in *Escherichia coli*, *European Journal of Clinical Microbiology & Infectious Diseases*, **2019**, *38*, 1765-1771.
- [19] Huang, L.; Huang, Y.-Y.; Mroz, P.; Tegos, G. P.; Zhiyentayev, T.; Sharma, S. K.; Lu, Z.; Balasubramanian, T.; Kraymer, M.; Ruzié, C.; Yang, E.; Kee, H. L.; Kirmaier, C.; Diers, J. R., *et al.*, Stable Synthetic Cationic Bacteriochlorins as Selective Antimicrobial Photosensitizers, *Antimicrobial Agents and Chemotherapy*, **2010**, *54*, 3834-3841.
- [20] Hurst, A. N.; Scarbrough, B.; Saleh, R.; Hovey, J.; Ari, F.; Goyal, S.; Chi, R. J.; Troutman, J. M.; Vivero-Escoto, J. L., Influence of Cationic meso-Substituted Porphyrins on the Antimicrobial Photodynamic Efficacy and Cell Membrane Interaction in *Escherichia coli*, *International Journal of Molecular Sciences*, **2019**, *20*, 134.
- [21] Gyulkhandanyan, G.; Paronyan, M.; Hovsepyan, A.; Ghazaryan, R.; Tovmasyan, A.; Gyulkhandanyan, A.; Gyulkhandanyan, A.; Amelyan, G., Photodynamic inactivation of Gram (-) and Gram (+) microorganisms by cationic porphyrins and metalloporphyrins, *Proceedings of SPIE*, **2009**, *7380*, *Photodynamic Therapy: Back to the Future*.
- [22] Hu, X.; Huang, Y. Y.; Wang, Y.; Wang, X.; Hamblin, M. R., Antimicrobial Photodynamic Therapy to Control Clinically Relevant Biofilm Infections, *Frontiers in Microbiology*, **2018**, *9*, 1299.
- [23] Clinical Laboratory Testing and in vitro Diagnostic Test Systems - Susceptibility Testing of Infectious Agents and Evaluation of Performance of AST Devices – Part 1: Reference Method for Testing the in vitro Activity of antimicrobial Agents Against Rapidly Growing Aerobic Bacteria Involved in Infectious Diseases. ISO 20776-1:2006.
- [24] Hamblin, M. R.; Jori, G., *Photodynamic Inactivation of Microbial Pathogens*. The Royal Society of Chemistry: Cambridge, **2011**.
- [25] Ronqui, M. R.; de Aguiar Coletti, T. M.; de Freitas, L. M.; Miranda, E. T.; Fontana, C. R., Synergistic antimicrobial effect of photodynamic therapy and ciprofloxacin, *Journal of Photochemistry and Photobiology B: Biology*, **2016**, *158*, 122-129.
- [26] Lambers, H.; Piessens, S.; Bloem, A.; Pronk, H.; Finkel, P., Natural skin surface pH is on average below 5, which is beneficial for its resident flora, *International Journal of Cosmetic Science*, **2006**, *28*, 359-370.
- [27] Sabbahi, S.; Ben Ayed, L.; Boudabbous, A., Cationic, anionic and neutral dyes: effects of photosensitizing properties and experimental conditions on the photodynamic inactivation of pathogenic bacteria, *Journal of Water and Health*, **2013**, *11*, 590-599.

- [28] Xuan, W.; Huang, L.; Wang, Y.; Hu, X.; Szewczyk, G.; Huang, Y.-Y.; El-Hussein, A.; Bommer, J. C.; Nelson, M. L.; Sarna, T.; Hamblin, M. R., Amphiphilic tetracationic porphyrins are exceptionally active antimicrobial photosensitizers: In vitro and in vivo studies with the free-base and Pd-chelate, *J Biophotonics*, **2019**, *12*, e201800318.
- [29] Loffredo, M. R.; Savini, F.; Bobone, S.; Casciaro, B.; Franzyk, H.; Mangoni, M. L.; Stella, L., Inoculum effect of antimicrobial peptides, *Proceedings of the National Academy of Sciences of the United States of America*, **2021**, *118*, e2014364118.
- [30] Rio-Marques, L.; Hartke, A.; Bizzini, A., The Effect of Inoculum Size on Selection of In Vitro Resistance to Vancomycin, Daptomycin, and Linezolid in Methicillin-Resistant *Staphylococcus aureus*, *Microbial Drug Resistance*, **2014**, *20*, 539-543.
- [31] Wozniak, A.; Grinholc, M., Combined Antimicrobial Activity of Photodynamic Inactivation and Antimicrobials-State of the Art, *Frontiers in Microbiology*, **2018**, *9*, 930.
- [32] Lorian, V., *Chapter 9 - Antimicrobial Combinations, in Antibiotics In Laboratory Medicine*. 5th Edition ed.; Lippincott Williams and Wilkins: Philadelphia, USA, **2005**.
- [33] Aroso, R. T.; Schaberle, F. A.; Arnaut, L. G.; Pereira, M. M., Photodynamic disinfection and its role in controlling infectious diseases, *Photochemical & Photobiological Sciences*, **2021**, *20*, 1497-1545.
- [34] Blair, J. M.; Webber, M. A.; Baylay, A. J.; Ogbolu, D. O.; Piddock, L. J., Molecular mechanisms of antibiotic resistance, *Nature Reviews Microbiology*, **2015**, *13*, 42-51.
- [35] Wang, Y.; Wang, Y.; Wang, Y.; Murray, C. K.; Hamblin, M. R.; Hooper, D. C.; Dai, T., Antimicrobial blue light inactivation of pathogenic microbes: State of the art, *Drug resistance updates*, **2017**, *33-35*, 1-22.
- [36] Abana, C. M.; Brannon, J. R.; Ebbott, R. A.; Dunigan, T. L.; Guckes, K. R.; Fuseini, H.; Powers, J.; Rogers, B. R.; Hadjifrangiskou, M., Characterization of blue light irradiation effects on pathogenic and nonpathogenic *Escherichia coli*, *MicrobiologyOpen*, **2017**, *6*, e00466.
- [37] Gupta, S.; Maclean, M.; Anderson, J. G.; MacGregor, S. J.; Meek, R. M. D.; Grant, M. H., Inactivation of micro-organisms isolated from infected lower limb arthroplasties using high-intensity narrow-spectrum (HINS) light, *The Bone & Joint Journal*, **2015**, *97-B*, 283-288.
- [38] Garcez, A. S.; Kaplan, M.; Jensen, G. J.; Scheidt, F. R.; Oliveira, E. M.; Suzuki, S. S., Effects of antimicrobial photodynamic therapy on antibiotic-resistant *Escherichia coli*, *Photodiagnosis and Photodynamic Therapy*, **2020**, *32*, 102029.
- [39] Morley, S.; Griffiths, J.; Philips, G.; Moseley, H.; O'Grady, C.; Mellish, K.; Lankester, C. L.; Faris, B.; Young, R. J.; Brown, S. B.; Rhodes, L. E., Phase IIa randomized, placebo-controlled study of antimicrobial photodynamic therapy in bacterially colonized, chronic leg ulcers and diabetic foot ulcers: a new approach to antimicrobial therapy, *British Journal of Dermatology*, **2013**, *168*, 617-624.
- [40] Feng, Y.; Coradi Tonon, C.; Ashraf, S.; Hasan, T., Photodynamic and antibiotic therapy in combination against bacterial infections: efficacy, determinants, mechanisms, and future perspectives, *Advanced Drug Delivery Reviews*, **2021**, *177*, 113941.

- [41] Sjöberg, B.; Foley, S.; Staicu, A.; Pascu, A.; Pascu, M.; Enescu, M., Protein reactivity with singlet oxygen: Influence of the solvent exposure of the reactive amino acid residues, *Journal of Photochemistry and Photobiology B: Biology*, **2016**, *159*, 106-110.
- [42] Azzopardi, E. A.; Azzopardi, E.; Camilleri, L.; Villapalos, J.; Boyce, D. E.; Dziewulski, P.; Dickson, W. A.; Whitaker, I. S., Gram Negative Wound Infection in Hospitalised Adult Burn Patients-Systematic Review and Metanalysis, *PloS One*, **2014**, *9*, e95042.
- [43] Xu, Z.; Gao, Y.; Meng, S.; Yang, B.; Pang, L.; Wang, C.; Liu, T., Mechanism and In Vivo Evaluation: Photodynamic Antibacterial Chemotherapy of Lysine-Porphyrin Conjugate, *Frontiers in Microbiology*, **2016**, *7*, 242.

CHAPTER 3

Computer-aided drug design of new *E. coli* gyrase B inhibitors

3.1 – Computational studies

Aiming to contribute towards the development of new antimicrobials through rational drug discovery methodologies, we will discuss computational approaches for the screening and design of new potential inhibitors for *E. coli*'s gyrase B (gyrB) throughout this chapter. Our goal consists in the discovery of new chemical entities, either by using readily available compounds that have not yet been tested for this application or by directing the chemical synthesis to new families of compounds. To achieve such goals, a virtual screening of the widely available National Cancer Institute (NCI) database and a *de novo* designed virtual library of compounds was performed. Among the virtual screening techniques, we highlight ligand and receptor-based techniques such as pharmacophore modeling and molecular docking.

Pharmacophore, as described by IUPAC, is “an ensemble of steric and electronic features that is necessary to ensure the optimal supramolecular interactions with a specific biological target and to trigger (or block) its biological response”. These tridimensional features can be based on topology and/or function (*i.e.* aromatic, hydrogen bond acceptors/donors, acidic/anionic groups, basic/positive groups, or hydrophobic groups). After appropriate validation, these models can be used as queries to virtually screen chemical libraries. For each molecule, a set of low-energy conformations is generated and each is fitted to the pharmacophore query by aligning the molecules with the established features. If a molecule can fit the query features, it is considered a hit.¹

Molecular docking is another important concept in the world of CADD, which will be used to complement the screening by pharmacophore model. It requires 3D structural information and evaluates the intermolecular interactions established between a target and its ligands. By first determining the best conformational pose of ligands, it is then possible to estimate in a quantitative manner the various forces (bonding and non-bonding) involved in the formation of the protein-ligand complex. In the case of the present work, as our interest is in non-covalent inhibitors, only non-bonding interactions, like electrostatic and van der Waals, were considered.

The combination of both techniques can be very beneficial. On the one hand, pharmacophore models allow a fast, albeit only qualitative, screening of big virtual compound libraries. On the other hand, screening by molecular docking takes considerably longer, but permits the ranking of compounds based on predicted activity and helps to define priorities regarding the synthesis or acquisition of compounds. Thus, in this chapter we focused on the construction of a pharmacophore model of *E. coli*'s gyrase subunit B inhibitors to screen large digital libraries, followed by molecular docking of the pharmacophore screening hits.

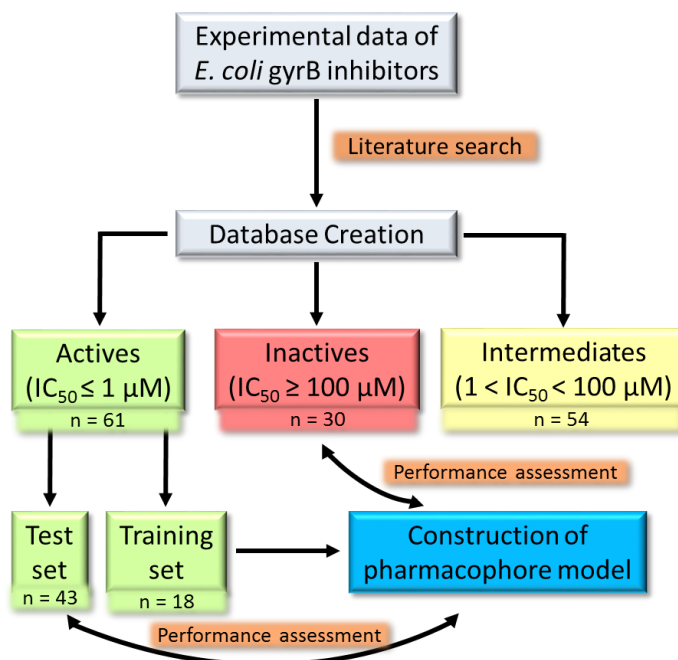
3.1.1 – Construction of pharmacophore model

Over this subsection, we explore the construction and optimization of multiple pharmacophore models, from a set of known inhibitors (ligand-based pharmacophores) that bind to the portion of *E. coli*'s gyrase B subunit responsible for the ATPase catalytic activity. These models were validated by using test sets containing active and inactive compounds, as well as computer-generated decoys. The model(s) that show better overall performance were used to screen the NCI database. In addition, this model was also used to screen a dataset of computer-generated compounds (*de novo* design) inspired by the chemical structures of known ligands, with the objective of finding synthetically amenable molecules/scaffolds with *E. coli* antimicrobial activity.

For the development of the pharmacophore model we used MOE (Molecular Operating Environment) software.² This program is a drug discovery software that integrates numerous valuable tools in a user-friendly environment to carry out visualization, modelling and simulation of biomolecules and small molecules.

Building databases of compounds with known biological activity

The flowchart presented in Scheme 3.1 illustrates the steps followed for the construction of ligand-based pharmacophore models.



Scheme 3.1: Flowchart for the construction of ligand-based pharmacophore models in MOE.

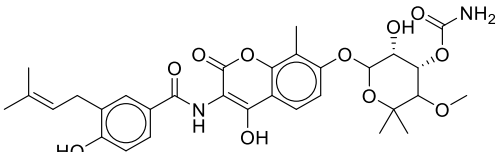
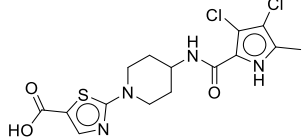
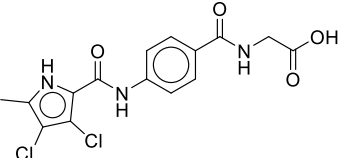
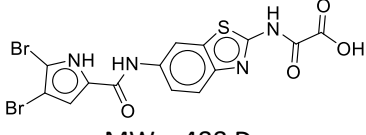
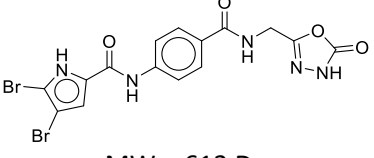
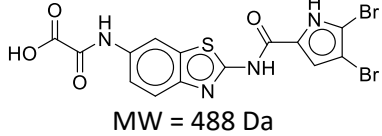
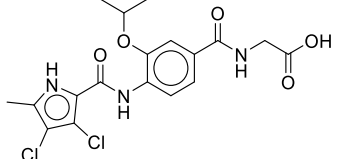
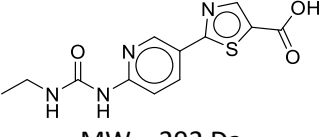
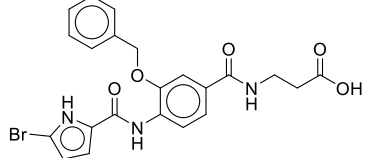
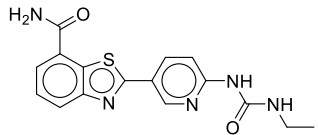
First, through a comprehensive literature search,³⁻¹³ we were able to retrieve experimental data for compounds with a known structure that were tested for inhibition of *E. coli*'s GyrB. Only literature reports with the following inclusion criteria were considered: i) small molecules amenable to chemical synthesis (*i.e.* no biomolecules); ii) biochemical data (IC_{50}) reported for *E. coli* gyrase; iii) identification of gyrB ATP binding site as probable target. This last aspect is of considerable importance since the presence of molecules in the created database that interact with gyrase through different binding sites prevent the identification of common structural features, as the required spatial interactions with the binding site's side-chains would not be the same. Indeed, as previously mentioned, quinolones are also small molecules with high *E. coli* gyrase inhibition, but they bind to subunit A and therefore, their structural information would have no use for the purpose of this work.

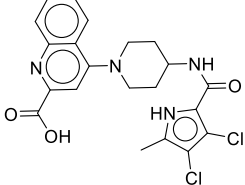
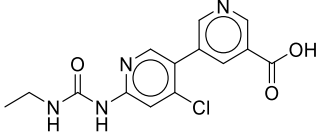
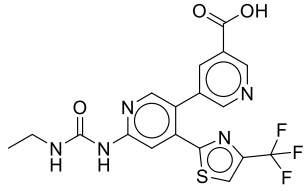
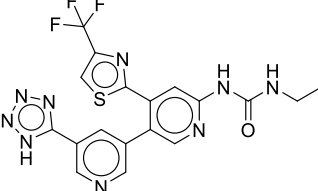
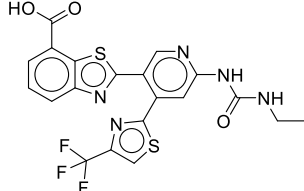
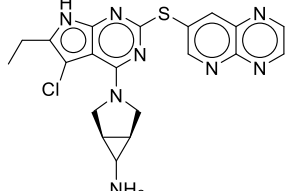
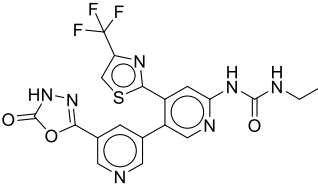
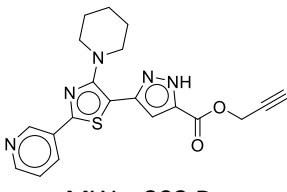
A total of 145 compounds and corresponding biological activity were retrieved. They were divided into three groups and classified according to their activity: 61 were

classified as actives ($IC_{50} \leq 1 \mu M$), 54 as intermediates ($1 \mu M < IC_{50} < 100 \mu M$) and 30 as inactive ($IC_{50} \geq 100 \mu M$).

From the actives database, the most structurally diverse 18 compounds were selected as the training set (Table 3.1), while the remaining 43 were included in the test set.

Table 3.1: Compounds included in the training set for the construction of the ligand-based pharmacophore models. LogP was estimated using MOE 2016.

#	Structure	#	Structure
1	 <p>MW = 613 Da IC₅₀ = 170 nM</p>	2	 <p>MW = 403 Da IC₅₀ = 25 nM</p>
3	 <p>MW = 370 Da IC₅₀ = 280 nM</p>	4	 <p>MW = 488 Da IC₅₀ = 38 nM</p>
5	 <p>MW = 613 Da IC₅₀ = 170 nM</p>	6	 <p>MW = 488 Da IC₅₀ = 58 nM</p>
7	 <p>MW = 428 Da IC₅₀ = 47 nM</p>	8	 <p>MW = 292 Da IC₅₀ = 240 nM</p>
9	 <p>MW = 565 Da IC₅₀ = 87 nM</p>	10	 <p>MW = 341 Da IC₅₀ = 94 nM</p>

11	 <p>MW = 447 Da IC₅₀ = 0.9 nM</p>	12	 <p>MW = 321 Da IC₅₀ = 58 nM</p>
13	 <p>MW = 437 Da IC₅₀ = 10 nM</p>	14	 <p>MW = 461 Da IC₅₀ = 10 nM</p>
15	 <p>MW = 493 Da IC₅₀ = 10 nM</p>	16	 <p>MW = 439 Da IC₅₀ = 1 nM</p>
17	 <p>MW = 477 Da IC₅₀ = 14 nM</p>	18	 <p>MW = 393 Da IC₅₀ = 11 nM</p>

In cases where multiple derivatives with the same base scaffold were present, the compound with the highest activity was chosen. It is worth noting that one of the compounds of the training set is novobiocin, the antibiotic from the class of aminocoumarins, but with little clinical use due to safety and effectiveness concerns, as mentioned in Chapter 1.¹⁴

Structural alignment of training set molecules

The first computational step in MOE consists in the loading of the training set molecules, followed by their spatial overlap through a stochastic conformer search (Figure 3.1). The best alignment is defined by the combination of two factors: i) low average strain energy of the conformer in the alignment and ii) high structural similarity

between spatially overlapped conformers for each molecule. We found that due to the presence of a high number of hydrogen bond acceptors and aromatic rings, some molecules were not properly aligned, even after several iterations. Indeed, it was common to observe only partial alignments (*i.e.* just one aromatic ring with another aromatic ring). As there are various poses where the spatial overlap was good but not optimal, the algorithms readily converged to these local energy minima. To circumvent this problem, the outlier molecules were manually aligned with the group of correctly aligned molecules and then a final automatic realignment was performed. A visual inspection of the final alignment (Figure 3.1) allowed us to identify four main regions which are essential to the generation of the pharmacophore hypothesis.

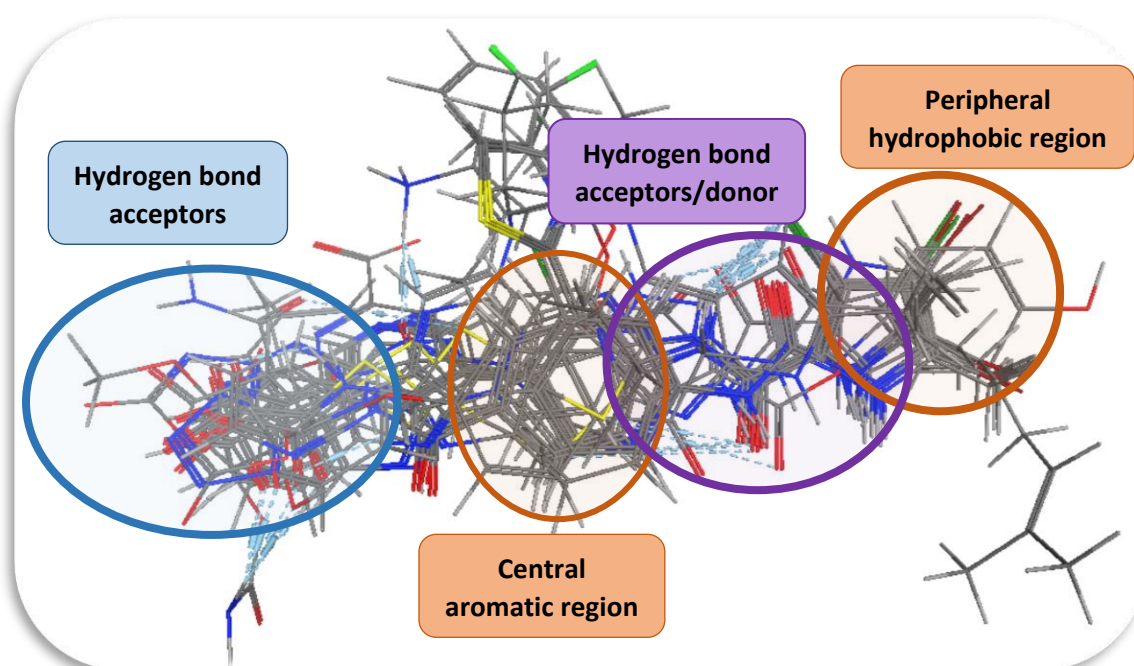


Figure 3.1: Optimized alignment of the 18 training set molecules that will be used as a basis for the generation of ligand-based pharmacophores. Atoms of different elements are color coded: Dark grey - Carbon; Light grey - Hydrogen; Light red - Oxygen; Blue - Nitrogen; Yellow - Sulphur; Dark red - Bromine; Light green - Fluorine; Dark green - Chlorine.

There is a peripheral hydrophobic region characterized by the presence of halogens (chlorine and bromine), alkylic or aromatic moieties. According to crystallographic data (see analysis below in this chapter), this portion of the molecules binds to the deepest, more inner part of the ATP binding pocket of gyrB subunit, which expectedly contains

more hydrophobic side-chains. In addition, there is a considerable amount of well-oriented hydrogen bond donors/acceptors between this region and a central aromatic region, as can be seen by the presence of numerous nitrogen (blue) and oxygen (light red) atoms. The central aromatic region is then linked to a peripheral region with a higher structural variability, containing many hydrogen bond acceptors. Overall, these molecules adopt a relatively planar structure throughout the four regions, with few freely rotatable bonds.

Generation of pharmacophores

For the generation of pharmacophore hypotheses, there are various annotation schemes in MOE, being Unified and EHT the most relevant. These annotation schemes define the type of structural characteristics (called annotation points) that can be included in a pharmacophore model. In other words, each annotation scheme confers a different interpretation if a given structural group is considered “hydrophobic”, “hydrogen bond acceptor” or “hydrogen bond donor”. As an example, for bromobenzene (Figure 3.2), the Unified scheme would attribute only the annotation point “hydrophobic” to the bromine atom. On the other hand, the EHT scheme would attribute “hydrophobic” and “hydrogen bond acceptor/donor”, as it considers the possibility of the bromine atom to participate in halogen bonding or serve as hydrogen bond acceptor. While these types of interactions are weaker than normal hydrogen bond interactions, they may be important in some protein-ligand interactions.¹⁵⁻¹⁶ Indeed, there are advantages and disadvantages of using each of these schemes, as the EHT scheme may overestimate the importance of these types of interactions and lead to poor differentiation between a good inhibitor, with the capability of establishing strong hydrogen bonds, and a poor inhibitor, with the capability of establishing only weak hydrogen bonds.

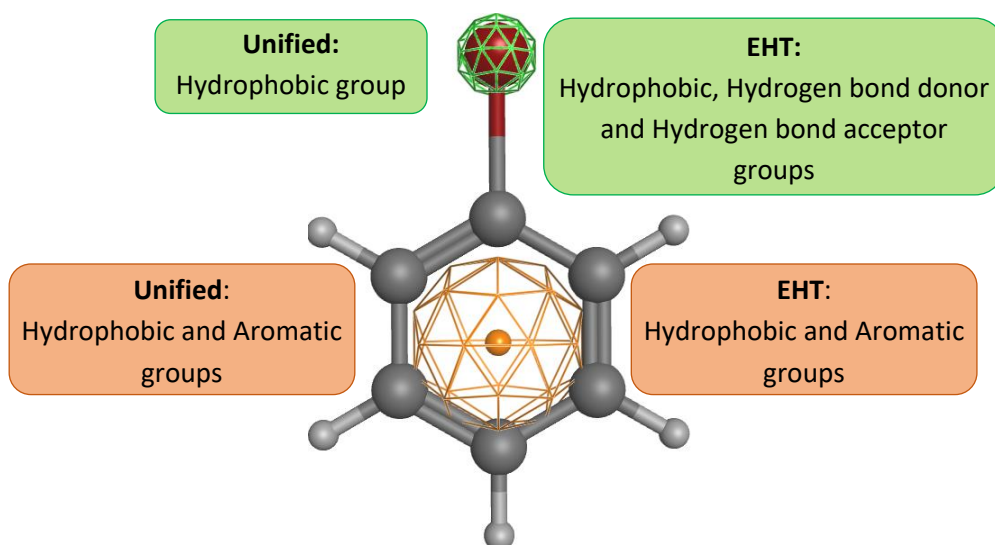


Figure 3.2: Schematic representation of the annotation points considered by each scheme (Unified and EHT) for the molecule of bromobenzene. Atoms of different elements are color coded: Dark grey - Carbon; Light grey - Hydrogen; Dark red – Bromine.

As each annotation scheme can lead to distinct pharmacophore models, with different performances in identifying hit molecules, we decided to create two pharmacophores based on Unified and EHT schemes.

Pharmacophore A (Unified scheme)

An initial pharmacophore hypothesis was first generated by choosing the five most common annotation points among the aligned molecules of the training set (Figure 3.1), as determined by MOE, using the Unified scheme. The obtained pharmacophore hypothesis was able to recognize as hits all the molecules of the training set as actives (18/18). However, when we assessed its performance in discriminating between active and inactive molecules, this hypothesis was considered unselective, with more than 90% of hits obtained in both datasets. Consequently, we chose the next two more common features, giving a pharmacophore hypothesis with seven features (Figure 3.3a). This hypothesis clearly improved its selectivity, with 50% hits retrieved in the actives set and only 6% hits from the inactives dataset. In this first hypothesis we have the following features: i) F1 – Central aromatic or hydrophobic group; ii) F2 – Peripheral aromatic or hydrophobic group; iii) F3 – Projected partner for hydrogen bond acceptor or donor; iv) F4 – Hydrogen bond acceptor or donor; v) F5 – Carboxylic, anionic or hydrogen bond

acceptor group; vi) F6 – Hydrogen bond donor; vii) F7 – Projected partner for hydrogen bond acceptor or donor.

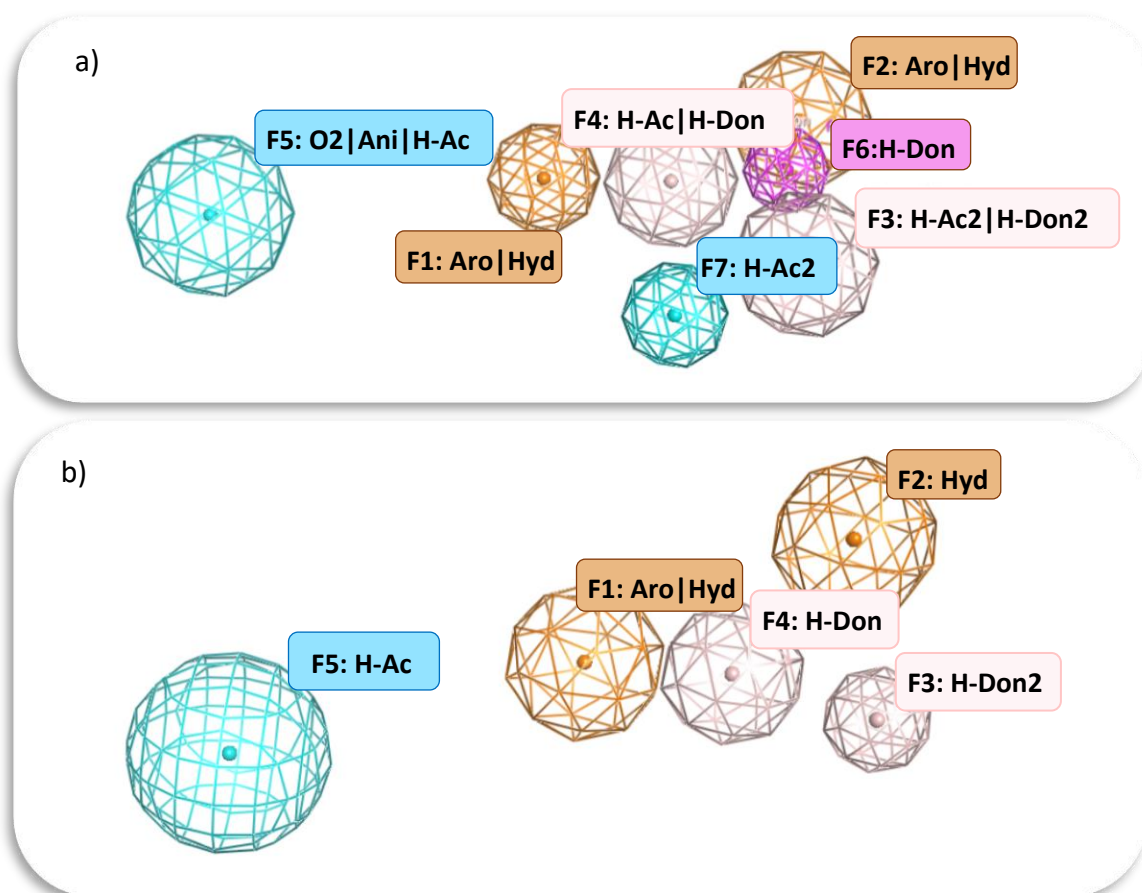


Figure 3.3: a) Pharmacophore hypothesis (Unified scheme) used as a starting point for further optimization; b) Optimized pharmacophore model obtained using the Unified scheme. The features are presented according to the following nomenclature: The vertical bar | denotes an “or” feature; H-Ac: Hydrogen bond acceptor; H-Ac2: Projected partner for hydrogen bond acceptor; Ani: Anionic; Aro: Aromatic; H-Don: Hydrogen bond donor; H-Don2: Projected partner for hydrogen bond donor; Hyd: Hydrophobic; O2: Carboxylic acid.

It is worth mentioning the relevance of making a distinction between the features “H-Don: Hydrogen bond donor”, “H-Ac: Hydrogen bond acceptor” and “H-Don2: Projected partner for hydrogen bond donor” or “H-Ac2: Projected partner for hydrogen bond acceptor”. While the features “H-Don” and “H-Ac” refer to functional groups located in the ligands, “H-Don2” and “H-Ac2” refer to features located outside the ligands, since they are projections of the localization of the hydrogen bond partner (side-chain of the protein). This is better clarified in Figure 3.4, where, as an example, the ligand molecule has hydroxyl groups, which will interact with a carbonyl group present in the protein.

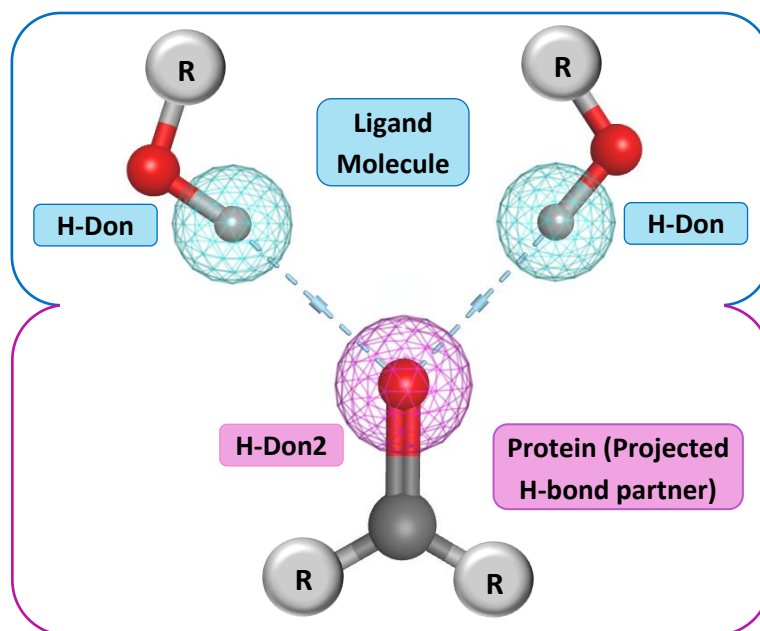


Figure 3.4: Representation of hydrogen bond donor features (H-Don and H-Don2) for the case of a ligand molecule containing hydroxyl groups and with a carbonyl group of a protein.

This first pharmacophore hypothesis containing seven features (Figure 3.3a), which was able to successfully differentiate actives from inactives, was used as a starting point for further optimization. The optimization process was performed with the purpose of having a model that could recognize all the molecules of the training set, without compromising the selectivity between actives and inactives. This was accomplished by removing structural features, simplifying existing features (*i.e.* reducing the number of “or” features) and altering their position and radii.

In this process, it was found that **F7:H-Ac2** was responsible for diminishing the training set recognition. Therefore, by removing this feature, the number of positives in the training set increased (15/18), but this tendency was also observed with the inactives set (19/30). However, by removing **H-Ac2** from **F3**, **H-Ac** from **F4** and **Ani** and **H-Ac** from **F5**, the positives in the inactives set were significantly reduced (7/30) with no appreciable difference in the active datasets. In addition, the removal of the feature **F6:H-Don** increased the number of positive hits in the training set (18/18), with no detrimental difference in the number of false positives. Removal of **Aro** from **F2** and minimal adjustments in the coordinates and radii of the features yielded the final pharmacophore hypothesis (Figure 3.3b). This model retrieved 95% and 17% hits from the active and inactives datasets, respectively.

Considering the false positives retrieved by the model, it can be observed that some molecules were too bulky to fit in the binding site of gyrB, which could explain their low activity. It is possible to fine-tune this model to avoid detection of these bulky molecules by placing volume exclusion spheres around **F2:Hyd** (Figure 3.5). Volume exclusion spheres, **F6: VES**, represent zones that cannot be occupied by the ligand, in order to avoid possible steric clashes with the proteins' residues.

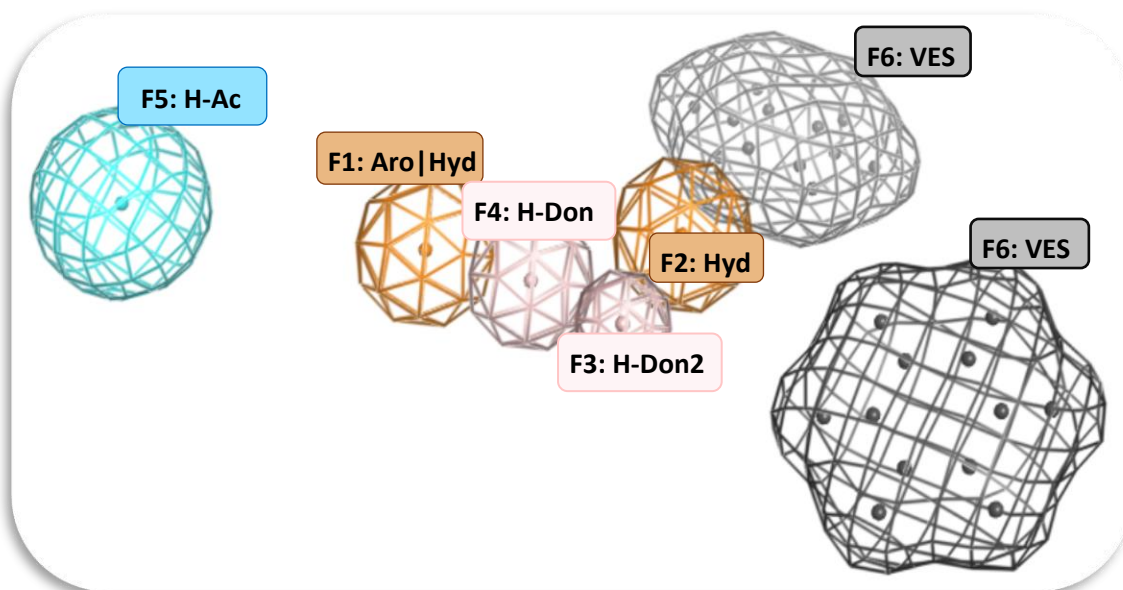


Figure 3.5: Representation of the final optimized pharmacophore model in Unified scheme, with the addition of volume exclusion spheres. H-Ac: Hydrogen bond acceptor; Aro: Aromatic; H-Don: Hydrogen bond donor; H-Don2: Projected partner for hydrogen bond donor; Hyd: Hydrophobic; VES: Volume exclusion sphere.

Pharmacophore B (EHT scheme)

Pharmacophore B was obtained using the same ligand alignment of the training set (Figure 3.1). Then, an initial pharmacophore hypothesis was performed using the EHT scheme, which allowed immediately to select five common features among the ligands that delivered selectivity towards active detection. This initial pharmacophore model (Figure 3.6a) was optimized using the same methodologies described above.

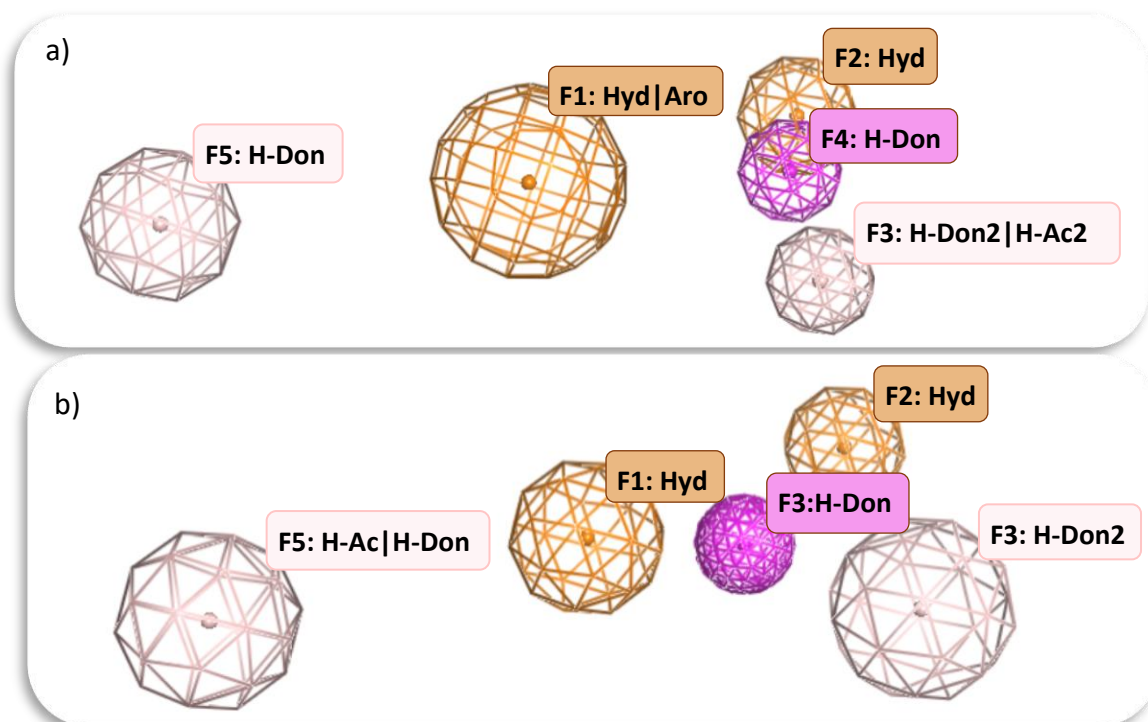


Figure 3.6: a) Initial pharmacophore hypothesis (EHT scheme) used as a starting point for further optimization; b) Optimized pharmacophore hypothesis obtained by the ligand-based method, using the EHT scheme. H-Ac: Hydrogen bond acceptor; Aro: Aromatic; H-Don: Hydrogen bond donor; H-Don2: Projected partner for hydrogen bond donor; H-Ac2: Projected partner for hydrogen bond acceptor; Hyd: Hydrophobic.

Briefly, a reduction in the number of false positives was possible by removing **H-Ac2** from **F3**, while the addition of **H-Ac** to **F5** increased the number of positives in the actives dataset. Unfortunately, only 13 (in 18) positives were retrieved from the training set, which means that there were still chemical scaffolds that this model was not able to identify as actives. This was improved by changing the coordinates of **F4: H-Don**, raising the number of positives in the training set to 16/18, along with the false positives (6/30). Finally, **Aro** from **F1** was removed and the position and radii of the features were slightly changed, which resulted in a decrease of false positives to 3/30. The optimized model is depicted in Figure 3.6b.

Comparative assessment of pharmacophore models' performance

For the final assessment of the performance of each pharmacophore model, we utilized the actives, intermediates and inactives datasets, as well as a decoy database.

Ideally, the choice of inactive compounds should be done based on experimental data, however given that the inactives dataset only contains 30 compounds, we also used a virtually generated decoy database to validate the models. Decoys are molecules that are presumably non-active, and can be generated from a set of active compounds. These molecules share similar properties to active molecules, namely molecular weight, predicted logP, number of rotatable bonds and hydrogen bond acceptor/donors, but with different spatial positioning of functional groups. In other words, these decoys are supposed to resemble ligands physically in order to challenge the models' accuracy, but at the same time have a different topology in order to minimize the likelihood of being true actives. To this effect, we selected DUD-E tool for generating a total of 3750 decoys based on our actives dataset.¹⁷ The results of this final assessment are presented in Figure 3.7.

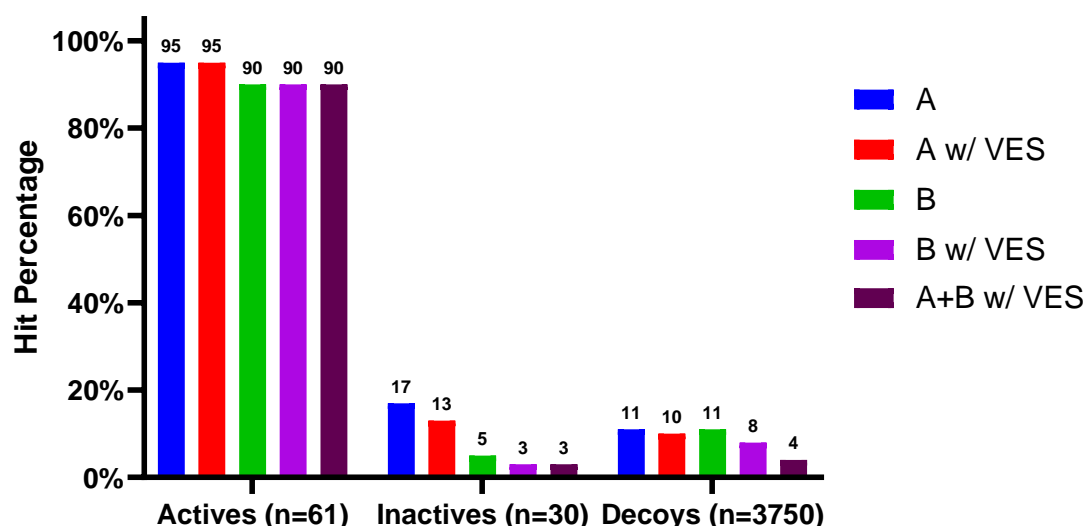


Figure 3.7: Performance of generated pharmacophores A and B, evaluated by hit percentage in actives, inactives and decoys datasets. In addition, the corresponding models with volume exclusion spheres are presented separately (A w/ VES and B w/VES), and also the performance of the combination of both pharmacophores (A+B w/VES).

Relatively to the detection of compounds from the actives dataset, pharmacophore A was better than B (95% and 90% respectively). Concerning the detection of inactives, B had a lower rate of false positives (5%) than A (17%). In addition, we found that the introduction of volume exclusion spheres (VES) helped to reduce the rate of false positives of A from 17% to 13% and of B from 5% to 3%. When comparing

the performance against decoys, model A was worse than B (11% and 10% false positive rate, respectively). The addition of volume exclusion spheres allowed to reduce the false positive rate of A from 11% to 10% and of B from 12% to 8%.

Finally, we found that the combination of pharmacophores A and B with volume exclusion spheres (A + B w/VES) maintained the same active and inactive hit rate of pharmacophore B w/VES alone (90% and 3%, respectively), but allowed a significant reduction of decoy hit rate to just 4%. We selected this combination for the next database screenings because it gave the highest ratio of true positives/false positives (decoys). Indeed, it is important to note that in a typical database screening, we expect to have a very small number of true active compounds mixed with a vast amount of inactives. The purpose of a pharmacophore model is therefore to generate a hit molecule database with a higher relative percentage of active molecules and a lower relative percentage of inactives. In other words, it will help to enrich our database with active compounds. Therefore, when choosing the best pharmacophore model, one of the most important aspects is to have a high proportion of true positives to false positives.

3.1.2 – Docking studies: selection of best scoring function for gyrB

To help refine the compound databases that will be screened, preliminary docking studies were conducted in order to determine the best model/scoring function that can more efficiently predict the biological activity of gyrB inhibitors. The goal was to test different software and scoring functions, and to determine the best model for an efficient correlation between docking score and experimental biological activity. For this purpose, some of the compounds included in the actives, intermediates and inactives datasets were used. In these docking studies, we selected a crystallographic structure of *E. coli*'s DNA GyrB from PDB (PDB entry 4KFG; Figure 3.8). This structure was chosen due to its good resolution (1.60 Å) and performance on the PDB validation tests, showing a low number of problematic torsion angles and steric clashes between protein residues. Next, a sequence of standard tasks was performed in MOE to prepare this structure for docking studies. These include small structural corrections and the addition of hydrogen

atoms to the binding site residues and assignment of correct tautomers and protonation states.

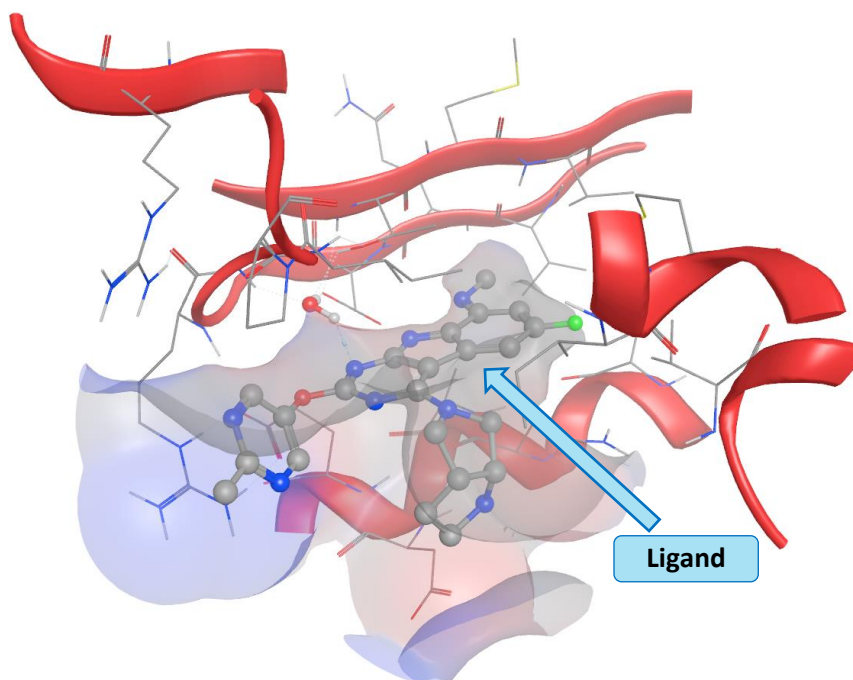


Figure 3.8: Binding site of the *E. coli* gyrase B ATP binding site (PDB: 4KFG), highlighting the crystallographic ligand.

After the preparation of the crystallographic structure, we created a training set composed of 11 compounds, retrieved from the actives, intermediates and inactives datasets previously assembled. As such, this group of molecules have diverse structural characteristics, resulting in multiple degrees of activity, ranging from reported IC_{50} values of 1 nM to 900 μ M. This training set was then used to determine the docking scoring function that could more accurately correlate the docking score to their reported experimental IC_{50} values. Overall, four scoring functions were evaluated. First, we tried MOE's docking tools, using the crystallographic ligand as reference for the target's binding site. Figure 3.9a represents the correlation obtained between the MOE docking score and the compounds' experimental IC_{50} values. It is worth mentioning that the docking score presented in MOE is in the form of the energy of the interaction, which means that a lower (more negative) score corresponds to a better predicted ligand-protein interaction. As such, the graph in Figure 3.9a does not give a meaningful correlation. To overcome this issue, we selected GOLD 5.4 (Cambridge Crystallographic

Data Centre) for the docking studies, one of the best software in this field.¹⁸ In GOLD, the binding site region was defined by the amino acid residues within a radius of 15 Å around the THR165 residue (localized in a central part of the binding site), and three different docking scoring functions were evaluated: ChemPLP, GoldScore and ChemScore. The correlation curves obtained for each are presented in Figure 3.9b-d.

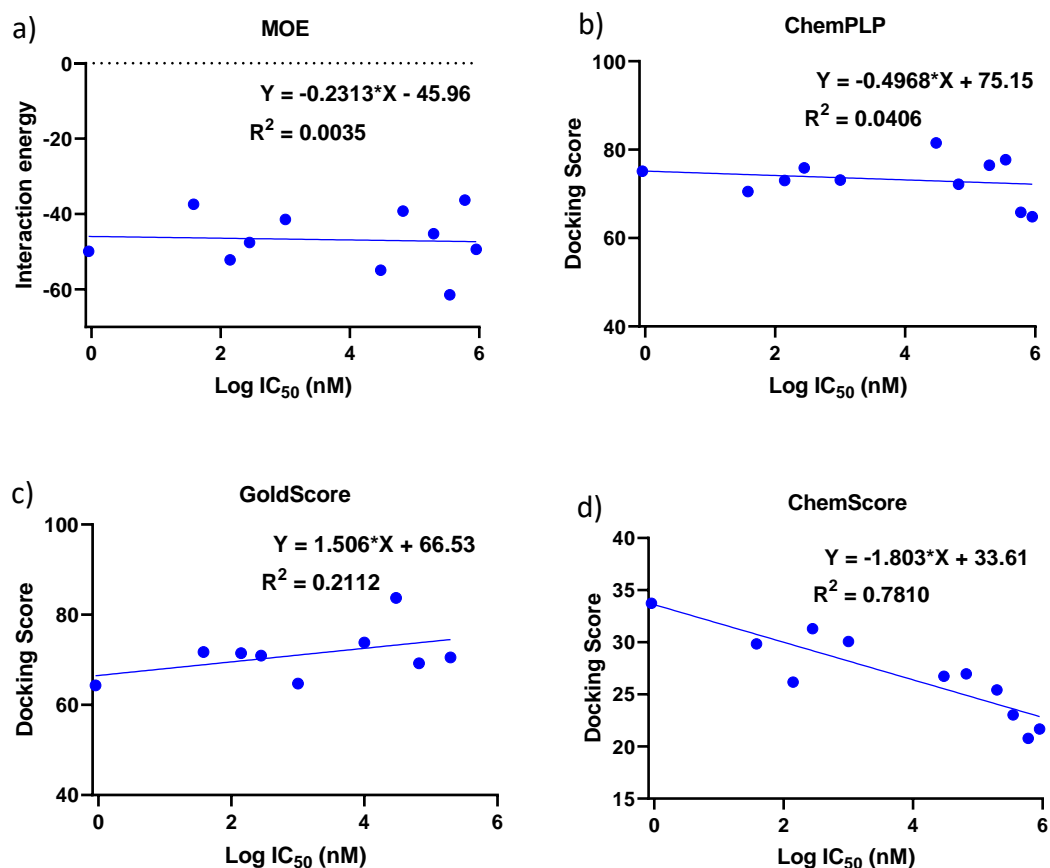


Figure 3.9: Interaction energy/Docking score correlation with experimental IC_{50} values of 11 gyRB inhibitors retrieved from literature.

In the case of the GOLD scoring functions, the docking score is a positive number, with the highest value corresponding to the highest predicted affinity. In a similar way to MOE, the graphs relative to ChemPLP and GoldScore scoring functions did not give meaningful correlations, again with R^2 close to 0 or with an inverted correlation, respectively. On the other hand, ChemScore (Figure 3.9d) gave a meaningful correlation, with a $R^2 = 0.78$. In other words, the most active compounds (with lower values of experimental log IC_{50}) gave higher scores than inactive compounds (with higher log IC_{50} values). This scoring function was used for the screening of the NCI database and a

database of *de novo* designed compounds, in combination with the previously developed pharmacophore models. These studies are described in the next subsections.

3.1.3 – Screening of the NCI database

From the multiple public virtual databases available, we selected the National Cancer Institute (NCI) database,¹⁹ which contains over 265,000 compounds. Although there are bigger databases, like ZINC (over 230 million purchasable compounds),²⁰ the NCI database allows for a quicker and cheaper (compounds are freely provided to researchers) initial screening effort. During the screening process, we applied some restrictions based on the most desirable drug-like properties, given by both Lipinski and Veber rules, and we defined three criteria: i) molecular weight below 500 Da; ii) topological polar surface area (TPSA) between 40-120 Å²; iii) number of rotatable bonds lower than 10. Given that the objective of this screening is to find active molecules that can in the future be synthesized and further modified to optimize their activity and properties, it is important to limit the molecular weight to 500 Da. In addition, both Veber rules relative to the maximum polar surface area and number of rotatable bonds are good indicators of membrane permeation and oral bioavailability. In this sense, the polar surface area has shown better correlation than logP values.²¹

The whole NCI database was screened using both pharmacophores A and B. Under the aforementioned conditions, the initial screening with pharmacophore A retrieved 1649 hits. This was followed by a second screening with pharmacophore B, which yielded 941 compounds. As was demonstrated previously (Figure 3.7), it is expected that the combination of both pharmacophores (A + B) increases the relative percentage of true active molecules relative to false positives. This is preferable, even if it results in some true actives being excluded during the screening process.

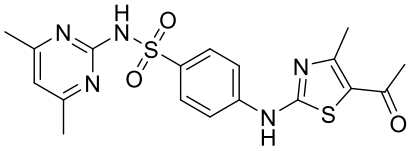
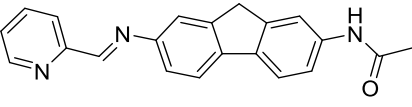
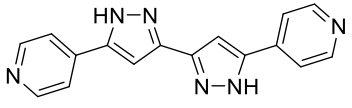
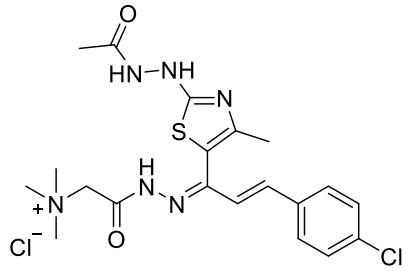
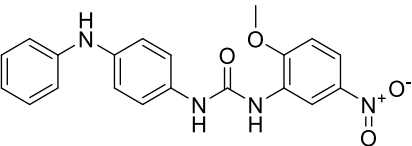
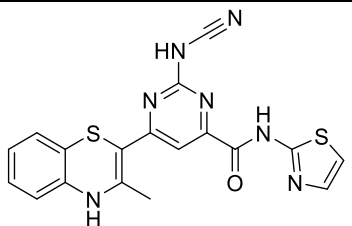
Next, it was important to identify compounds with problematic functional groups (structural alerts), potential covalent inhibitors and pan-assay interference compounds (PAINS), using the online tool FAFDrugs4.²² Structural alerts are responsible for around 80% of the toxicity in clinically approved drugs, with the majority being caused by the production of toxic metabolites.²³ Some examples of these groups are 5-membered ring

heterocycles (pyrrole, thiophene, thiazole, furan) and benzene derivatives (nitrobenzene, phenol, catechol, p-hydroxyanilines, arylacetic acids).²⁴

Relatively to the covalent inhibitors, it is worth noting that there are many clinically approved covalent inhibitors with low to no safety concerns.²⁵ Although β -lactams are the prime example of the successful use of covalent inhibitors in antimicrobial therapy, there is an increased risk of generalized toxicity. Indeed, penicillins are known to be more immunogenic (allergenic) than other antibiotics, a feature that may be attributed to its covalent inhibition mechanism.²⁶ Taking into account the fact that the known inhibitors for gyrB present in the actives dataset act through a competitive and reversible mechanism, we decided to remove covalent inhibitors from the hit list. In addition, we also excluded PAINS, which are compounds with a promiscuous activity, giving false positives in biological assays. In other words, they can interact non-specifically with various targets, through mechanisms such as chemical aggregation, chelation, singlet oxygen production, redox activity, membrane disruption, among other non-selective reactions with proteins.²⁷

Overall, from the 941 pharmacophore hits, 34 were considered duplicates and discarded, 332 possessed structural alerts, 251 were identified as covalent inhibitors, and 156 were considered as potential PAINS. Among them are reactive electrophilic groups such as alkyl halides, thioketones, Michael acceptors, aliphatic ketones and quinones. There are other groups such as nitro, anthracene, phenol and *p*-hydroxyaniline, which are known to undergo chemical modifications *in vivo*, producing metabolites with high toxicity. It is worth noting that, of all compounds with the mentioned problematic groups, only those that were considered of high risk were discarded, while low risk compounds were maintained in the dataset. Overall, this selection process resulted in the exclusion of 506 compounds, decreasing the hit list to 435 compounds. To further refine the NCI compound search, we carried out docking studies using the best scoring function (ChemScore function; Figure 3.9d). The structures of the best scoring compounds are presented in Table 3.2. These compounds were acquired from the NCI database for biological studies (*E. coli* gyrase inhibition and MIC studies), the results of which will be discussed in section 3.3.

Table 3.2: Compounds acquired from the NCI database, aiming biological studies, and corresponding docking scores.

#	Structure/ NCI identification	Mw (Da)	Docking score (ChemScore)
1	 659383 (NCI-1)	418	32.2
2	 90716 (NCI-2)	327	31.0
3	 371704 (NCI-3)	288	30.5
4	 647083 (NCI-4)	485	29.9
5	 213814 (NCI-5)	378	29.1
6	 624478 (NCI-6)	407	29.0

3.1.4 – De novo design and screening of a virtual library

Based on the previously developed pharmacophore models and on the structures of known active ligands, it is possible to automatically generate derivatives of these molecules in MOE, in a process called *de novo* design. This allows the construction

of smaller, more focused, libraries of theoretical compounds that are not necessarily present in any purchasable chemical database. However, this prevents facile access to hit molecules from the computational models, as they have to be synthesized before proceeding to the biological studies.

Taking into account some of the structural motifs present in known inhibitors of gyrB,^{3,6-7} namely benzo-fused heteroaromatic rings, we chose the benzimidazole ring as a scaffold for the design of potential new gyrB inhibitors (Figure 3.10).

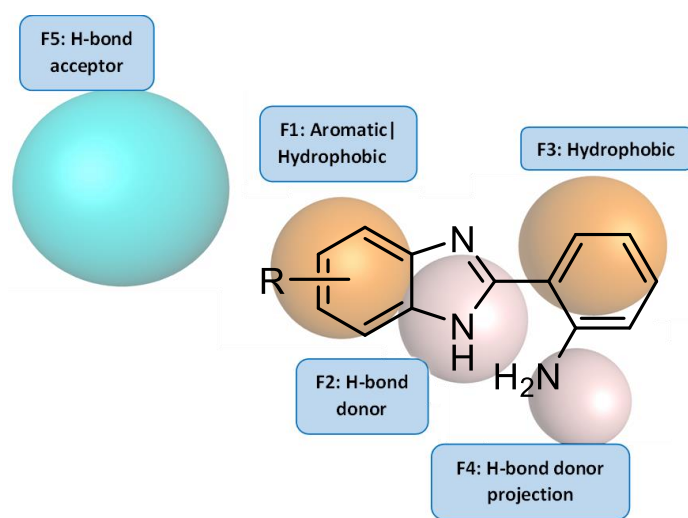
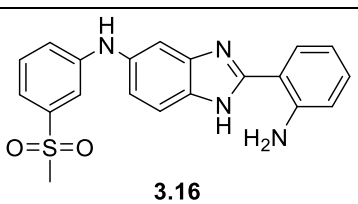
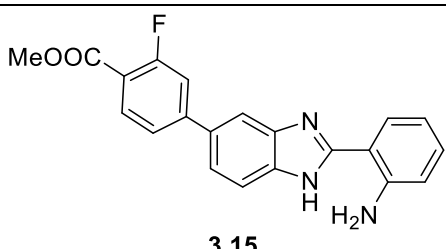
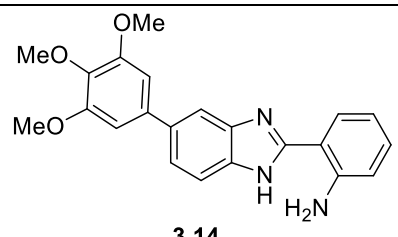


Figure 3.10: Overlap of the base scaffold 5(6)-substituted-2-(2-aminophenyl)-1H-benzimidazole with the pharmacophore model developed.

According to the previously developed pharmacophore model (Unified Scheme, Figure 3.3b), the core benzimidazole ring fulfills two important structural features: F1: Aromatic|Hydrophobic and F2: H-bond acceptor. Then, we placed a phenyl group at the benzimidazole 2-position (between both nitrogen atoms), containing an amine in the *ortho* position. This fulfills two additional pharmacophore criteria: F3: Hydrophobic and F4: H-bond donor projection. Using the scaffold in Figure 3.10 as starting point, we proceeded with the virtual design of chemical derivatives with different substituents in the 5(6)-position (denoted by R in the figure), in order to fulfill the last structural feature (F5: H-bond acceptor). This was done in MOE using the tool “Add group to ligand”, where a number of different substituents are added, in accordance with some user-defined restrictions. In this case, the following restrictions were applied: MW < 500 Da, TPSA < 40-120 Å² and number of rotatable bonds < 10. In total, 23,832 unique structures were generated. This virtual library underwent pharmacophore (A + B models) and docking

(ChemScore function) screening, and the most promising compounds obtained are presented in Table 3.3. It is worth noting that the selection of these molecules was based not only in the docking score, but also in their synthetic feasibility. Its total synthesis and chemical characterization are described in section 3.2.

Table 3.3: Structures and corresponding docking score of computationally designed 5(6)-substituted-2-(2-aminophenyl)-1*H*-benzimidazole derivatives, selected for chemical synthesis.

#	Structure	Mw (Da)	Docking score (ChemScore)
1	 <p style="text-align: center;">3.16</p>	378	33.7
2	 <p style="text-align: center;">3.15</p>	361	28.7
3	 <p style="text-align: center;">3.14</p>	375	27.5

3.2 – Synthesis and modulation of 2,5(6)-substituted benzimidazole derivatives

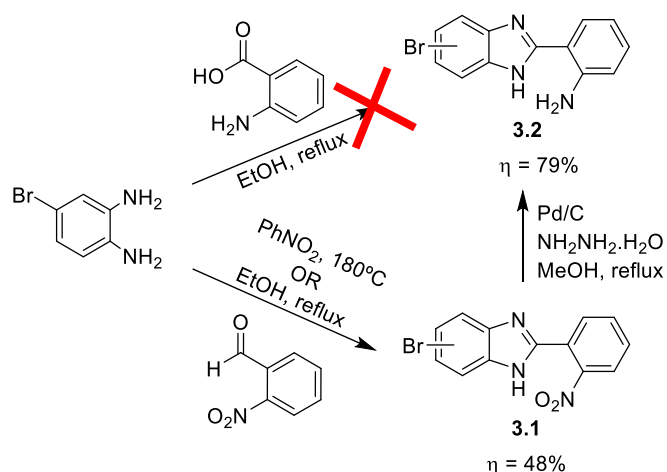
From a synthetic point of view, the chosen 2,5(6)-substituted benzimidazole scaffold is a good starting point due to the easiness in obtaining and modulating 2-arylbenzimidazoles.²⁸⁻³⁰ In order to allow easy manipulation of the desired 5(6) position of the benzimidazole ring, it was important to start with a set of reagents containing transformable functional groups to further yield chemically distinct derivatives. To this effect, we started with a brominated aromatic *ortho*-diamine (4-bromo-1,2-

diaminobenzene; Scheme 3.2) as one of the condensation pairs for this reaction. Bromoarenes offer numerous possibilities for modulation and are one of the most suited substrates for palladium-catalyzed reactions, due to their: i) low C-Br bond dissociation energy; ii) higher availability and lower cost than the corresponding iodo-arenes; iii) higher comparable efficiency in Buchwald-Hartwig amination.

Synthesis of the core benzimidazole ring

The synthesis of 2-arylbenzimidazoles is generally carried by condensation of the *ortho*-diamine with carbonyl groups, being carboxylic acids and aldehydes the most commonly used.³¹ To obtain the desired base benzimidazole ring **3.2**, two reaction attempts were carried out using different condensation partners to the *ortho*-diamine (Scheme 3.2).

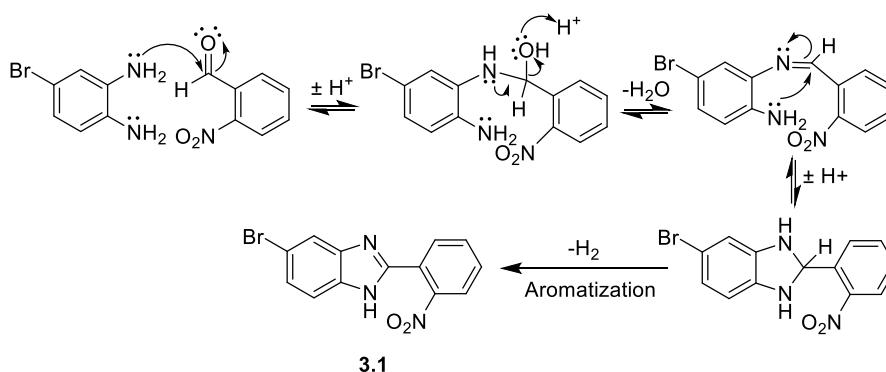
As a first approach, the condensation of 4-bromo-1,2-diaminobenzene with anthranilic acid (2-aminobenzoic acid) was attempted, following a protocol previously reported using 1,2-diaminobenzene.³² This reaction was carried out in ethanol at reflux temperature for 24 h. However, we were unable to obtain the desired product, and only the starting materials were recovered. Changing to a higher boiling solvent like 1,4-dioxane and carrying the reaction at reflux temperature for 24 h gave the same outcome.



Scheme 3.2: Methodology used in the synthesis of 2-(2-aminophenyl)-5(6)-bromo-1H-benzimidazole (**3.2**).

The presence of the strong electron donor amino group in the anthranilic acid triggers two undesirable effects: i) decreased reactivity of the carboxylic group; ii) possibility of self-polymerization. Based on these results, we offer no justification as to how the authors of the aforementioned publication have successfully carried out this reaction in such mild conditions. Indeed, the only difference in the structure of the reagents is the presence of a bromine in the diamine, which should not yield such a pronounced difference in reactivity.

As a second approach, we substituted the anthranilic acid for the more reactive 2-nitrobenzaldehyde. It is expected that the inherent higher reactivity of benzaldehyde coupled with the electron withdrawing capabilities of the nitro group improve the outcome of the reaction. In this case, the nitro group can be regarded as a form of “protected amine” as it can then be readily converted into the desired amine group using mild reaction conditions, such as catalytic hydrogenation. The synthesis of the nitro derivative **3.1** (Scheme 3.2) was carried out by mixing equimolar amounts of the diamine and the aldehyde in nitrobenzene, and the reaction was left at 180 °C for 8 h. This procedure was based on a method used for the synthesis of bis-benzimidazoles³³ and the rationale for the use of nitrobenzene is its oxidative capability at high temperatures.³⁴ The reaction mechanism (Scheme 3.3) involves the formation of an imine through nucleophilic attack of the amine to the aldehyde, followed by the nucleophilic attack of the second amine to yield a benzimidazoline or 2,3-dihydro-1*H*-benzimidazole.



Scheme 3.3: Simplified reaction mechanism proposal involved in the formation of compound **3.1**.

Nitrobenzene plays a role in the last step as it requires the oxidation of this intermediate to the final benzimidazole ring. Naturally, this aromatization final step can be regarded as the driving force of the product formation, as the intermediate reaction steps are reversible, especially the imine formation step as it can be promptly hydrolyzed back to the starting materials. Despite our best attempts, it was not possible to induce the product precipitation from the reaction mixture and thus, the nitrobenzene was distilled under reduced pressure. The product was purified by column chromatography using silica gel as stationary phase and dichloromethane as first eluent (to remove the residual nitrobenzene) followed by a gradient elution with a mixture of dichloromethane and ethyl acetate (100:1 to 20:1). The product **3.1** was obtained in 48% isolated yield. The moderate yield can be explained by the instability of the diamine at high temperatures, as it is also prone to oxidation, and also the formation of black colored polymers that are retained at the top of the silica gel column.

The product was fully characterized by 1D and 2D NMR spectroscopy and mass spectrometry. The most relevant NMR spectra for the assignment of all ^1H and ^{13}C resonances are presented in Figures 3.11 and 3.12. Before proceeding to the assignment of the spectra, it should be noted that, due to tautomeric equilibrium (Figure 3.11a), the numbering for each tautomer species varies, since numbering priority must be given to the $-\text{NH}$ of the imidazole portion of the ring. Therefore, the ^1H and ^{13}C assignment are given for both tautomers, separated by a "/" (e.g. $\text{H}_{4/7}$, $\text{H}_{7/4}$, $\text{H}_{6/5}$). A very broad singlet corresponding to the $-\text{NH}$ proton at 12.5 - 14.0 ppm can be observed, a consequence of a rapid exchange due to tautomerism. The aromatic protons' resonances can be easily assigned taking into account the chemical environment and the coupling constants of each signal, even though these correlations were confirmed by ^1H - ^1H COSY (not shown). This molecule possesses two independent aromatic spin systems, composed of three and four resonances with different coupling patterns. The coupling pattern pertaining to the core benzimidazole ring can be easily identified by three resonances consisting of: a doublet with a ^4J type coupling (7.82 ppm, $J = 2.0$ Hz, $\text{H}_{4/7}$); a doublet with a ^3J type coupling (7.59 ppm, $J = 8.5$ Hz, $\text{H}_{7/4}$) and a doublet of doublets with both a ^3J and a ^4J coupling (7.39 ppm, $J = 8.5, 2.0$ Hz, $\text{H}_{6/5}$). Expectedly, the resonances concerning the nitrophenyl group are shifted to a lower field due to the electron-withdrawing nature of the nitro group. The two doublets of doublets at 8.05 ppm and 7.97 ppm can be

attributed to $H_{3'}$ and to $H_{6'}$, which are *ortho* and *meta* in respect to the nitro group. Following the same logic, the two triple doublets at 7.88 and 7.78 ppm correspond to $H_{5'}$ and $H_{4'}$, which are *para* and *meta* to the nitro group, respectively.

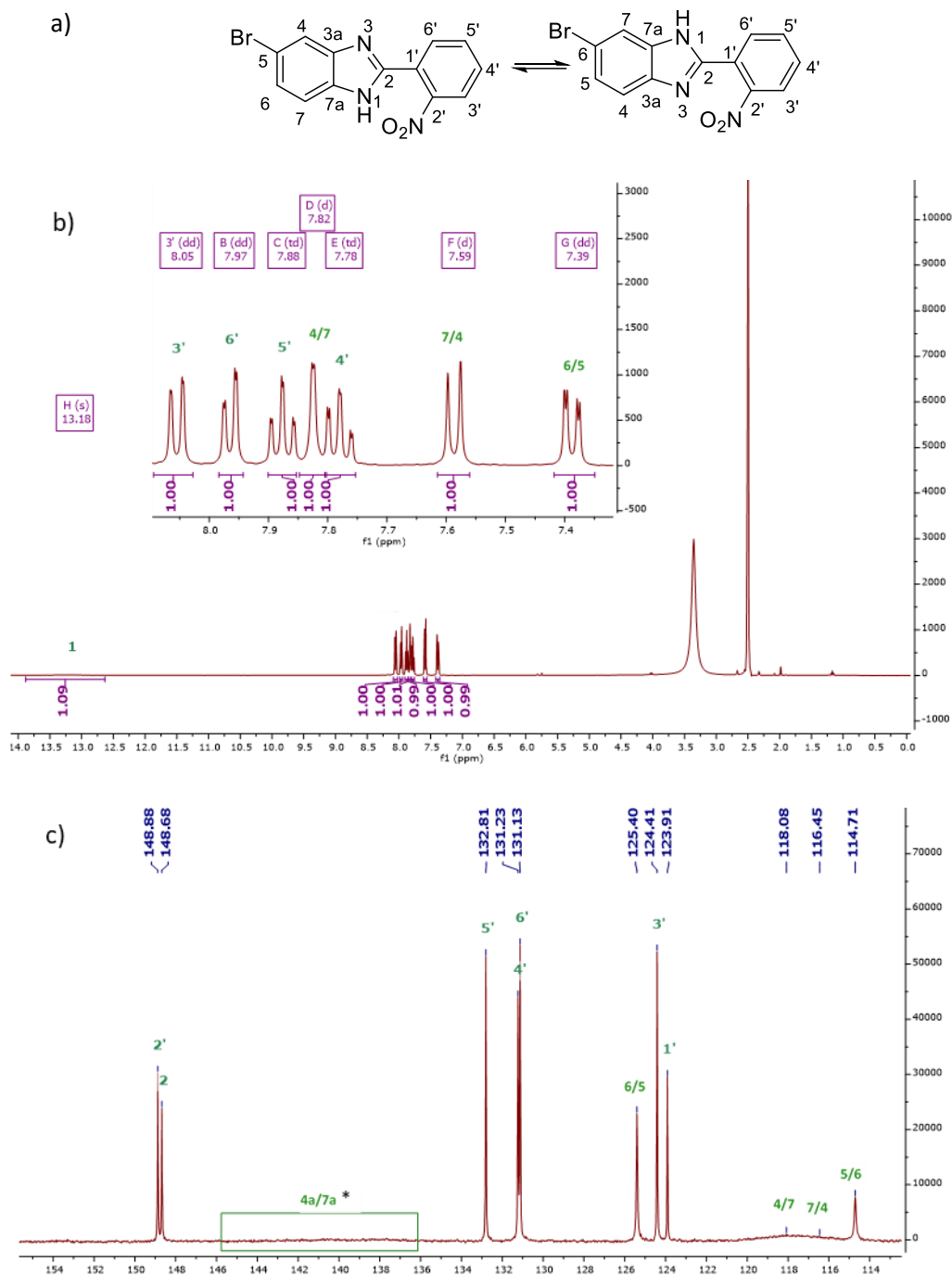
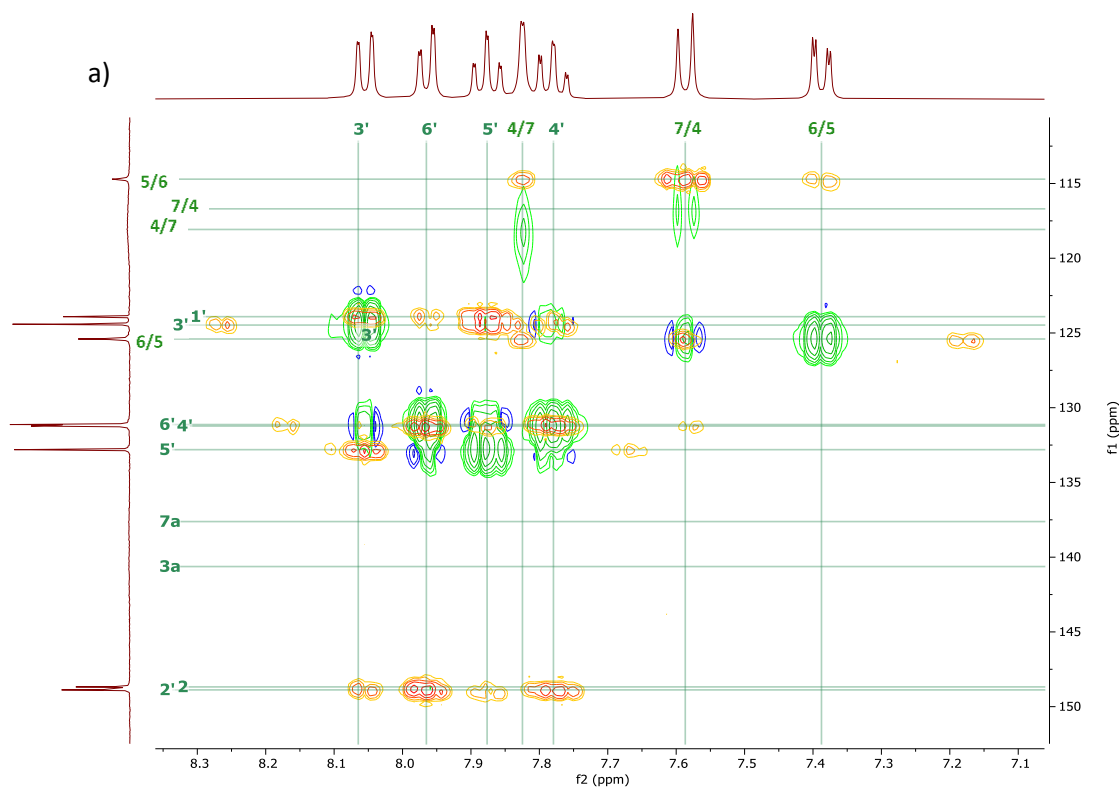


Figure 3.11: a) Tautomeric equilibrium of compound **3.1** and correspondent atom numbering; b) ^1H NMR of **3.1** in DMSO-d_6 c) ^{13}C NMR of **3.1** in DMSO-d_6 . *approximate resonance position predicted by MestreNova software.



b)

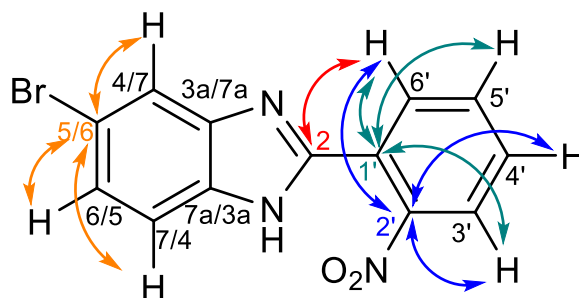


Figure 3.12: a) Overlap of **3.1** ^1H - ^{13}C HSQC (green) with ^1H - ^{13}C HMBC (orange), in DMSO-d_6 ; b) main HMBC correlations used for resonance assignment.

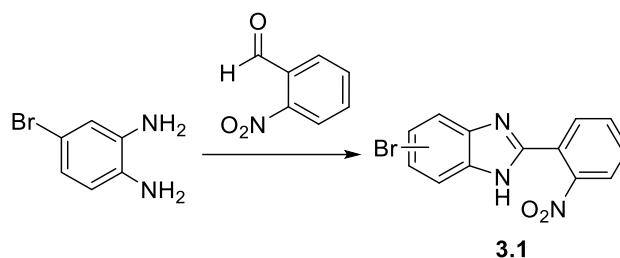
Relatively to the ^{13}C resonances, the dynamic process associated with tautomerism is even more prevalent and severely hinders the visualization and assignment of all signals. It is worth mentioning that the portion of the molecule that, by symmetry, is exposed to the same chemical environment independently of the tautomer present (C_2 and the nitrophenyl ring), possesses sharp carbon signals with the expected relative intensities. All signals related to $-\text{CH}-$ carbons could be assigned based on the HSQC cross-peaks. Since the $-\text{CH}-$ carbons that compose the benzimidazole ring are susceptible to chemical shift changes due to tautomerism (C_4 to C_7), they possess signals that are broader than usual or even indistinguishable from the baseline.

The $\underline{C}_{6/5}$ resonance could be identified in the 1D ^{13}C NMR spectrum and was assigned based on the HSQC cross-peak with $\underline{H}_{6/5}$. However, $\underline{C}_{4/7}$ (118.08 ppm) and $\underline{C}_{7/4}$ (116.45 ppm) could not even be observed in a 1D ^{13}C NMR spectrum, which means that their chemical shifts are heavily influenced by the different tautomers, resulting in signals so broad that can be hardly distinguished from the baseline. Taking advantage of the higher sensitivity of the HSQC experiment, we can observe the cross-peaks $\underline{H}_{4/7}/\underline{C}_{4/7}$ and $\underline{H}_{7/4}/\underline{C}_{7/4}$ and therefore, it's possible to pinpoint the mean chemical shifts of both of these carbons. The assignment of the quaternary carbons was carried out using the HMBC correlations. In short, \underline{C}_2 (148.68 ppm) possesses only one cross-peak with \underline{H}_6 ; $\underline{C}_{2'}$ (148.88 ppm) and $\underline{C}_{1'}$ (123.21 ppm) both possess cross-peaks with protons from the nitrophenyl group, although $\underline{C}_{2'}$ is predictably shifted to lower field due to being *ipso* to the nitro group. Relatively to the quaternary carbons of the benzene portion of benzimidazole ($\underline{C}_{3a/7a}$, $\underline{C}_{7a/3a}$ and $\underline{C}_{5/4}$) it is expected that carbon $\underline{C}_{5/4}$ (114.71 ppm) possesses a lower chemical shift given that it is the only one not linked to nitrogen and suffers a shielding heavy-atom effect due to being directly linked to bromine. Despite our best attempts, it was not possible to identify cross-peaks in HMBC to identify the position of carbons $\underline{C}_{3a/7a}$ and $\underline{C}_{7a/3a}$. This is likely due to: i) lower sensitivity of quaternary carbons and HMBC experiments in general, when compared to HSQC; ii) an even greater influence of tautomerism on the chemical shift fluctuation, which is expected given that they will be alternatively linked to either a sp^3 or a sp^2 nitrogen.

The condensation reaction to obtain product **3.1** was optimized, according to Table 3.4. By exchanging the solvent from nitrobenzene (entry 1) to ethanol (entry 2) and carrying the reaction at reflux temperature (80 °C), during 3 h, we found that the product could be obtained in similar yield. Indeed, this means that oxidation can proceed with atmospheric oxygen, without the need of any additional oxidative species. Despite no obvious advantage regarding improved yields, this methodology offers two considerable conveniences: i) the use of a lower boiling point solvent, which can be easily evaporated; ii) different impurity profile, with lower prevalence of impurities with similar polarity to the product, allowing swifter and easier purification by silica gel chromatography. In addition, the reaction also proceeded well at room temperature (entry 3), albeit in 6 h, at similar yield (50%). Furthermore, the addition of Montmorillonite K10 as a heterogeneous acidic clay catalyst (entries 4 and 5) to promote

activation of the carbonyl group increased both the reproducibility of the reaction and the final isolated yield (up to 62% when performed at room temperature), while also slightly reducing the reaction time.

Table 3.4: Optimization of the reaction conditions for the formation of **3.1** through the condensation reaction between 4-bromo-1,2-diaminobenzene and 2-nitrobenzaldehyde.^(a)



#	T (°C)	Time (h)	Solvent	Catalyst	Isolated yield (%)
1	180	8	Nitrobenzene	-	48
2	80	3	Ethanol	-	47
3	25	6	Ethanol	-	50
4	25	4	Ethanol	Montmorillonite K10	62
5	80	2	Ethanol	Montmorillonite K10	54

^(a) Typical reaction conditions: 4-bromo-1,2-diaminobenzene (1.1 mmol), 2-nitrobenzaldehyde (1.2 mmol) and the catalyst (20 mg) were mixed in the solvent (3 mL) and heated to the designated temperature, over a variable time period.

Since **3.1** was the substrate for all the synthesis leading up to the obtaining of the designed compounds (Table 3.3), its synthesis was transposed into a multi-gram scale (up to 5 g). This molecule fulfils three out of five pharmacophore features (Figure 3.13) and is thus a good starting material for nitro reduction and further modifications in the 5(6)- position of the benzimidazole ring.

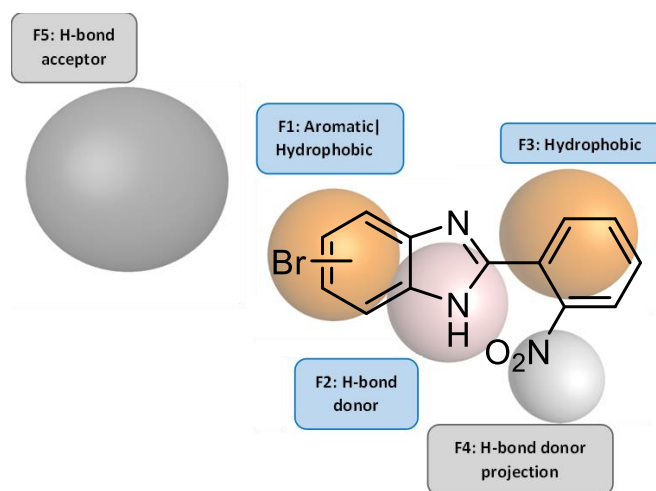


Figure 3.13: Overlap of compound **3.1** with the developed pharmacophore model, highlighting the three features (F1-F3) that it possesses and the two features that need to be inserted (F4 and F5).

Pd-Catalyzed nitro reduction

Our initial strategy involved the reduction of the nitro group of **3.1** to the corresponding amine and thus to obtain the originally intended *2-ortho*-aniline benzimidazole **3.2**, according to Scheme 3.2. Of the wide range of possible reaction conditions to obtain the desired product, we chose a catalytic method and thus avoid the more severe classic conditions, involving Fe or Zn in acidic media. One of the possibilities would be to utilize Pd/H₂, however, it is well known that this combination can react with bromine and promote dehalogenation.³⁵ We selected a milder method that employed hydrazine monohydrate as a substitute for hydrogen gas.³⁶ This reaction, if carried out in an open vessel, where hydrogen pressure is at most 1 atm, selectivity promotes the reduction of nitro groups over dehalogenation, which only occurs in closed vessels, where higher H₂ pressures would be achieved. In a typical experiment, the reagent **3.1** was dissolved in methanol and Pd/C (5%) and hydrazine monohydrate were added. The reaction was carried out at reflux temperature for 30 min. The product **3.2** was easily purified by column chromatography using ethyl acetate as eluent and was isolated in 79% yield. This compound fulfils four features, with only “F5: H-bond acceptor” missing, which will be introduced *via* functionalization of the benzimidazole 5(6) position (Figure 3.14).

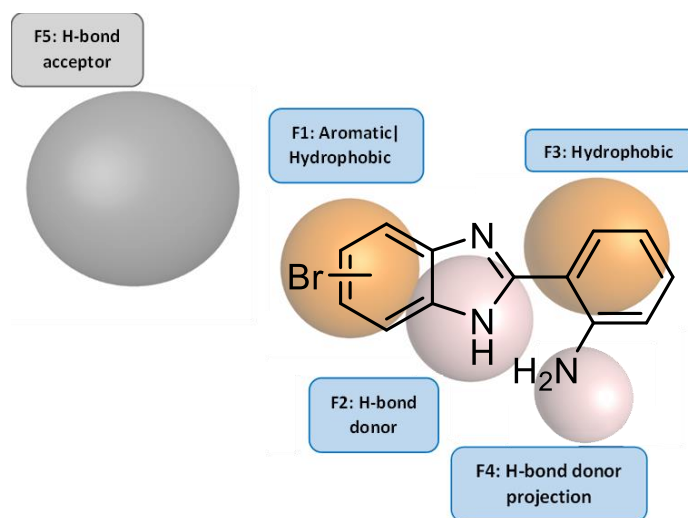
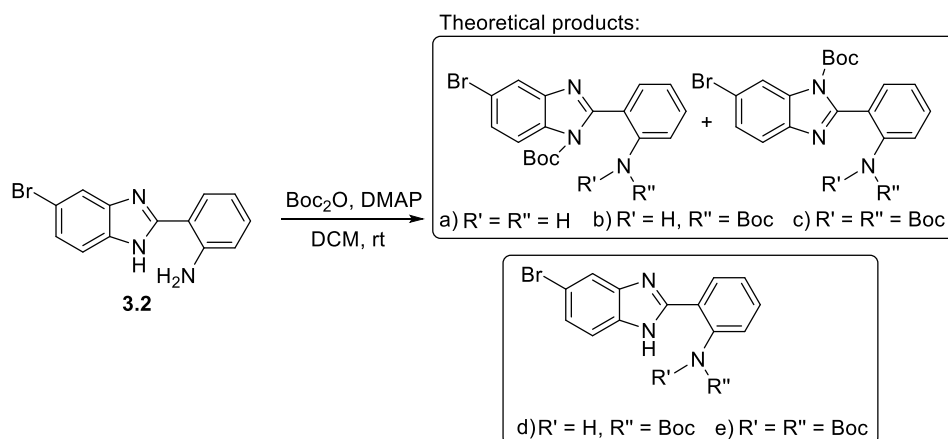


Figure 3.14: Overlap of compound **3.2** with the developed pharmacophore model, highlighting the four features (F1-F4) that it possesses and the feature that need to be inserted (F5).

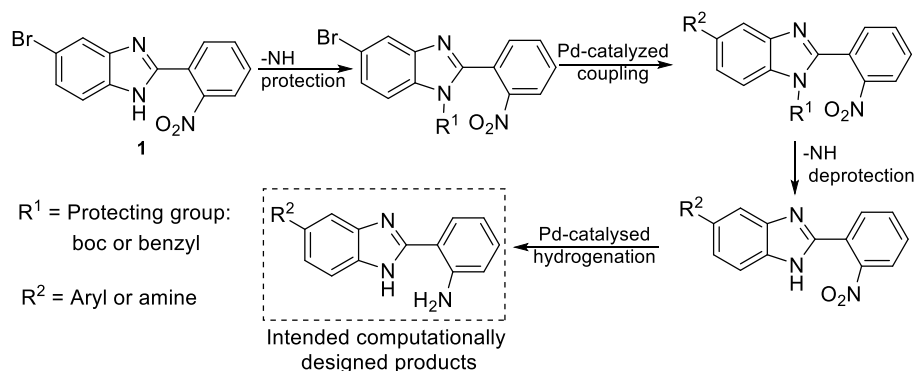
Pd-Catalyzed couplings for 5(6)-benzimidazole functionalization

Taking into account the initially proposed goal to functionalize the benzimidazole at the 5(6) position through Pd-catalyzed reactions, it was necessary to protect both the interior NH group of the benzimidazole ring as well as the aniline -NH₂ group. Given its simplicity and straightforwardness in both protection and deprotection reactions, we chose the boc protecting group. The reaction was carried out by dissolving **3.2**, di-*tert*-butyl dicarbonate and a catalytic amount of DMAP (4-(dimethylamino)pyridine) in dichloromethane. The reaction was left stirring for several hours and the product formation was monitored by TLC. Despite our best attempts, we could not promote the formation of a single reaction product, as multiple TLC spots could be visible, even after the addition of more di-*tert*-butyl dicarbonate and DMAP. The several formed products can be explained by two factors: i) up to three boc groups can react with the molecule; ii) the protection of the interior NH of the benzimidazole ring renders two different constitutional isomers (Scheme 3.4).



Scheme 3.4: Theoretical product mixture that can be obtained by protection of the -NH groups of **3.2**.

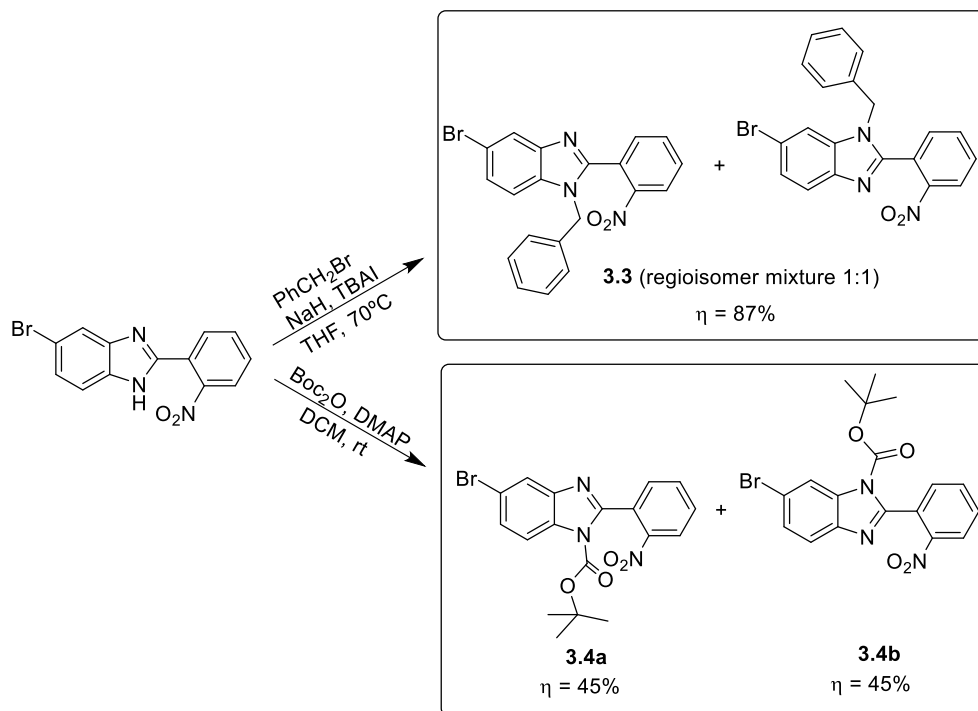
Due to these setbacks, we decided to optimize our synthetic route and proceed first with the benzimidazole N-H protection, followed by the functionalization at the 5(6) position, and finally perform the nitro reduction in the last step. Scheme 3.5 summarizes the general synthetic pathway.



Scheme 3.5: General overview of the synthetic route utilized for the preparation of the intended computationally designed products based on the 2,5(6)-substituted benzimidazole scaffold.

We decided to perform the protection of the -NH group of the benzimidazole ring because i) there is prior knowledge that benzimidazoles are more amenable to Pd-catalyzed couplings when the heterocyclic N-H is protected³⁷ and ii) the aromatic benzimidazole -NH could, in theory, compete with the intended coupling partner during amination reactions. Hence, we selected two possible protecting groups that are known to be stable in the basic conditions required for the intended Pd-catalyzed couplings:

benzyl and boc groups. The corresponding protection reactions were carried out for both groups and are depicted in Scheme 3.6.



Scheme 3.6: Synthesis of benzimidazole *N*-boc (**3.3** as 1:1 mixture of regioisomers) and *N*-benzyl (**3.4a** and **3.4b**, isolated regioisomers) protected derivatives.

The protection reactions involving the synthesis of **3.3** was adapted from methods previously reported.³⁷ In short, to a solution of the starting material **3.1**, dissolved in dry THF at 0 °C and in an inert atmosphere, NaH (60% in mineral oil) was added, followed by benzyl bromide and a catalytic amount of tetra-*N*-butylammonium iodide (TBAI). The reaction was heated to reflux temperature (70 °C) for 2 h. After completion, the reaction was quenched with methanol and the product **3.3** was purified by column chromatography, obtained in 87% isolated yield, as a 1:1 mixture of two regioisomers. Given the tautomeric nature of the benzimidazole ring, both nitrogens could react, as they can interchange between a non-hydrogen bearing (sp^2) state and a hydrogen bearing (sp^3) state, being the sp^3 nitrogen the one that participates in the reaction. Consequently, this led to the formation of 5-bromo-*N*-protected-1*H*-benzimidazoles and 6-bromo-*N*-protected-benzimidazoles. For the protection with the boc group, the reaction was carried out in DCM, for 24h at room temperature, with addition of di-*tert*-butyl dicarbonate and DMAP as base. After a standard work-up, the

products were purified through column chromatography in silica gel using hexane/ethyl acetate 4:1 as eluent. Contrary to the previous case, the polarity of both isomers was sufficiently different to allow their total chromatographic separation and both 5-bromo (**3.4a**) and 6-bromo regioisomers (**3.4b**) were isolated in 45% yield each (90% combined yield).

Given that the *N*-protection removes the dynamic process associated with tautomerism, both isolated isomers gave well-defined and resolved ^1H and ^{13}C NMR spectra. In Figure 3.15, the full assignment is shown for the 5-bromo regioisomer (**3.4a**). Here, unlike what was shown for **3.1**, all proton and carbon resonances are presented as sharp peaks, which facilitates their interpretation. The proton resonances were assigned in accordance with the same principles that were used for compound **3.1**. Relatively to the ^{13}C NMR spectrum, the assignment of the carbons directly bonded to hydrogens was done using the HSQC and the quaternary carbons with HMBC. Of particular interest are the resonances of carbons $\underline{\text{C}}_{3\text{a}}$ and $\underline{\text{C}}_{7\text{a}}$, which could not be observed in compound **3.1** due to tautomerism, and here clearly demonstrate a significant chemical shift difference between them. In order to correctly assign each regioisomer, a ^1H - ^1H NOESY experiment was performed on **3.4a** (Figure 3.16a) and **3.4b** (Figure 3.16b). Here, given the rigidity of the benzimidazole ring, it is expected that each regioisomer presents a different correlation between the $-\text{CH}_3$ of the boc protecting group ($\underline{\text{H}}_{3''}$, $\underline{\text{H}}_{4''}$, $\underline{\text{H}}_{5''}$) and the protons of the benzimidazole ring. In the case of isomer **3.4a**, a correlation was observed with $\underline{\text{H}}_7$, which is *meta* relative to the bromine atom (Figure 3.16a) and in the case of isomer **3.4b** a correlation was observed with $\underline{\text{H}}_7$, which is *ortho* to the bromine atom (Figure 3.16b). Of the two protected benzimidazole derivatives obtained, we first chose **3.3** to continue the synthetic route. Since the final step of the synthetic route involves a catalytic hydrogenation of the nitro group, the benzyl group protected benzimidazole offers a synthetic advantage, in the sense that it can be deprotected in the same step. Given the difficulty in separating the two isomers of **3.3**, and since both yield the same compound with tautomeric properties after deprotection, all described reactions were pursued with the 1:1 mixture of isomers.

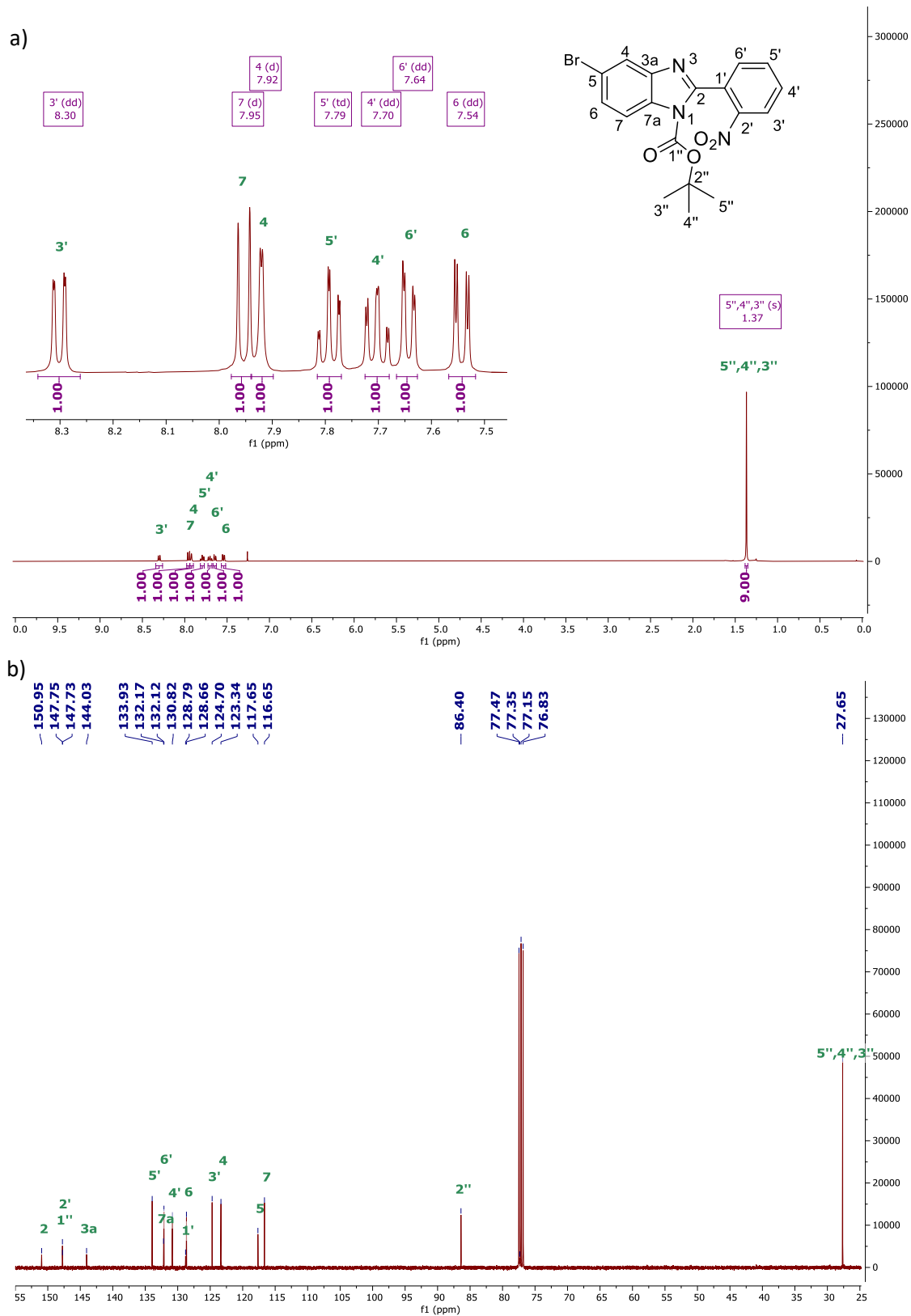


Figure 3.15: 1D NMR spectra of compound **3.4a** performed in CDCl₃: a) ^1H ; b) ^{13}C .

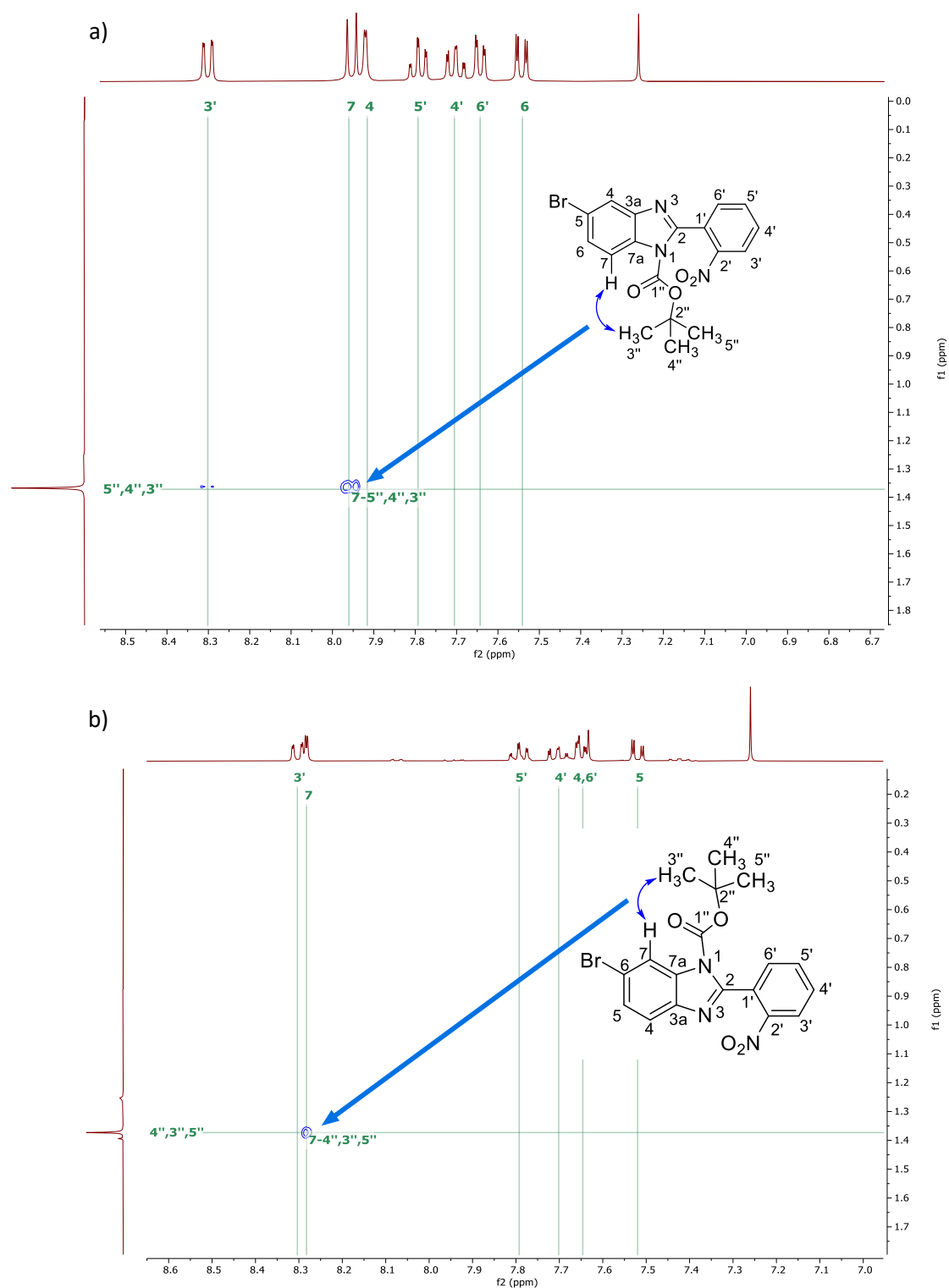
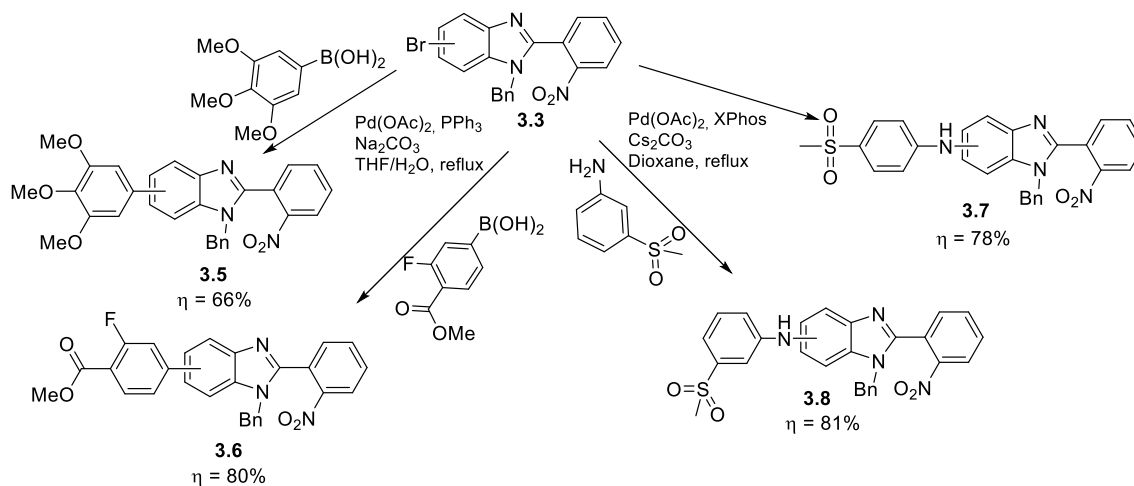


Figure 3.16: ^1H - ^1H NOESY NMR spectra performed in CDCl_3 of a) **3.4a**; b) **3.4b**.

Scheme 3.7 contains an overview of the attempted Pd-catalyzed reactions, with the optimized reaction conditions and corresponding yields. Starting from compound **3.3**, four new products were obtained (**3.5** - **3.8**) through Suzuki-Miyaura and Buchwald-Hartwig reactions. Details on each reaction are given in the next sections.



Scheme 3.7: Pd-catalyzed reactions involving the 1:1 regioisomer mixture of benzyl protected benzimidazole **3.3**.

Suzuki-Miyaura Pd-coupling reactions

Compounds **3.5** and **3.6** were obtained through a Suzuki-Miyaura Pd-coupling reaction, which involves the reaction between an aryl halide (or triflate) with an organoboron species, using a palladium catalyst and a base. In accordance with the computational studies (section 3.1), we proceeded with the synthesis of two molecules that could be obtained by the modulation of the benzimidazole 5(6) position with commercially available boronic acids, containing hydrogen bond acceptors.

In organometallic reactions, oxygen could be detrimental to the catalyst's efficiency, slowing down reactions and increasing the formation of side products. In the case of Suzuki reactions, besides the phosphine ligands being prone to oxidation, oxygen can interact with intermediate Pd(0) species of the catalytic cycle, forming Pd(II) peroxo complexes that are able to consume two molecules of boronic acid to yield homocoupling side-products.³⁸ For this reason, for all reactions described herein, we used the freeze-pump-thaw method for solvent degassing.

As a first approach, our method employed a mixture of DME/EtOH/H₂O 7.5:7.5:1 as solvent for the reaction. Briefly, the substrate and the boronic acid were dissolved in a mixture of DME/EtOH 1:1 and the solvent was degassed. Then, Pd(OAc)₂ and PPh₃ were added and, after an incubation time of 15 min at room temperature, an aqueous solution of Na₂CO₃ was added and the reaction was heated to 90 °C during 72 h. After the usual work-up procedure followed by purification by column chromatography in

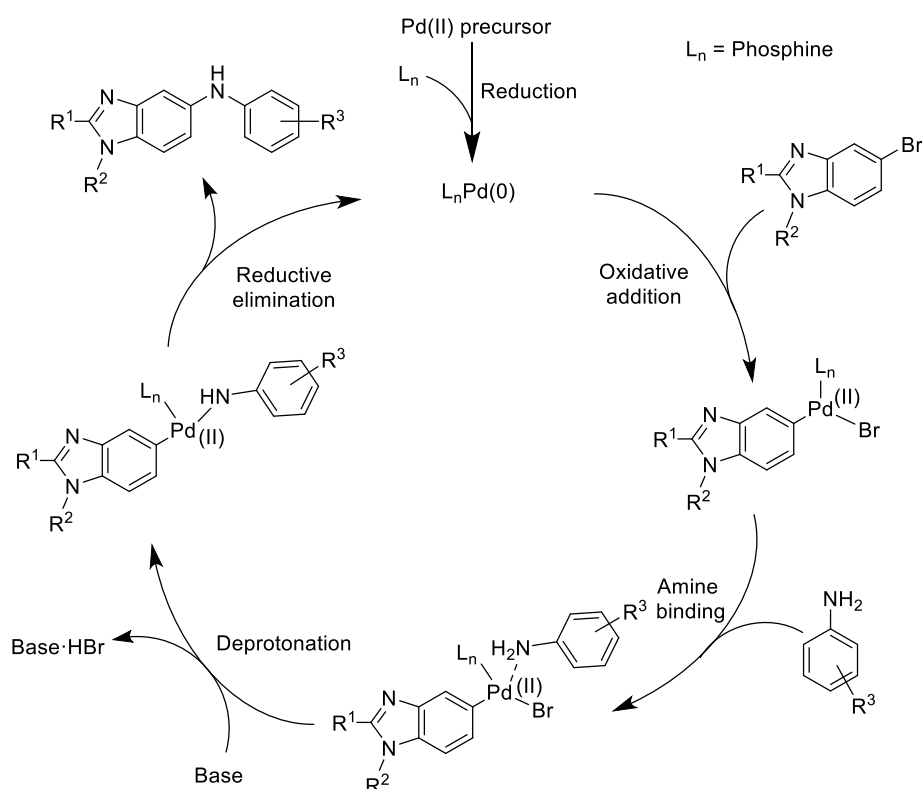
silica gel as stationary phase, compound **3.5** was obtained as a mixture of isomers in 30% yield. Expectedly, we obtained the ethyl ester derivative of compound **3.6** in a similar yield using the same methodology, as result of a heat-promoted transesterification with ethanol, present in the solvent mixture.

Aiming to improve this reaction's outcome, we changed the solvent mixture to THF/H₂O 4:1. After solvent degassing, Pd(OAc)₂, PPh₃ and K₂CO₃ were added and the reaction was carried out at 70 °C. The complete substrate conversion was observed after just 16 h, which constitutes a clear improvement over the previous method. In addition, significantly increased yields were obtained (66% for **3.5** and 80% for **3.6**) and no ester hydrolysis/transesterification was observed. The solvent choice for this reaction seems of particular importance, as an aqueous solution of an inorganic base is a crucial component for the successful transmetallation of the boronic acid in the catalytic cycle,³⁸ and therefore, the use of a water-miscible coordinating co-solvent like THF can aid in keeping all inorganic and organic components in the same phase. Indeed, this mixture of THF/H₂O allowed the dissolution of all components, unlike the DME/EtOH/H₂O mixture, which may have helped to speed-up the reaction, while preventing the formation of undesired side-products.

Pd-catalyzed Buchwald-Hartwig amination

Compounds **3.7** and **3.8** were obtained by a Pd-catalyzed Buchwald-Hartwig amination using 4-(methylsulfonyl)aniline and 3-(methylsulfonyl)aniline in 78 and 81% yields, respectively. Briefly, the catalytic cycle of this reaction (Scheme 3.8) started with activation of Pd(II) precursor through reduction to the catalytically active Pd(0) species. Typically, this occurs through a β-hydride elimination in the amine, when it possesses hydrogens in β position relative to the nitrogen. In the present case, as we are dealing with a primary aniline, reduction of the Pd(II) is purportedly mediated by the phosphine ligand.³⁹ This is followed by coordination with a “n” number of phosphines, yielding the active L_nPd(0) species. In case of bulky phosphines, only one phosphine is coordinated with each metallic center. Then, oxidative addition to the C-Br bond allows substrate activation through formation of a Pd(II) coordination complex with the aryl substrate and bromine. Although this step would be more favorable when using aryl iodides, it is

known that Pd(II) complexes are prone to formation of stable dimers with iodine, when compared with other halogens.⁴⁰ This decreases the overall reactivity of aryl iodides, as dimers inhibit amine binding and continuation of the catalytic cycle. For this specific reason, we designed this synthetic pathway using aryl bromides, as it avoids delicate reaction conditions optimization. After amine binding and deprotonation, with consequent formation of HBr, the final step occurs, consisting of a reductive elimination. Here, a new C-N bond forms, with concomitant reduction of the Pd(II) species to Pd(0), restarting the catalytic cycle.



Scheme 3.8: Proposed catalytic cycle for Buchwald-Hartwig coupling of 5-bromo-*N*-protected-1*H*-benzimidazole with an aniline.

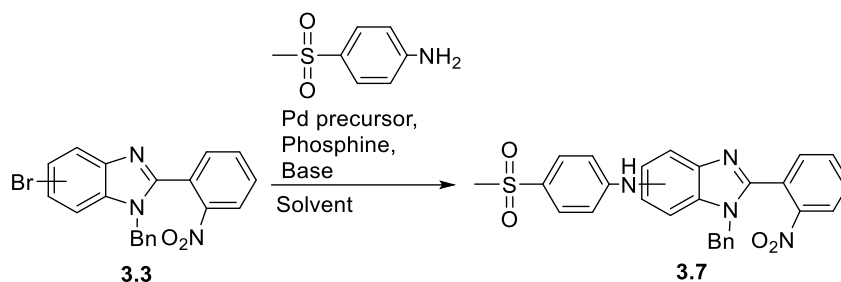
The optimal reaction conditions for this Buchwald-Hartwig coupling are highly dependent on the substrate and nucleophile. Previous reports³⁷ on the catalytic amination of similar benzimidazole substrates have highlighted that 5-bromo-*N*-protected-1*H*-benzimidazoles could be coupled with alkyl amines in modest yields (60%), while the 6-bromo-*N*-protected-1*H*-benzimidazoles isomer was not reactive under the same catalytic system employed. Indeed, the benzene portion of the benzimidazole ring is less electron-deficient than, for example, the 2 position of

benzimidazoles,⁴¹⁻⁴⁴ which should have a detrimental effect on metal oxidative addition. In an effort to overcome some challenges described in the literature for the amination of the benzimidazole 5(6) position, namely low yields, use of non-appropriately substituted amines and/or the need for huge amounts of catalyst,^{37,45-48} we proceeded to do an optimization of the reaction conditions, using the synthesis of **3.7** as model reaction. A screening of solvents, type of phosphine, substrate/catalyst relation and reaction time was carried out, and is presented in Table 3.5. It is worth noting that, despite compound **3.8** having a more favorable computational docking score, due to the considerably higher price of the commercial 3-(methylsulfonyl)aniline, all optimization studies were performed with 4-(methylsulfonyl)aniline (to obtain product **3.7**) and then adapted for 3-(methylsulfonyl)aniline, to obtain **3.8**.

In a typical experiment, the substrate **3.3**, 4-(methylsulfonyl)aniline, Cs₂CO₃, Pd(OAc)₂ and the selected phosphine were dissolved in either rigorously dried toluene or dioxane and the reaction was carried out at 100 °C for 16 h. First, the reaction was performed in toluene, using BINAP, DPEphos and XPhos and a remarkable effect of phosphine structure was observed (Table 3.5, entries 1-3). The palladium/XPhos system gave clearly the best performance, yielding 91% conversion after 16 h (entry 3). Then, to improve the solubility of the reaction components and evaluate the solvent effect, toluene was then replaced by dioxane and the reaction was performed under the same conditions. Again, BINAP and DPEphos did not originate an active catalytic system (entries 5-6), being the palladium/XPhos the one with best performance (100% conversion). Then, we reduced the reaction time from 16 h to 8 h, and 79% conversion was obtained (entry 7). Finally, we increased the substrate/catalyst ratio from 10 to 20 and, after 16 h, only 57% substrate conversion was obtained (entry 8).

Overall, these results show that the activity of the catalytic system is strongly dependent on the structure of palladium/phosphine catalyst, being the monodentate sterically hindered XPhos much more active under these conditions, as previously reported.³⁹ The greater reactivity of the Pd/XPhos is a consequence of the phosphine's structure (Figure 3.17). In contrast to BINAP and DPEphos, which are bidentate aryl phosphines, XPhos is a bulky monodentate phosphine, linked to one aryl group and two cyclohexyl groups.

Table 3.5: Optimization of the reaction conditions for the Buchwald-Hartwig coupling of benzyl protected benzimidazole **3.3** with 4-(methylsulfonyl)aniline.^(a)



#	Phosphine	Solvent	Substrate/Catalyst	Conversion (%)
1	15 mol% BINAP	Toluene	10	trace
2	15 mol% DPEphos	Toluene	10	trace
3	15 mol% XPhos	Toluene	10	91
4	15 mol% BINAP	Dioxane	10	trace
5	15 mol% DPEphos	Dioxane	10	trace
6	15 mol% XPhos	Dioxane	10	100 (78) ^(b)
7 ^(c)	15 mol% XPhos	Dioxane	10	79
8	7.5 mol% XPhos	Dioxane	20	57

BINAP: (2,2'-bis(diphenylphosphino)-1,1'-binaphthyl); DPEphos: bis[(2-diphenylphosphino)phenyl] ether; Xphos: [2-Dicyclohexylphosphino-2',4',6'-triisopropylbiphenyl]; ^(a) Typical reaction conditions: **3.3** (0.74 mmol); 4-(methylsulfonyl)aniline (0.88 mmol); Cs₂CO₃ (1.47 mmol); Pd(OAc)₂ (0.074 mmol); phosphine (0.11 mmol); solvent (5 ml); Temperature = 100 °C; Time = 16 h; ^(b) Isolated yield; ^(c) Time = 8 h.

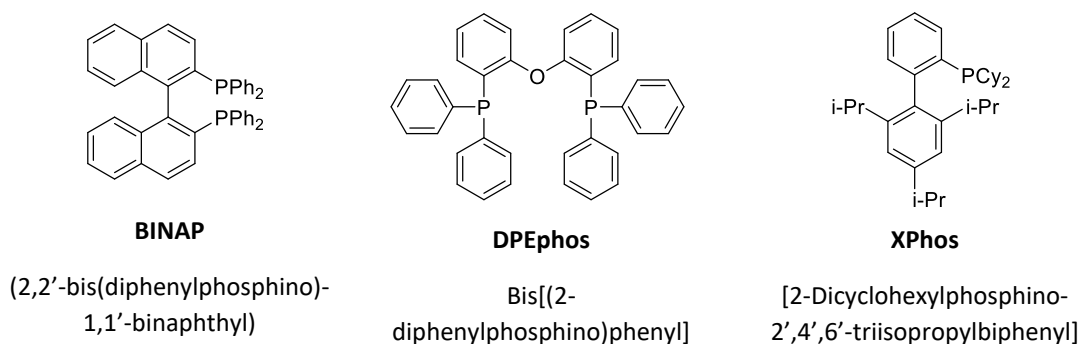


Figure 3.17: Structures of phosphine ligands used for the optimization of the Buchwald-Hartwig reaction.

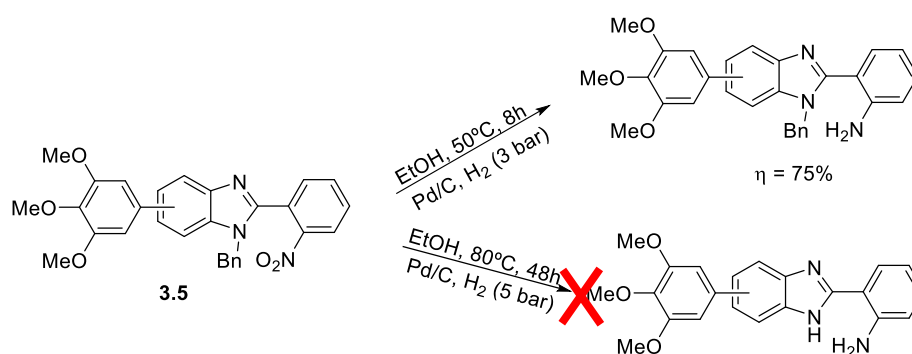
This type of dialkylbiaryl phosphines corresponds to a newer generation of phosphines, which are suitable to a wider range of substrates and improves on reactions' conversion

and reproducibility. Indeed, the presence of the cyclohexyl groups increase the rate of oxidative addition, which may be important when dealing with less suitable substrates, like in this case. In addition, these cyclohexyl and the isopropyl groups increase the phosphine's steric bulkiness, promoting the formation of the mono-ligated $L_1Pd(0)$ species, which is considered to be the most important catalytic species.

Following the optimized conditions reported in entry 6 of Table 3.5, and after the usual work-up and purification by column chromatography, the product **3.7** was obtained in 78%. Given that our computational studies demonstrated that the *meta* derivative had a higher docking score to the protein, we utilized the same optimized conditions, but this time using 3-(methylsulfonyl)aniline, and the desired product **3.8** was obtained in 81%. Despite the *para* derivative having a predicted lower nucleophilicity than the *meta* derivative, such did not translate into a noteworthy difference in reaction yield, under these conditions.

Catalytic *N*-benzyl deprotection and nitro reduction

The last step of the synthetic pathway is the catalytic hydrogenation of all the newly obtained compounds, **3.5** to **3.8**, for which we used **4.1** for the optimization of the reaction conditions (Scheme 3.9).

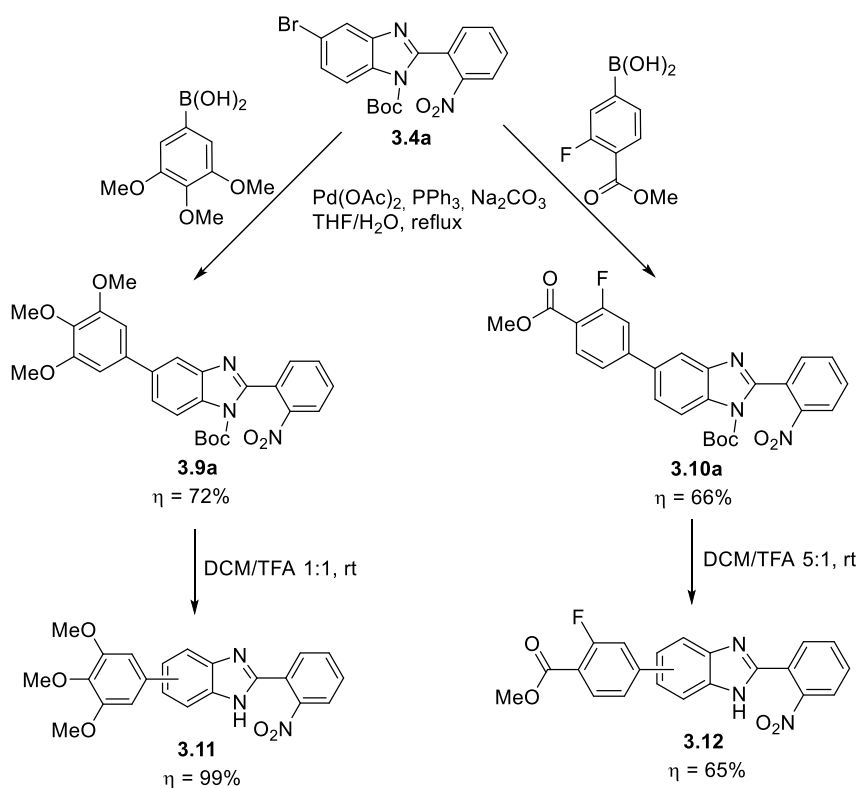


Scheme 3.9: Catalytic hydrogenation of **3.5**.

Our first approach used Pd/C in ethanol and employed mild reaction conditions, namely 3 bar of H₂ and 50 °C, during 8 h. Under these conditions, complete conversion of the substrate was achieved, however only the nitro group had been reduced, with the benzyl group untouched. Next, the pressure of H₂ was raised to 5 bar, the temperature to 80 °C, and the reaction was carried out for 48 h. No traces of starting

material were observed and multiple new products were identified by TLC but, after purification through column chromatography, none corresponded to the intended product, as determined through NMR analysis. It is possible that the harsher reaction conditions required for benzyl removal may have resulted in the degradation of the substrate.

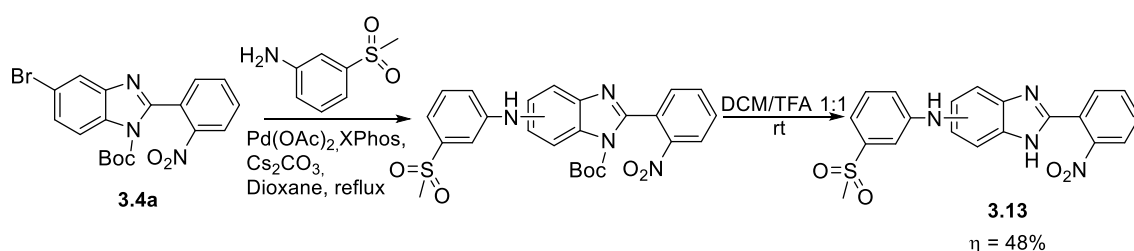
To circumvent these issues posed by the removal of the benzyl group, we decided to perform the same Pd-catalyzed couplings with the *N*-boc protected benzimidazole (**3.4a** and **3.4b**), whose synthesis was previously described in Scheme 3.6. Using the reaction conditions described above, **3.4a** or **3.4b** were coupled with 3,4,5-trimethoxyphenyl boronic acid or 3-fluoro-4-(methoxycarbonyl)phenyl boronic acid, giving products **3.9a** or **3.9b** and **3.10a** or **3.10b** with approximately the same NMR yields (75% and 70%, respectively). This result points out that both regioisomers have similar reactivity towards Suzuki-Miyaura coupling. For further studies, isolation and full characterization, only the products **3.9a** and **3.10a** have been isolated upon column chromatography, in 72% and 66% isolated yields, respectively (Scheme 3.10).



Scheme 3.10: Suzuki couplings involving boc-protected benzimidazole (**3.4a**), and subsequent deprotection.

For **3.9a**, deprotection was performed under TFA/DCM 1:1 for 2 h, resulting in quantitative yield of product **3.11**. For **3.10a**, due to the presence of the methyl ester group, we decided to use TFA/DCM 1:5 (5 h) and, following purification, **3.12** was obtained in 65% yield. Even with a lower percentage of TFA, some hydrolysis of the methyl ester was observed. Indeed, the presence of the electron-withdrawing fluorine *ortho* to the methyl ester may have contributed to the ester group vulnerability towards hydrolysis.

It should be noted that in the amination reaction of **3.4a** with 3-(methylsulfonyl)aniline (Scheme 3.11), using the reaction conditions described above, without isolation of the protected product, we obtained product **3.13** in 48% isolated yield. This slightly lower yield may be attributed to partial deprotection of the boc group during the reaction, since it is known that carbamates with *N*-heterocycles such as imidazole and indole are much easier to cleave under basic conditions.⁴⁹ As the nitrogen's lone electron pairs participate in the aromaticity of the benzimidazole ring, the resonance stabilization of the carbamate group is smaller, making it more susceptible towards nucleophilic attacks. Therefore, the boc-protected product was not isolated, and we proceeded directly to the deprotection step. When the amination reaction was finished, the solid was filtered, the solvent was evaporated and the solid was re-dissolved in a mixture of TFA/DCM 1:1 for 2 h. After basic work-up to neutralize the acid, product **3.13** was purified by column chromatography, and isolated in 48% yield.



Scheme 3.11: Buchwald–Hartwig coupling involving boc-protected benzimidazole (**3.4a**), and subsequent deprotection.

Finally, to prepare our initially designed compounds (Table 3.2) with all the appropriate functional groups, according to the pharmacophore model developed, we proceeded with the catalytic hydrogenation of the nitrophenyl group to an aminophenyl using the conditions previously described for the synthesis of **3.2**. Briefly, the substrate,

required pharmacophore features and this is highlighted in Figure 3.19, where **3.16** is overlapped with the pharmacophore model.

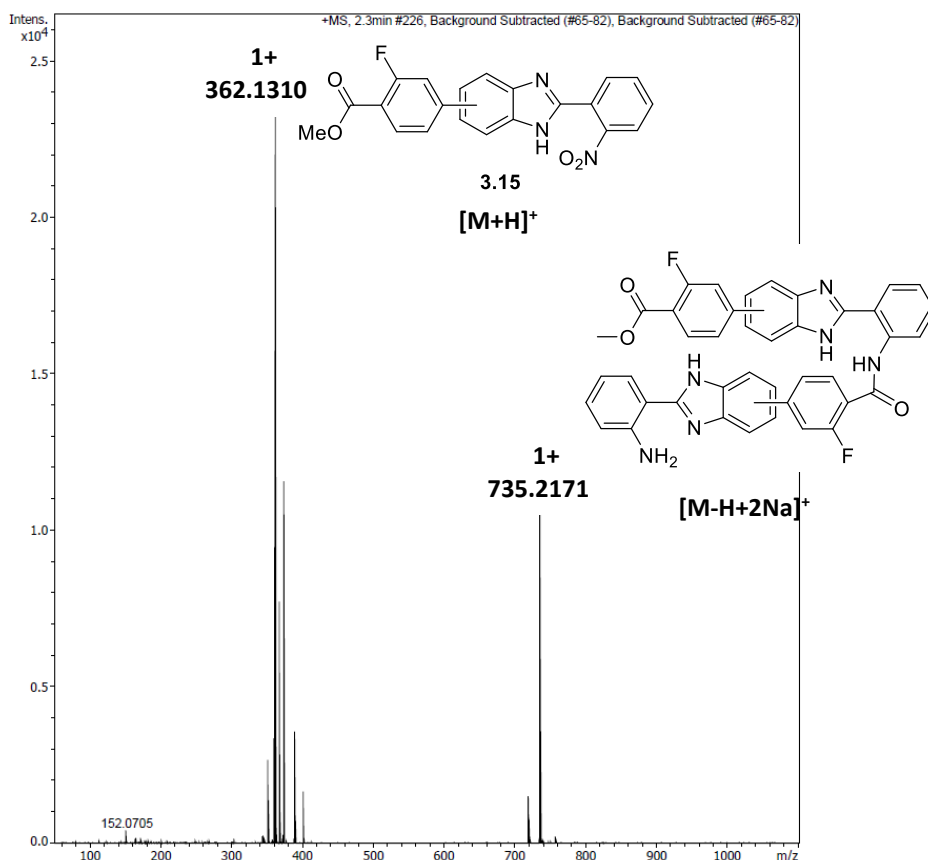


Figure 3.18: Mass spectrum (ESI positive mode) of product **3.15**, showing its contamination with a dimeric species.

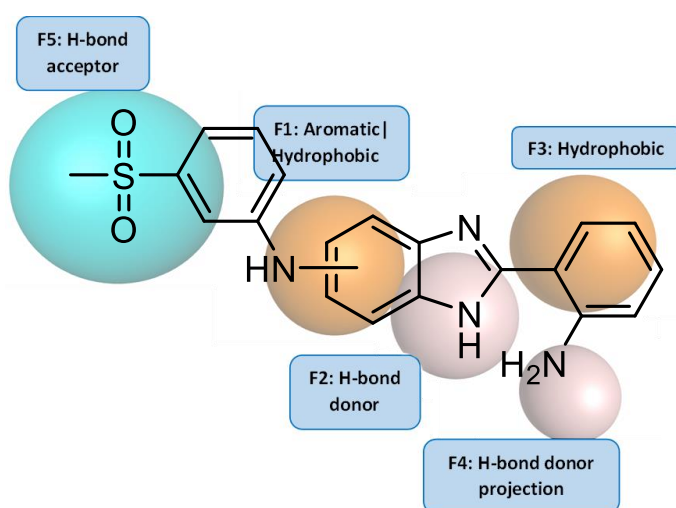


Figure 3.19: Overlap of compound **3.16** with the developed pharmacophore model, highlighting all the five required features (F1-F5) that it possesses.

Thus, the studies pursued with biological assays against *E. coli*, using both molecules acquired from the NCI database and the novel 2,5(6)-substituted benzimidazole derivatives synthesized in this chapter.

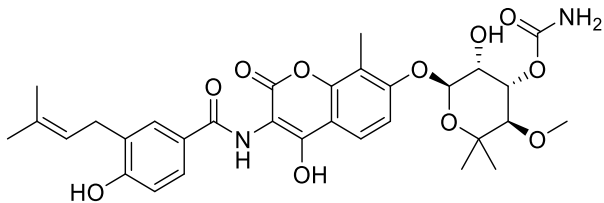
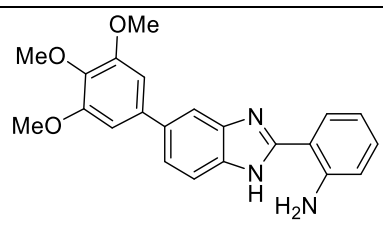
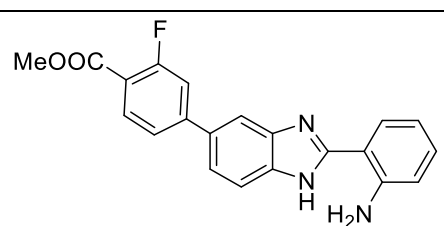
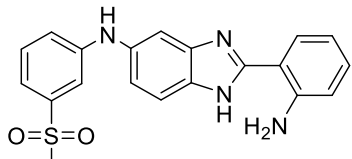
3.3 – Biological studies

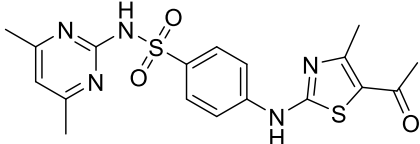
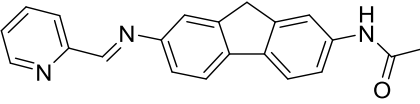
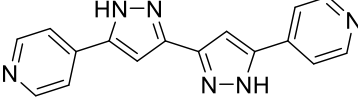
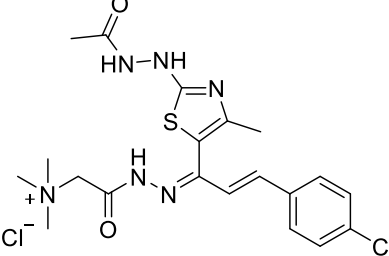
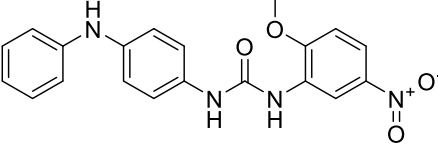
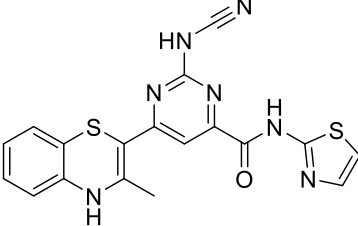
Biochemical assays on *E. coli* DNA gyrase

The biological studies started with the biochemical assays involving the evaluation of direct inhibition of *E. coli*'s DNA gyrase comparing the 2,5(6)-substituted benzimidazoles previously synthesized with the NCI database commercial compounds. The biochemical studies in *E. coli*'s gyrase were conducted by Catarina Madeira from the Metabolism and Genetics group at iMed.Ulisboa (group leader: Ana Paula Leandro). This assay utilized a commercial testing kit (HTS assay kit for *E. coli* gyrase, from Inspiralis),⁵⁰ containing all required components for a standardized test. As mentioned in the introductory chapter, DNA gyrase acts by forming negative supercoils of DNA, which facilitates its replication and transcription. Briefly, this biochemical assay determines the DNA gyrase activity by quantifying the amount of plasmid (circular DNA strand) that is supercoiled. When this plasmid is supercoiled, it will bind to a specific oligonucleotide that is immobilized in a 96-well plate. This plasmid/oligonucleotide complex can then be detected by using a DNA-specific probe that emits fluorescence. Thus, a decrease in fluorescence relative to the control is indicative of a lower amount of supercoiled plasmid, which means a decrease of enzyme activity. In Table 3.6 are presented the fluorescence (%) registered, and corresponding inhibition result, in the DNA gyrase inhibition assay. Novobiocin, an inhibitor of the ATPase binding site of *E. coli* gyrase subunit B, was used as positive control.³ As expected, it exerted a significant inhibitory activity ($67 \pm 27.7\%$), when compared with the negative control. Of all tested compounds, only **NCI-1** and **NCI-5** decreased the average fluorescence intensity registered (11 and 32%, respectively). However, further statistical analysis has revealed that none of these values were significant, when compared to the negative control. In sum, none of the tested compounds showed a detectable inhibitory activity towards *E. coli* gyrase, under the concentrations tested (up to 100 μM). The assays using

compounds **3.14**, **3.15**, **3.16**, **NCI-2** and **NCI-4** display an average fluorescence intensity above 100%, which can be attributed to some intrinsic fluorescence. Thus, for these cases the results cannot be considered valid and alternative tests that rely on agarose gel electrophoresis to assess DNA gyrase activity should be used.⁵⁰

Table 3.6: Biochemical studies in *E. coli* gyrase inhibition, using compounds (100 μ M concentration) synthesized 2,5(6)-substituted benzimidazoles and retrieved from the NCI database. Fluorescence percentage is relative to the negative control (no compound).

#	Compound	Fluorescence intensity (%)	Inhibition (%)
1	Negative control (no compound)	100.0 \pm 13.8	-
2	 Positive control (Novobiocin, commercial antibiotic) ³	32.5 \pm 27.7	67 \pm 27.7
3	 3.14	149.2 \pm 9.3	0
4	 3.15	211.0 \pm 5.5	0
5	 3.16	137.8 \pm 26.5	0

6	 <p>659383 (NCI-1)</p>	88.6 ± 17.4	11.4 ± 17.4 (No statistical significance)
7	 <p>90716 (NCI-2)</p>	150.2 ± 13.3	0
8	 <p>371704 (NCI-3)</p>	98.2 ± 19.1	0
9	 <p>647083 (NCI-4)</p>	123.7 ± 8.3	0
10	 <p>213814 (NCI-5)</p>	68.0 ± 24.0	32.0 ± 24.0 (No statistical significance)
11	 <p>624478 (NCI-6)</p>	99.9 ± 29.2	0

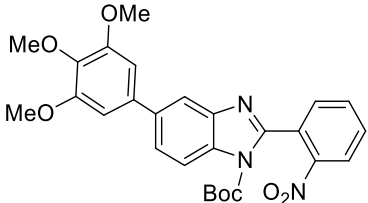
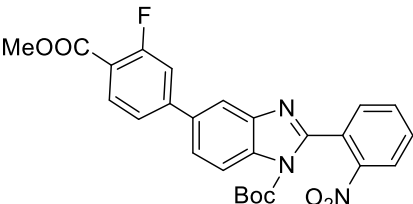
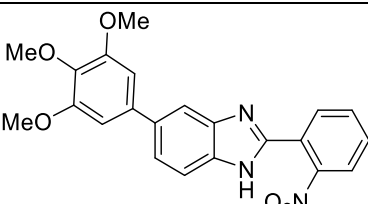
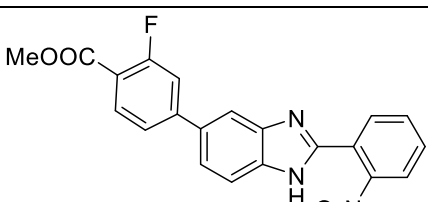
As was discussed before, the inhibition of *E. coli* does not occur only by DNA Gyrase inhibition and can occur by several mechanisms, including i) degradation of structure and function of the cell wall; ii) inhibition of protein, DNA or RNA synthesis; iii) inhibition of metabolic pathways (e.g. folic acid synthesis), among others.⁵¹ So, we

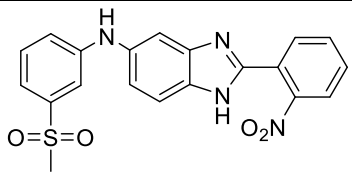
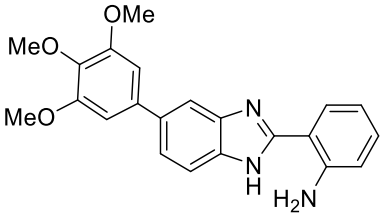
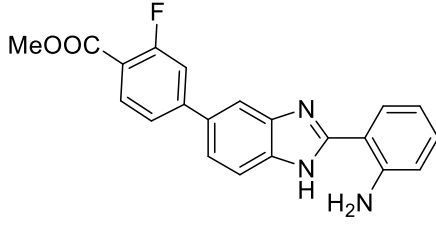
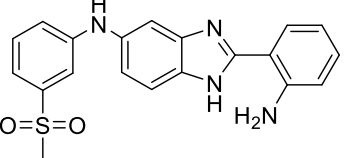
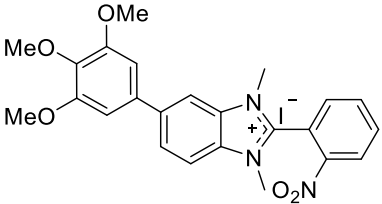
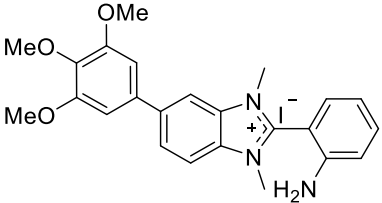
decided to pursue the studies by determining the MIC of the synthesized compounds from the benzimidazole family and from the NCI database against *E. coli*.

MIC determination on bacteria

The MIC studies were first conducted for the compounds of the benzimidazole family (Table 3.7).

Table 3.7: MIC values determined for compounds from the benzimidazole family in *E. coli* planktonic suspensions.

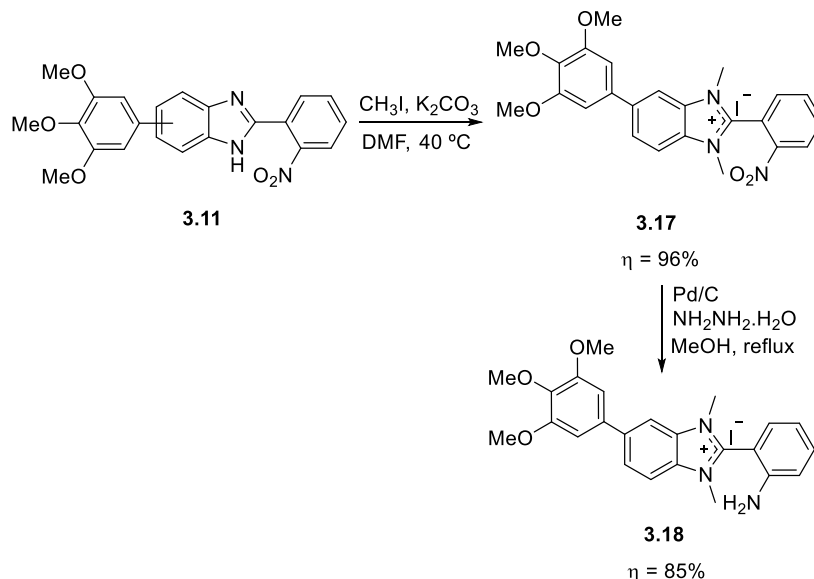
#	Compound	MIC in <i>E. coli</i> (mg/L)
1	 <p>3.9a</p>	>250
2	 <p>3.10a</p>	>250
3	 <p>3.11</p>	>250
4	 <p>3.12</p>	>250

5	 <p style="text-align: center;">3.13</p>	>250
6	 <p style="text-align: center;">3.14</p>	>500
7	 <p style="text-align: center;">3.15</p>	>250
8	 <p style="text-align: center;">3.16</p>	>250
9	 <p style="text-align: center;">3.17</p>	>500
10	 <p style="text-align: center;">3.18</p>	>500

Briefly, an aqueous solution of each compound was prepared, containing the minimum amount of DMSO required for solubilization (10-40%). Since DMSO possesses

antimicrobial activity by itself, appropriate control experiments were conducted to ensure that the observed MIC values could be attributed to the tested compounds. The experimental procedure followed the same guidelines presented in Chapter 2 for the appraisal of the ciprofloxacin MIC.

First, we evaluated the neutral compounds **3.9a** to **3.16** and no significant *E. coli* inhibitory activity was observed (MIC > 500 mg/L, Table 3.7, entries 1-8). Since it is well demonstrated that the enhancement of antimicrobial activity occurs from the presence of cationic groups in the antibiotic's structure,⁵²⁻⁵⁴ we proceeded with the cationization of **3.11** (Scheme 3.13). Briefly, **3.11** was dissolved in DMF, and a large excess of methyl iodide and K₂CO₃ were added. The reaction, carried out at 40 °C, was complete in 24 h. The solvent was evaporated and the resulting solid was washed with acetone, giving the cationic product, **3.17** in 96% yield. Finally, reduction of the nitro group was performed under the previously described conditions (Pd/C and hydrazine method), giving **3.18** in 85% yield. The antimicrobial activity of these two new cationic benzimidazole derivative compounds against *E. coli* is presented in Table 3.7 (entries 9 and 10) and once again, no significant *E. coli* inactivation was observed.



Scheme 3.13: Cationization of **3.11** with methyl iodide and subsequent catalytic reduction.

Then, the MIC studies were extended to all NCI database compounds (**NCI-1** to **NCI-6**) and in all cases, an *E. coli* MIC ≥ 500 mg/L was observed. It is worth reminding that the lower permeability of *E. coli*'s cell wall, combined with the presence of efflux

pumps, plays an important role in limiting the uptake of antibiotics. These are among the major obstacles for the pharmaceutical development of new antibiotics against *E. coli*. Thus, having in hand a group of compounds with potential antimicrobial activity against other gram-positive bacterial strains, we decided to conclude the studies by evaluating them against *S. aureus* and the results are collected in Table 3.8.

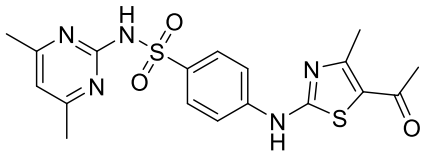
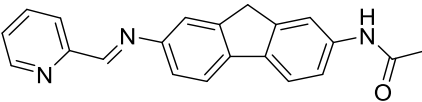
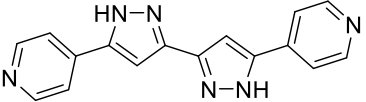
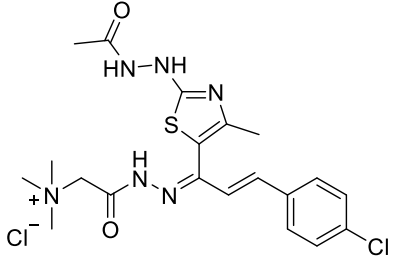
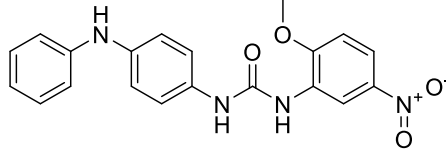
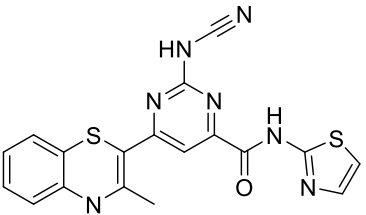
Table 3.8: MIC values determined for compounds from the benzimidazole family in *S. aureus* planktonic suspensions.

#	Compound	MIC in <i>S. aureus</i> (mg/L)
1	3.9a	250
2	3.10a	>250
3	3.11	250
4	3.12	>500
5	3.13	>250
6	3.14	>250
7	3.15	>500
8	3.16	>500
9	3.17	125
10	3.18	>500

In *S. aureus*, neutral benzimidazole compounds **3.9a** and **3.11** gave significant MIC values (Table 3.8, entries 1-2, MIC = 250 mg/L). It is worth mentioning that both compounds encompass nitro and a 3,4,5-trimethoxyphenyl groups in the 2 and 5(6) benzimidazole positions, respectively, which may be important for the observed antimicrobial activity. Regarding the evaluation of the cationic benzimidazoles, the compound with the nitro group (**3.17**) significantly decreased the *S. aureus* MIC (from 250 to 125 mg/L; Table 3.8 entry 9), when compared with the neutral **3.11**. Once again, the structure-activity relevance is evidenced, since the simple reduction of the nitro group towards -NH₂ (**3.18**; Table 3.8, entry 10) gave a significant decrease in antimicrobial activity against *S. aureus*. These experimental results open the way for the implementation of future CADD studies directed towards the inhibition of *S. aureus* specific targets.

Next, MIC studies were conducted for the most promising compounds acquired from the NCI database, in *S. aureus* planktonic suspensions. The results are presented in Table 3.9.

Table 3.9: MIC values determined for compounds from the NCI database in *S. aureus* planktonic suspensions.

#	Compound	MIC in <i>S. aureus</i> (mg/L)
1	 659383 (NCI-1)	500
2	 90716 (NCI-2)	>250
3	 371704 (NCI-3)	>250
4	 647083 (NCI-4)	42
5	 213814 (NCI-5)	>250
6	 624478 (NCI-6)	500

Among this selection of NCI compounds, **NCI-4** had promising *S. aureus* antimicrobial activity, with MIC = 42 mg/L. Although the observed MIC value is higher than antibiotics currently used in clinic,⁵⁵ it highlights the potential of this base scaffold for further chemical modifications and improvement of its antimicrobial activity, through CADD and structure/activity studies.

3.4 – Conclusion

The urgent need for the development of new antibiotics effective against *E. coli* prompted us to the design and synthesis of new molecules, aiming DNA gyrase B inhibition. Using CADD tools, two optimized pharmacophore models (Unified and EHT annotation schemes) were constructed for inhibition of *E. coli*'s *gyrB*, based on the structural and biological data of known inhibitors available in literature. Both models identified five common structural features, such as the presence of hydrogen bond acceptors/donors, aromatic rings and hydrophobic portions. Their performance in discriminating between active and inactive compounds was assessed, revealing a > 90% true active hit rate and a < 10% false positive rate. Additionally, it was found that the combination of both Unified and EHT pharmacophore models improved the ratio of true positives/false positives, being this approach selected for screening of the virtual libraries.

After obtaining the pharmacophore models, the work described in this chapter followed two different development strands: i) virtual screening of chemical databases such as the one from the NCI and ii) computationally-assisted design of new molecules based on the acquired structural information from known inhibitors. Regarding the screening of the NCI database, a total of 435 promising pharmacophore hit compounds were selected for molecular docking studies using the crystallographic structure of *E. coli*'s *gyrB* as target. The GOLD ChemScore function was determined to be the most accurate for predicting the interaction between ligand and target, yielding six promising structures that were supplied by NCI. These compounds did not display a statistically significant inhibition of *E. coli*'s gyrase in concentrations up to 500 mg/L and also did not have any *E. coli* inhibitory activity through other gyrase-independent mechanisms.

Relatively to the development of new molecules aiming *E. coli* DNA gyrase B inhibition, a set of derivatives of 2-(2-aminophenyl)-5(6)-substituted-1H-benzimidazoles were designed in MOE and screened using the pharmacophore models and docking. This led to the selection of three promising molecules that were selected for chemical synthesis. The optimization of the condensation/oxidation reaction of 4-bromo-1,2-diaminobenzene with 2-nitrobenzaldehyde, yielding 5(6)-bromo-2-(2-nitrophenyl)-1H-benzimidazole **3.1**, led us to find a sustainable synthetic approach, using ethanol as solvent and Montmorillonite K10 as a reusable catalyst, which allowed a significant improvement in product yield and isolation process. Additionally, boc revealed to be the ideal benzimidazole protecting group since its deprotection does not lead to any significant formation of the side products, as obtained when using benzyl protecting group. The studies herein described pave the way for efficient functionalization of the more synthetically challenging 5(6) position, *via* cross-coupling Suzuki–Miyaura and Buchwald–Hartwig reactions, using functionalized phenylboronic acids (products **3.9a** and **3.10a** were isolated with 72% and 66%, respectively) and amines (3-methylsulfonyl)aniline), catalyzed by Pd/XPhos (product **3.13**). Finally, the use of $\text{NH}_2\text{NH}_2 \cdot \text{H}_2\text{O}$ or H_2 and Pd/C revealed to be a clean strategy to promote the reduction of the nitro group to the corresponding amine, giving **3.14**, **3.15** and **3.16** with 91%, 90% and 80% yields respectively.

The final neutral benzimidazole-based compounds (**3.14-3.16**) did not show *E. coli*'s gyrase inhibition in concentrations up to 100 μM and also did not gave a significant *E. coli* MIC value ($> 500 \text{ mg/L}$), even when the cationic ones (**3.17-3.18**) was evaluated. However, the neutral benzimidazole derivative **3.11** containing the nitro and 3,4,5-trimethoxyphenyl groups at 2 and 5(6) positions, respectively, led to a significant *S. aureus* inhibition (MIC = 250 mg/L). Furthermore, its corresponding monocationic derivative **3.17** showed a higher *S. aureus* inhibition, with a MIC of 125 mg/L.

Regarding the *S. aureus* MIC results for the NCI compounds, we should highlight the compound **NCI-4** which showed a promising MIC = 42 mg/L. These results reinforce the idea that the development of antibiotics for gram-positive bacteria is facilitated, since intracellular targets are more accessible due to a higher cell wall permeation by antimicrobial molecules.

The main focus of this topic was the discovery of new families of compounds with activity for *E. coli*, for which pharmaceutical drug development has been practically inexistent. However, the antimicrobial activity of the tested compounds from both strands of development highlight a serendipitous discovery of potential *S. aureus* antibiotics, a bacterial species for which development of new therapies is also urgently needed, according to WHO.⁵⁶ Given that DNA gyrase is a generally well preserved protein among bacteria, it is possible that compounds designed for *E. coli*'s DNA gyrase may show better *S. aureus*'s DNA gyrase inhibitory. On the other hand, these molecules may be interacting with a different target, for which complementary biochemical studies would be needed, to give further insights on their action mechanism.

3.5 – References

- [1] Santosh, A. K.; Alpeshkumar, K. M.; Evans, C. C.; Sudha, S., Pharmacophore Modeling in Drug Discovery and Development: An Overview, *Medicinal Chemistry*, **2007**, *3*, 187-197.
- [2] <https://www.chemcomp.com/> (accessed in 25/03/2022).
- [3] Tomašič, T.; Barančoková, M.; Zidar, N.; Ilaš, J.; Tammela, P.; Kikelj, D., Design, synthesis, and biological evaluation of 1-ethyl-3-(thiazol-2-yl)urea derivatives as Escherichia coli DNA gyrase inhibitors, *Archiv der Pharmazie*, **2018**, *351*, 1700333.
- [4] Durcik, M.; Tammela, P.; Barančoková, M.; Tomašič, T.; Ilaš, J.; Kikelj, D.; Zidar, N., Synthesis and Evaluation of N-Phenylpyrrolamides as DNA Gyrase B Inhibitors, *ChemMedChem*, **2018**, *13*, 186-198.
- [5] Ostrov, D. A.; Hernández Prada, J. A.; Corsino, P. E.; Finton, K. A.; Le, N.; Rowe, T. C., Discovery of Novel DNA Gyrase Inhibitors by High-Throughput Virtual Screening, *Antimicrobial Agents and Chemotherapy*, **2007**, *51*, 3688-3698.
- [6] Gjorgjieva, M.; Tomašič, T.; Barančokova, M.; Katsamakas, S.; Ilaš, J.; Tammela, P.; Peterlin Mašič, L.; Kikelj, D., Discovery of Benzothiazole Scaffold-Based DNA Gyrase B Inhibitors, *Journal of Medicinal Chemistry*, **2016**, *59*, 8941-8954.
- [7] Jakopin, Ž.; Ilaš, J.; Barančoková, M.; Brvar, M.; Tammela, P.; Sollner Dolenc, M.; Tomašič, T.; Kikelj, D., Discovery of substituted oxadiazoles as a novel scaffold for DNA gyrase inhibitors, *European Journal of Medicinal Chemistry*, **2017**, *130*, 171-184.
- [8] Ronkin, S. M.; Badia, M.; Bellon, S.; Grillot, A.-L.; Gross, C. H.; Grossman, T. H.; Mani, N.; Parsons, J. D.; Stamos, D.; Trudeau, M.; Wei, Y.; Charifson, P. S., Discovery of pyrazolthiazoles as novel and potent inhibitors of bacterial gyrase, *Bioorganic & Medicinal Chemistry Letters*, **2010**, *20*, 2828-2831.
- [9] Eakin, A. E.; Green, O.; Hales, N.; Walkup, G. K.; Bist, S.; Singh, A.; Mullen, G.; Bryant, J.; Embrey, K.; Gao, N.; Breeze, A.; Timms, D.; Andrews, B.; Uria-Nickelsen, M., *et al.*, Pyrrolamide DNA Gyrase Inhibitors: Fragment-Based

- Nuclear Magnetic Resonance Screening To Identify Antibacterial Agents, *Antimicrobial Agents & Chemotherapy*, **2012**, *56*, 1240-1246.
- [10] Cotman, A. E.; Trampuž, M.; Brvar, M.; Kikelj, D.; Ilaš, J.; Peterlin-Mašič, L.; Montalvão, S.; Tammela, P.; Frlan, R., Design, Synthesis, and Evaluation of Novel Tyrosine-Based DNA Gyrase B Inhibitors, *Archiv der Pharmazie*, **2017**, *350*, 1700087.
- [11] Basarab, G. S.; Manchester, J. I.; Bist, S.; Boriack-Sjodin, P. A.; Dangel, B.; Illingworth, R.; Sherer, B. A.; Sriram, S.; Uria-Nickelsen, M.; Eakin, A. E., Fragment-to-Hit-to-Lead Discovery of a Novel Pyridylurea Scaffold of ATP Competitive Dual Targeting Type II Topoisomerase Inhibiting Antibacterial Agents, *Journal of Medicinal Chemistry*, **2013**, *56*, 8712-8735.
- [12] Trzoss, M.; Bensen, D. C.; Li, X.; Chen, Z.; Lam, T.; Zhang, J.; Creighton, C. J.; Cunningham, M. L.; Kwan, B.; Stidham, M.; Nelson, K.; Brown-Driver, V.; Castellano, A.; Shaw, K. J., *et al.*, Pyrrolopyrimidine inhibitors of DNA gyrase B (GyrB) and topoisomerase IV (ParE), Part II: Development of inhibitors with broad spectrum, Gram-negative antibacterial activity, *Bioorganic & Medicinal Chemistry Letters*, **2013**, *23*, 1537-1543.
- [13] Shirude, P. S.; Madhavapeddi, P.; Tucker, J. A.; Murugan, K.; Patil, V.; Basavarajappa, H.; Raichurkar, A. V.; Humnabadkar, V.; Hussein, S.; Sharma, S.; Ramya, V. K.; Narayan, C. B.; Balganes, T. S.; Sambandamurthy, V. K., Aminopyrazinamides: Novel and Specific GyrB Inhibitors that Kill Replicating and Nonreplicating Mycobacterium tuberculosis, *ACS Chemical Biology*, **2013**, *8*, 519-523.
- [14] Bisacchi, G. S.; Manchester, J. I., A New-Class Antibacterial—Almost. Lessons in Drug Discovery and Development: A Critical Analysis of More than 50 Years of Effort toward ATPase Inhibitors of DNA Gyrase and Topoisomerase IV, *ACS Infectious Diseases*, **2014**, *1*, 4-41.
- [15] Lin, F.-Y.; MacKerell, A. D., Do Halogen–Hydrogen Bond Donor Interactions Dominate the Favorable Contribution of Halogens to Ligand–Protein Binding?, *The Journal of Physical Chemistry B*, **2017**, *121*, 6813-6821.
- [16] Panigrahi, S. K.; Desiraju, G. R., Strong and weak hydrogen bonds in the protein–ligand interface, *Proteins*, **2007**, *67*, 128-141.
- [17] Mysinger, M. M.; Carchia, M.; Irwin, J. J.; Shoichet, B. K., Directory of Useful Decoys, Enhanced (DUD-E): Better Ligands and Decoys for Better Benchmarking, *Journal of Medicinal Chemistry*, **2012**, *55*, 6582-6594.
- [18] Pagadala, N. S.; Syed, K.; Tuszynski, J., Software for molecular docking: a review, *Biophysical reviews*, **2017**, *9*, 91-102.
- [19] <https://cactus.nci.nih.gov/download/nci/index.html> (accessed in 20/03/2018).
- [20] <https://zinc.docking.org/> (accessed in 20/03/2018).
- [21] Veber, D. F.; Johnson, S. R.; Cheng, H.-Y.; Smith, B. R.; Ward, K. W.; Kopple, K. D., Molecular Properties That Influence the Oral Bioavailability of Drug Candidates, *Journal of Medicinal Chemistry*, **2002**, *45*, 2615-2623.
- [22] Lagorce, D.; Bouslama, L.; Becot, J.; Miteva, M. A.; Villoutreix, B. O., FAF-Drugs4: free ADME-tox filtering computations for chemical biology and early stages drug discovery, *Bioinformatics*, **2017**, *33*, 3658-3660.

- [23] Limban, C.; Nuță, D. C.; Chiriță, C.; Negreș, S.; Arsene, A. L.; Goumenou, M.; Karakitsios, S. P.; Tsatsakis, A. M.; Sarigiannis, D. A., The use of structural alerts to avoid the toxicity of pharmaceuticals, *Toxicology Reports*, **2018**, *5*, 943-953.
- [24] Stepan, A. F.; Walker, D. P.; Bauman, J.; Price, D. A.; Baillie, T. A.; Kalgutkar, A. S.; Aleo, M. D., Structural Alert/Reactive Metabolite Concept as Applied in Medicinal Chemistry to Mitigate the Risk of Idiosyncratic Drug Toxicity: A Perspective Based on the Critical Examination of Trends in the Top 200 Drugs Marketed in the United States, *Chemical Research in Toxicology*, **2011**, *24*, 1345-1410.
- [25] Ghosh, A. K.; Samanta, I.; Mondal, A.; Liu, W. R., Covalent Inhibition in Drug Discovery, *ChemMedChem*, **2019**, *14*, 889-906.
- [26] Weltzien, H. U.; Padovan, E., Molecular Features of Penicillin Allergy, *Journal of Investigative Dermatology*, **1998**, *110*, 203-206.
- [27] Dahlin, J. L.; Nissink, J. W. M.; Strasser, J. M.; Francis, S.; Higgins, L.; Zhou, H.; Zhang, Z.; Walters, M. A., PAINS in the Assay: Chemical Mechanisms of Assay Interference and Promiscuous Enzymatic Inhibition Observed during a Sulfhydryl-Scavenging HTS, *Journal of Medicinal Chemistry*, **2015**, *58*, 2091-2113.
- [28] Sreerama, R.; Barnali, M.; Balamurali, M. M.; Kaushik, C., Synthesis and Medicinal Applications of Benzimidazoles: An Overview, *Current Organic Synthesis*, **2017**, *14*, 40-60.
- [29] Jyoti, S.; Pradeep, K. S.; Ravi, B.; Anand, K. H., Synthetic Approaches Towards Benzimidazoles by the Reaction of o-Phenylenediamine with Aldehydes Using a Variety of Catalysts: A Review, *Current Organic Chemistry*, **2018**, *22*, 2280-2299.
- [30] Faheem, M.; Rathaur, A.; Pandey, A.; Kumar Singh, V.; Tiwari, A. K., A Review on the Modern Synthetic Approach of Benzimidazole Candidate, *ChemistrySelect*, **2020**, *5*, 3981-3994.
- [31] Siva, S. P.; Ritu, M.; Subhash, C. J., Synthetic Approaches to 2-Arylbenzimidazoles: A Review, *Current Organic Chemistry*, **2012**, *16*, 1905-1919.
- [32] Pandey, R.; Yadav, M.; Shahid, M.; Misra, A.; Pandey, D. S., Design and synthesis of fluorescent 6-aryl[1,2-c]quinazolines serving as selective and sensitive 'on-off' chemosensor for Hg²⁺ in aqueous media, *Tetrahedron Letters*, **2012**, *53*, 3550-3555.
- [33] Mann, J.; Baron, A.; Opoku-Boahen, Y.; Johansson, E.; Parkinson, G.; Kelland, L. R.; Neidle, S., A New Class of Symmetric Bisbenzimidazole-Based DNA Minor Groove-Binding Agents Showing Antitumor Activity, *Journal of Medicinal Chemistry*, **2001**, *44*, 138-144.
- [34] Gonsalves, A. M. d. A. R.; Varejão, J. M. T. B.; Pereira, M. M., Some new aspects related to the synthesis of meso-substituted porphyrins, *Journal of Heterocyclic Chemistry*, **1991**, *28*, 635-640.
- [35] Ma, X.; Liu, S.; Liu, Y.; Gu, G.; Xia, C., Comparative study on catalytic hydrodehalogenation of halogenated aromatic compounds over Pd/C and Raney Ni catalysts, *Scientific Reports*, **2016**, *6*, 25068.
- [36] Li, F.; Frett, B.; Li, H.-y., Selective Reduction of Halogenated Nitroarenes with Hydrazine Hydrate in the Presence of Pd/C, *Synlett*, **2014**, *25*, 1403-1408.
- [37] López-Rodríguez, M. a. L.; Benhamú, B.; Ayala, D.; Rominguera, J. L.; Murcia, M.; Ramos, J. A.; Viso, A., Pd(0) Amination of Benzimidazoles as an Efficient Method

- towards New (Benzimidazolyl)piperazines with High Affinity for the 5-HT_{1A} Receptor, *Tetrahedron*, **2000**, *56*, 3245-3253.
- [38] Lennox, A. J. J.; Lloyd-Jones, G. C., Selection of boron reagents for Suzuki–Miyaura coupling, *Chemical Society Reviews*, **2014**, *43*, 412-443.
- [39] Surry, D. S.; Buchwald, S. L., Dialkylbiaryl phosphines in Pd-catalyzed amination: a user's guide, *Chemical Science*, **2011**, *2*, 27-50.
- [40] Borojeni, S. B. *Studies on the optimization of buchwald-hartwig amination of aryl halides*, PhD thesis. Queen's University, Ontario, Canada, **2014**.
- [41] Hooper, M. W.; Utsunomiya, M.; Hartwig, J. F., Scope and Mechanism of Palladium-Catalyzed Amination of Five-Membered Heterocyclic Halides, *The Journal of Organic Chemistry*, **2003**, *68*, 2861-2873.
- [42] Kawasaki, I.; Taguchi, N.; Yoneda, Y.; Yamashita, M.; Ohta, S., Highly Effective Procedure for Introduction of Amino Group into the 2-Position of Imidazole Ring, *Heterocycles*, **1996**, *43*, 1375-1379.
- [43] Coon, T.; Moree, W. J.; Li, B.; Yu, J.; Zamani-Kord, S.; Malany, S.; Santos, M. A.; Hernandez, L. M.; Petroski, R. E.; Sun, A.; Wen, J.; Sullivan, S.; Haelewyn, J.; Hedrick, M., *et al.*, Brain-penetrating 2-aminobenzimidazole H₁-antihistamines for the treatment of insomnia, *Bioorganic & Medicinal Chemistry Letters*, **2009**, *19*, 4380-4384.
- [44] Sang, W.; Gavi, A. J.; Yu, B.-Y.; Cheng, H.; Yuan, Y.; Wu, Y.; Lommens, P.; Chen, C.; Verpoort, F., Palladium-Catalyzed Ligand-Free C-N Coupling Reactions: Selective Diheteroarylation of Amines with 2-Halobenzimidazoles, *Chemistry – An Asian Journal*, **2020**, *15*, 129-135.
- [45] Kasai, S.; Igawa, H.; Takahashi, M.; Maekawa, T.; Kakegawa, K.; Yasuma, T.; Kina, A.; Aida, J.; Khamrai, U.; Kundu, M. Benzimidazole derivatives as mch receptor antagonists. WO/2013/105676, **2013**.
- [46] Chang, S.-y.; Lin, G.-T.; Cheng, Y.-C.; Huang, J.-J.; Chang, C.-L.; Lin, C.-F.; Lee, J.-H.; Chiu, T.-L.; Leung, M.-k., Construction of Highly Efficient Carbazol-9-yl-Substituted Benzimidazole Bipolar Hosts for Blue Phosphorescent Light-Emitting Diodes: Isomer and Device Performance Relationships, *ACS Applied Materials & Interfaces*, **2018**, *10*, 42723-42732.
- [47] Boydston, A. J.; Vu, P. D.; Dykhno, O. L.; Chang, V.; Wyatt, A. R.; Stockett, A. S.; Ritschdorff, E. T.; Shear, J. B.; Bielawski, C. W., Modular Fluorescent Benzobis(imidazolium) Salts: Syntheses, Photophysical Analyses, and Applications, *Journal of the American Chemical Society*, **2008**, *130*, 3143-3156.
- [48] Chen, Y.-C.; Faver, J. C.; Ku, A. F.; Miklossy, G.; Riehle, K.; Bohren, K. M.; Ucisik, M. N.; Matzuk, M. M.; Yu, Z.; Simmons, N., C–N Coupling of DNA-Conjugated (Hetero)aryl Bromides and Chlorides for DNA-Encoded Chemical Library Synthesis, *Bioconjugate Chemistry*, **2020**, *31*, 770-780.
- [49] Greene, T. W.; Wuts, P. G. M., Protection for the Amino Group (3rd edition). In *Protective Groups in Organic Synthesis*, John Wiley & Sons, Inc.: New York, **1999**; pp 494-653.
- [50] <https://www.inspiralis.com/products/topoisomerases/topoisomerase-enzymes-and-assay-kits/e-coli-gyrase/> (accessed in 25/03/2022).
- [51] Kohanski, M. A.; Dwyer, D. J.; Collins, J. J., How antibiotics kill bacteria: from targets to networks, *Nature Reviews Microbiology*, **2010**, *8*, 423-435.

- [52] Gravel, J.; Schmitzer, A. R., Imidazolium and benzimidazolium-containing compounds: from simple toxic salts to highly bioactive drugs, *Organic & Biomolecular Chemistry*, **2017**, *15*, 1051-1071.
- [53] Li, Y.-X.; Zhong, Z.; Zhang, W.-P.; Qian, P.-Y., Discovery of cationic nonribosomal peptides as Gram-negative antibiotics through global genome mining, *Nature Communications*, **2018**, *9*, 3273.
- [54] Vaara, M.; Fox, J.; Loidl, G.; Siikanen, O.; Apajalahti, J.; Hansen, F.; Frimodt-Møller, N.; Nagai, J.; Takano, M.; Vaara, T., Novel polymyxin derivatives carrying only three positive charges are effective antibacterial agents, *Antimicrobial Agents and Chemotherapy*, **2008**, *52*, 3229-3236.
- [55] Bauer, J.; Siala, W.; Tulkens, P. M.; Bambeke, F. V., A Combined Pharmacodynamic Quantitative and Qualitative Model Reveals the Potent Activity of Daptomycin and Delafloxacin against *Staphylococcus aureus* Biofilms, *Antimicrobial Agents & Chemotherapy*, **2013**, *57*, 2726-2737.
- [56] World Health Organization - Global Priority List of Antibiotic Resistant Bacteria to Guide Research, Discovery, and Development of New Antibiotics, *World Health Organization, Geneva*, **2017**, 1-7.

CHAPTER 4

Experimental

In this chapter, detailed information regarding reaction procedures, techniques and instruments used during the experimental work are given. It is divided into four sections: General information (section 4.1), experimental of Chapter 2 (section 4.2), experimental of Chapter 3 (section 4.3) and references (section 4.4).

4.1 – General information

All reagents and solvents were purchased from Sigma-Aldrich, Fluorochem, Acros Organics and José M. Vaz Pereira. All reagents were used as supplied, without further purification. Air and moisture-sensitive reactions were handled under nitrogen or argon atmosphere, in a vacuum system, using Schlenk techniques. For anhydrous reactions, all the glassware was dried by heating overnight at 150 °C and then stored in a desiccator using activated silica gel. When required, the solvents were degassed and dried according to standard procedures, as detailed below.

Instrumentation and methodologies

Thin-layer chromatography

The reactions progress were controlled using thin-layer chromatography (TLC) as a standard method. Silica 60 (Fluka) plates with UV₂₅₄ indicator were used as stationary phase. The eluents used were typically composed of hexane, dichloromethane or ethyl

acetate, or a mixture composed by hexane/dichloromethane, hexane/ethyl acetate or dichloromethane/ethyl acetate, in variable ratios.

Column adsorption chromatography

Most reaction products were purified by column adsorption chromatography, using silica gel 60 (Merck) as stationary phase. The eluents used are described in the synthetic methods relative to each compound.

Size exclusion chromatography

For the cases where size exclusion chromatography was used, Sephadex® G-10 was selected as stationary phase (size exclusion for compounds with MW > 700 g/mol) and deionized water as eluent. The preparation of the Sephadex® G-10 resin is as follows: i) the dry powder is added to a 1 M NaCl solution and the resin will swell at 90 °C for 3 h; ii) the supernatant is decanted; iii) the slurry is added to a column and packed by gravity flow; iv) copious amounts of deionized water are added to remove NaCl salts from the resin; v) the reaction crude is added to the top of the column and eluted with water.

Microwave-assisted chemistry

All microwave-assisted reactions were performed in a CEM Discover SP equipment. Appropriate microwave glass vessels with 10 mL capacity were used, tightly sealed with a Teflon lid. In all cases, the reaction vessel was loaded with the reaction components and sealed in a glove-box, under N₂ atmosphere.

Ultrasound

All ultrasound-assisted reactions were carried out in a 3 L OVAN ultrasonic equipment.

Nuclear Magnetic Resonance Spectroscopy (NMR)

The proton (^1H) and carbon (^{13}C) Nuclear Magnetic Resonance Spectroscopy (NMR) were recorded in a Bruker Avance 400 (400, 101 MHz, respectively), located in the Chemistry Department of the University of Coimbra. In both cases, tetramethylsilane (TMS) ($\delta=0.00$ ppm) was used as internal standard. NMR data is presented as follows: Nucleus (frequency, solvent): chemical shift (δ , ppm) [signal multiplicity (s-singlet, d-duplet, t-triplet, q-quartet, dd-doublet of doublets, ddd- doublet of doublet of doublets, td-triplet of doublets), coupling constant (J , in Hz), relative intensity (nH, where n is the proton number), proton/carbon assignment].

Mass spectrometry (MS)

The electron impact (EI) mass spectra were recorded in an Autospec Micromass by Unidade de Masas e Proteómica – University of Santiago de Compostela, Spain. The electrospray-time of flight (ESI-TOF) mass spectra were recorded in a Bruker Microtof by Unidade de Masas e Proteómica.

UV-Visible spectroscopy

The UV-Visible spectra were recorded in a Hitachi U-2010 spectrophotometer, using quartz cells with an optical path of 1 cm.

Solvent degassing

Solvents used in the Pd-catalyzed couplings were degassed using the freeze-pump-thaw method. Briefly, the oxygen of the system was removed by 3x cycles of vacuum/argon; then, the solvent was frozen with liquid nitrogen and was placed under vacuum for 5 min; then, the vacuum stopcock was closed, and the solution was warmed to room temperature; the system was degassed with 3x cycles of vacuum/argon and the aforementioned steps were repeated for a total of 3 times.

Solvent drying

When anhydrous conditions were required, toluene and 1,4-dioxane were dried using the Na/benzophenone method. In a round-bottom flask, sodium flakes and benzophenone were added to the solvent. The mixture was kept under reflux until a strong blue color was observed. After distillation, the solvents were stored under nitrogen atmosphere and activated 4 Å molecular sieves.¹

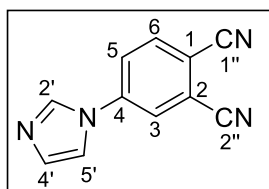
4.2 – Experimental of Chapter 2

4.2.1 – Synthesis of photosensitizers

4-(1*H*-imidazol-1-yl)phthalonitrile (2.1)

Conventional synthesis: In a round-bottom flask, imidazole (0.82 g, 12 mmol), 4-nitrophthalonitrile (1.7 g, 10 mmol) and K₂CO₃ (2.1 g, 15 mmol) were mixed in DMF (5 mL). The reaction was kept at room temperature for 48 h, with vigorous stirring. Then, the base was filtered off and the filtrate was washed with DMF. The product was precipitated from the reaction mixture by addition of cold water. The precipitate was washed with hot methanol (50 mL) under vigorous stirring. After filtering and drying, a yellow solid was obtained in 56% yield (1.1 g).

Ultrasound multi-gram synthesis: In a round-bottom flask, imidazole (2.45 g, 36 mmol), 4-nitrophthalonitrile (5.1 g, 30 mmol) and K₂CO₃ (6.2 g, 45 mmol) were mixed in DMSO (15 mL). The reaction was carried out under ultrasounds for 8 h. Then, cold water was added to the reaction mixture and the precipitated product was filtered off and dried. A yellow solid was obtained in 68% yield (4.75 g). Characterization data in accordance to literature.²



¹H NMR (400 MHz, DMSO-*d*₆): δ, ppm 8.58 (d, *J* = 1.7 Hz, 1H, H₃), 8.53 (s, 1H, H_{2'}), 8.29-8.22 (m, 2H, H₅, H₆), 7.98 (s, 1H, H_{5'}), 7.18 (s, 1H, H_{4'})

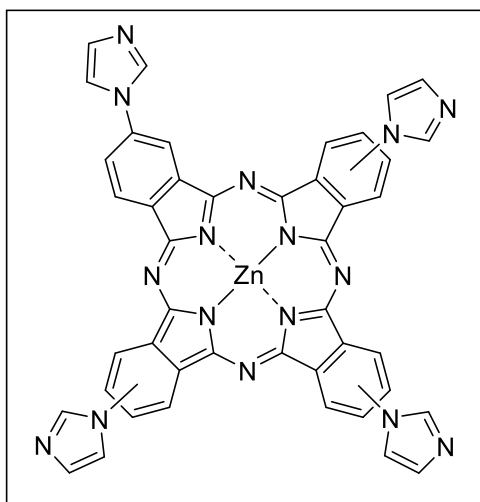
¹³C NMR (101 MHz, DMSO-*d*₆): δ, ppm 140.2 (C₄), 136.0 (C_{2'}), 135.7 (C₆), 130.9 (C_{4'}), 124.4 (C₃), 117.6 (C_{5'}), 116.4 (C₁), 115.6 (C_{1''}), 115.4 (C_{2''}), 111.7 (C₂)

MS (EI): *m/z* calculated for [C₁₁H₆N₄] 194.0592; Found: 194.0591 [M]⁺

2(3),9(10),16(17),23(24)-tetrakis(1H-imidazol-1-yl)phthalocyaninato zinc (II) (2.2)

Conventional synthesis: In a round-bottom flask, **2.1** (288 mg, 1.5 mmol) and Zn(OAc)₂·2H₂O (110 mg, 0.50 mmol) were dissolved in DMAE (2 mL). The reaction was stirred at 140 °C for 24 h, under inert atmosphere. After cooling, methanol was added to the reaction mixture and the resulting precipitate was filtered off and washed with water, methanol and acetone. After drying, a green precipitate was obtained in 71% yield (222 mg).

Microwave-assisted synthesis: A microwave vessel was loaded with **2.1** (288 mg, 2.6 mmol), Zn(OAc)₂·2H₂O (110 mg, 0.50 mmol) and DMAE (0.5 mL) as solvent. The reaction was carried at 140 °C during 1 h, with a P_{max} = 150 W. After cooling down, the product was precipitated using methanol, filtered and washed with water, methanol and acetone. The product was obtained in 69% yield (215 mg). Characterization data in accordance to literature.²



¹H NMR (400 MHz, pyridine-d₅): δ, ppm 9.41-9.24 (m, 8H, H_{Ar}), 8.91-8.83 (m, 4H, H_{Ar}), 8.31-8.06 (m, 8H, H_{Ar}), 7.80-7.72 (m, 4H, H_{Ar})

MS (ESI-TOF): m/z calculated for [C₄₄H₂₅N₁₆Zn] 841.1740; Found: 841.1735 [M+H]⁺

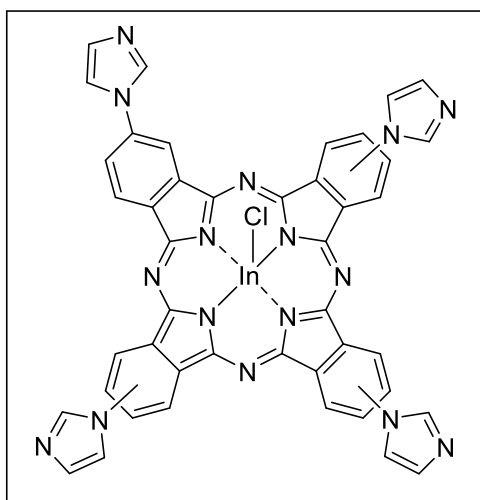
2(3),9(10),16(17),23(24)-tetrakis(1H-imidazol-1-yl)phthalocyaninato chloroindium (III) (2.3)

Conventional synthesis: In a round-bottom flask, **2.1** (288 mg, 1.5 mmol) and InCl₃ (111 mg, 0.50 mmol) were dissolved in quinoline (3 mL). The reaction was stirred at 180 °C for 8 h, under inert atmosphere. After cooling, methanol was added to the reaction mixture and the resulting precipitate was filtered off and washed with water,

methanol and acetone. After drying, a green precipitate was obtained in 67% yield (245 mg).

Microwave-assisted synthesis: A microwave vessel was loaded with **2.1** (288 mg, 2.6 mmol) and InCl_3 (111 mg, 0.50 mmol) and DMAE (0.5 mL) as solvent. The reaction was carried at 180 °C during 1 h, with a $P_{\text{max}} = 150$ W. After cooling down, the product was precipitated using methanol, filtered and washed with water, methanol and acetone. After drying, a green precipitate was obtained in 76% yield (278 mg).

Characterization data in accordance to literature.²

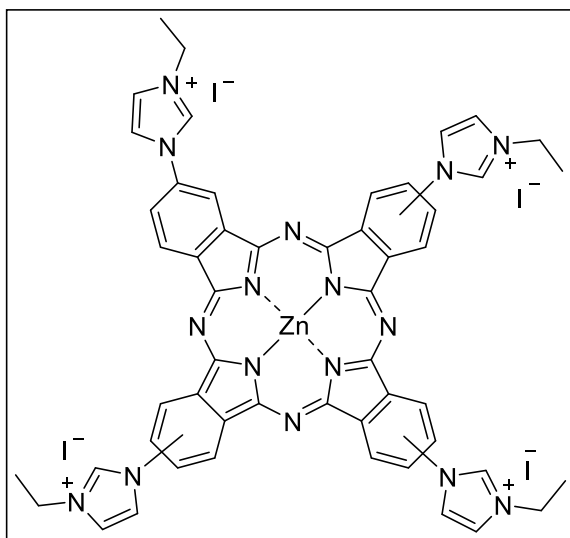


^1H NMR (400 MHz, DMSO- d_6): δ , ppm 8.54 (s, 4H, H_{Ar}), 8.17 (d, $J = 2.0$ Hz, 4H, H_{Ar}), 8.12 (dd, $J = 8.1, 2.0$ Hz, 4H, H_{Ar}), 8.01 (s, 4H, H_{Ar}), 7.94 (d, $J = 8.1$ Hz, 4H, H_{Ar}), 7.17 (s, 4H, H_{Ar})

MS (ESI-TOF): m/z calculated for $[\text{C}_{44}\text{H}_{26}\text{N}_{16}\text{Na}]$ 801.2424; Found: 801.4744 $[\text{M-InCl}+2\text{H}+\text{Na}]^+$

2(3),9(10),16(17),23(24)-tetrakis(3-ethyl-1H-imidazol-1-yl)phthalocyaninato zinc (II) tetraiodide (IPc-Zn-Et⁴⁺)

A microwave vessel was loaded with **2.2** (50 mg, 0.059 mmol) and iodoethane (94 μL , 1.18 mmol) and DMSO (0.3 mL). The reaction was carried at 120 °C during 5 min, with a $P_{\text{max}} = 150$ W. After cooling down, the product was precipitated using acetone and washed with diethyl ether. After drying, a green precipitate was obtained in 59% yield (51 mg). Characterization data in accordance to literature.²

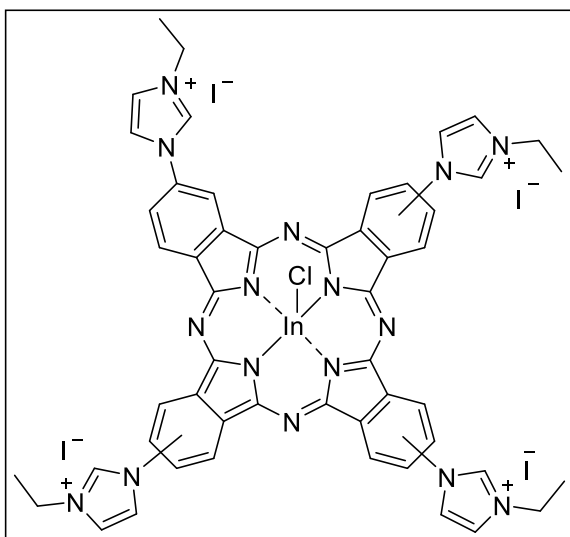


¹H NMR (400 MHz, DMSO-*d*₆): δ , ppm
 10.50-10.10 (m, 4H, H_{Ar}), 9.80-9.05 (m, 4H, H_{Ar}), 9.00-8.50 (m, 8H, H_{Ar}), 8.44-8.08 (m, 8H, H_{Ar}), 4.45 (br, 8H, H_{CH2}), 1.62 (brs, 12H, H_{CH3})

MS (ESI-TOF): *m/z* calculated for [C₅₂H₄₄I₃N₁₆Zn] 1337.0344; Found: 1337.0394 [M-I]⁺

2(3),9(10),16(17),23(24)-tetrakis(3-ethyl-1*H*-imidazol-1-yl)phthalocyaninato chloroindium (II) tetraiodide (IPc-In-Et⁴⁺)

A microwave vessel was loaded with **2.2** (50 mg, 0.054 mmol) and iodoethane (86 μ L, 1.08 mmol) and DMSO (0.3 mL). The reaction was carried at 120 °C during 5 min, with a P_{\max} = 150 W. After cooling down, the product was precipitated using acetone and washed with diethyl ether. After drying, a green precipitate was obtained in 63% yield (53 mg). Characterization data in accordance to literature.²

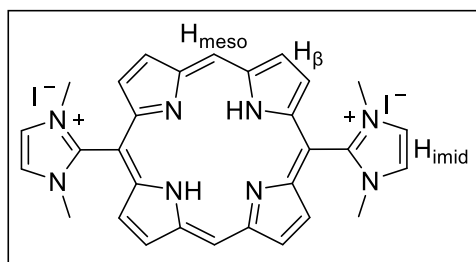


¹H NMR (400 MHz, DMSO-*d*₆): δ , ppm
 10.42 (brs, 4H, H_{Ar}), 9.94-9.50 (m, 8H, H_{Ar}), 8.89-8.77 (m, 8H, H_{Ar}), 8.33 (br, 4H, H_{Ar}), 4.53 (br, 8H, H_{CH2}), 1.74 (brs, 12H, H_{CH3})

MS (ESI-TOF): *m/z* calculated for [C₅₂H₄₄I₂N₁₆In]/2 630.5536; Found: 1337.0394 [M-Cl-2I]²⁺/2 630.5526

5,15-bis(1,3-dimethylimidazol-2-yl)porphyrinate diiodide (IP-H-Me²⁺)

A microwave vessel was loaded with 5,15-bis(1-methylimidazol-2-yl)porphyrin (50 mg, 0.11 mmol), iodomethane (68 μ L, 1.1 mmol) and DMSO (0.3 mL). The reaction was carried at 120 °C during 5 min, with a $P_{\max} = 150$ W. After cooling down, the product was precipitated using a mixture of acetone and pentane, filtered and dried. The desired porphyrin was obtained as a dark purple solid in 95% yield (82 mg). Characterization data in accordance to literature.³



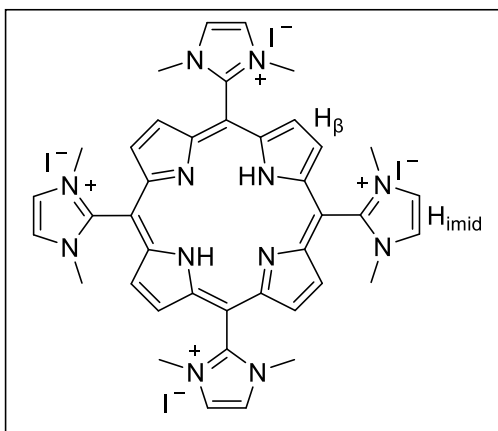
¹H NMR (400 MHz, CD₃OD): δ , ppm 10.89 (s, 2H, H_{meso}), 9.87-9.86 (m, 4H, H _{β}), 9.17-9.15 (m, 4H, H _{β}), 8.38 (s, 4H, H_{imid}), 3.85 (s, 12H, H_{Me})

MS (ESI-TOF): m/z calculated for [C₃₀H₂₈N₈]/2

250.1213; Found: 250.1218 [M-2I]²⁺/2.

5,10,15,20-tetrakis(1,3-dimethylimidazol-2-yl)porphyrinate tetraiodide (IP-H-Me⁴⁺)

A microwave vessel was loaded with 5,10,15,20-tetrakis(1-methylimidazol-2-yl)porphyrin (50 mg, 0.08 mmol), iodomethane (100 μ L, 1.6 mmol) and DMSO (0.3 mL). The reaction was carried at 120 °C during 5 min, with a $P_{\max} = 150$ W. After cooling down, the product was precipitated using a mixture of acetone and pentane, filtered and dried. The desired porphyrin was obtained as a dark brown solid in 92% yield (88 mg). Characterization data in accordance to literature.⁴

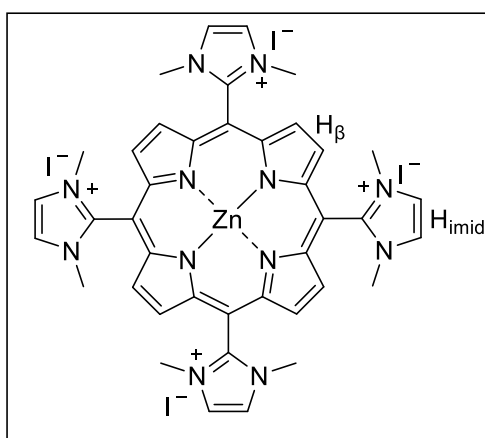


¹H NMR (400 MHz, DMSO-d₆): δ , ppm 9.35 (brs, 8H, H _{β}), 8.53 (s, 8H, H_{imid}), 3.75 (s, 24H, H_{Me}), -3.21 (brs, 2H, H_{NH})

MS (ESI-TOF): m/z calculated for [C₄₀H₄₂N₁₂]/4
172.5908; Found: 172.5908 [M-4I]⁴⁺/4

5,10,15,20-tetrakis(1,3-dimethylimidazol-2-yl)porphyrinate zin(II) tetraiodide (IP-Zn-Me⁴⁺)

A microwave vessel was loaded with IP-H-Me⁴⁺ (20 mg, 0.016 mmol), Zn(OAc)₂·2H₂O (35 mg, 0.16 mmol) and methanol (0.3 mL). The reaction was carried at 120 °C during 5 min, with a P_{max} = 150 W. After cooling down, the solvent was evaporated. Then, the crude was dissolved in water and purified through size exclusion chromatography, using Sephadex G10 as stationary phase. The desired porphyrin was obtained as a dark purple solid in 90% yield (18 mg). Characterization data in accordance to literature.⁴



¹H NMR (400 MHz, DMSO-d₆): δ, ppm 9.23 (brs, 8H, H_β), 8.51 (brs, 8H, H_{imid}), 3.69 (s, 24H, H_{Me})

MS (ESI-TOF): m/z calculated for [C₄₀H₄₀N₁₂Zn]/4 188.0692; Found: 188.0693 [M-4I]⁴⁺/4

4.2.2 – EcoScale calculations

The detailed calculations used for the assessment of the Ecoscale values⁵ in the optimization of the synthesis of phthalonitrile **2.1**, and of phthalocyanines **2.2** and **2.3** are presented in this subsection.

a) Synthesis of 4-(1H-imidazol-1-yl)phthalonitrile (2.1)

1. Conventional heating (room temperature), DMF as solvent, 48 h reaction time, 56% isolated yield (Table 2.1, entry 1):

Parameter	Deduction points
1. Yield: (100 - yield%)/2	22
2. Price of reaction components to obtain 10 mmol final product	0 (Inexpensive, < 10 \$)
3. Safety	10 (DMF, extremely toxic) 5 (DMF, highly flammable) 10 (imidazole, extremely toxic) 10 (K ₂ CO ₃ , extremely toxic)
4. Technical setup	0 (Common setup)
5. Temperature/time	2 (Room temperature < 48 h)
6. Workup and purification	2 (2x Crystallization and filtration)
7. Total (100 - deduction points)	39

2. Ultrasound (room temperature), DMF as solvent, 9 h reaction time, 62% isolated yield (Table 2.1, entry 2):

Parameter	Deduction points
1. Yield: (100 - yield%)/2	19
2. Price of reaction components to obtain 10 mmol final product	0 (Inexpensive, < 10 \$)
3. Safety	10 (DMF, extremely toxic) 5 (DMF, highly flammable) 10 (Imidazole, extremely toxic) 10 (K ₂ CO ₃ , extremely toxic)
4. Technical setup	2 (Ultrasound activation)
5. Temperature/time	1 (Room temperature < 24 h)
6. Workup and purification	2 (2x Crystallization and filtration)
7. Total (100 - deduction points)	41

3. Ultrasound (room temperature), DMSO as solvent, 8 h reaction time, 68% isolated yield (Table 2.1, entry 4):

Parameter	Deduction points
1. Yield: (100 - yield%)/2	16
2. Price of reaction components to obtain 10 mmol final product	0 (Inexpensive, < 10 \$)
3. Safety	10 (Imidazole, extremely toxic) 10 (K ₂ CO ₃ , extremely toxic)
4. Technical setup	2 (Ultrasound activation)
5. Temperature/time	1 (Room temperature < 24 h)
6. Workup and purification	1 (Crystallization and filtration)
7. Total (100 - deduction points)	60

b) Synthesis of 2(3),9(10),16(17),23(24)-tetrakis(1*H*-imidazol-1-yl)phthalocyaninato zinc (II) (2.2)

1. Conventional heating (140 °C), DMAE as solvent, 24 h reaction time, 71% isolated yield (Table 2.3, entry 1):

Parameter	Deduction points
1. Yield: (100 - yield%)/2	14.5
2. Price of reaction components to obtain 10 mmol final product	0 (Inexpensive, < 10 \$)
3. Safety	10 (Zinc acetate, extremely toxic) 5 (Zinc acetate, dangerous for environment) 5 (DMAE, toxic) 5 (DMAE, highly flammable)
4. Technical setup	0 (Common setup)
5. Temperature/time	3 (Heating, > 1 h)
6. Workup and purification	1 (Crystallization and filtration)
7. Total (100 - deduction points)	56.5

2. Microwave heating (140 °C), DMAE as solvent, 1 h reaction time, 69% isolated yield (Table 2.3, entry 2):

Parameter	Deduction points
1. Yield: (100 - yield%)/2	15.5
2. Price of reaction components to obtain 10 mmol final product	0 (Inexpensive, < 10 \$)
3. Safety	10 (Zinc acetate, extremely toxic) 5 (Zinc acetate, dangerous for environment) 5 (DMAE, toxic) 5 (DMAE, highly flammable)
4. Technical setup	2 (Microwave activation)
5. Temperature/time	2 (Heating, < 1 h)
6. Workup and purification	1 (Crystallization and filtration)
7. Total (100 - deduction points)	56.5

c) 2(3),9(10),16(17),23(24)-tetrakis(1*H*-imidazol-1-yl)phthalocyaninato chloroindium (III) (2.3)

1. Conventional heating (180 °C), Quinoline as solvent, 8 h reaction time, 67% isolated yield (Table 2.3, entry 3):

Parameter	Deduction points
1. Yield: (100 - yield%)/2	16.5
2. Price of reaction components to obtain 10 mmol final product	0 (Inexpensive, < 10 \$)
3. Safety	10 (Indium chloride, extremely toxic) 10 (Quinoline, extremely toxic) 5 (Quinoline, dangerous for the environment)
4. Technical setup	0 (Common setup)
5. Temperature/time	3 (Heating, > 1 h)
6. Workup and purification	1 (Crystallization and filtration)
7. Total (100 - deduction points)	56.5

2. Microwave heating (180 °C), Quinoline as solvent, 1 h reaction time, 66% isolated yield (Table 2.3, entry 4):

Parameter	Deduction points
1. Yield: (100 - yield%)/2	17
2. Price of reaction components to obtain 10 mmol final product	0 (Inexpensive, < 10 \$)
3. Safety	10 (Indium chloride, extremely toxic) 10 (Quinoline, extremely toxic) 5 (Quinoline, dangerous for the environment)
4. Technical setup	2 (Microwave activation)
5. Temperature/time	2 (Heating, < 1 h)
6. Workup and purification	1 (Crystallization and filtration)
7. Total (100 - deduction points)	56.5

3. Microwave heating (180 °C), DMAE as solvent, 1 h reaction time, 76% isolated yield (Table 2.3, entry 5):

Parameter	Deduction points
1. Yield: (100 - yield%)/2	12
2. Price of reaction components to obtain 10 mmol final product	0 (Inexpensive, < 10 \$)
3. Safety	10 (Indium chloride, extremely toxic) 5 (DMAE, toxic) 5 (DMAE, highly flammable)
4. Technical setup	2 (Microwave activation)
5. Temperature/time	2 (Heating, < 1 h)
6. Workup and purification	1 (Crystallization and filtration)
7. Total (100 - deduction points)	63

4.2.3 – *In vitro* biological studies

Bacterial strains and culture conditions

In this study, we selected a standard *E. coli* strain from American Type Culture Collection (ATCC 25922), which is used as a control in evaluation of antibiotic susceptibility tests (clinical antibiograms)⁶ that shows susceptibility to ciprofloxacin and an *E. coli* strain from our laboratory that shows reduced susceptibility to ciprofloxacin

(MIC = 0.25 mg/L; just a \log_2 below the breakpoint that defines clinical resistance), herein referred to as reduced susceptibility (RS) *E. coli* strain.

The MDR *E. coli* strain used was isolated from an aviary, showing resistance to ciprofloxacin (MIC = 32 mg/L), tetracyclines and amoxicillin.

Mueller-Hinton broth (Sigma Aldrich) was used for overnight incubation in MIC determination of ciprofloxacin and for dual phototherapy studies. For CFU counting, plates coated with Mueller Hinton agar (MH, Sigma Aldrich) were used.

Photosensitizers and antibiotics

Stock solutions of the photosensitizers were prepared by dissolving 1.0 mg in 1.0 mL DMSO. Further dilutions to the appropriate concentration were made using distilled water. Ciprofloxacin was commercially acquired as its corresponding HCl salt (Sigma-Aldrich). Stock solutions (1 mg/mL) of ciprofloxacin in water slightly acidified with HCl (pH = 5) were prepared and further diluted using distilled water.

Light sources

For phthalocyanine irradiation (**IPc-Zn-Et⁴⁺**, **IPc-In-Et⁴⁺**), a custom-made red LED (λ_{\max} = 659 nm) with fluence of 4.0 mW/cm² was used. For porphyrin irradiation (**IP-H-Me²⁺**, **IP-H-Me⁴⁺**, **IP-Zn-Me⁴⁺**), a custom-made blue LED (λ_{\max} = 415 nm) with fluence of 3.0 mW/cm² was used.

Ciprofloxacin MIC determination

The planktonic *E. coli* strains were cultured in Mueller–Hinton agar (MH) at 37 °C overnight. Cell density was adjusted to 0.5 optical density in MacFarland grade in double distilled (ddH₂O), which corresponds to approximately 1-2 x 10⁸ CFU/mL, and was diluted 20-fold. The range of CIP concentrations tested was 500 mg/L to 0.004 mg/L. Sterile microplates with 96 round-bottomed wells were filled with MH broth, CIP, and 10 μ L of the bacteria solutions, in order to have a final inoculum size of approximately 5 x 10⁵ CFU/mL. For experiments where the effect of the inoculum size on MIC was measured, further dilutions of the 5 x 10⁵ CFU/mL inoculum were performed accordingly. Wells with only MH medium, or bacteria were used as sterile, and growth

controls, respectively. The microplates were incubated at 37 °C for 20 h. The lowest concentration of the compound that prevented visible growth was considered to be the minimal inhibitory concentration (MIC). The experiments were performed in triplicate.

Photodynamic inactivation of planktonic cultures

The planktonic *E. coli* strains were cultured in Mueller–Hinton agar (MH) at 37 °C overnight. Cell density was adjusted to 0.5 optical density in MacFarland grade in ddH₂O, which corresponds to approximately $1 - 2 \times 10^8$ CFU/mL, and was diluted 20-fold. In 96-well plates, 10 µL of the diluted inoculum were added to a solution of 90 µL of photosensitizer in ddH₂O at the desired concentration, for a final inoculum size of 5×10^5 CFU/mL. The plates were incubated in the dark, at room temperature, for 1h. Following incubation, the wells were irradiated with the appropriate light source, using light doses between 1.8 - 5.4 J/cm². Dark controls were covered in aluminum foil during the time of irradiation. The light dose used represents the actual light dose absorbed by each compound, corrected by LED light emission overlap with compound absorption ⁷, using the following multiplicative factors: **IPc-In-Et⁴⁺** = 0.28; **IPc-Zn-Et⁴⁺** = 0.34; **IP-H-Me²⁺** = 0.25; **IP-H-Me⁴⁺** = 0.69; **IP-Zn-Me⁴⁺** = 0.63. After irradiation, 10 µL aliquots were taken from each well and dilutions in water were done as needed and plated in Petri dishes with MH agar. After 37 °C incubation during 24 h, the colony-forming units (CFU) were counted. Experiments were performed in triplicate. Data analysis was carried out in GraphPad Prism 8.0 (GraphPad Software, San Diego, California USA).

Dual phototherapy

The planktonic *E. coli* strains were cultured in Mueller–Hinton agar (MH) at 37 °C overnight. Cell density was adjusted to 0.5 optical density in MacFarland grade in ddH₂O, which corresponds to approximately $1-2 \times 10^8$ CFU/mL, and was diluted 20-fold. In 96-well plates, 10 µL of the diluted inoculum were added to a solution of 80 µL of photosensitizer in ddH₂O at the desired concentration, for a final inoculum size of 5×10^5 CFU/mL. Then, 10 µL of several 2-fold diluted stock solutions of CIP at different concentrations were added (for PDI + CIP simultaneous treatment modality **A**) or 10 µL of ddH₂O (for PDI before CIP, modality **B**). The plates were incubated in the dark, at room

temperature, for 1 h. Following incubation, the wells were irradiated with the appropriate light source, using light doses between 1.8 – 45.3 J/cm². After irradiation of the wells, an aliquot of 10 µL of ddH₂O (PDI + CIP simultaneous treatment modality **A**) or from several 2-fold diluted stock solutions of CIP were added (for PDI before CIP, modality **B**), in order to calculate the MIC_{CIP}. Next, 100 µL of MH broth were added to each well, and the plates were incubated at 37 °C during 20 h. The MIC_{CIP} was determined as the minimum concentration of ciprofloxacin required to inhibit visible bacterial growth. Experiments were performed in triplicate. Data analysis was carried out in GraphPad Prism 8.0.

Bacterial growth curve under dual phototherapy

Following the general procedure **B** for dual phototherapy, deep 96-well plates of 1 mL volume were used. Volumes were scaled up ≈ 5-fold: 400 µL of photosensitizer solution and 50 µL of bacterial inoculum were used. After irradiation, 50 µL of stock solution of CIP were added to achieve the desired final concentrations, followed by 500 µL of MH broth. Then, the plates were left at 4 °C or 20 °C for 18 h. After this time, the content of each well was homogenized and transferred to 1 mL plastic cuvettes, which were incubated at 37 °C and 300 rpm, corresponding to t = 0 time point. The optical density was measured at 610 nm for each sample hourly, using Thermo Scientific Genesys 10UV spectrophotometer. Growth curves were constructed in GraphPad Prism 8.0.

4.2.4 – *In vivo* dual phototherapy

Escherichia coli (ATCC 25922) was used for contamination of mice wounds. The inoculum maintained in glycerol (40%) in Brain Heart Infusion liquid culture (BHI, Kasvi, São José dos Pinhais, Brazil) medium at -20 °C was reactivated in BHI (9:1) at 37 °C, 150 rpm for 16 h in a rotary incubator (model Q315IA Quimis® - Brazil) and centrifuged to remove the culture medium. All procedures were approved by the Institutional Committee for the Use and Care of Animals (protocol 3375250621) of the São Carlos Institute of Physics. The induction of skin wounds in Swiss mice was performed using the methodology proposed by Takakura *et al.* (2003).⁸ The animals were immunosuppressed

on the first and fifth day of the experiment by two subcutaneous injections of methylprednisolone acetate 40 mg/kg body weight using 40 mg/mL. The animals were anesthetized on the second day of the experiment with an intraperitoneal injection of a solution of ketamine (30 mg/kg), xylazine (13 mg/kg) and diazepam 5 mg/kg. The wound was made with the animals shaved using a punch of 3 mm in diameter, and 50 μ L of *E. coli* suspension in 10^8 CFU/mL was added to the wound. The animals were anesthetized with a solution of ketamine and xylazine (the same concentration) after 6 days of bacterial inoculation, and separated in groups containing three animals each. The mice in the PDI + CIP group received a topical application of 50 μ L of **IP-H-Me⁴⁺** at 20 μ M, followed by 1 h dark incubation and then LED illumination was performed with 50 J/cm² at 410 nm, and in sequence 1.25 μ g/mL of ciprofloxacin was added during 1h. Other animals only received the application of PS, light or ciprofloxacin in the same parameters, and the control group didn't receive any treatment. Immediately after the application of treatments, the microorganisms were collected using a sterile swab soaked in saline solution (5x) and rubbed for 30 seconds on the wound. The collection was subjected to serial dilutions and seeded in duplicate on BHI agar medium (HIMEDIA, India). The plates were incubated for 24 h at 37 °C and, the values of CFU/mL were calculated. A second collection was also carried out 72 h after the treatments, following the same procedure. Then, the mice were euthanized in accordance with the procedure approved by the Ethic Committee on Animal Use of the Physics Institute of Sao Carlos - Sao Paulo University (CEUA/IFSC) (Figure 4.1).



CERTIFICADO

Certificamos que a proposta intitulada "Uso combinado de antibióticos e terapia fotodinâmica para o tratamento de feridas contaminadas", protocolada sob o CEUA nº 3375250621, sob a responsabilidade de **Kate Cristina Blanco e equipe; Vanderlei Salvador Bagnato** - que envolve a produção, manutenção e/ou utilização de animais pertencentes ao filo Chordata, subfilo Vertebrata (exceto o homem), para fins de pesquisa científica ou ensino - está de acordo com os preceitos da Lei 11.794 de 8 de outubro de 2008, com o Decreto 6.899 de 15 de julho de 2009, bem como com as normas editadas pelo Conselho Nacional de Controle da Experimentação Animal (CONCEA), e foi **aprovada** pela Comissão de Ética no Uso de Animais da Instituto de Física de São Carlos - Universidade de São Paulo (CEUA/IFSC) na reunião de 05/08/2021.

We certify that the proposal "Combined use of antibiotics and photodynamic therapy for the treatment of contaminated wounds", utilizing 40 Heterogenics mice (40 females), protocol number CEUA 3375250621, under the responsibility of **Kate Cristina Blanco and team; Vanderlei Salvador Bagnato** - which involves the production, maintenance and/or use of animals belonging to the phylum Chordata, subphylum Vertebrata (except human beings), for scientific research purposes or teaching - is in accordance with Law 11.794 of October 8, 2008, Decree 6899 of July 15, 2009, as well as with the rules issued by the National Council for Control of Animal Experimentation (CONCEA), and was **approved** by the Ethic Committee on Animal Use of the Physics Institute of São Carlos - São Paulo University (CEUA/IFSC) in the meeting of 08/05/2021.

Finalidade da Proposta: **Pesquisa (Acadêmica)**

Vigência da Proposta: de **08/2021 a 10/2021** Área: **Grupo de Óptica / Fcm**

Origem: **Serviço de Biotério da Prefeitura da USP - Campus de Ribeirão Preto**
Espécie: **Camundongos heterogênicos** sexo: **Fêmeas** idade: **6 a 6 meses** N: **40**
Linhagem: **Swiss** Peso: **25 a 25 g**

Local do experimento: **Biotério do Laboratório de Biofotônica**

Sao Carlos, 24 de novembro de 2021

Prof. Dr. Fernando Fernandes Paiva
Coordenador da Comissão de Ética no Uso de Animais
Instituto de Física de São Carlos - Universidade de São Paulo

Profa. Dra. Ana Paula Ulian de Araújo
Vice-Coordenadora da Comissão de Ética no Uso de Animais
Instituto de Física de São Carlos - Universidade de São Paulo

Figure 4.1: Certificate of approval from the Ethic Committee on Animal Use of the Physics Institute of São Carlos - São Paulo University (CEUA/IFSC).

4.3 – Experimental of Chapter 3

4.3.1 – Computer-aided drug design methods

Generation of the pharmacophore model

Through a comprehensive literature search,⁹⁻¹⁹ several ligands of the *E. coli* DNA gyrase subunit B with different affinities were identified. From a total of 145 compounds, 61 were classified as actives ($IC_{50} \leq 1.0 \mu M$), 54 as intermediates ($1.0 \mu M < IC_{50} < 100 \mu M$) and 30 as inactives ($IC_{50} \geq 100 \mu M$). From the actives dataset, the most structurally diverse 18 compounds were selected as the training set while the remaining 43 were included in the test set. In cases where multiple derivatives were present, the compound with the highest activity was chosen. For the purpose of generating the pharmacophore queries, MOE (Molecular Operating Environment) 2018.0802 software was used,²⁰ using the Unified and EHT annotation schemes. After the training set ligands' structural alignment, common features were identified using MOE's annotation schemes. From a set of about 50 pharmacophoric queries generated through variation of feature type, number and radii, the best models were selected based on their performance in discriminating between actives and inactives in the test sets and computer-generated decoys. The 3750 computer-generated decoys were obtained with the DUD-E tool, based on the actives dataset.²¹

Docking studies on *E. coli* DNA gyrB

Docking studies were performed in GOLD 5.4 (Cambridge Crystallographic Data Centre),²² using *E. coli*'s DNA gyrase subunit B ATPase binding domain crystallographic structure (PDB entry 4KFG).²³ For protein preparation, hydrogen atoms were added to the binding site residues and correct tautomers and protonation states were assigned. Water molecules and the ligand were deleted from the crystal structure before the docking studies. The binding site region was defined by a radius of 15 Å around the THR165 residue. To validate our protocol, the crystal structure ligand was docked into the defined binding site and the best scoring pose was able to reproduce the crystallographic pose with an RMSD value of 0.57 Å. A set of 10 structurally diverse

compounds with varying values of IC_{50} was docked using the defined pro-tocol. The following scoring functions were tested: ChemScore, GOLDScore and ChemPLP. The scoring function that yielded a better docking score correlation with experimental IC_{50} (ChemScore) was selected. From a set containing 6681 computationally generated derivatives of 2-aminophenyl-5(6)-substituted benzimidazoles, GOLD's ChemScore function was used to rank their predicted inhibitory activity. The best scoring poses were then graphically analyzed in MOE and the relevant protein side-chain interactions were determined.

Screening of NCI database

The NCI database (Release 4 File Series - May 2012) containing 265,242 structures in sdf format was downloaded²⁴ and loaded into MOE. The dataset was washed and protonated considering pH = 7. Using the tool "pharmacophore search", the NCI database was screened using the optimized pharmacophore A (unified scheme) with volume exclusion spheres. The resulting hit database was further screened using the optimized pharmacophore B (EHT scheme) with volume exclusion spheres. The hit list from both pharmacophores was analyzed using the online tool FAFDrugs4,²⁵ in order to identify problematic functional groups (structural alerts), potential covalent inhibitors and pan-assay interference compounds (PAINS). The dataset composed of compounds with no to low risk were docked in the crystallographic structure of *E. coli*'s DNA gyrase subunit B ATPase binding domain crystallo-graphic structure (PDB entry 4KFG).²³ The best scoring compounds were acquired from the NCI for biological testing.

***De novo* design and screening of a virtual library**

The *de novo* design of a virtual library was carried out using the "Add group to ligand" tool in MOE, using a 2-(2-aminophenyl)-1*H*-benzimidazole as base scaffold. The benzimidazole 5(6) position was selected for adding multiple computer-generated substituents. The following restrictions were applied for the final structures: Mw < 500 Da, TPSA < 40-120 Å² and number of rotatable bonds < 10. In total, 23,832 unique structures were generated. The dataset was washed and protonated considering pH = 7. The dataset was screened using pharmacophore A and B with volume exclusion

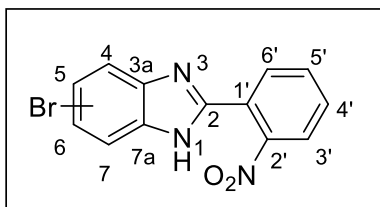
spheres and through molecular docking, using *E. coli*'s DNA gyrase subunit B ATPase binding domain crystallographic structure (PDB entry 4KFG),²³ under the same conditions reported for the screening of the NCI database.

4.3.2 – Synthesis of benzimidazole compound family

5(6)-bromo-2-(2-nitrophenyl)-1H-benzimidazole (3.1)

Nitrobenzene method: In a round-bottom flask, 4-bromo-1,2-benzenediamine (900 mg, 4.83 mmol) and 2-nitrobenzaldehyde (800 mg, 5.31 mmol) were mixed in nitrobenzene (10 mL). The reaction was stirred at 180 °C for 8 h, after which the nitrobenzene was distilled, under reduced pressure. The obtained black slurry was dissolved in ethyl acetate, followed by the addition of silica powder and evaporation of the solvent to dryness. The resulting solid was loaded into a silica gel column, and the crude was purified with a gradient elution with dichloromethane/ethyl acetate, starting with pure dichloromethane and finishing with 20:1. The product was obtained as a yellow solid in 48% yield (738 mg).

Ethanol method: In a round-bottom flask, 4-bromo-1,2-benzenediamine (5.0 g; 26.8 mmol), 2-nitrobenzaldehyde (4.46 g; 29.6 mmol) and 500 mg of Montmorillonite K10 were mixed in ethanol (60 mL). The reaction was stirred at room temperature for 4 h. The mixture was filtered, the solvent was evaporated, and the obtained dark orange slurry was dissolved in ethyl acetate, followed by the addition of silica powder and the evaporation of the solvent to dryness. The resulting solid was loaded into a silica gel column, and the crude was purified dichloromethane/ethyl acetate 10:1. The product was obtained as a yellow solid in 62% yield (5.28 g).



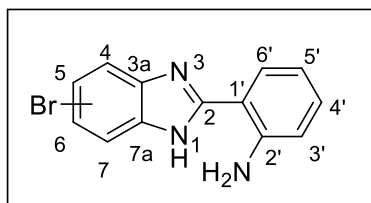
¹H NMR (400 MHz, DMSO-*d*₆): δ , ppm 14.50-12.00 (brs, 1H, N-H), 8.05 (dd, $J = 8.0, 1.3$ Hz, 1H, H_{3'}), 7.97 (dd, $J = 7.8, 1.5$ Hz, 1H, H_{6'}), 7.88 (td, $J = 7.6, 1.3$ Hz, 1H, H_{5'}), 7.82 (d, $J = 1.9$ Hz, 1H, H_{4/7}), 7.78 (td, $J = 7.8, 1.5$ Hz, 1H, H_{4'}), 7.59 (d, $J = 8.5$ Hz, 1H, H_{7/4}), 7.39 (dd, $J = 8.5, 2.0$ Hz, 1H, H_{6/5})

¹³C NMR (101 MHz, DMSO-*d*₆): δ, ppm 148.9 (C_{2'}), 148.7 (C₂), 132.8 (C_{5'}), 131.2 (C_{4'}), 131.1 (C_{6'}), 125.4 (C_{6/5}), 124.4 (C_{3'}), 123.9 (C_{1'}), 118.1 (C_{4/7}), 116.5 (C_{7/4}), 114.7 (C_{5/6}). C_{3a} and C_{7a} not visible due to tautomerism.

MS (ESI-TOF): m/z calculated for [C₁₃H₉BrN₃O₂] 317.9878; Found: 317.9877 [M+H]⁺

2-(2-aminophenyl)-5(6)-bromo-1*H*-benzimidazole (3.2)

In a round-bottom flask, 5(6)-bromo-2-(2-nitrophenyl)-1*H*-benzimidazole (1.5g, 4.72 mmol), hydrazine monohydrate (2.3 mL, 47.2 mmol) and Pd/C 5% (117 mg) were mixed in methanol (20 mL). The solution was stirred for 30 min at reflux temperature (70 °C). The resulting solution was filtrated, and ethyl acetate was added. The organic phase was washed 5x with water and dried with anhydrous Na₂SO₄. The product was purified by silica gel chromatography using ethyl acetate as eluent. A dark yellow compound was obtained in 79% yield (1.07g).



¹H NMR (400 MHz, CDCl₃): δ, ppm 7.73 (d, *J* = 1.8 Hz, 1H, H_{4/7}), 7.52 (dd, *J* = 7.9, 1.5 Hz, 1H, H_{6'}), 7.45 (d, *J* = 8.5 Hz, 1H, H_{7/4}), 7.35 (dd, *J* = 8.5, 1.8 Hz, 1H, H_{6/5}), 7.22 (ddd, *J* = 8.2, 7.2, 1.5 Hz, 1H, H_{4'}), 6.81 (dd, *J* = 8.2, 1.1 Hz, 1H, H_{3'}), 6.75 (ddd, *J* = 7.9, 7.2, 1.1 Hz, 1H, H_{5'})

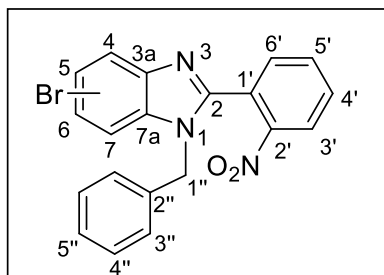
¹³C NMR (101 MHz, CDCl₃): δ, ppm 152.8, 147.6, 131.5, 126.7, 126.0, 117.9, 117.3, 117.1, 116.0, 115.8, 110.9. C_{3a} and C_{7a} not visible due to tautomerism.

MS (ESI-TOF): m/z calculated for [C₁₃H₁₁BrN₃] 288.0136; Found: 288.0131 [M+H]⁺

1-benzyl-5(6)-bromo-2-(2-nitrophenyl)-1*H*-benzimidazole (3.3)

In an oven-dried *Schlenk* tube coupled with a condenser, 5(6)-bromo-2-(2-nitrophenyl)-1*H*-benzimidazole (2.5 g, 7.86 mmol) was dissolved in dry THF (5 mL). The system was degassed with 5x vacuum/argon cycles. To the stirring solution at 0 °C, NaH (60% in mineral oil) (226 mg, 9.43 mmol) was slowly added under an argon flow. After the evolution of the hydrogen gas, benzyl bromide (1.12 mL, 9.43 mmol) and a catalytic amount of tetra-*n*-butylammonium iodide were added. The mixture was heated at reflux

temperature (70 °C) for 2h. After cooling, the reaction was quenched with methanol, and the solvent was evaporated. The crude was purified by column chromatography using dichloromethane/ethyl acetate 1:20. The isomer mixture was obtained as a yellow solid in 87% yield (2.8 g).



¹H NMR (400 MHz, CDCl₃): 1:1 regioisomer mixture; δ , ppm 8.17-8.10 (m, 1H, H_{Ar}), 7.89 (d, $J = 1.8$ Hz, 0.5H, H_{Ar}), 7.65-7.59 (m, 2.5H, H_{Ar}), 7.44 – 7.33 (m, 2H, H_{Ar}), 7.30 (dd, $J = 8.6, 1.8$ Hz, 0.5H, H_{Ar}), 7.22-7.16 (m, 3H, H_{4''}, H_{5''}), 7.03 (d, $J = 1.8$ Hz, 0.5H, H_{Ar}), 6.96-6.90 (m, 2H, H_{3''}), 5.13 (s, 1H, H_{1'''}), 5.11 (s, 1H, H_{1'''})

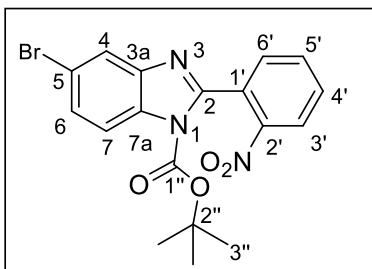
¹³C NMR (101 MHz, CDCl₃): 1:1 regioisomer mixture; δ , ppm 150.9, 150.5, 148.8, 144.1, 141.8, 136.2, 135.1, 135.0, 134.1, 133.6, 133.5, 132.73, 132.70, 131.58, 131.56, 129.2, 129.1, 128.41, 128.38, 126.8, 126.76, 126.72, 126.4, 125.38, 125.4, 125.2, 125.1, 123.1, 121.5, 117.0, 116.0, 113.8, 112.1, 48.7, 48.6

MS (ESI-TOF): m/z calculated for [C₁₃H₉BrN₃O₂] 408.0348; Found: 408.0345 [M+H]⁺

1-boc-5-bromo-2-(2-nitrophenyl)-1H-benzimidazole and 1-boc-6-bromo-2-(2-nitrophenyl)-1H-benzimidazole (3.4)

In a round-bottom flask, 5(6)-bromo-2-(2-nitrophenyl)-1H-benzimidazole (1.66 g, 5.22 mmol), di-tert-butyl dicarbonate (2.28g, 10.44 mmol) and DMAP (638 mg, 5.22 mmol) were mixed in dichloromethane (30 mL) and the reaction was left stirring at room temperature for 24 h. The solvent was evaporated, and the product was purified by column chromatography using hexane/ethyl acetate 4:1 as eluent. Two pure fractions of light yellow solids (isomers **3.4a** and **3.4b**) were obtained in a 1:1 ratio with an overall yield of 89% (1.95 g).

1-boc-5-bromo-2-(2-nitrophenyl)-1H-benzimidazole (3.4a)

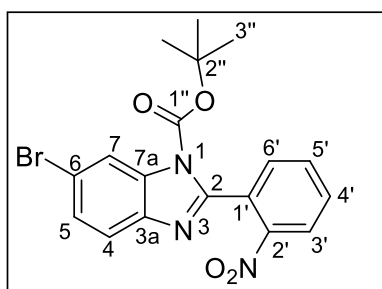


^1H NMR (400 MHz, CDCl_3): δ , ppm 8.30 (dd, $J = 8.2, 1.3$ Hz, 1H, $\text{H}_{3'}$), 7.95 (d, $J = 8.7$ Hz, 1H, H_7), 7.92 (d, $J = 1.9$ Hz, 1H, H_4), 7.79 (td, $J = 7.5, 1.3$ Hz, 1H, $\text{H}_{5'}$), 7.70 (ddd, $J = 8.2, 7.5, 1.6$ Hz, 1H, $\text{H}_{4'}$), 7.64 (dd, $J = 7.5, 1.6$ Hz, 1H, $\text{H}_{6'}$), 7.54 (dd, $J = 8.7, 1.9$ Hz, 1H, H_6), 1.37 (s, 9H, $\text{H}_{3''}$)

^{13}C NMR (101 MHz, CDCl_3): δ 151.0 (C_2), 147.74 ($\text{C}_{1''}$), 147.73 (C_2'), 144.0 (C_{3a}), 133.9 ($\text{C}_{5'}$), 132.2 (C_{7a}), 132.1 ($\text{C}_{6'}$), 130.8 ($\text{C}_{4'}$), 128.8 ($\text{C}_{1'}$), 128.7 (C_6), 124.7 ($\text{C}_{3'}$), 123.4 (C_4), 117.7 (C_5), 116.7 (C_7), 86.4 ($\text{C}_{2''}$), 27.7 ($\text{C}_{3''}$)

MS (ESI-TOF): m/z calculated for $[\text{C}_{18}\text{H}_{17}\text{BrN}_3\text{O}_4]$ 418.0402; Found: 418.0403 $[\text{M}+\text{H}]^+$

1-boc-6-bromo-2-(2-nitrophenyl)-1H-benzimidazole (3.4b)



^1H NMR (400 MHz, CDCl_3): δ , ppm 8.30 (dd, $J = 8.2, 1.3$ Hz, 1H, $\text{H}_{3'}$), 8.28 (d, $J = 1.9$ Hz, 1H, H_7), 7.79 (td, $J = 7.5, 1.3$ Hz, 1H, $\text{H}_{5'}$), 7.70 (ddd, $J = 8.2, 7.5, 1.5$ Hz, 1H, $\text{H}_{4'}$), 7.65 (dd, $J = 7.5, 1.5$ Hz, 1H, $\text{H}_{6'}$), 7.64 (d, $J = 8.5, 1$ Hz, H_4), 7.52 (dd, $J = 8.5, 1.9$ Hz, 1H, H_5), 1.37 (s, 9H, $\text{H}_{3''}$)

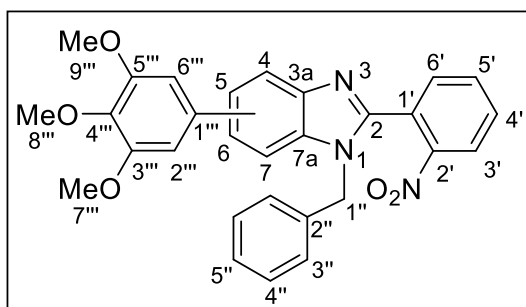
^{13}C NMR (101 MHz, CDCl_3): δ 150.2 (C_2), 147.6 (C_2'), 147.6 ($\text{C}_{1''}$), 141.6 (C_{3a}), 133.94 (C_{7a}), 133.8 ($\text{C}_{5'}$), 132.0 ($\text{C}_{6'}$), 130.7 ($\text{C}_{4'}$), 128.7 ($\text{C}_{1'}$), 127.9 (C_5), 124.6 ($\text{C}_{3'}$), 121.4 (C_4), 119.0 (C_6), 118.5 (C_7), 86.4 ($\text{C}_{2''}$), 27.5 ($\text{C}_{3''}$)

MS (ESI-TOF): m/z calculated for $[\text{C}_{18}\text{H}_{17}\text{BrN}_3\text{O}_4]$ 418.0402; Found: 418.0403 $[\text{M}+\text{H}]^+$

1-benzyl-5(6)-(3,4,5-trimethoxyphenyl)-2-(2-nitrophenyl)-1H-benzimidazole (3.5)

In a *Schlenk* tube, 1-benzyl-5(6)-bromo-2-(2-nitrophenyl)-1H-benzimidazole (500 mg, 1.22 mmol) and 3,4,5-trimethoxyphenylboronic acid (526 mg, 2.48 mmol) were dissolved in a mixture of THF/ H_2O 4:1 (15 mL). Under an argon flow, $\text{Pd}(\text{OAc})_2$ (27 mg; 0.12 mmol), PPh_3 (80 mg; 0.30 mmol) and K_2CO_3 (380 mg, 9.2 mmol) were added and the reaction was heated to 70 °C for 16 h. After cooling, ethyl acetate was added to the reaction, and the insoluble solid was filtered. The organic phase was then washed with

a 1M solution of NaOH (5x), followed by water (2x). After drying with Na₂SO₄ and filtering, the solvent was evaporated. Then, a column chromatography in silica gel was performed using dichloromethane/ethyl acetate 5:1 as eluent. The isomer mixture was obtained as a yellow solid in 66% yield (399 mg).



¹H NMR (400 MHz, CDCl₃): 1:1 regioisomer mixture; δ , ppm 8.20-8.11 (m, 1H, H_{Ar}), 7.94 (d, $J = 1.6$ Hz, 0.5H, H_{Ar}), 7.79 (d, $J = 8.4$ Hz, 0.5H, H_{Ar}), 7.67 – 7.58 (m, 2H, H_{Ar}), 7.48 – 7.40 (m, 2H, H_{Ar}), 7.27-7.18 (m, 4H, H_{Ar}), 7.02-6.95 (m, 2H, H_{Ar}), 6.76 (s, 1H, H_{2''}), 6.63

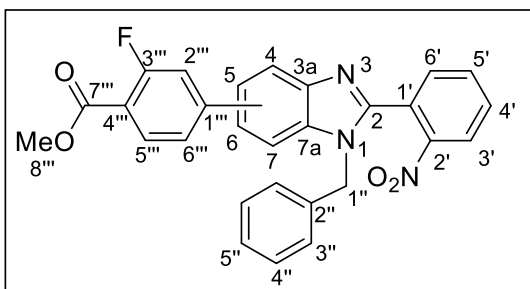
(s, 1H, H_{2'''}, H_{6'''}), 5.19 (s, 1H, H_{1''}), 5.17 (s, 1H, H_{1''}), 3.87-3.80 (m, 9H, H_{7''}, H_{8''}, H_{9''})

¹³C NMR (101 MHz, CDCl₃): 1:1 regioisomer mixture; δ 153.57, 153.55, 150.4, 150.3, 148.9, 137.71, 137.67, 137.5, 137.1, 135.6, 135.4, 135.3, 134.5, 133.54, 133.51, 132.83, 132.77, 131.54, 131.46, 129.12, 129.08, 128.3, 128.2, 126.9, 126.8, 125.7, 125.2, 125.1, 123.6, 122.9, 120.2, 118.4, 111.0, 109.3, 105.0, 104.9, 61.1, 56.3, 48.7

MS (ESI-TOF): m/z calculated for [C₂₉H₂₆N₃O₅] 496.1872; Found: 496.1870 [M+H]⁺

1-benzyl-5(6)-(3-fluoro-4-(methoxycarbonyl)phenyl)-2-(2-nitrophenyl)-1H-benzimidazole (3.6)

In a *Schlenk* tube, 1-benzyl-5(6)-bromo-2-(2-nitrophenyl)-1H-benzimidazole (300 mg, 0.74 mmol) and 3-fluoro-4-(methoxycarbonyl)phenylboronic acid (293 mg, 1.48 mmol) were dissolved in a mixture of THF/H₂O 4:1 (8 mL). Under an argon flow, Pd(OAc)₂ (16 mg; 0.074 mmol), PPh₃ (48 mg; 0.18 mmol) and K₂CO₃ (100 mg, 1.38 mmol) were added and the reaction was heated to 70 °C for 16 h. After cooling, ethyl acetate was added to the reaction, and the insoluble solid was filtered. The organic phase was then washed with water (2x). After drying with Na₂SO₄ and filtering, the solvent was evaporated. Then, a column chromatography in silica gel was performed using dichloromethane/ethyl acetate 5:1 as eluent. The isomer mixture was obtained as a yellow solid in 80% yield (286 mg).



^1H NMR (400 MHz, acetone- d_6): 1:1 regioisomer mixture; δ , ppm 8.28-8.20 (m, 1H, H_{Ar}), 8.06 (d, $J = 1.7$ Hz, 0.5H, H_{Ar}), 8.04-7.95 (m, 1H, H_{Ar}), 7.95 (d, $J = 1.7$ Hz, 0.5H, H_{Ar}), 7.90-7.83 (m, 2H, H_{Ar}), 7.80 (d, $J = 8.5$

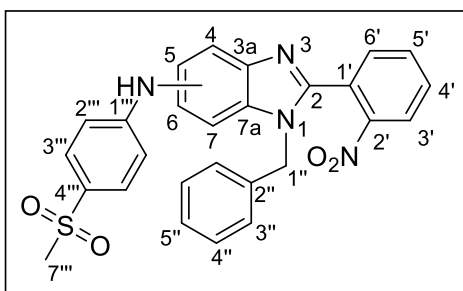
Hz, 0.5H, H_{Ar}), 7.76-7.52 (m, 4.5H, H_{Ar}), 7.33-7.23 (m, 3H, H_{Ar}), 7.20-7.15 (m, 2H, H_{Ar}), 5.28 (s, 1H, $H_{1''}$), 5.25 (s, 1H, $H_{1''}$), 3.94 (s, 1.5H, $H_{8'''}$), 3.93 (s, 1.5H, $H_{8'''}$)

^{13}C NMR (101 MHz, acetone- d_6): 1:1 regioisomer mixture; δ , ppm: 165.0, 164.9, 164.9, 164.9, 164.3, 164.2, 161.7, 161.6, 152.0, 151.9, 150.4, 150.3, 149.3, 149.2, 149.1, 149.0, 144.9, 144.9, 137.2, 137.1, 137.1, 136.9, 134.4, 134.3, 134.3, 134.2, 133.8, 133.8, 133.3, 133.2, 133.2, 132.3, 132.3, 129.6, 129.5, 128.6, 128.6, 127.9, 127.9, 126.5, 126.4, 125.8, 125.7, 123.6, 123.6, 123.4, 122.6, 121.2, 119.4, 117.6, 117.5, 117.5, 117.4, 116.1, 116.1, 115.9, 115.8, 112.5, 110.7, 52.5, 52.5, 49.0, 48.8

MS (ESI-TOF): m/z calculated for $[\text{C}_{28}\text{H}_{21}\text{FN}_3\text{O}_4]$ 482.1516; Found: 482.1513 $[\text{M}+\text{H}]^+$

1-benzyl-*N*-(4-(methylsulfonyl)phenyl)-2-(2-nitrophenyl)-1*H*-benzimidazol-5(6)-amine (3.7)

In a *Schlenk* tube, $\text{Pd}(\text{OAc})_2$ (0.074 mmol, 16.5 mg), XPhos (0.11 mmol, 53 mg), 1-benzyl-5(6)-bromo-2-(2-nitrophenyl)-1*H*-benzimidazole (300 mg, 0.74 mmol), 4-(methylsulfonyl)aniline (151 mg, 0.88 mmol) and Cs_2CO_3 (1.47 mmol, 479 mg) were added to dry dioxane (5 mL) and the temperature was set to 100 °C. The reaction was carried out at reflux temperature for 16 h. After cooling, the crude mixture was filtered and the solid was washed with acetone. The filtrate was evaporated and a column chromatography in silica gel was performed using dichloromethane/ethyl acetate 1:1 as eluent. After drying, a brown solid was obtained in 78% yield (282 mg).



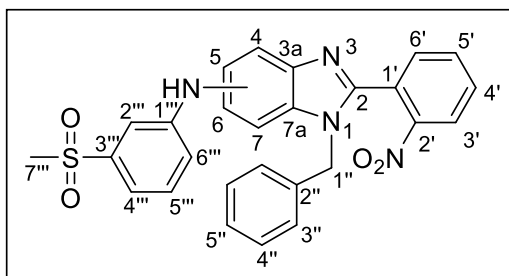
^1H NMR (400 MHz, acetone- d_6): 1:1 regioisomer mixture; δ , ppm 8.25-8.10 (m, 2H, H_{Ar} , H_{NH}), 7.90-7.80 (m, 2H, H_{Ar}), 7.80-7.55 (m, 4H, H_{Ar}), 7.42 (d, $J = 8.6$ Hz, 0.5H, H_{Ar}), 7.36-7.16 (m, 6H, H_{Ar}), 7.16-7.08 (m, 1.5H, H_{Ar}), 7.04 (d, $J = 8.9$ Hz, 1H, H_{Ar}), 5.46 (s, 1H, $H_{1''}$), 5.44 (s, 1H, $H_{1''}$), 3.01 (s, 3H, $H_{7''}$)

^{13}C NMR (101 MHz, acetone- d_6): 1:1 regioisomer mixture; δ , ppm 151.6, 151.3, 150.8, 150.6, 150.4, 145.1, 141.0, 137.6, 137.3, 136.9, 136.8, 134.21, 134.15, 133.4, 133.3, 133.2, 132.2, 132.1, 130.8, 130.4, 130.1, 130.0, 129.62, 129.57, 128.6, 127.91, 127.87, 126.60, 126.56, 125.73, 125.70, 121.4, 119.9, 118.4, 114.5, 114.2, 114.1, 113.7, 112.5, 104.1, 48.9, 44.94, 44.88;

MS (ESI-TOF): m/z calculated for $[\text{C}_{27}\text{H}_{23}\text{N}_4\text{O}_4\text{S}]$ 499.1440; Found: 499.1434 $[\text{M}+\text{H}]^+$

1-benzyl-*N*-(3-(methylsulfonyl)phenyl)-2-(2-nitrophenyl)-1*H*-benzimidazol-5(6)-amine (3.8)

In a *Schlenk* tube, $\text{Pd}(\text{OAc})_2$ (0.074 mmol, 16.5 mg), XPhos (0.11 mmol, 53 mg), 1-benzyl-5(6)-bromo-2-(2-nitrophenyl)-1*H*-benzimidazole (300 mg, 0.74 mmol), 3-(methylsulfonyl)aniline (151 mg, 0.88 mmol) and Cs_2CO_3 (1.47 mmol, 479 mg) were added to dry dioxane (5 mL) and the temperature was set to 100 °C. The reaction was carried out at reflux temperature for 16 h. After cooling, the crude mixture was filtered and the solid was washed with acetone. The filtrate was evaporated and a column chromatography in silica gel was performed using dichloromethane/ethyl acetate 1:1 as eluent ($R_f = 0.23$). After drying, a brown solid was obtained in 81% yield (300 mg).



^1H NMR (400 MHz, acetone- d_6): 1:1 regioisomer mixture; δ , ppm 8.12 (s, 1H, H_{NH}), 7.77 (dd, $J = 7.6, 1.7$ Hz, 1H, H_{Ar}), 7.45-7.36 (m, 2H, H_{Ar}), 7.31 (dd, $J = 7.3, 1.8$ Hz, 1H, H_{Ar}), 7.04-6.95 (m, 4H, H_{Ar}), 6.85-6.75 (m, 5H, H_{Ar}),

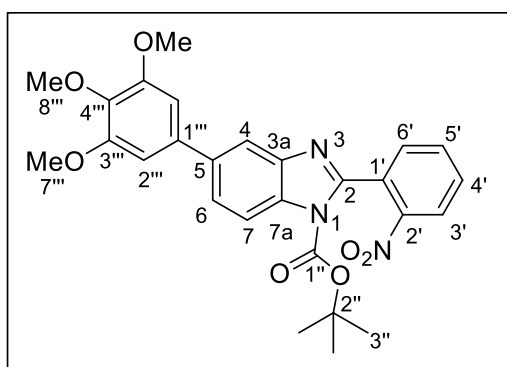
6.70-6.64 (m, 3H, H_{Ar}), 4.95 (m, 2H, $H_{1''}$), 2.70 (s, 3H, $H_{7''}$)

¹³C NMR (101 MHz, acetone-d₆): 1:1 regioisomer mixture; δ, ppm 149.7, 149.0, 146.3, 143.5, 141.8, 136.9, 136.3, 133.6, 132.2, 131.6, 131.2, 130.3, 128.6, 127.7, 127.0, 124.94, 124.93, 118.7, 117.6, 116.0, 111.9, 111.6, 109.9, 47.6, 43.7

MS (ESI-TOF): m/z calculated for [C₂₇H₂₃N₄O₄S] 499.1440; Found: 499.1436 [M+H]⁺

1-boc-5-(3,4,5-trimethoxyphenyl)-2-(2-nitrophenyl)-1H-benzimidazole (3.9a)

In a *Schlenk* tube, 1-boc-5-bromo-2-(2-nitrophenyl)-1H-benzimidazole (300 mg, 0.72 mmol) and 3,4,5-trimethoxyphenylboronic acid (229 mg, 1.08 mmol) were dissolved in a mixture of THF/H₂O 4:1 (5 mL). Under an argon flow, Pd(OAc)₂ (16 mg; 0.72 mmol), PPh₃ (47 mg; 0.18 mmol) and K₂CO₃ (89 mg, 2.2 mmol) were added and the reaction was heated to 70 °C for 16 h. After cooling, ethyl acetate was added to the reaction, and the insoluble solid was filtered. The organic phase was then washed with a 1M solution of NaOH (5x), followed by water (2x). After drying with Na₂SO₄ and filtering, the solvent was evaporated. Then, a column chromatography in silica gel was performed using a gradient mixture as eluent, starting with dichloromethane and ending in dichloromethane/ethyl acetate 20:1. The light yellow solid was obtained in 72% yield (260 mg).



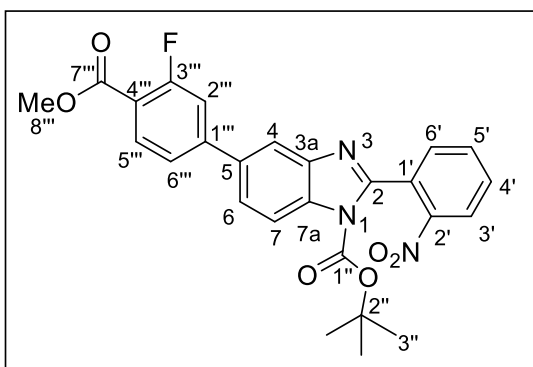
¹H NMR (400 MHz, acetone-d₆): δ, ppm 8.36 (m, 1H, H_{3'}), 8.14 (d, *J* = 8.6 Hz, 1H, H₇), 8.00-7.95 (m, 2H, H₄, H_{5'}), 7.91-7.85 (m, 2H, H_{4'}, H_{6'}), 7.78 (dd, *J* = 8.6, 1.8 Hz, 1H, H₆), 7.04 (s, 2H, H_{2'''}), 3.96 (s, 6H, H_{7'''}), 3.79 (s, 3H, H_{8'''}), 1.39 (s, 9H, H_{3''})

¹³C NMR (101 MHz, acetone-d₆): δ, ppm 154.9, 151.3, 148.93, 148.91, 144.6, 139.1, 139.0, 137.6, 135.0, 133.5, 133.3, 131.8, 130.1, 125.5, 125.4, 119.2, 116.2, 105.8, 86.5, 60.73, 60.65, 56.7, 27.7

MS (ESI-TOF): m/z calculated for [C₂₇H₂₈N₃O₇] 506.1927; Found: 506.1924 [M+H]⁺

1-boc-5-(3-fluoro-4-(methoxycarbonyl)phenyl)-2-(2-nitrophenyl)-1H-benzimidazole (3.10a)

In a *Schlenk* tube, 1-boc-5-bromo-2-(2-nitrophenyl)-1H-benzimidazole (300 mg, 0.74 mmol) and 3-fluoro-4-(methoxycarbonyl)phenylboronic acid (170 mg, 0.86 mmol) were dissolved in a mixture of THF/H₂O 4:1 (5 mL). Under an argon flow, Pd(OAc)₂ (16 mg; 0.074 mmol), PPh₃ (48 mg; 0.18 mmol) and K₂CO₃ (298 mg, 2.15 mmol) were added and the reaction was heated to 70 °C for 16h. After cooling, ethyl acetate was added to the reaction, and the insoluble solid was filtered. The organic phase was then washed with water (2x). After drying with Na₂SO₄ and filtering, the solvent was evaporated. Then, a column chromatography in silica gel was performed using dichloromethane as eluent. The product was obtained as a yellow solid in 66% yield (235 mg).



¹H NMR (400 MHz, acetone-d₆): δ, ppm 8.45 (d, *J* = 1.8 Hz, 1H, H₄), 8.39-8.36 (m, 1H, H_{3'}), 8.07 (t, *J* = 7.9 Hz, 1H, H_{5''}), 8.02-7.97 (m, 1H, H_{5'}), 7.92-7.87 (m, 2H, H_{4'}, H_{6'}), 7.86 (d, *J* = 8.4, 1H, H₇), 7.82 (dd, *J* = 8.4, 1.8 Hz, 1H, H₆), 7.72 (dd, *J* = 8.0, 1.8 Hz, 1H, H_{6''}), 7.65 (dd, *J* = 12.3, 1.8 Hz, 1H, H_{2''}), 3.93 (s, 6H, H_{8''}), 1.40 (s, 9H, H_{3''})

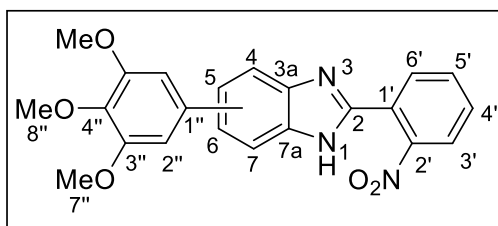
¹³C NMR (101 MHz, acetone-d₆): δ, ppm 165.0 (d, *J* = 3.7 Hz), 163.1 (d, *J* = 258.1 Hz), 152.0, 148.87 (d, *J* = 8.8 Hz), 148.84, 148.79, 144.5, 136.8 (d, *J* = 2.0 Hz), 135.1, 134.8, 133.7 (d, *J* = 1.7 Hz), 133.3, 131.9, 129.9, 125.4, 124.8, 123.9 (d, *J* = 3.4 Hz), 121.6, 118.2 (d, *J* = 10.6 Hz), 116.4 (d, *J* = 23.6 Hz), 115.0, 86.8, 52.6, 27.7

MS (ESI-TOF): *m/z* calculated for [C₂₆H₂₃FN₃O₆] 492.1571; Found: 492.1564 [M+H]⁺

5(6)-(3,4,5-trimethoxyphenyl)-2-(2-nitrophenyl)-1H-benzimidazole (3.11)

In a round-bottom flask, 1-boc-5-(3,4,5-trimethoxyphenyl)-2-(2-nitrophenyl)-1H-benzimidazole (0.28 mmol, 140 mg) was dissolved in a mixture of DCM/TFA 1:1 (2.0 mL). After 3 h, the acid was neutralized by slow addition of a saturated aqueous solution of

NaHCO₃. Dichloromethane was added and the organic phase was washed 2x with a saturated solution of NaHCO₃ and then 2x with H₂O, followed by drying over anhydrous Na₂SO₄, filtering and solvent evaporation. The product was purified by column chromatography in silica gel using DCM/Ethyl acetate 1:2 as eluent (R_f = 0.37). After drying, a yellow solid was obtained in 99% yield (112 mg).



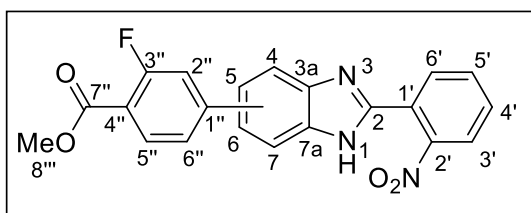
¹H NMR (400 MHz, DMSO-d₆): δ, ppm 13.09 (brs, 1H, H_{NH}), 8.04 (dd, *J* = 8.1, 1.2 Hz, 1H, H_{3'}), 8.00 (dd, *J* = 7.6, 1.4 Hz, 1H, H_{6'}), 7.91 – 7.87 (m, 2H, H_{5'}, H_{4/7}), 7.77 (ddd, *J* = 8.1, 7.6, 1.4 Hz, 1H, H_{4'}), 7.67 (d, *J* = 8.4 Hz, 1H, H_{7/4}), 7.59 (dd, *J* = 8.4, 1.7 Hz, 1H, H_{6/5}), 6.97 (s, 2H, H_{2''}), 3.89 (s, 6H, H_{7''}), 3.70 (s, 3H, H_{8''})

¹³C NMR (101 MHz, DMSO-d₆): δ, ppm 153.2, 149.0, 148.0, 136.80, 136.78, 135.3, 132.7, 131.0, 130.9, 124.3, 124.1, 122.2, 104.4, 60.1, 56.0. Missing ¹³C resonances are not visible due to tautomerism.

MS (ESI-TOF): *m/z* calculated for [C₂₂H₂₀N₃O₅] 406.1403; Found: 406.1404 [M+H]⁺

5(6)-(3-fluoro-4-(methoxycarbonyl)phenyl)-2-(2-nitrophenyl)-1H-benzimidazole (3.12)

In a round-bottom flask, 1-boc-5-(3,4,5-trimethoxyphenyl)-2-(2-nitrophenyl)-1H-benzimidazole (0.42 mmol, 208 mg) was dissolved in DCM (2.0 mL) and TFA (0.4 mL) was added. After 5 h, the acid was neutralized by slow addition of a saturated aqueous solution of NaHCO₃. Dichloromethane was added and the organic phase was washed 2x with a saturated solution of NaHCO₃ and then 2x with H₂O, followed by drying over anhydrous Na₂SO₄, filtering and solvent evaporation. The product was purified by column chromatography in silica gel using DCM/Ethyl acetate 6:1 as eluent (R_f = 0.27). After drying, a yellow solid was obtained in 65% yield (107 mg).



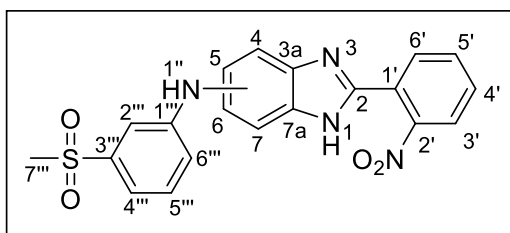
^1H NMR (400 MHz, acetone- d_6): δ , ppm 12.20-12.15 (m, 1H, $\underline{H_{NH}}$), 8.09 – 7.93 (m, 4H, $\underline{H_{Ar}}$), 7.88 (td, $J = 7.6, 1.4$ Hz, 1H, $\underline{H_{Ar}}$), 7.83 – 7.59 (m, 5H, $\underline{H_{Ar}}$), 3.92 (s, 3H, $\underline{H_{8''}}$)

^{13}C NMR (101 MHz, acetone- d_6): δ , ppm 165.0 (d, $J = 3.8$ Hz), 163.0 (d, $J = 258.1$ Hz), 150.5, 149.9, 149.3 (d, $J = 8.8$ Hz), 133.5, 133.4 (d, $J = 1.7$ Hz), 132.1, 131.8, 125.8, 125.3, 123.6 (d, $J = 3.2$ Hz), 117.4, 116.0 (d, $J = 23.4$ Hz), 52.5. Missing ^{13}C resonances are not visible due to tautomerism.

MS (ESI-TOF): m/z calculated for $[\text{C}_{21}\text{H}_{15}\text{FN}_3\text{O}_4]$ 392.1047; Found: 392.1042 $[\text{M}+\text{H}]^+$

***N*-(3-(methylsulfonyl)phenyl)-2-(2-nitrophenyl)-1*H*-benzimidazol-5(6)-amine (3.13)**

In a *Schlenk* tube, $\text{Pd}(\text{OAc})_2$ (0.072 mmol, 16.1 mg), XPhos (0.11 mmol, 52 mg), 1-benzyl-5(6)-bromo-2-(2-nitrophenyl)-benzimidazole (300 mg, 0.72 mmol), 3-(methylsulfonyl)aniline (147 mg, 0.86 mmol) and Cs_2CO_3 (1.43 mmol, 467 mg) were added to dry dioxane (5 mL) and the temperature was set to 100 °C. The reaction was carried out at reflux temperature for 16 h. After cooling, the crude mixture was filtered and the solid was washed with acetone. The filtrate was evaporated and dissolved in a mixture of DCM/TFA 1:1 (4.0 mL). After 2 h, the acid was neutralized by slow addition of a saturated aqueous solution of NaHCO_3 . Ethyl acetate was added to the mixture and the organic phase was washed 2x with a saturated solution of NaHCO_3 and then 2x with H_2O . The organic phase was dried with anhydrous Na_2SO_4 , filtered and evaporated. Purification by column chromatography in silica gel was performed using dichloromethane/ethyl acetate 1:1 as eluent. After drying, a brown solid was obtained in 48% yield (140 mg).



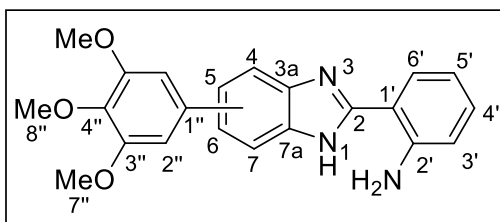
^1H NMR (400 MHz, acetone- d_6): δ , ppm 11.95 (brs, 1H, $\underline{H_1}$), 8.02 (dd, $J = 7.6, 1.4$ Hz, 1H, $\underline{H_{6'}}$), 7.98 (dd, $J = 8.0, 1.2$ Hz, 1H, $\underline{H_{3'}}$), 7.87 (brs, 1H, $\underline{H_{1''}}$), 7.84 (td, $J = 7.6, 1.2$ Hz, 1H, $\underline{H_{5'}}$), 7.74 (ddd, $J = 8.0, 7.6, 1.4$ Hz, 1H, $\underline{H_{4'}}$), 7.65-7.55 (m, 2H, $\underline{H_{6/5}}$, $\underline{H_{2''}}$), 7.47 (brs, 1H, $\underline{H_{4/7}}$), 7.44 (t, $J = 7.9$ Hz, 1H, $\underline{H_{5''}}$), 7.35 (d, $J = 7.9$ Hz, 1H, $\underline{H_{4''}}$), 7.31 (d, $J = 7.9$ Hz, 1H, $\underline{H_{6''}}$), 7.16 (d, $J = 8.6$ Hz, 1H, $\underline{H_{7/4}}$), 3.08 (s, 3H, $\underline{H_{7''}}$)

¹³C NMR (101 MHz, acetone-d₆): δ, ppm 150.4, 143.4, 133.3, 131.8, 131.4, 131.1, 125.9, 125.2, 117.8, 113.7, 44.3. Missing ¹³C resonances are not visible due to tautomerism.

MS (ESI-TOF): m/z calculated for [C₂₀H₁₇N₄O₄S] 409.0971; Found: 409.0964 [M+H]⁺

2-(2-aminophenyl)-5(6)-(3,4,5-trimethoxyphenyl)-1H-benzimidazole (3.14)

In a round-bottom flask, 5(6)-(3,4,5-trimethoxyphenyl)-2-(2-nitrophenyl)-1H-benzimidazole (50 mg, 0.125 mmol), hydrazine monohydrate (45 μL, 1.25 mmol) and Pd/C 5% (10 mg) were mixed in methanol (1.0 mL). The solution was stirred for 30 min at reflux temperature (70 °C). The resulting solution was filtrated and the solvent evaporated. A white solid was obtained in 91% yield (43 mg).



¹H NMR (400 MHz, CD₃OD): δ, ppm 7.77 (brs, 1H, H_{Ar}), 7.72 (dd, *J* = 8.0, 1.5 Hz, 1H, H_{6'}), 7.61 (brs, 1H, H_{Ar}), 7.48 (dd, *J* = 8.3, 1.6 Hz, 1H, H_{6/5}), 7.19 (ddd, *J* = 8.2, 7.2, 1.6 Hz, 1H, H_{4'}), 6.88 (dd,

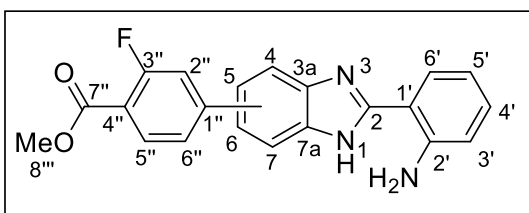
J = 8.2, 1.2 Hz, 1H, H_{3'}), 6.75 (ddd, *J* = 8.0, 7.2, 1.2 Hz, 1H, H_{5'}), 3.92 (s, 6H, H_{7''}), 3.81 (s, 3H, H_{8''})

¹³C NMR (101 MHz, CD₃OD): δ, ppm 154.8, 154.7, 149.1, 139.7, 138.4, 131.8, 128.6, 123.1, 117.9, 117.7, 113.2, 105.8, 61.2, 56.7

MS (ESI-TOF): m/z calculated for [C₂₂H₂₂N₃O₃] 376.1661; Found: 376.1655 [M+H]⁺

2-(2-aminophenyl)-5(6)-(3-fluoro-4-(methoxycarbonyl)phenyl)-1H-benzimidazole (3.15)

In a closed reactor, 5(6)-(3-fluoro-4-(methoxycarbonyl)phenyl)-2-(2-nitrophenyl)-1H-benzimidazole (20 mg, 0.051 mmol) and Pd/C 5% (2 mg) were mixed in methanol (2.0 mL). The reactor was charged with H₂ (5 bar) and the reaction was stirred at room temperature during 8 h. After gas depressurization, the solid Pd/C was filtered off and the methanolic solution was evaporated. A light-yellow solid was obtained in 90% yield (25 mg).



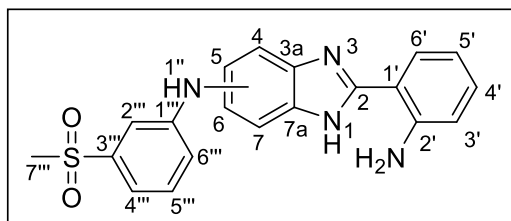
^1H NMR (400 MHz, CD_3OD): δ , ppm 8.00-7.84 (m, 3H, H_{Ar}), 7.72 (t, $J = 8.4$ Hz, 1H, H_{Ar}), 7.57-7.41 (m, 3H, H_{Ar}), 7.72 (t, $J = 7.7$ Hz, 1H, H_{Ar}), 6.90-6.80 (m, 2H, H_{Ar}), 3.89 (s, 3H, $\text{H}_{8''''}$)

^{13}C NMR (101 MHz, CD_3OD): δ , ppm 164.0, 161.8 (d, $J = 295$ Hz), 154.0 (d, $J = 24$ Hz), 148.4, 143.7, 134.3, 132.3, 130.7, 127.4, 122.6, 121.9, 121.1, 118.6, 116.2, 115.0, 111.3, 109.7 (d, $J = 6.8$ Hz), 52.3. Missing ^{13}C resonances are not visible due to tautomerism.

MS (ESI-TOF): m/z calculated for $[\text{C}_{21}\text{H}_{16}\text{FN}_3\text{O}_2]$ 362.1305; Found: 362.1310 $[\text{M}+\text{H}]^+$

2-(2-aminophenyl)-N-(3-(methylsulfonyl)phenyl)-1H-benzimidazol-5(6)-amine (3.16)

In a round-bottom flask, *N*-(3-(methylsulfonyl)phenyl)-2-(2-nitrophenyl)-1H-benzimidazol-5(6)-amine (40 mg, 0.098 mmol), hydrazine monohydrate (50 μL , 1.5 mmol) and Pd/C 5% (8 mg) were mixed in methanol (2.0 mL). The solution was stirred for 30 min at reflux temperature (70 $^\circ\text{C}$). The resulting solution was filtrated and the solvent evaporated. A white solid was obtained in 80% yield (30 mg).



^1H NMR (400 MHz, CD_3OD): δ , ppm 7.68 (dd, $J = 8.0, 1.5$ Hz, 1H, $\text{H}_{6'}$), 7.54 (m, 2H, H_{Ar}), 7.39 (m, 2H, H_{Ar}), 7.27 (m, 2H, H_{Ar}), 7.18 (ddd, $J = 8.2, 7.2, 1.5$ Hz, 1H, $\text{H}_{4'}$), 7.07 (dd, $J = 8.6, 2.1$ Hz, 1H, H_{Ar}), 6.87 (dd, $J = 8.2, 1.2$ Hz, 1H, $\text{H}_{3'}$),

6.74 (ddd, $J = 8.0, 7.2, 1.2$ Hz, 1H, $\text{H}_{5'}$), 3.08 (s, 3H, $\text{H}_{7''''}$)

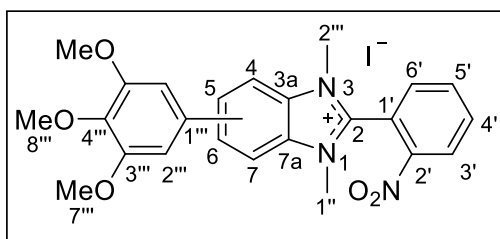
^{13}C NMR (101 MHz, CD_3OD): δ , ppm 154.4, 148.9, 148.5, 142.8, 131.6, 131.3, 128.5, 120.7, 117.9, 117.8, 117.4, 113.5, 113.3, 44.4

MS (ESI-TOF): m/z calculated for $[\text{C}_{20}\text{H}_{19}\text{N}_4\text{O}_2\text{S}]$ 379.1229; Found: 379.1228 $[\text{M}+\text{H}]^+$

1,3-dimethyl-5(6)-(3,4,5-trimethoxyphenyl)-2-(2-nitrophenyl)-1H-benzimidazol-3-ium iodide (3.17)

In a round-bottom flask, 5(6)-(3,4,5-trimethoxyphenyl)-2-(2-nitrophenyl)-1H-benzimidazole (70 mg, 0.17 mmol), iodomethane (54 μL , 0.86 mmol) and K_2CO_3 (48 mg, 0.35 mmol) were mixed in DMF (2.0 mL) at 50 $^\circ\text{C}$ during 24 h, with more addition of

iodomethane (54 μ L, 0.86 mmol) after 16 h. Afterwards the base was filtered off and washed with THF. The solvent was evaporated under reduced pressure and the resulting solid was washed with 10 mL of acetone, filtered and dried. A yellow solid was obtained in 96% yield (93 mg).



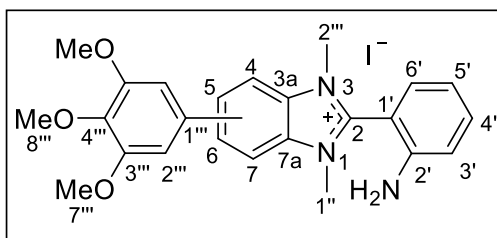
^1H NMR (400 MHz, DMSO- d_6): δ , ppm 8.71 (dd, $J = 8.1, 1.4$ Hz, 1H, H_{Ar}), 8.43 (brs, 1H, H_{Ar}), 8.27 – 8.14 (m, 5H), 7.14 (s, 2H, $H_{2''}$), 3.93 (s, 6H, $H_{7''}$), 3.90 (s, 3H, $H_{1''/2''}$), 3.86 (s, 3H, $H_{1''/2''}$), 3.73 (s, 3H, $H_{8''}$).

^{13}C NMR (101 MHz, DMSO- d_6): δ , ppm 153.4, 148.1, 146.8, 139.6, 137.9, 136.0, 135.2, 134.6, 133.1, 132.4, 131.1, 126.7, 126.3, 115.9, 113.8, 111.3, 105.1, 60.2, 56.3, 32.68, 32.65

MS (ESI-TOF): m/z calculated for $[\text{C}_{24}\text{H}_{24}\text{N}_3\text{O}_5]$ 434.1711; Found: 434.1709 $[\text{M-I}]^+$

2-(2-aminophenyl)-1,3-dimethyl-5(6)-(3,4,5-trimethoxyphenyl)-1H-benzimidazol-3-ium iodide (3.18)

In a round-bottom flask, 1,3-dimethyl-5(6)-(3,4,5-trimethoxyphenyl)-2-(2-nitrophenyl)-1H-benzimidazol-3-ium iodide (25 mg, 0.045 mmol), hydrazine monohydrate (22 μ L, 0.45 mmol) and Pd/C 5% (5 mg) were mixed in methanol (2.0 mL). The solution was stirred for 30 min at reflux temperature (70 $^{\circ}\text{C}$). The resulting solution was filtrated and the solvent evaporated. A white compound was obtained in 85% yield (20 mg).



^1H NMR (400 MHz, CD_3OD): δ , ppm 8.19 (brs, 1H, H_{Ar}), 8.02 (brs, 2H, H_{Ar}), 7.54-7.46 (m, 1H, H_{Ar}), 7.35 (dd, $J = 7.8, 1.6$ Hz, 1H, H_{Ar}), 7.09-7.00 (m, 3H, H_{Ar}), 6.93 (t, $J = 7.4$ Hz, 1H, H_{Ar}), 4.00 (s, 3H, H_{Me}), 3.97 (br, 9H, H_{Me}), 3.84 (s, 3H, H_{Me})

^{13}C NMR (101 MHz, CD_3OD): δ , ppm 154.8, 152.1, 149.9, 141.7, 139.2, 137.0, 135.5, 134.4, 133.1, 132.1, 127.4, 118.4, 118.1, 114.1, 112.0, 106.2, 105.0, 61.2, 57.0, 33.4, 33.1

MS (ESI-TOF): m/z calculated for $[\text{C}_{24}\text{H}_{26}\text{N}_3\text{O}_3]$ 404.1969; Found: 404.1968 $[\text{M-I}]^+$

4.4 – References

- [1] Armarego, W. L. F., *Purification of Laboratory Chemicals*. 7th edition ed.; Butterworth-Heinemann: United Kingdom, **2012**.
- [2] Aroso, R. T.; Calvete, M. J. F.; Pucelik, B.; Dubin, G.; Arnaut, L. G.; Pereira, M. M.; Dąbrowski, J. M., Photoinactivation of microorganisms with sub-micromolar concentrations of imidazolium metallophthalocyanine salts, *European Journal of Medicinal Chemistry*, **2019**, *184*, 111740.
- [3] Arnaut, Z. A. Development of cationic photosensitizers for photoinactivation of microorganisms, **2021**, MSc thesis in Medicinal Chemistry, University of Coimbra.
- [4] Vinagreiro, C. S.; Zangirolami, A.; Schaberle, F. A.; Nunes, S. C. C.; Blanco, K. C.; Inada, N. M.; da Silva, G. J.; Pais, A.; Bagnato, V. S.; Arnaut, L. G.; Pereira, M. M., Antibacterial Photodynamic Inactivation of Antibiotic-Resistant Bacteria and Biofilms with Nanomolar Photosensitizer Concentrations, *ACS Infectious Diseases*, **2020**, *6*, 1517-1526.
- [5] Van Aken, K.; Strekowski, L.; Patiny, L., EcoScale, a semi-quantitative tool to select an organic preparation based on economical and ecological parameters, *Beilstein Journal of Organic Chemistry*, **2006**, *2*, 3.
- [6] *Clinical and Laboratory Standards Institute, Performance Standards for Antimicrobial Disk Susceptibility Tests; CLSI standard M02*. 13th Edition ed.; Clinical and Laboratory Standards Institute: Wayne, PA, **2018**.
- [7] Schaberle, F. A., Assessment of the actual light dose in photodynamic therapy, *Photodiagnosis and Photodynamic Therapy*, **2018**, *23*, 75-77.
- [8] Takakura, N.; Sato, Y.; Ishibashi, H.; Oshima, H.; Uchida, K.; Yamaguchi, H.; Abe, S., A Novel Murine Model of Oral Candidiasis with Local Symptoms Characteristic of Oral Thrush, *Microbiology and Immunology*, **2003**, *47*, 321-326.
- [9] Tomašič, T.; Barančoková, M.; Zidar, N.; Ilaš, J.; Tammela, P.; Kikelj, D., Design, synthesis, and biological evaluation of 1-ethyl-3-(thiazol-2-yl)urea derivatives as Escherichia coli DNA gyrase inhibitors, *Archiv der Pharmazie*, **2018**, *351*, 1700333.
- [10] Durcik, M.; Tammela, P.; Barančoková, M.; Tomašič, T.; Ilaš, J.; Kikelj, D.; Zidar, N., Synthesis and Evaluation of N-Phenylpyrrolamides as DNA Gyrase B Inhibitors, *ChemMedChem*, **2018**, *13*, 186-198.
- [11] Ostrov, D. A.; Hernández Prada, J. A.; Corsino, P. E.; Finton, K. A.; Le, N.; Rowe, T. C., Discovery of Novel DNA Gyrase Inhibitors by High-Throughput Virtual Screening, *Antimicrobial Agents and Chemotherapy*, **2007**, *51*, 3688-3698.
- [12] Gjorgjieva, M.; Tomašič, T.; Barančokova, M.; Katsamakos, S.; Ilaš, J.; Tammela, P.; Peterlin Mašič, L.; Kikelj, D., Discovery of Benzothiazole Scaffold-Based DNA Gyrase B Inhibitors, *Journal of Medicinal Chemistry*, **2016**, *59*, 8941-8954.
- [13] Jakopin, Ž.; Ilaš, J.; Barančoková, M.; Brvar, M.; Tammela, P.; Sollner Dolenc, M.; Tomašič, T.; Kikelj, D., Discovery of substituted oxadiazoles as a novel scaffold for DNA gyrase inhibitors, *European Journal of Medicinal Chemistry*, **2017**, *130*, 171-184.
- [14] Ronkin, S. M.; Badia, M.; Bellon, S.; Grillot, A.-L.; Gross, C. H.; Grossman, T. H.; Mani, N.; Parsons, J. D.; Stamos, D.; Trudeau, M.; Wei, Y.; Charifson, P. S., Discovery of pyrazolthiazoles as novel and potent inhibitors of bacterial gyrase, *Bioorganic & Medicinal Chemistry Letters*, **2010**, *20*, 2828-2831.

- [15] Eakin, A. E.; Green, O.; Hales, N.; Walkup, G. K.; Bist, S.; Singh, A.; Mullen, G.; Bryant, J.; Embrey, K.; Gao, N.; Breeze, A.; Timms, D.; Andrews, B.; Uria-Nickelsen, M., *et al.*, Pyrrolamide DNA Gyrase Inhibitors: Fragment-Based Nuclear Magnetic Resonance Screening To Identify Antibacterial Agents, *Antimicrobial Agents & Chemotherapy*, **2012**, *56*, 1240-1246.
- [16] Cotman, A. E.; Trampuž, M.; Brvar, M.; Kikelj, D.; Ilaš, J.; Peterlin-Mašič, L.; Montalvão, S.; Tammela, P.; Frlan, R., Design, Synthesis, and Evaluation of Novel Tyrosine-Based DNA Gyrase B Inhibitors, *Archiv der Pharmazie*, **2017**, *350*, 1700087.
- [17] Basarab, G. S.; Manchester, J. I.; Bist, S.; Boriack-Sjodin, P. A.; Dangel, B.; Illingworth, R.; Sherer, B. A.; Sriram, S.; Uria-Nickelsen, M.; Eakin, A. E., Fragment-to-Hit-to-Lead Discovery of a Novel Pyridylurea Scaffold of ATP Competitive Dual Targeting Type II Topoisomerase Inhibiting Antibacterial Agents, *Journal of Medicinal Chemistry*, **2013**, *56*, 8712-8735.
- [18] Trzoss, M.; Bensen, D. C.; Li, X.; Chen, Z.; Lam, T.; Zhang, J.; Creighton, C. J.; Cunningham, M. L.; Kwan, B.; Stidham, M.; Nelson, K.; Brown-Driver, V.; Castellano, A.; Shaw, K. J., *et al.*, Pyrrolopyrimidine inhibitors of DNA gyrase B (GyrB) and topoisomerase IV (ParE), Part II: Development of inhibitors with broad spectrum, Gram-negative antibacterial activity, *Bioorganic & Medicinal Chemistry Letters*, **2013**, *23*, 1537-1543.
- [19] Shirude, P. S.; Madhavapeddi, P.; Tucker, J. A.; Murugan, K.; Patil, V.; Basavarajappa, H.; Raichurkar, A. V.; Humnabdkar, V.; Hussein, S.; Sharma, S.; Ramya, V. K.; Narayan, C. B.; Balganesh, T. S.; Sambandamurthy, V. K., Aminopyrazinamides: Novel and Specific GyrB Inhibitors that Kill Replicating and Nonreplicating Mycobacterium tuberculosis, *ACS Chemical Biology*, **2013**, *8*, 519-523.
- [20] Chemical Computing Group ULC. Molecular Operating Environment (MOE). <https://www.chemcomp.com/Products.htm> (accessed on 07/01/2021).
- [21] Mysinger, M. M.; Carchia, M.; Irwin, J. J.; Shoichet, B. K., Directory of Useful Decoys, Enhanced (DUD-E): Better Ligands and Decoys for Better Benchmarking, *Journal of Medicinal Chemistry*, **2012**, *55*, 6582-6594.
- [22] Jones, G.; Willett, P.; Glen, R. C.; Leach, A. R.; Taylor, R., Development and validation of a genetic algorithm for flexible docking, *Journal of Molecular Biology*, **1997**, *267*, 727-748.
- [23] Tari, L. W.; Li, X.; Trzoss, M.; Bensen, D. C.; Chen, Z.; Lam, T.; Zhang, J.; Lee, S. J.; Hough, G.; Phillipson, D.; Akers-Rodriguez, S.; Cunningham, M. L.; Kwan, B. P.; Nelson, K. J., *et al.*, Tricyclic GyrB/ParE (TriBE) Inhibitors: A New Class of Broad-Spectrum Dual-Targeting Antibacterial Agents, *PLoS One*, **2013**, *8*, e84409.
- [24] <https://cactus.nci.nih.gov/download/nci/index.html> (accessed in 02/03/2019).
- [25] Lagorce, D.; Bouslama, L.; Becot, J.; Miteva, M. A.; Villoutreix, B. O., FAF-Drugs4: free ADME-tox filtering computations for chemical biology and early stages drug discovery, *Bioinformatics*, **2017**, *33*, 3658-3660.